The Road to the Unitary Bose Gas

Benno S. Rem

Département de physique
École Normale Supérieure

Laboratoire Kastler Brossel

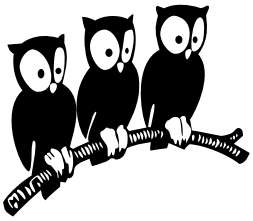

THÉSE de DOCTORAT de l'École Normale Supérieure

Spécialité : Physique Quantique

présentée par

Benno Sebastiaan Rem

pour obtenir le grade de DOCTEUR de l'École Normale Supérieure

---

The Road to the Unitary Bose Gas

Soutenue le 17 Decembre 2013

devant le jury composé de :

M.	**Zoran Hadzibabic**	Rapporteur
M.	**Philippe Lecheminant**	Rapporteur
M.	**Rudolf Grimm**	Examinateur
M.	**Klaus Sengstock**	Examinateur
M.	**Roland Combescot**	Président
M.	**Frédéric Chevy**	Membre invité
M.	**Christophe Salomon**	Directeur de thèse

We shall not cease from exploration
And the end of all our exploring
Will be to arrive where we started
And know the place for the first time.

T.S. Eliot – "Little Gidding" (1922)

Contents

Introduction

In recent years, the field of ultracold quantum gases has rapidly expanded. One of the reasons of this growth is the fact that experiments in the field have the ability to observe quantum correlations without them being washed out by the disturbances caused by thermal fluctuations. These quantum correlations arise as soon as temperatures close to the absolute zero are reached. When a dilute gas is cooled to these temperatures, the wavefunction of an atom starts to overlap with the wavefunctions of neighboring atoms. At this point, the system can no longer be described in terms of individual particles and a formulation in terms of many-body states is required [1].

A many-body state has to obey particle exchange statistics. In a 3 dimensional (3d) world, Nature dictates the existence of two types of particles, which behave differently under particle exchange. These particles are distinguished by a property called spin. On the one hand, there are bosons with integer spin, on the other hand fermions with half-integer spin. Bosons preferably occupy the same quantum state (this behavior is called bunching or bosonic amplification). For fermions, the occupation of a quantum state by more than one particle is forbidden. This phenomenon is called Pauli blocking or anti-bunching [2]. These occupation effects are of purely statistical nature and interactions do not play any role.

Quantum effects due to particle exchange statistics become prominent at low temperatures, when the thermal deBroglie wavelength $\lambda_{\mathrm{th}} = h/\sqrt{2\pi m k_{\mathrm{B}} T}$ becomes of the order of the interparticle distance $l \equiv n^{-1/3}$, where n is the density, h is Planck's constant, k_{B} is Boltzmann's constant, m is the mass of a particle and T the temperature of the system.

In dilute ultracold gases, typical densities are in the range of 10^{12} to 10^{15} cm^{-3}, which implies a typical interparticle distance of 0.1 to 1 μm. To have a deBroglie wavelength comparable to the interparticle distance, the system has to be extremely cold. The advancement of laser [3] and evaporative [4] cooling techniques led to the observation of quantum effects in the 10 to 100 nK temperature range. In 1995, Bose-Einstein condensation (BEC) in ^{87}Rb [5] and ^{23}Na [6] was observed. BEC was predicted by S. N. Bose and A. Einstein in 1924 [7, 8]. It is a form of bunching, where a majority of the atoms occupy the same external state. The advancement

of cooling techniques in bosonic systems also advanced the cooling of fermionic gases. This allowed for the observation of the inset of quantum degeneracy in a fermionic system in 1999 in ^{40}K [9] and shortly afterwards also in ^{6}Li [10, 11].

During my PhD at ENS from december 2010 to december 2013, I worked on a system of ultracold bosonic ^{7}Li with tunable interactions. In the beginning, I participated in the measurements of the Lee-Huang-Young corrections due to increasing two-particle interactions in a BEC. I will not discuss this in detail in this manuscript, however for the interested reader I have included the paper in Appendix B.1). The bulk of this thesis is dedicated to the study of the Bose gas with resonant two-particle interactions. The lifetime of such a gas is limited by three-particle recombination, which we analyze both experimentally and theoretically in this manuscript. Finally, I have also worked on the implementation of a new laser cooling technique, which efficiently cools alkaline atoms below the standard Doppler limit. This topic will not be covered here and for more information the reader is revered to the paper in Appendix B.3.

Quantum Many-Body Systems

Due to their complexity, commonly found quantum many-body systems are usually difficult to study. For example, in High-T_c superconductors, the electron gas is submerged in a complex lattice structure, forcing the electrons to occupy complex orbits [12]. Furthermore, the description of the movement of conductance electrons is complicated by impurities. In special cases, impurities can even cause localization of the wavefunction of the electrons. This phenomenon is called Anderson localization [13]. Another striking example of a hard-to-study quantum system is neutron matter. In this system it is difficult to directly probe interesting observables. It is proposed that the system is described by a Hamiltonian with short-range interactions [14], which facilitates the quantum simulation of the problem with a well controlled quantum gas.

Understanding and probing the detailed properties of the many-body quantum state in these situations is difficult. Using well-controlled environments to simulate these systems will help to understand the properties. This is where ultracold dilute systems come into play, because these systems have quantum correlations together with an unprecedented degree of control over the system parameters. In quantum gases, the density of the system can be well controlled [15]. Lasers can be employed to trap a gas [16], and phase imprinting on these lasers allows to create, among others, flat-box potentials [17, 18] or tightly confining 2d geometries [19]. A

retroreflected laser beam has a standing wave intensity pattern that can be used as a periodic potential that mimics crystal lattices [20]. A major milestone has been the recent advancement of single site imaging [21, 22] and addressing [23] of atoms in optical lattices.

In recent years, several interesting systems with quantum correlations have been studied. The bosonic superfluid-to-Mott-insulator transition [20] was observed in an optical lattice with ultracold atoms [24]. Similarly, the fermionic equivalent [25] was studied with fermions in optical lattices. Lattices were also used to simulate the classic Ising model in frustrated systems [26]. Furthermore, the phase transition to a quantum anti-ferromagnetic state was simulated using a single-site imaging system [27]. Additionally, short-range quantum magnetic spin-correlations in dimerized and anisotropic systems have been observed [28].

The control of the dimensionality opens the opportunity to study low dimensional systems. In a 2d atomic system, the transition from a superfluid to a normal fluid has been observed through the proliferation of vortex-pairs of oppositely rotating vortices above the transition temperature T_c. This transition is the so-called Berezinskii-Kosterlitz-Thouless (BKT) phase transition, which was predicted in 1972 [29, 30]. In 2d, superfluidity occurs with no long-range order, as in the case of BEC [31]. The BKT phase transition happens when the 2d phase-space-density (PSD) reaches the value $n\lambda_{\mathrm{th}}^2 \sim 4$. It was observed for the first time in quantum gases, using the interference of several 2d clouds to probe for coherence and vortices [32]. Afterwards, a direct superfluid signature was seen while stirring an object in a 2d quantum gas [33]. A 1d gas is an exceptional system that can be described with a powerful theoretical many-body method (Density Matrix Renormalization Group (DMRG)) [34]. The Tonk-Girardeau gas, as an example, has been observed [35, 36] and the process of thermalization of a 1d system has been studied in [37].

The problem of a charged particle in a magnetic field is described by Quantum Hall physics (QHP) [38, 39]. The energy spectrum of these states is known as the Hofstadter Butterfly [40].

Neutral atoms in rotating systems can be used to simulate charged particles in a magnetic field [41–45]. The Coriolis force $\boldsymbol{F}_{\mathrm{C}}$ is mathematically analog to the magnetic Lorentz force $\boldsymbol{F}_{\mathrm{L}}$

$$\boldsymbol{F}_{\mathrm{C}} = -2m(\boldsymbol{\Omega} \times \boldsymbol{v}) \quad \longleftrightarrow \quad \boldsymbol{F}_{\mathrm{L}} = -q(\boldsymbol{B} \times \boldsymbol{v}).$$

The Hamiltonian of a charged particle, with charge q and velocity $\boldsymbol{v}$, in a magnetic field $\boldsymbol{B}$ can thus be projected onto the Hamiltonian of a neutral particle, with mass m and velocity $\boldsymbol{v}$, in a rotating frame with angular momentum $\boldsymbol{\Omega}$.

QHP can also be simulated with the use of artificial gauge fields, which arise from the motion of a neutral particle in a properly designed laser field (see [46] for an extensive review). Quantum gases evolving in gauge fields are an ideal simulator, because they have the possibility of simulating extremely strong magnetic fields and reaching interesting regimes with strong interaction between the particles.

In this work, we will use another powerful tool for tuning the parameters of ultracold atomic systems: Feshbach resonances [47, 48].

Quantum Gases with Feshbach Resonances

By employing a Feshbach resonance, the inter-particle scattering properties can be tuned using a magnetic field [49]. A Feshbach resonance appears, when a weakly-bound dimer state approaches the energy of the scattering threshold of the two-particle system [47, 50]. A magnetic field can be used to change the energy of this weakly-bound state, which changes the two-particle scattering properties through the scattering length a. Around a Feshbach resonance, the scattering length can be tuned from $-\infty$ to $+\infty$. On the negative-a side, the interaction between the two-particles is attractive and on the positive-a side repulsive.

Feshbach resonances in dilute gases were first considered in 1976 in the context of hydrogen [51] and first observed in hydrogen in 1986 [52]. The first Feshbach resonances in ultracold alkali gases were observed in 1998 in ^{23}Na [53] and ^{85}Rb [54]. In some atomic species, tuning of the interactions using Feshbach resonances is required to obtain BEC at all, *e.g.* ^{85}Rb [55], ^{133}Cs [56, 57] and ^{39}K [58] or to obtain large stable BECs, *e.g.* ^{7}Li [59–61].

The observation of Feshbach resonances led to the creation of Feshbach molecules of ^{85}Rb [62] and ^{133}Cs [63, 64]. As well as composite bosonic molecules of ^{6}Li and ^{40}K. These composite molecules turned out to be long-lived and opened up the possibility to study molecular condensates [65–68]. These Feshbach molecules can be brought to more deeply bound states using techniques like stimulated Raman adiabatic passage (STIRAP) [69, 70]. STIRAP enabled the formation of ground-state molecule of $^{87}Rb_2$ [71] and ^{40}K-^{87}Rb [72].

Quantum Simulation of the BCS-BEC Crossover

The carriers of electric current in superconducting materials are pairs of electrons, with weakly attractive interactions. These pairs form Cooper pairs [73], which lie at the basis of a theory developed by Bardeen, Cooper and Schieffer (BCS) [74].

BEC and BCS initially seemed like completely different phenomena. Eagles and Legett [75, 76], however, noticed that the BCS wavefunction also describes a Bose-Einstein condensate of tightly bound pairs. The transition between these regimes was termed the BEC-BCS crossover. The phase diagram around the crossover was first predicted by P. Nozières and S. Schmitt-Rink (NSR), who calculated the critical temperature for the normal-to-superfluid phase transition as a function of the interaction strength [77].

In a system of neutral fermions around a Feshbach resonance the scattering length can be arbitrarily tuned and fermions will either form Cooper pairs or bound molecules. With a Feshbach resonance in a system of fermions the interaction could, for the first time, be smoothly tuned across the BEC-BCS crossover [78, 79].

In recent years, the simulator system has been used to observe several interesting phenomena. Collective oscillation modes in a pair condensate around the BEC-BCS crossover were first observed by [80]. Afterwards, the frequency of these modes [81] and the effect of strong interactions [82] were characterized in the crossover. The superfluid pairing gap, which determines the energy needed to break up the fermionic pairs, across the crossover was measured using RF-spectroscopy [83]. The superfluidity of fermionic systems around the crossover was probed by observing vortices, while rotating the system [45]. More recently, the thermodynamic equation of state was measured across the crossover for ^{6}Li in spin-polarized and unpolarized systems as well as for varying temperature [84–87]. The results were compared to Quantum Monte Carlo calculations [88][1].

State of the Art: The Resonant Bose gas

Depending on the strength of the atom-atom interactions bosonic systems can be classified into several regimes. The zero-temperature Bose gas with no interactions is a purely statistical form of BEC. Increasing the interactions increases the many-body effects [89]. For weak interactions, the diluteness parameter na^3 vanishes ($na^3 \ll 1$) and a mean-field approximation describes the system remarkably well. The wavefunction in the mean-field approximation is given by the Gross-Pitaevskii Equation [90, 91], in which the quantum many-body wavefunction is simply a product state of N identical wavefunctions.

The first-order correction to mean-field theory is the Lee-Huang-Yang (LHY) correction, which was derived in 1957 [92]. The correction is due to interactions

[1] As implied by the title of the paper "Feynman diagrams versus Fermi-gas Feynman emulator", a direct comparison of classical simulation versus quantum simulation was made.

and quantum-fluctuations and induces a reduction of the condensate fraction. For weak interactions ($n|a|^3 \ll 1$), the systems ground state energy E (per volume V) is given by the expansion

$$\frac{E}{V} = \frac{gn^2}{2}\left(1 + \frac{128}{15\sqrt{\pi}}\sqrt{na^3} + \dots\right),$$

where $g = 4\pi\hbar^2 a/m$ is the coupling constant for particles with mass m. The first term is the mean-field contribution to the energy. The term proportional to $\sqrt{na^3}$ is the LHY correction. The LHY correction to the excitation spectrum of a cloud was first seen in bosonic ^{85}Rb using Bragg spectroscopy [93]. The correction was also observed through the modification of the frequency of collective oscillations with varying interactions in molecules of ^{6}Li on the BEC side of the resonance [82]. These molecules were also used to probe the corrections of the *in situ* density profile [94]. A direct measure of the LHY correction in the equation of state was measured in [85], also using bosonic molecules of ^{6}Li. In atomic Bose systems, the LHY correction was measured through the equation of state in ^{7}Li [95], and using Bragg spectroscopy to determine the LHY correction in Tan's contact parameter [96]. In Figure 0.1, the introduction of interactions into the zero-temperature Bose gas corresponds to a path on the x-axis ($\propto 1/(n|a|^3)$) going from $+\infty$ towards 0.

In this thesis, we take a different approach. We start with a gas with unitary interaction ($a \to \infty$) and cool the system towards quantum degeneracy (see the arrow along the y-axis ($\propto 1/(n\lambda_{\text{th}}^3)$) in Figure 0.1). Interactions will start to play an important role when we approach the onset of quantum degeneracy. The equation of state in the high temperature limit is described by the virial expansion for the pressure P (see for example [97])

$$P = \frac{1}{\beta\lambda_{\text{th}}^3}\sum_{k=1}^{\infty}\tilde{b}_k e^{k\beta\mu},$$

where $\tilde{b}_k$ is the k-th virial coefficient described by the k-particle problem and $\beta \equiv 1/(k_{\text{B}}T)$. The term $e^{\beta\mu}$ is the fugacity and is used as a small parameter, because in the high-temperature limit, $k_{\text{B}}T \gg \mu$. In the case of a Boltzmann gas, all terms except for the first vanish, which yields $\tilde{b}_1 = 1$, resulting in the ideal gas law. Using the two-particle problem, the theoretical prediction of $\tilde{b}_2 = 9\sqrt{2}/8 \approx 1.59$ can be found (see for example [98]). Recently, $\tilde{b}_3$ was predicted analytically using the three-particle problem [99].

The hypothetical unitary Bose gas is a system with unitary interactions at zero

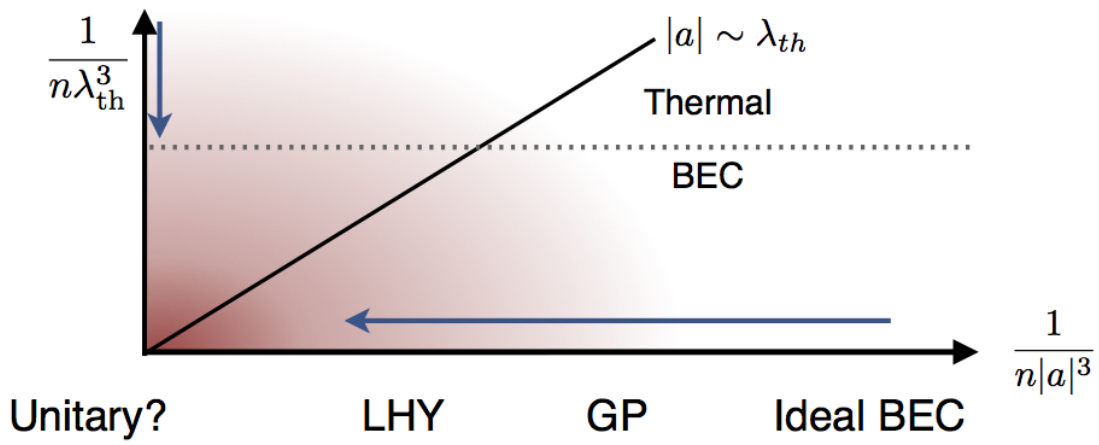

Figure 0.1.: The hypothetical phase diagram of a Bose gas with varying interactions, $n|a|^3$, and varying temperature, $n\lambda_{\rm th}^3$. The dotted line shows the critical temperature. The darkness of red indicates the strength of the interactions. The blue arrow parallel to the x-axis indicates the research on zero-temperature BECs with increasing interactions. The blue arrow parallel to the y-axis is the different approach that we will use in this thesis. In this approach, we will start with a gas with resonant interactions and lower the temperature.

temperature. There is a prediction that the unitary Bose gas is described by the fermionic equation of state [100], with the only length scale being the interparticle distance, hence the chemical potential μ is given by

$$\mu = \xi E_{\rm F},$$

where $E_{\rm F} \propto n^{2/3}$ is the Fermi energy and ξ is the Bertsch parameter introduced first for fermions [1, 101]. For a unitary Bose gas, a lower bound on ξ using measurements of the equation of state was experimentally found to be $\xi > 0.44(8)$ [95]. This result is satisfied for both the prediction of $\xi = 0.66$, based on renormalization group theory [102] and the upper bounds given by variational calculations of $\xi < 0.8$ [103] and $\xi < 2.93$ [104]. It was also predicted that the unitary Bose gas, unlike the unitary Fermi gas, has an interesting first-order quantum phase transition (QPT). When tuning the interactions across the resonance, there will be a QPT between a mixture of an atomic and pair superfluid, on the positve-a side, and a pure superfluid of pairs, on the negative-a side [105–107]. Afterwards, it was predicted that this transition should become second-order when thermal functions become more prominent [108]. In 2009, using the same method as was used by P. Nozières and

S. Schmitt-Rink for fermions, the critical temperature for a bosonic gas across a Feshbach resonance was predicted [109]. In the same year, it was predicted that the momentum distribution tail should also be described by Tan's contact for resonant Bose systems [110]. In 2011, predictions about thermodynamical quantities of the ground state of a Bose system across a Feshbach resonance, such as Tan's contact and the chemical potential, were made [111]. In 2012, a generalized NSR method was used to predict the phase diagram of the ground state for varying interactions and temperature [112].

Unlike fermionic systems, where Pauli blocking inhibits three-particle recombination, bosonic systems suffer from severe losses that scale rapidly with increasing interaction. The change of the density, due to three-particle recombination, is given by the differential equation

$$\dot{n} = -L_3 n^3,$$

where L_3 is the three-particle loss coefficient. For zero-temperature bosons with scattering length a, the three-particle loss coefficient was initially expected to scale as $L_3 \propto a^4$ [113]. Later, several theory groups [48, 114–117] showed that this prediction is modified by a log-periodic term $C(a)$, whose origin lies in Efimov Physics

$$L_3(a) = 3C(a)\frac{\hbar}{m}a^4,$$
$$C(a) = \begin{cases} 67.12\, e^{-2\eta_+}\left(\cos^2\left[s_0 \ln(a/a_+)\right] + \sinh^2\eta_+\right) + 16.84(1 - e^{-4\eta_+}), & a > 0 \\ 4590\, \sinh(2\eta_-)/\left(\sin^2\left[s_0 \ln(a/a_-)\right] + \sinh^2\eta_-\right), & a < 0 \end{cases}$$

where a_+ indicate the position and η_+ the width of the loss minimum and a_- indicate the position and η_- the width of the Efimov resonances, on the positive-a (+) respectively negative-a (-) side of the Feshbach resonance, for three identical bosons ($s_0 \approx 1.00624$).

In 1970, Efimov predicted that in a system with short-range unitary interactions ($|a| \to \infty$), there exist infinitely many three-particle bound states, without the necessity of a two-particle bound state [118, 119]. Making this system the quantum mechanical counterpart of Borromean rings [120].

If $E_{\mathrm{T}}^{(n)}$ is the energy of trimer bound state n, then Efimov showed that the ratios

between the different energy levels in the Efimov spectrum are given by

$$\frac{E_{\mathrm{T}}^{(n)}}{E_{\mathrm{T}}^{(n+1)}} = \left(e^{-\pi/s_0}\right)^2 \approx (1/22.7)^2 \,. \tag{0.1}$$

This result shows the log-periodic dependence of the energy of the trimer states, in the limit of unitary interactions ($a \to \infty$).

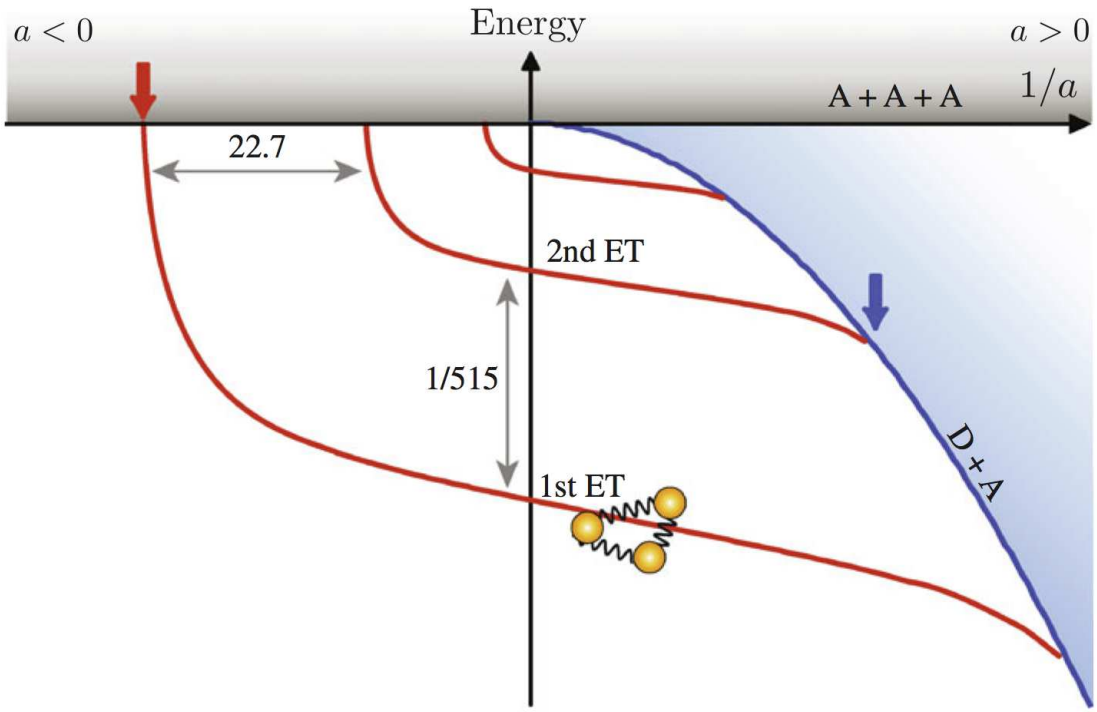

Figure 0.2.: The Efimov bound states as a function of energy and interactions (taken from [121]). The gray shaded area, with $E > 0$ corresponds to the three-particle threshold. The red curves are the bound state energies of the Efimov states. On the left ($a < 0$) they cross the three-particle threshold (the gray region) and on the right ($a > 0$) they connect to the two-particle bound state (blue line). Three of the infinitely many Efimov states are shown.

In the zero-energy limit, Efimov introduced the energy spectrum shown in Figure 0.2. On the y-axis the energy is varied and on the x-axis the inverse scattering length $1/a$ across a Feshbach resonance. The zero-energy line marks the energy of the scattering threshold of three particles. The blue parabola shows the bound state energy of the dimer associated to the Feshbach resonance, for $a > 0$. The red lines indicate the energy of the bound trimer states predicted by Efimov. At

$1/a = 0$, the energy scaling factor between neighboring states (see Equation (0.1)) is shown. On the negative-a side, these trimer states connect to the zero energy threshold. These connection points are given by $a_-^{(n)} = a_- e^{n\pi/s_0}$ with $n \in \mathbb{Z}$. The oscillating term $C(a)$ of the loss coefficient shows an increase at these points ($a = a_-^{(n)}$, see the red arrow in Figure 0.2), these are the so called Efimov resonances. On the positive-a side the trimer energy connects to the energy of the weakly bound dimers state. The signature of Efimov physics in the loss coefficient on the positive-a side is given by a oscillations in $C(a)$, due to the interference of two recombination paths [114, 115].

A quantitative experimental study of the three-particle loss coefficient in ^{133}Cs revealed signatures of Efimov physics in the three-particle losses rate on both the positive-a (oscillations) and negative-a (loss maximum resonance) side of the resonance [122]. This was the first direct observation of Efimov's prediction. The same group used a mixture of weakly-bound molecules and atoms in ^{133}Cs on the positive-a side to probe the connection of the dimer and trimer energy (see the blue arrow in Figure 0.2). At this scattering length they observed an increase in the loss rate coefficient for atom-dimer losses [123].

The log-periodic behavior between two consecutive loss features was confirmed in ^{7}Li [61] and ^{39}K [124] on the positive-a side, where they observed two minima in the three-particle loss coefficient. On the negative-a side one Efimov resonance was seen [125] in ^{7}Li. Seeing two Efimov resonances on the negative-a side would be a more direct verification of the log-periodicity of the energy of the trimer-states, because on the negative-a the distance between the energy states themselves is directly probed. Recently, some preliminary evidence for the log-periodicity in two consecutive resonances in ^{133}Cs was reported [126].

Universality of the position and the width of the Efimov resonance for atoms in different hyperfine states of ^{7}Li was shown in 2010 [127, 128]. Furthermore, an Efimov resonance in ^{85}Rb was reported in [96]. Efimov resonances around several Feshbach resonances in both ^{133}Cs [129] and ^{39}K [130] were reported and the results suggest a relation between the Efimov resonance position and the van der Waals length R_{vdW} associated to the two-particle scattering potential [120]. The relation based on these result and earlier results is given by $a_-/\bar{a} \simeq -9.5$ [129], where $\bar{a} = 0.955978\ldots R_{\mathrm{vdW}}$ [48]. Predictions concerning universality were done in [131–136].

The systems discussed above only consisted of three identical bosons. However, in ^{6}Li, Efimov trimers have been created using Radio-Frequency (RF) association of three distinguishable fermions [137]. In a Bose-Fermi mixture of ^{87}Rb and ^{40}K

a Feshbach resonance was used to see a Efimov resonance [138, 139].

The measurements in systems with three identical bosons were all performed in the limit of weak interactions ($n|a|^3 \ll 1$) and analyzed using a theory that assumes $|a| \ll \lambda_{\text{th}}$. In this limit, the loss coefficient scales as $C(a)\, a^4$. However, as soon as a becomes on the order of λ_{th} the loss coefficient will saturate to a unitarity limited value. This behavior was seen in ^{133}Cs [122], ^{39}K [124], ^{7}Li [61, 125] and ^{85}Rb, although these were never quantitatively explained nor studied and show large variations in the value of the loss coefficient close to resonance. Saturation behavior was predicted theoretically, however the prediction is only valid for in the weakly interacting limit [140], because the prediction did not take Efimov physics into account. Additionally, numerical simulations assuming model potentials have been used to calculate the three-particle loss coefficient, in which case the loss coefficient shows a discontinuity at unitarity [141, 142]. To summarize, no exact theory nor thorough experimental study has so far been dedicated to three-particle losses in a Bose gas with resonant interactions. This motivated the main question of this thesis:

What happens to the system when $a \gg \lambda_{\text{th}}$?

Outline: The Road to the Unitary Bose Gas

This thesis is dedicated to the study of the Bose gas with resonant interactions ($a \ll \lambda_{\text{th}}$). In order to study this state of matter, the stability of the system needs to be understood. The logical first step in the process is the study of its lifetime. The limiting process for the lifetime is three-particle loss, which we will analyze in detail.

In the following, we will describe the different parts of this thesis.

- In **Chapter 1**, an overview of the quantum mechanical description of the two-particle scattering problem is given. Useful concepts like the scattering amplitude, scattering cross section, unitary limit and scattering length are discussed. We will also mention Feshbach resonances, which we will use to tune the interactions.

The following two chapters discuss the theory derived by Dmitry Petrov and Felix Werner, published in [143]. The discussion presented is strongly based on their notes [144].

- In **Chapter 2**, the concepts discussed in Chapter 1 will be extended to understand three-particle scattering. The special case of Efimov physics will be covered. Afterwards, the concept of three-particle losses and the adaptation of the three-particle scattering problem to include them is discussed. In this formulation, the loss coefficient is obtained by comparing the incoming and outgoing flux of particles. Furthermore, we will extensively discuss the resulting three-particle loss coefficient. Finally, at unitarity the log-periodic oscillations in the three-particle loss coefficient when varying the temperature are shown. Finally, we will numerically study the properties of the loss coefficient.

- In **Chapter 3**, the specific details of three-particle losses in a trap are discussed. Furthermore, we will discuss the heating effects due to three-particle losses. We will compare these heating effects to evaporation effects due to finite trap depth.

Chapters 4 and 5 present the experimental results.

- **Chapter 4** will describe the Lithium machine in detail. We will discuss the main steps to obtain an ultracold gas of ^{7}Li. Also, the Feshbach resonance that we employed for the measurements is discussed.

- **Chapter 5** is dedicated to the experimental test of the theory presented in Chapter 2. We will start by describing the specific experimental conditions under which the measurements were performed. Afterwards, we portray the experiments performed by our group and show a quantitative test of the predicted three-particle loss coefficient. We have a complete model describing a system with three-particle recombination for $a<0$ and across the resonance that includes Efimov physics and finite temperature effects. Employing the model, we predict the appearance of a second Efimov resonance for $a<0$. Furthermore, this model is used to quantitatively explain the results of experiments at both Innsbruck using ^{133}Cs and Cambridge using ^{39}K.

- In the **Concluding remarks**, we give several perspectives for this work.

Part I.

Theory

1. Two-Particle Problem

This chapter is dedicated to two-particle scattering. We will remind the reader of the ideas behind the system. These ideas are used in Chapter 2 to derive the three-particle scattering. We will discus concepts like the scattering amplitude, scattering cross-section, unitary limit and scattering length, as well as the zero-temperature limit, which allows us to only consider scattering in the lowest collisional channel (s-wave scattering, for bosons). Afterwards, we will summarize the results by introducing a Zero-Range Model, in which case a boundary condition at $r = 0$ contains all the information about the two-particle scattering. Finally, we will touch upon the subject of Feshbach resonances, which we will use to tune interactions between particles.

1.1. Scattering

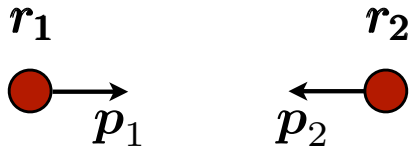

Figure 1.1.: The scattering of two particles.

Consider two particles of mass m. Their quantum state is described by the Hamiltonian for two particles interacting via a potential $U(|\boldsymbol{r}_1 - \boldsymbol{r}_2|)$:

$$H = \frac{\boldsymbol{p}_1^2}{2\,m} + \frac{\boldsymbol{p}_2^2}{2\,m} + U(|\boldsymbol{r}_1 - \boldsymbol{r}_2|), \tag{1.1}$$

where $\boldsymbol{p}_n$ is the momentum operator and $\boldsymbol{r}_n$ the position operator of particle n. Figure 1.1 depicts this system.

1.1.1. Center of Mass (CoM) Motion

The first step in solving the problem is to separate the center of mass motion from the relative motion, because we are only interested in the latter. In order to do so, let us introduce the following CoM variables

$$\begin{aligned} \boldsymbol{r}_{\mathrm{CoM}} &= \frac{\boldsymbol{r}_1 + \boldsymbol{r}_2}{2} \\ \boldsymbol{p}_{\mathrm{CoM}} &= \boldsymbol{p}_1 + \boldsymbol{p}_2 \end{aligned}$$

and also the relative motion variables

$$\begin{aligned} \boldsymbol{r} &= \boldsymbol{r}_1 - \boldsymbol{r}_2 \\ \frac{\boldsymbol{p}}{\mu} &= \frac{\boldsymbol{p}_1}{m} - \frac{\boldsymbol{p}_2}{m}. \end{aligned}$$

Here $\mu = m/2$ is the reduced mass of the system of two particles.

Using the CoM and relative variables introduced above the Hamiltonian can be written in the following form,

$$\begin{aligned} H &= \frac{\boldsymbol{p}_{\mathrm{CoM}}^2}{4m} + \frac{\boldsymbol{p}^2}{2\mu} + U(\boldsymbol{r}) \\ &\equiv H_{\mathrm{CoM}} + H_{\mathrm{rel}}. \end{aligned} \tag{1.2}$$

Since H_{CoM} commutes with H_{rel}, we diagonalize them independently. The solutions of H_{CoM} for the free particle are the plane waves ($\varphi_{\mathrm{CoM}} = e^{i\boldsymbol{k}_{\mathrm{CoM}}\cdot\boldsymbol{r}_{\mathrm{CoM}}}$ with $\boldsymbol{k}_{\mathrm{CoM}}$ the wavevector of the CoM system). In the following, we will study the relative motion.

1.1.2. Radial Schrödinger Equation

The Schrödinger Equation for the relative motion can be cast into the following form

$$\left[-\frac{\hbar^2}{2\mu}\boldsymbol{\Delta}_{\boldsymbol{r}} + U(r) - \frac{\hbar^2 k^2}{2\mu}\right]\psi = 0, \tag{1.3}$$

where $E_k = \hbar^2 k^2/(2\mu)$ is the energy of the relative motion for a scattering state ($E_k > 0$).

The Laplacian operator $\Delta_{\boldsymbol{r}}$ can be rewritten in spherical coordinates using the

radius r and angular momentum operator[1] $\boldsymbol{L}$. The Schrödinger Equation becomes

$$\left[T_r + \frac{1}{2\mu}\frac{\boldsymbol{L}^2}{r^2} + U(r) - \frac{\hbar^2 k^2}{2\mu}\right]\psi = 0, \tag{1.4}$$

here the operator $T_r = -\frac{\hbar^2}{2\mu}\left(\frac{\partial^2}{\partial r^2} + \frac{2}{r}\frac{\partial}{\partial r}\right)$ is the radial kinetic energy operator. The interest of this Schrödinger Equation comes from the separation of the radial and angular part. Since the operator $\boldsymbol{L}^2$ commutes with the Hamiltonian, the radial and angular part of the wavefunction can be separated

$$\begin{aligned}\psi_{lm} &= R_l(r)Y_l^m(\theta,\phi)\\ R_l(r) &= \frac{1}{r}\,u_{kl}(r),\end{aligned} \tag{1.5}$$

where $R_l(r)$ is the radial wavefunction and $Y_l^m(\theta,\phi)$ the spherical harmonics. The spherical harmonics are defined by the following differential equation

$$\boldsymbol{L}^2 Y_l^m(\theta,\phi) = \hbar^2 l(l+1)Y_l^m(\theta,\phi), \tag{1.6}$$

where the quantum numbers l give the eigenvalues of the equation. These spherical harmonics describe the relative angular motion of the two particles.

The quantum number l, indicates in which scattering channel the scattering takes place (this is usually called s-, p-, d-,... wave scattering, for $l=0$, $l=1$, $l=2$,..., respectively). The quantum number m is used to describe the motion in the ϕ-direction. The possible scattering channels are different for distinguishable and indistinguishable particles. Distinguishable particle will use all channels, indistinguishable particles, however, either scattering in even (bosons) or odd (fermions) channels.

When the definition of the spherical harmonics in Equation (1.6) is applied to the Schrödinger Equation we are left with the radial Schrödinger Equation. The introduction of the radial wavefunction $u_{kl}(r)$ in Equation (1.5) allows us to write down the simplified radial Schrödinger Equation

$$\left[\frac{d^2}{dr^2}\underbrace{-\frac{l(l+1)}{r^2} - \frac{2\mu}{\hbar^2}U(r)}_{-U_{\text{eff}}(r)} + k^2\right] u_{kl}(r) = 0. \tag{1.7}$$

[1] We will see that using this notations simplifies the generalization of the Schrödinger Equation to more than two particles, see Section 2.1.2 for three particles

Note that $R_l(r)$ needs to be regular at the origin and to impose this, the condition $u_{kl}(0) = 0$ is required. The effective potential $U_{\text{eff}}(r)$ is graphically depicted in Figure 1.2 for different values of l.

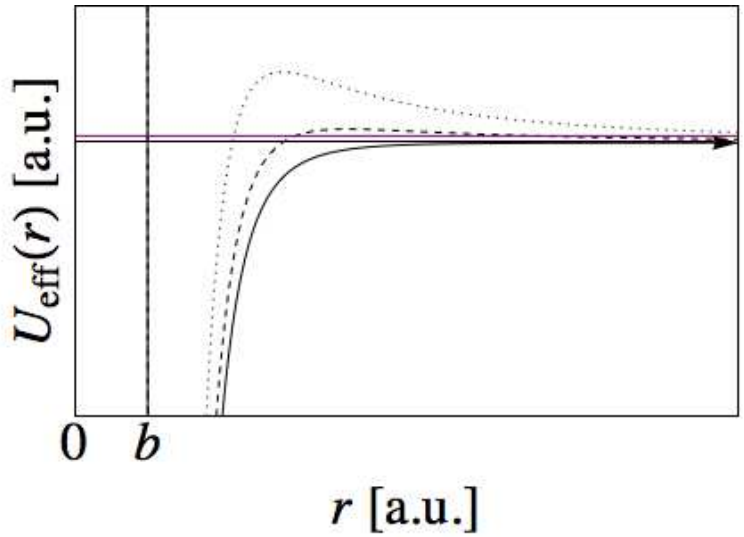

Figure 1.2.: The van der Waals potentials with a hard-core at $r = b$ and centrifugal contributions $U_{\text{eff}}(r)$. The solid black line is the potential for $l = 0$ and is monotonic. The black dashed line is the effective potential with $l = 1$ and the black dotted line the effective potential with $l = 2$. The potentials for $l = 1$ and $l = 2$ are not monotonic and have a maximum. This maximum creates an effective barrier for particles with an relative energy lower than the barrier. The purple line shows the energy of such a particle pair in the limit of cold collisions $k \to 0$. This shows that for sufficiently cold gases, only the $l = 0$ (s-wave) scattering contributes to the problem.

1.1.3. Scattering Potential

In the previous section, we have introduced the relative potential $U(r)$ without putting constraints on it. Here we will filter out a certain class of potentials.

In the framework of ultracold atomic gases, we are interested in collisions between two neutral atoms. This means that the considered interaction is an induced dipole-dipole interaction and is described by a van der Waals type potential, which is attractive at the long-range and has a hard-core at $r = b$. For more detailed information about the atomic potentials we refer the reader to the following references [48, 145–149]. At intermediate-long distances this interaction is described

by a $-C_6/R^6$ potential, which has a length scale given by the C_6 parameter: the van der Waals length $R_{\mathrm{vdW}} = \frac{1}{2}\left(\frac{2\mu C_6}{\hbar^2}\right)^{1/4}$.

This length scale has an interesting physical interpretation [150]. At the length scale $r \sim R_{\mathrm{vdW}}$, the potential energy becomes comparable to the collision energy $E \sim U(R_{\mathrm{vdW}})$. This means that the effect of the potential outside of this range vanishes and the wavefunction approximates the free space wavefunction. In other words, the van der Waals length indicates a range over which the potential modifies the behavior of the wavefunction. In the following, we will only discuss the wavefunction outside the range of the interaction and condense the effect of the potential into a boundary condition at $r = 0$.

1.1.4. Spherical Waves

Outside the range of the potential $r \gg R_{\mathrm{vdW}}$ the solutions of the problem are given by a linear combination of an incoming and outgoing wave

$$\begin{aligned}\varphi_{lm} &\underset{r\to\infty}{\simeq} \sqrt{\frac{2k^2}{\pi}} Y_l^m(\theta,\phi)\frac{1}{2ikr}\left[A^{\mathrm{out}} e^{+i(kr-l\pi/2)} - A^{\mathrm{in}} e^{-i(kr-l\pi/2)}\right], \\ &\equiv A^{\mathrm{out}}\varphi_{lm}^{(\mathrm{out})} - A^{\mathrm{in}}\varphi_{lm}^{(\mathrm{in})}. \end{aligned} \tag{1.8}$$

The amplitudes $A^{\mathrm{out/in}}$ are determined by the details of the problem, which we will see in the following section.

1.1.5. Elastic Scattering

In the above, we have written the solutions of the Schrödinger Equation in the basis of the spherical harmonics. The next step is to describe the effect of the scattering potential on each of the spherical waves. We will use the fact that the potential has a finite range R_{vdW} and start by considering an incoming wave outside of the range of the potential $r \gg R_{\mathrm{vdW}}$. Outside the range of the potential, the incoming wave is described by the $r \gg R_{\mathrm{vdW}}$ solution. We will consider a virtual propagation of the wave to the scattering center and as soon as the wave starts to feel the potential, it is deformed and finally reflected within the range of the potential. The potential is norm conserving (elastic scattering), so when the wave is coming back out of the range of the potential it will again be the $r \gg R_{\mathrm{vdW}}$ solution, but with an acquired phase δ_l due to the potential $U(r)$ in the $r < R_{\mathrm{vdW}}$ region. Let us write

this in terms of the wavefunction

$$\psi_{lm} \underset{r\to\infty}{\simeq} \sqrt{\frac{2k^2}{\pi}} Y_l^m(\theta,\phi)\frac{1}{2ikr}\left[e^{+i(kr-l\frac{\pi}{2}+2\delta_l)} - e^{-i(kr-l\frac{\pi}{2})}\right], \tag{1.9}$$

which at far distance will behave as $1/r\sin(kr-l\pi/2+\delta_l)$. If we write this in terms of the incoming and outgoing waves, the wavefunction takes the form

$$\psi_{lm} \underset{r\to\infty}{\simeq} s_l\varphi_{lm}^{(\text{out})} - \varphi_{lm}^{(\text{in})}, \tag{1.10}$$

where we have introduced $s_l \equiv A^{\text{out}}/A^{\text{in}} = e^{2i\delta_l}$. This s_l described the scattering of a wave in channel l due to the potential $U(r)$. This is a trivial case of the scattering matrix diagonal (corresponding to one channel), but as we will see in Chapter 2, it becomes useful when several channels are coupled.

As a final step, let us separate the outgoing wave with no interaction from the part with the phase factor

$$s_l\varphi_{lm}^{(\text{out})} = \varphi_{lm}^{(\text{out})} + (s_l-1)\varphi_{lm}^{(\text{out})}, \tag{1.11}$$

where $(s_l-1) = 2ie^{i\delta_l}\sin\delta_l$. When the result is written into the form of the wavefunction, it is given by

$$\begin{aligned}\psi_{lm} &\underset{r\to\infty}{\simeq} \varphi_{lm}^{(\text{out})} - \varphi_{lm}^{(\text{in})} + (s_l-1)\varphi_{lm}^{(\text{out})} \\ &\underset{r\to\infty}{\simeq} \varphi_{lm} + 2ie^{i\delta_l}\sin\delta_l\ \varphi_{lm}^{(\text{out})}.\end{aligned} \tag{1.12}$$

This is the result of scattering in a specific channel l. To summarize the elastic scattering let us note that the scattering potential fixes a boundary condition on the long-range result.

In the next section we will apply this on the initial condition of the problem: the plane wave.

1.1.6. Scattering Amplitude

The spherical waves are practical to introduce the effect of the scattering into the wavefunction, however, the initial condition is the incoming plane wave $\psi^{(0)}$. In order to use the spherical waves, let us project the plane wave onto the basis of

spherical waves. The projection is given by

$$\psi^{(0)} = e^{+ikz} = \sum_{l=0}^{\infty} i^l \sqrt{4\pi(2l+1)}\, j_l(kr)\, Y_l^0(\theta,\phi) = \sum_{l=0}^{\infty} c_l\, \varphi_{l0}(\boldsymbol{r}). \tag{1.13}$$

The fact that there are only terms with $m=0$ in the projection of the plane wave, shows the cylindrical symmetry of the scattering. Here we have made, without loss of generality, the choice of having an incoming plane wave traveling along the z-axis towards the center, which means that θ is defined as the angle between r and z.

To implement what we have derived in Section 1.1.5, let us do the replacement $\varphi_{l0} \to \psi_{l0}$ and write the resulting scattering wavefunction ψ,

$$\begin{aligned}\psi = \sum_{l=0}^{\infty} c_l \psi_{l0}(\boldsymbol{r}) &= \sum_{l=0}^{\infty} c_l \varphi_{l0} + \sum_{l=0}^{\infty} c_l\ 2i\ e^{i\delta_l} \sin\delta_l\ \varphi_{l0}^{(\mathrm{out})} \\ &= \psi^{(0)} + f_{\boldsymbol{k}}(\theta)\frac{e^{ikr}}{r}\end{aligned} \tag{1.14}$$

Here $f_{\boldsymbol{k}}(\theta)$ is the **scattering amplitude** given by

$$f_{\boldsymbol{k}}(\theta) \equiv \frac{1}{k}\sum_{l=0}^{\infty} \sqrt{4\pi(2l+1)} Y_l^0(\theta) e^{i\delta_l} \sin\delta_l. \tag{1.15}$$

The scattering amplitude $f_{\boldsymbol{k}}(\theta)$ is a measure for the strength of the scattering. For a more detailed description and higher-order corrections we refer the reader to [145, 151].

The two parts in Equation (1.14) are the incoming wave $\psi^{(0)} = e^{+ikz}$ and the outgoing scattered wave $\psi^{\mathrm{sc}} = f_{\boldsymbol{k}}(\theta)\ e^{ikr}/r$. This result is the well-known two-particle scattering wavefunction in the long-range. In Chapter 2 we will use a similar method to described the scattering of three particles.

1.1.7. Scattering Cross Section

In order to characterize the scattering, an often used property is the scattering cross section. The total scattering cross section is defined by the amount of initial plane wave $\psi^{(0)}$ scattered into the scattered wave ψ^{sc}. In order to calculate the total scattering cross section, we have to consider the differential cross section. This is given by the ratio of the current density of the scattered wave through a surface element on a sphere and the current density of the incoming wave (see

Figure 1.3).
Let us start by calculating the incoming current density

$$\begin{aligned} \boldsymbol{j}_z(r) &= +\frac{\hbar}{\mu}\,\mathrm{Im}\left[(\psi^{(0)})^*\,\boldsymbol{\nabla}_z\,\psi^{(0)}\right] \\ &= \hat{\boldsymbol{z}}\frac{\hbar k}{\mu} = \hat{\boldsymbol{z}}v. \end{aligned} \tag{1.16}$$

To calculate the outgoing current density, we will use a radial current density operator and the result is given by

$$\begin{aligned} \boldsymbol{j}_r(r) &= \frac{\hbar}{\mu}\,\mathrm{Im}\left[(\psi^{\mathrm{sc}})^*\,\hat{\boldsymbol{r}}\frac{\partial}{\partial r}\,\psi^{\mathrm{sc}}\right] \\ &= |f_{\boldsymbol{k}}|^2\frac{j_z}{r^2}\hat{\boldsymbol{r}}. \end{aligned} \tag{1.17}$$

The differential cross section $d\sigma_{\boldsymbol{k}}$ is equal to

$$\begin{aligned} d\sigma_{\boldsymbol{k}} &= \frac{\boldsymbol{j}_r(r)\cdot d\boldsymbol{S}}{j_z} = |f_{\boldsymbol{k}}|^2 d\Omega \\ \frac{d\sigma_{\boldsymbol{k}}}{d\Omega} &= |f_{\boldsymbol{k}}|^2, \end{aligned} \tag{1.18}$$

where we have used that the surface $d\boldsymbol{S}$ is given by $r^2\,\hat{\boldsymbol{n}}\,d\Omega$ and $\boldsymbol{\Omega}$ is the solid angle given by (θ,ϕ). The vectors $\hat{\boldsymbol{r}}$ and $\hat{\boldsymbol{n}}$ are the same.

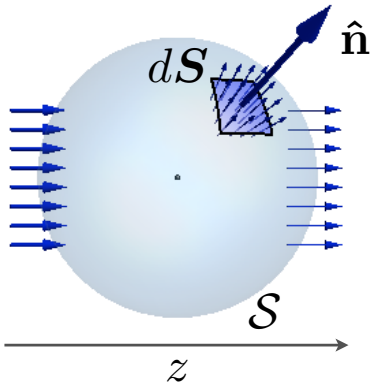

Figure 1.3.: A two-dimensional representation of the spherical surface $\mathcal{S}$. The small vectors designate the current density vector $\boldsymbol{j}_r[\psi]$ perpendicular to a surface element $d\boldsymbol{S}$, with its normal vector given by $\hat{\boldsymbol{n}}$.

Taking into account indistinguishability and integrating over the solid angle Ω,

gives the total scattering cross section

$$\sigma_{\boldsymbol{k}} = 2\pi \int_0^{\pi/2} d\theta \sin\theta \, |f_{\boldsymbol{k}}(\theta) + f_{\boldsymbol{k}}(\pi - \theta)|^2 \,. \tag{1.19}$$

As a final step, we can use the result from Equation (1.15) and plug it into Equation (1.19). The spherical functions $Y_l^0(\theta)$ are orthonormal and satisfy $Y_l^0(\pi - \theta) = (-1)^l Y_l^0(\theta)$. This allows us to write the total scattering cross section in the following forms:

$$\begin{aligned}
\text{for identical bosons :} \quad \sigma_{\boldsymbol{k}} &= \frac{8\pi}{k^2} \sum_{l \text{ even}} (2l+1) \sin^2 \delta_l(k), \\
\text{for identical fermions :} \quad \sigma_{\boldsymbol{k}} &= \frac{8\pi}{k^2} \sum_{l \text{ odd}} (2l+1) \sin^2 \delta_l(k), \\
\text{for distinguishable particles :} \quad \sigma_{\boldsymbol{k}} &= \frac{4\pi}{k^2} \sum_{l \text{ all}} (2l+1) \sin^2 \delta_l(k).
\end{aligned} \tag{1.20}$$

1.1.8. The Unitary Limit

The Equations (1.20) are bounded by the maximum value of $\sin^2 \delta_l(k)$, which is 1. The scattering cross section for a specific partial wave ($\sigma_{\boldsymbol{k}} = \sum_l \sigma_l$) is bounded by

$$\begin{aligned}
\text{For identical bosons :} \quad \sigma_l &\leq \frac{8\pi}{k^2}(2l+1) \\
\text{For identical fermions :} \quad \sigma_l &\leq \frac{8\pi}{k^2}(2l+1) \\
\text{For distinguishable particles :} \quad \sigma_l &\leq \frac{4\pi}{k^2}(2l+1).
\end{aligned} \tag{1.21}$$

These inequalities give the maximum value the scattering cross section can attain. The limit in which the maximum possible cross section is obtained, is the so called **Unitary Limit**.

1.1.9. Low-Temperature Limit: Bosons versus Fermions

Let us reconsider Figure 1.2 in the limit of low energy. In the figure, the effective potentials for $l = 0$, $l = 1$ and $l = 2$ are shown. The purple line shows the energy of an incoming wave $\psi^{(0)}$, given by $\hbar^2 k^2/(2\mu)$. For $l > 0$, we can associate a length scale r_l to the rotational barrier by comparing the energy of the incoming wave to

the rotational energy. Following from the Schrödinger Equation, we find

$$kr_l = \sqrt{l(l+1)}. \tag{1.22}$$

The point $r = r_l$ corresponds to the classical turning point, where the kinetic energy is 0 and we neglect the interaction potential $U(r)$ (which is true for $r_l \gg R_{\mathrm{vdW}}$). Comparing the two length scales gives

$$R_{\mathrm{vdW}} \ll r_l = \frac{\sqrt{l(l+1)}}{k}. \tag{1.23}$$

The first inequality in this equation defines the zero-temperature limit. Following, this limit can be expressed as $k_{\mathrm{th}} \to 0$. So if this limit is reached, the waves in the $l > 0$ channels will avoid the scattering center. This means that for $l > 0$, the phase shift δ_l vanishes *i.e.* $\lim_{k\to 0} \delta_l = 0$.

When considering bosons, the scattering cross section can, in the limit of cold-collisions, be written as

$$\sigma_{\boldsymbol{k}} \underset{k\to 0}{\simeq} \frac{8\pi}{k^2} \sin^2 \delta_0(k). \tag{1.24}$$

From here on, we will, unless otherwise specified, assume *s*-wave scattering of identical bosons.

1.1.10. Scattering Length

In the previous section, we have seen that the limit of cold-collisions greatly simplifies the problem, because we only need to consider *s*-wave scattering. This same limit allows us to further simplify the problem. In order to do so, let us define a which is the zero-temperature limit of $f_{\boldsymbol{k}}$ [151],

$$a \equiv -\lim_{k\to 0} f_{\boldsymbol{k}} = -\lim_{k\to 0} \frac{\delta_0(k)}{k}. \tag{1.25}$$

The length scale that is defined here is the **scattering length** a, which is a measure of the strength of the scattering. When this result is plugged into Equation (1.24), the zero-energy limit of the collisional cross section is found

$$\sigma_{\boldsymbol{k}} \underset{k\to 0}{\simeq} 8\pi a^2. \tag{1.26}$$

To physically understand the scattering length, we will consider the long-range

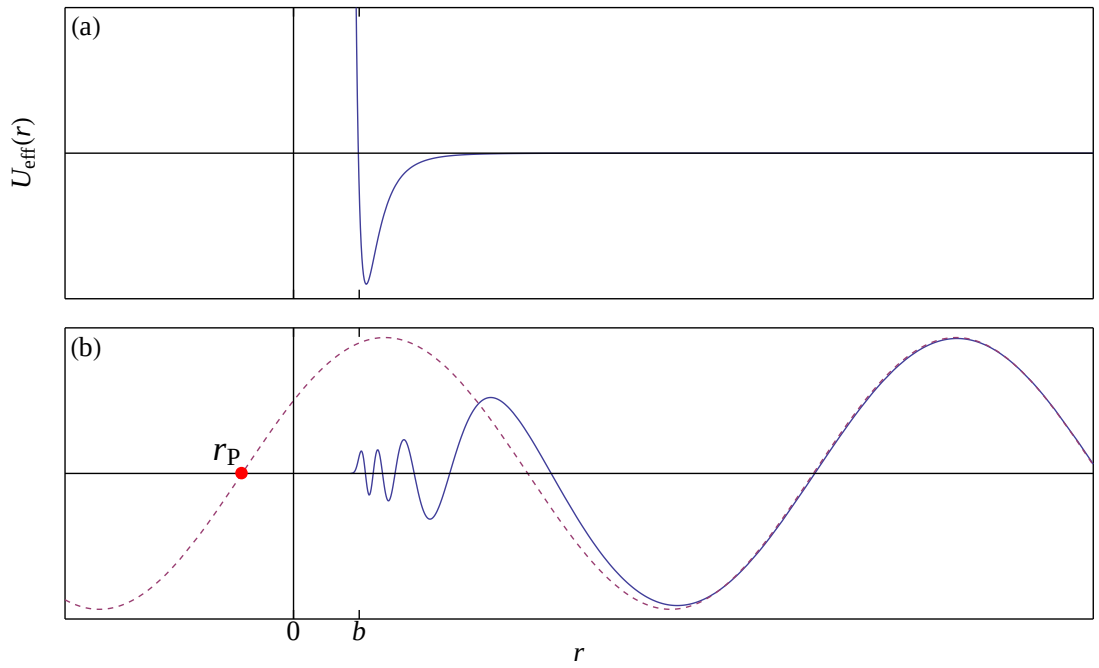

Figure 1.4.: (a) Interatomic induced dipole-dipole interaction potential $U_{\text{eft}}(r)$. (b) Numerical solution of the wavefunction $u_{k0}(r)$ for the interatomic potential (solid blue line) and the long-range solution extended towards $r = 0$: $v_{k0}(r)$ (dashed red line). In the low energy limit, the red dot corresponds to $r = r_{\text{P}} \equiv a$ and geometrically shows the scattering length a as the distance between the point r_{P} and the origin.

behavior of the wavefunction (see Equation (1.5) for the definition of $u_{k0}(r)$) and extend that to the short range region:

$$\begin{aligned} v_{k0}(r) &\equiv \lim_{r\to\infty} u_{k0}(r) \\ &= C\sin\left(kr + \delta_0(k)\right). \end{aligned} \tag{1.27}$$

In Figure 1.4, the long-range behavior extended to the short-range is depicted. The red dot in the figure corresponds to the point $r = r_P \equiv -\delta_0/k$. In the limit of cold collisions $k \to 0$ this point corresponds to the scattering length a (see Equation (1.25)).

We can also define a in a different manner, which, in the limit of cold-collisions, is equivalent to the above definition. In order to do so let us look at the expansion of $v_{k0}(r)$ (Equation (1.27)) in terms of k up to first order in k

$$v_{k0}(r) \underset{k\to 0}{\simeq} kr\cos\delta_0 + \sin\delta_0. \tag{1.28}$$

In this case, the zero-crossing is given by $r_P = -(1/k)\sin\delta_0/\cos\delta_0 = -\tan\delta_0/k$. So an equivalent definition of the scattering length a is

$$a = -\lim_{k\to 0}\frac{\tan\delta_0(k)}{k}. \tag{1.29}$$

This definition shows that $\delta_0(k)$ needs to be defined up to a factor of π and it is sufficient to consider $\delta_0(k)$ to be between $-\pi/2$ and $\pi/2$. This statement can be graphically interpreted by considering Figure 1.4 and imagining that π was added to δ_0. This would shift the wavefunction and change the slope direction of the first intersection, but it would not change the position of the intersection.

Using the previous results, we are in a position to write down the wavefunction v_{k0}. Here we have chosen the normalization $v_{k0}(0) = C$.

$$v_{k0}(r) = \begin{cases} C\left(1 - \frac{r}{a}\right) & \text{if } k = 0 \\ C\left(\frac{\sin(kr+\delta_0(k))}{\sin\delta_0(k)}\right) & \text{if } k \neq 0, \end{cases} \tag{1.30}$$

where the first case follows directly from Equations (1.28) and (1.29).

The result for $k = 0$ is the Bethe-Peierls boundary condition for two particles

[152]. In terms of the wavefunction, this condition is written as

$$\psi \underset{r\to 0}{\simeq} C\left(\frac{1}{r}-\frac{1}{a}\right). \tag{1.31}$$

This result includes all the information about the short-range in a single condition close to zero. In the rest of this thesis, we will be interested in the long-range behavior of the two-particle system and use the boundary condition to include the short-range physics.

1.2. Feshbach Resonances - Tuning the Scattering Length

1.2.1. Two-Channel Model

In this section, we will consider a simple model to understand the properties and the physical origin of Feshbach resonances. For a more elaborated discussion, we refer the reader to a review on Feshbach resonances [48].

In Figure 1.5a we have plotted two molecular potentials: $V_{\mathrm{bg}}(r)$ (the entrance or open channel) and $V_{\mathrm{c}}(r)$ (the closed channel). Let us consider to be in the limit of ultracold collisions, then the collisional energy $E\approx 0$. When there is a bound state in the closed channel, with energy E_{c}, that is close to the asymptotic potential energy in the open channel (by definition $E=0$) the scattering in the open channel is modified. Due to the different magnetic moments of the two channels, the relative offset of the closed channel can be modified by changing the magnetic field, which will change the value of E_{c}. Around the point $E_{\mathrm{c}}=0$ the scattering length can be tuned from -0 to $+0$, through $\pm\infty$. This resonant behavior is called a Feshbach-resonance and is described by the following equation [153],

$$a(B)=a_{\mathrm{bg}}\left(1-\frac{\Delta}{B-B_0}\right), \tag{1.32}$$

where a_{bg} is the background scattering length, Δ is the width of the resonance in magnetic field and B_0 is the resonance position.

In order to have a Feshbach resonance, however, there needs to be a small coupling of the bound state to the open channel threshold. Usually in alkali atoms, this coupling is mediated by hyperfine interactions between the nuclear spin and the spin of the valence electrons of the colliding atoms. The state of the coupled system[2], is the so called dressed state with energy E_{b}. The coupling strength of

[2] The coupling of a discrete state to the continuum is described in [154]

the bound state to the continuum determines the width of the resonance. When E_b is positive the dressed bound state is "virtual", meaning that it influences the scattering, but it is not an accessible state. This situation corresponds to the right side of Figure 1.5b. The other situation is a negative E_b, in this case there is a real bound state, because it is below the continuum. This state is a molecular state and named the weakly bound dimer. In Figure 1.5b this situation corresponds to the left side of the Feshbach resonance or the positive-a side.

The energy of the dressed state on the positive-a side is indicated by the blue solid line in Figure 1.5b. Far away from the resonance, the dressed state is dominated by the closed channel, indicated by the linear slope given by the difference in magnetic moment of the molecule in the closed channel an the free atoms in the open channel $d\mu$. Closer to the resonance the behavior becomes quadratic and the weakly bound dimer becomes a dressed state, see the inset of Figure 1.5b. Even closer to the resonance, the dimer energy approaches the continuum energy and its character becomes open channel dominated. At the resonance, the dressed state crosses the continuum. These different regimes are determined by the strength of the resonance s_{res}, which is related to the width of the resonance, the background scattering length a_{bg} and $d\mu$ [48].

Close to the resonance, when $a \gg R_{vdW}$, the scattering becomes universal. This means that all the scattering properties are described by a universal parameter: the scattering length a. The energy of the weakly bound dimer is given by

$$E_b = -\frac{\hbar^2}{2\mu a^2} = -\frac{\hbar^2}{ma^2}, \tag{1.33}$$

which varies quadratically with the scattering length. This is depicted in the inset of Figure 1.5b.

1.2.2. Determining the Position and Width

Theoretically predicting the position and width of a Feshbach resonance is difficult, because the calculation of the scattering length depends on complex atom-atom interaction potentials and is very sensitively upon the details of the long-range potentials. To fully characterize the Feshbach resonance we need the position of the resonance B_0, the background scattering length a_{bg} and the resonance width Δ, see Equation (1.32).

The background scattering length a_{bg} is usually determined away from Feshbach resonances by thermalization measurements [48].

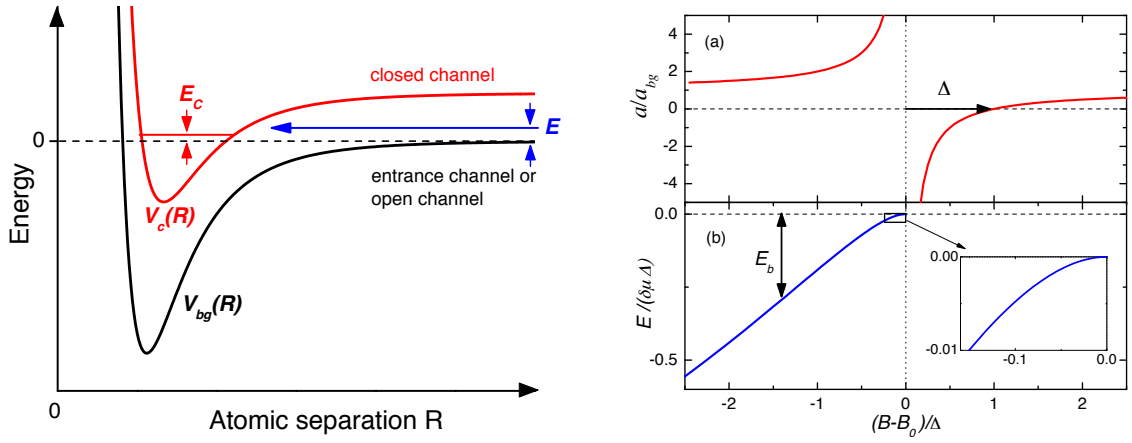

(a) **(b)**

Figure 1.5.: Simplified two-channel model for Feshbach resonances (images taken from [48]). **(a)** Two-channel model for describing Feshbach resonances (in our notation $r = R$). The molecular potential $V_{\mathrm{bg}}(R)$ (black) is the potential that two free-particles enter by coming from $R \to \infty$: it is termed the entrance or open channel. The atomic potential $V_{\mathrm{c}}(R)$ (red) is a potential that has a bound state with energy E_{c}. At low energy, a Feshbach resonance appears when the energy $E_{\mathrm{c}} \to 0$. The relative energy of the bound state can be tuned with a magnetic field. **(b)** Scattering length and dressed bound state energy as a function of magnetic field. Varying the magnetic field allows us to tune the offset of the closed channel potential with respect to the open channel. This moves the bound state and modifies the scattering properties through a. The red line is the scattering length a and the blue line is the energy of the dressed bound state E_{b} (*i.e.* weakly bound dimer) as a function of magnetic field. The inset shows the quadratic behavior close to the Feshbach resonance of the dressed bound state. Around the point $E_{\mathrm{b}} = 0$ or $B = B_0$ a Feshbach resonance appears.

There are several methods to determine the position of the Feshbach resonance B_0. A rough indication of the position can be given by characterizing the inelastic losses [53, 56, 155–157]. This technique is based on the direct relation between three-particle losses and the scattering length a: $L_3 \propto a^4$ [113]. Hence, on resonance the particle losses are most severe and a rough indication of the resonance position can be given.

Furthermore, the bound state energy of the dimer is converted into kinetic energy. These dimers might also collide with the other atoms and heat up the cloud. Three-particle recombination is more severe in high density parts of a cloud, which in a trap correspond to the atoms with low potential energy. Hence, on average the particles with less potential energy are lost and anti-evaporation takes place [56]. These two heating effects can also be used to determine the resonance position [54, 63].

A more accurate method to determine the resonance position is to measure the binding energy of the weakly bound dimer using Radio Frequency (RF) spectroscopy [158–160]. RF-radiation tuned to the binding energy of the weakly bound dimer stimulates the formation of the dimer, on resonance ($h\nu = -E_b$), this results in an increased loss of free atoms. Recently, this technique was used to determine the position of the Feshbach resonance between the states $|1\rangle$ and $|2\rangle$ in ^{6}Li. The result is $B_0 = 832.18(8)$ G, with a remarkable precision of 80 mG [161].

The width of the resonance is given by the difference in magnetic field between the position of the resonance B_0 and the zero-crossing of the scattering length. The zero-crossing is usually determined by monitoring elastic collisions, through the thermalization rate [78, 78, 162–167]. When the scattering length crosses zero the rethermalization rate vanishes and no evaporation occurs.

Combining the results of both photo-association spectroscopy and these precision measurements, theorists predict $a(B)$ using multi-channel analysis (see for example [48]).

Together the Feshbach resonance position B_0, the resonance width Δ and the background scattering length a_{bg} fully characterize the properties of the Feshbach resonance.

1.3. Summary

In this chapter, we have discussed two-particle scattering. We have derived the effect of scattering from first principle and by doing so introduced the concepts scattering amplitude, scattering cross section and scattering length. These prop-

erties are useful in the many-particle scattering problem, as we will see for the three-particle problem in Chapter 2.

To summarize the results of this chapter let us construct a Zero Range Model (ZRM), which condenses all the information about the scattering potential into a boundary condition at $r = 0$

1. **Free particle Hamiltonian:** when the two particles i and j are not on top of each other ($r_{ij} > 0$):

$$-\frac{\hbar^2}{2m}\sum_{i=1}^{2}\mathbf{\Delta}_{r_i}\,\psi = E\,\psi \tag{1.34}$$

2. **Two-particle contact condition:** when the two particles i and j come close to each other (*i.e.* $r_{ij} \to 0$):

$$\psi(r_{ij}) \underset{r_{ij}\to 0}{\simeq} C\left(\frac{1}{r_{ij}} - \frac{1}{a}\right). \tag{1.35}$$

The usage of a ZRM turns out to be useful in the extension of few- to many-particle physics.

Finally, we have discussed the tuning of the scattering length through the usage of Feshbach resonances and introduced the weakly bound dimer state.

2. Three-Particle Scattering

In this chapter, we are going to investigate the quantum mechanical three-particle problem as a first step towards many-particle systems. In quantum mechanics, the three-particle problem initially became of interest to describe the orbit of electrons around the nucleus of an atom. Later on, the nuclear physics community grew interested in the three-particle problem for better describing the interactions between nuclei and between quarks in these nuclei.

In the following, we will describe the scattering of three particles in free space. We will derive the quantities of interest using the analogies to the two-particle scattering system. We will start with the introduction of the three-particle Hamiltonian, which will then be written in hyperspherical coordinates. To solve the Hamiltonian, we will consider three scattering regimes: the range of the interaction, the short-range and the long-range.

In this limit the short-distance ($R \ll a$), the system simplifies to the unitary interactions case ($a \to \infty$). The wavefunction is greatly simplified due to the possibility to separate the hyperradial from the hyperangular part. The hyperradial Schrödinger Equation is written down and a set of effective potentials, due to geometrical effects, is identified. These potentials have a $1/R^2$ behavior. In the case of three identical bosons, there is one attractive $1/R^2$ potential, the Efimov channel [118]. We will give the solutions of the radial Schrödinger equation and identify them as incoming and outgoing waves. The incoming and outgoing hyperradial waves are used to include the effect of the scattering center by adding a phase factor to the outgoing wave. Afterwards, we will introduce a toy model to understand the physical meaning of the phase shift. Then, the full model is used to show that the potential allows for infinitely many trimer bound states: the Efimov trimers. These trimer states are separated in energy by a universal factor.

In the long-range there are two possible cases: unitary ($a \to \infty$, hence $R \ll a$) and finite ($R \gg a$) interactions. We will couple both cases to the short-range and show that the coupling is analogues for both cases.

Afterwards, inelastic scattering is introduced into the three-particle scattering problem. We will replace the results obtained in the elastic scattering problem by an analog for inelastic scattering. Furthermore, the flux of the wavefunction is used

to calculate the three-particle loss coefficient, which is discussed in great detail. Finally, we will show that at unitarity the three-particle losses show log-periodic oscillation behavior.

The theory that will be presented in this chapter was derived by Dmitry Petrov and Felix Werner; *cf.* [143], and are strongly based on their unpublished notes [144].

2.1. Elastic Scattering

Having discussed the two particle scattering problem, in Chapter 1, we are now in a position to extend this to the three-particle problem. We will start by introducing the hyperspherical Hamiltonian in the two-particle Zero-Range model (ZRM) and introduce an additional three-particle condition to the ZRM. In order to find the wavefunction of the problem, we will apply a separability of coordinates ansatz (in Appendix A.4, we show the validity of this ansatz). Finally, the wavefunctions are given and the properties of the three-particle scattering system are discussed (for more information about the three-particle problem, we refer the reader to a review of the subject in [168]).

2.1.1. Three-Particle Hamiltonian

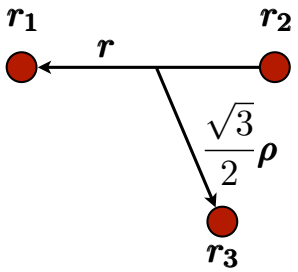

Figure 2.1.: The three-particle system. The vectors $\boldsymbol{r_i}$ with $i \in \{1, 2, 3\}$ correspond to the positions of the individual particles. The Jacobi coordinates $\boldsymbol{r}$ and $\boldsymbol{\rho}$ are defined by $\boldsymbol{r} = \boldsymbol{r_1} - \boldsymbol{r_2}$ and $\sqrt{3}/2\ \boldsymbol{\rho} = \boldsymbol{r_3} - (\boldsymbol{r_1} + \boldsymbol{r_2})/2$, respectively.

The three-particle Hamiltonian in the center of mass frame is given by

$$\left[-\frac{\hbar^2}{m}\left(\Delta_r + \Delta_\rho\right) + V(\boldsymbol{r}, \boldsymbol{\rho})\right] \psi(\boldsymbol{r}, \boldsymbol{\rho}) = E\ \psi(\boldsymbol{r}, \boldsymbol{\rho}),$$

where we have introduced the Jacobian coordinates $\boldsymbol{r} = \boldsymbol{r}_1 - \boldsymbol{r}_2$ and $\boldsymbol{\rho} = 2/\sqrt{3}\,(\boldsymbol{r}_3 - (\boldsymbol{r}_1 + \boldsymbol{r}_2)/2)$. $V(\boldsymbol{r}, \boldsymbol{\rho})$ is the interaction potential for the three particles. The kinetic part of this Hamiltonian includes two terms: on the one hand the relative motion $\boldsymbol{r}$ through $\Delta_{\boldsymbol{r}}$ and on the other hand the relative motion $\boldsymbol{\rho}$ through $\Delta_{\boldsymbol{\rho}}$. In Figure 2.1, these relative coordinates are depicted.

2.1.2. Hyperangular Problem

In order to solve the problem, we use a new set of coordinates: the hyperspherical coordinates. In the Jacobian coordinate system, the coordinates are given by $\{\boldsymbol{r}, \boldsymbol{\rho}\} = \{r, \hat{\boldsymbol{r}}, \rho, \hat{\boldsymbol{\rho}}\}$. Transforming these coordinates to hyperspherical coordinates gives us $\boldsymbol{R} = \{R, \alpha, \hat{\boldsymbol{r}}, \hat{\boldsymbol{\rho}}\}$, where R is the hyperradius given by $R = \sqrt{(r^2 + \rho^2)/2}$ and $\alpha = \arctan(r/\rho) \in [-\pi/2, \pi/2]$ is the angle that marks the ratio between the distances r and ρ. It is practical to use the hyperspherical angles: $\boldsymbol{\Omega} = \{\alpha, \hat{\boldsymbol{r}}, \hat{\boldsymbol{\rho}}\}$.

Using the notation introduced in [168], the Hamiltonian can be rewritten in the following form:

$$\left(T_R + T_\alpha + \frac{1}{2m}\frac{\Lambda^2}{R^2} + V(R, \boldsymbol{\Omega})\right)\psi(R, \boldsymbol{\Omega}) = E\ \psi(R, \boldsymbol{\Omega}), \tag{2.1}$$

where we have separated the distance parts T_R and T_α from the angular part given by the generalized angular momentum operator Λ^2.

$$\begin{aligned}
\Lambda^2 &= \frac{L_{\boldsymbol{r}}^2}{\sin^2\alpha} + \frac{L_{\boldsymbol{\rho}}^2}{\cos^2\alpha}, \\
T_R &= -\frac{\hbar^2}{2m}\left[\frac{\partial^2}{\partial R^2} + \frac{5}{R}\frac{\partial}{\partial R}\right], \\
T_\alpha &= -\frac{\hbar^2}{2m}\frac{1}{R^2}\left[\frac{\partial^2}{\partial \alpha^2} + 4\cot(2\alpha)\frac{\partial}{\partial \alpha}\right].
\end{aligned}$$

Λ^2 is the sum of the angular momentum of each pair weighted by their relative pair sizes. T_R is the kinetic energy associated to the hyperradial movement, T_α is the kinetic energy associated to the relative pair movement. It is convenient to combine the relative pair and angular movement into one hyperangular operator $T_{\boldsymbol{\Omega}} \equiv R^2 T_\alpha + \frac{1}{2m}\Lambda^2$.

In general, the solution $\psi(R, \boldsymbol{\Omega})$ is not factorizable into a hyperradial and hyperangular part. A convenient way of writing the wavefunction, is to use the adiabatic hyperspherical representation [168], which expresses the wavefunction ψ in each

point R in terms of the orthonormal set of hyperangular functions $\Phi_n(R, \mathbf{\Omega})$,

$$\psi(R, \mathbf{\Omega}) = R^{-5/2} \sum_n f_n(R) \Phi_n(R, \mathbf{\Omega}). \tag{2.2}$$

where $\Phi_n(R, \mathbf{\Omega})$ are the solutions of the hyperangular equation

$$\left[\frac{T_{\mathbf{\Omega}}}{R^2} + V(R, \mathbf{\Omega}) \right] \Phi_n(R, \mathbf{\Omega}) = V_n(R)\, \Phi_n(R, \mathbf{\Omega}), \tag{2.3}$$

where $V_n(R)$ are the eigenvalues for a specific hyperradius R.

2.1.3. Scattering Regimes

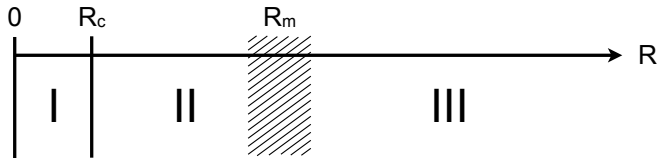

Figure 2.2.: The scattering regimes. I. the range of the interactions, typically $R_c \sim R_{vdW}$. II. the short-range $R_c < R < R_m$, where $R_m \equiv \min(|a|, 1/k_{th})$. III. the long-range $R > R_m$

The three-particle problem can be separated into three-regimes (see Figure 2.2): I. range of the interactions, typically $R \ll R_c \sim R_{vdW}$; II. short-range (SR): $R_c \ll R \ll R_m \equiv \min(|a|, 1/k_{th})$; III. long-range (LR): $R_m \ll R$. In the two-particle problem, Regime II and III are combined, because the solutions are known over the whole range. In other words, there is only the range of the interaction defined by the van der Waals length R_{vdW} and the long-range. In the three-particle problem, the solutions, in general, are not analytically known across the boundary between Regimes II and III. However, the limiting cases $R \ll a$ and $R \gg a$ are analytically solvable. The first case corresponds to the solutions in Regime II and the second case to the solutions in Regime III. Let us note that for resonant interactions $a \to \infty$ the condition $R \ll a$ is always fulfilled and the solutions are known over the whole range. It would then not be necessary to consider Regime II and III separately. However, to keep the analogy with the finite interactions case we will use it. When the solutions in both regimes are known, we will connect the long-range regime III to the short-range regime II. Let us start with the resonant interactions case.

2.2. Unitary Interactions - Efimov's Ansatz

The solutions of Equation (2.1) are, in general, not factorizable and solving the hyperangular problem is difficult (see, for example [168], and references therein). However, in 1970, Efimov showed that the problem is simplified if unitary two-particle interactions are considered ($a \to \infty$). In this case, a separability Ansatz can be used (see Appendx A.4). For all R, the wavefunction can then be projected onto the orthonormal set of hyperangular Efimov states $\lim_{a\to\infty} \Phi_n(R, \boldsymbol{\Omega}) = \phi_n(\boldsymbol{\Omega})$ which do not depend on the hyperradius R,

$$\psi(R, \boldsymbol{\Omega}) = R^{-2} \sum_n F_n(R)\, \phi_n(\boldsymbol{\Omega}). \tag{2.4}$$

The hyperradial wavefunctions $F_n(R)$ are the known solutions of the one-dimensional hyperradial Schrödinger Equation

$$-\frac{\hbar^2}{2m}\left[\frac{\partial^2}{\partial R^2} + \frac{1}{R}\frac{\partial}{\partial R} - \frac{\lambda_n^2}{R^2}\right] F_n(R) = E\ F_n(R), \tag{2.5}$$

and the hyperangular wavefunctions ϕ_n are the solutions of the hyperangular equation

$$T_{\boldsymbol{\Omega}}\, \phi_n(\boldsymbol{\Omega}) = \lambda_n\, \phi_n(\boldsymbol{\Omega}).$$

The projection of the wavefunction onto these states we will call a wave in Channel n. For three identical bosons the spectrum of solutions is given by

$$\lambda = \{i\, s_0, s_1, s_2, \ldots\},$$

where $s_n \in \mathbb{R}_+$. The 0^{th}-channel with $s_0 \approx 1.00624$ indicates the Efimov Channel.

2.2.1. Hyperspherical Waves

In Equation (2.5), we see that the term s_n^2/R^2 can be regarded as a potential term, which is graphically depicted in Figure 2.3a. The potentials with $\lambda \in \mathbb{R}$ are purely repulsive at $R \to 0$ and do not support any bound states. We will ignore these potentials and focus on the attractive $-s_0^2/R^2$ Efimov potential, which has some interesting properties.

Let us consider the case where the particles are outside of the range of the interactions, in Regime II. The solutions of the hyperradial Schrödinger Equation

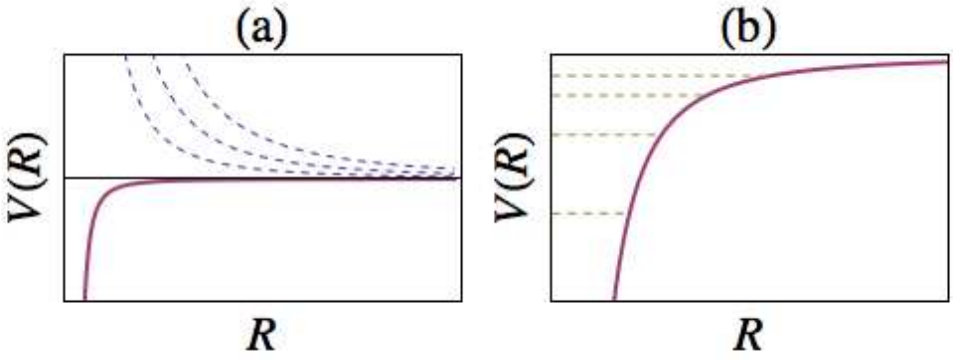

Figure 2.3.: The potentials corresponding to the Efimov potential channels in Equation (2.5). In (a) we see a selection of Efimov potentials where the dashed blue lines correspond to the collection of repulsive potentials given by the spectrum $\{s_1, s_2, s_3, ...\} = \{4.47, 6.82, 9.32, ...\}$ [169]. In bold red, we depict the attractive $-s_0^2/R^2$ potential giving rise to Efimov physics. In (b) only the attractive $-s_0^2/R^2$ is shown (bold red), and in dashed gold we render part of the infinite spectrum of three-particle bound states supported by the Efimov potential.

for s_0 with $E > 0$ are given by a linear combination of Bessel functions $J_\nu(x)$

$$F_{i\,s_0}(R) = A\,J_{+i\,s_0}(kR) + B\,J_{-i\,s_0}(kR), \tag{2.6}$$

where k is the hyperradial wavenumber defined by the hyperspherical plane wave energy $E = \hbar^2 k^2/(2m)$, evolving in a 6d space. We will solve the problem for any value of k and later on integrate over k to describe finite temperature effects. The solution consists of two parts: a wave going towards the center ($R = 0$): $J_{-i\,s_0}(kR)$ and a wave going away from the center: $J_{+i\,s_0}(kR)$ (see Appendix A.2 for the behavior of these "waves"). The coefficients A and B are the amplitudes of the waves.

2.2.2. Short-Distance Scattering - $R < R_\mathrm{m}$

We will start this section by discussing Regime II. In that regime the Schrödinger Equation is simplified and we are able to write down the solution in the form of an incoming and outgoing wave. The effect of Regime I is imposed by a boundary condition at $R = 0$ in Regime II (see Section 1.1.5, for analogy with two-particle scattering) and used to show the existence of trimer bound-states (the Efimov trimers). To do so let us look at the short-range solutions of Equation 2.6.

Close to $R=0$, but still outside of the range of the interactions, $R \gg R_c$, the hyperradial wavefunction is given by

$$\begin{aligned} F_{i\,s_0}(R) &\underset{R\to 0}{\simeq} \tfrac{1}{\sqrt{s_0}} \left[A_1^{\text{in}} \, (kR)^{+i\,s_0} + A_1^{\text{out}} \, (kR)^{-i\,s_0} \right] \\ &= \tfrac{1}{\sqrt{s_0}} \left[A_1^{\text{in}} \, e^{+i\,s_0 \ln(kR)} + A_1^{\text{out}} \, e^{-i\,s_0 \ln(kR)} \right] . \end{aligned} \tag{2.7}$$

The amplitudes A_1^{in} and A_1^{out} are introduced to define the solution in the short-range (Regime II, which is indicated by the index 1). In terms of the wavefunction, this becomes

$$\psi(R, \mathbf{\Omega}) \underset{R\to 0}{\simeq} A_1^{\text{in}} \; \varphi_1^{\text{in}} + A_1^{\text{out}} \; \varphi_1^{\text{out}}, \tag{2.8}$$

where we have used the following definitions for the incoming and outgoing waves:

$$\begin{aligned} \varphi_1^{\text{in}} &\equiv \phi_{i\,s_0}(\mathbf{\Omega}) \frac{(kR)^{+i\,s_0}}{R^2\sqrt{s_0}}, \\ \varphi_1^{\text{out}} &\equiv \phi_{i\,s_0}(\mathbf{\Omega}) \frac{(kR)^{-i\,s_0}}{R^2\sqrt{s_0}} = (\varphi_1^{\text{in}})^*. \end{aligned} \tag{2.9}$$

We have defined incoming and outgoing waves with respect to the boundary between Regime II and III ($R=R_m$). This means that waves going away from $R=R_m$ are outgoing waves and waves coming towards $R=R_m$ are incoming. In Appendix A.2, we will show that these waves have a flux vector in the radial direction, which distinguishes the incoming from the outgoing wave. With the short-range non-interacting wavefunctions at hand, we are now able to introduce elastic scattering, coming from Regime I, into the problem.

2.2.2.1. Elastic Scattering

In Section 1.1.5, we have seen the procedure to include scattering into the two-particle problem. This was done by a phase factor between the incoming and outgoing waves. This phase was acquired in the interaction regime, but only used outside the range of the interactions. A boundary condition at $r=0$ contained all the information about the interactions.

For the three-particle system, we will employ the same principle. The interactions from Regime I are included by introducing a phase factor between the incoming and outgoing waves in Regime II (outside the range of the interactions).

In Equation (2.7), the radial wavefunction was given and if we include a phase

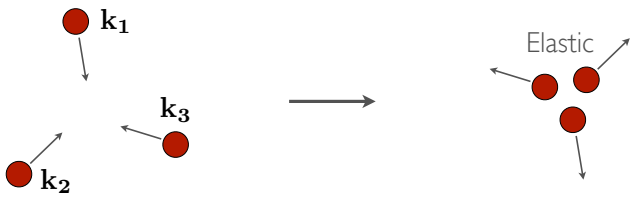

Figure 2.4.: Elastic scattering. The total kinetic energy and total momentum are conserved. The incoming and outgoing wavefunctions differ only by a phase factor.

due to scattering into that equation, the following is obtained:

$$F_{i\,s_0}(R) \underset{R\to 0}{\simeq} \frac{A_1^{\text{out}}}{\sqrt{s_0}} \left[e^{-i\,s_0 \ln(kR)} + e^{+i\,s_0 \ln(kR)+i\,2\delta(k)}\right].$$

Following Efimov, let us cast δ into the form $\delta(k) \equiv -\,s_0 \ln kR_{\text{t}} + \pi/2$. Here R_{t} is the three-particle Efimov parameter. We can then reformulate the radial wavefunction as:

$$F_{i\,s_0}(R) \underset{R\to 0}{\simeq} \frac{A_1^{\text{out}}}{\sqrt{s_0}} \left[e^{-i\,s_0 \ln R/R_{\text{t}}} - e^{+i\,s_0 \ln R/R_{\text{t}}}\right].$$

The physical meaning of R_{t} will be extensively discussed in Section 2.2.2.2.

In terms of the full wavefunction the effect of the elastic scattering can be written as:

$$\psi \underset{R\to 0}{\simeq} A_1^{\text{out}} \left[\varphi_1^{\text{out}} + \mathcal{A}_{\text{el}} \varphi_1^{\text{in}}\right], \tag{2.10}$$

where $\mathcal{A}_{\text{el}} \equiv -\,(kR_{\text{t}})^{-2is_0}$ can be considered as the boundary condition of the problem at $R = 0$. This is analogous to the s_l in Section 1.1.5.

2.2.2.2. Efimov Bound States

The $-1/R^2$ potential is scale-invariant[1], which means that there is no characteristic scale of the potential (unlike R_{vdW} for a $-1/R^6$ van der Waals potential) and the potential supports an infinite number of bound states. The introduction of R_{t} into the wavefunction gives a characteristic scale to the $-1/R^2$ potential and fixes the

[1] If the Hamiltonian is of the form $H(x) = \frac{p^2}{2m} + V(x)$ and $V(x)$ has the form $V(x) \propto 1/x^2$, then for a scaling parameter λ, we can write $H(\lambda x) = \frac{1}{\lambda^2} H(x)$. This marks the scale invariance of the Hamiltonian.

positions of the bound states.

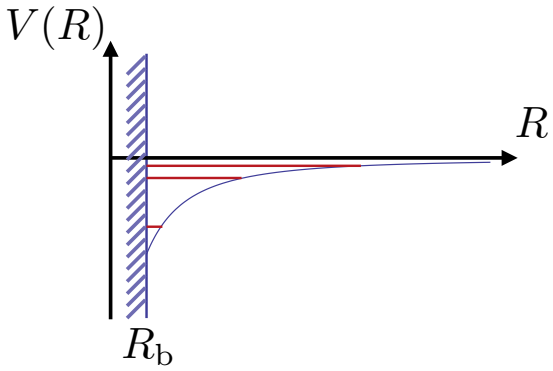

Figure 2.5.: A toy-model describing the physics of the three-particle problem using a wall at $R = R_b$. The blue curve is the $-s_0^2/R^2$ potential describing the Efimov physics. The red lines are graphical representations of the bound states of the Efimov potential given by Equation (2.11). Imposing a node for the wavefunction at $R = R_b$ implies that the three-particle parameter $R_t = R_b e^{in s_0}$ with $n \in \mathbb{Z}$.

To get a more physical meaning of this R_t let us look at a toy model. This system has a potential barrier placed at some distance $R = R_b$ from the origin. The potential is shown in Figure 2.5 and it shows that the energy of the bound states is bounded from below and that R_b is a characteristic length scale of the potential.

The infinite wall at $R = R_b$ implies that the wavefunction has a node at R_b. At the points $R = R_b$, the wavefunction reads

$$\psi(R_b, \Omega) \underset{R\to 0}{\simeq} A \frac{\phi_{i s_0}(\Omega)}{R^{-5/2}} \left[e^{-i s_0 \ln R_b/R_t} - e^{+i s_0 \ln R_b/R_t} \right]$$

from here we can see that R_b should be equal to R_t for the wavefunction to vanish.

Returning to the full problem the energy spectrum is given by [168]

$$E_t = \frac{\hbar^2}{m} \frac{2}{R_t^2} e^{-(2\pi/s_0)(n-n_t)+2\arg\Gamma(1+i s_0)/s_0} \quad \text{with} \quad n \in \mathbb{Z}, \tag{2.11}$$

which is defined up to a factor $e^{2\pi/s_0} \approx (22.7)^2$. The integer number n_t is the energy state with characteristic length R_t. This is the infinite serie of Efimov states as predicted in [118]. For the toy model, we use $n \in \mathbb{N}$, because the energy spectrum is bounded from below by the barrier at $R = R_b$. The resulting bound states are

graphically depicted in Figure 2.3 and for the toy model with a barrier at R_b in Figure 2.5.

The parameter R_t is predicted to depend on the characteristic length scale of the two-particle problem R_vdW [131–136]. Initial experiments on different atoms suggested this remarkable universality (see for a comparison [121]). Experiments on ^{133}Cs with six different Feshbach resonances found that $a_-/\bar{a} \simeq -9.5(4)$ [121, 129]. For ^{39}K five intermediate Feshbach resonances were studied and they also found values close to $a_-/\bar{a} \simeq -9.5$. The parameters a_- and $\bar{a}$ are the position of the Efimov resonance[2] and the mean scattering length[3], respectively. This topic is still debated and a strong motivation to further explore three-particle physics.

2.2.2.3. Zero-Range Model

The result from Section 2.2.2.1, includes elastic scattering of three-particles into the wavefunction. This result can be used in a ZRM as a three-particle contact condition at $R=0$. Together with the condition from the ZRM for two-particle scattering these conditions form a ZRM for three-particle systems. Let us list the conditions for the three-particle ZRM:

1. **Free particle Hamiltonian:** when two particles are not on top of each other ($r_{ij}>0$):

$$-\frac{\hbar^2}{2m}\sum_{i=1}^{2}\boldsymbol{\Delta}_{r_i}\,\psi = E\,\psi \tag{2.12}$$

2. **Two-particle contact condition:** when $r_{ij}\to 0$:

$$\psi \underset{r_{ij}\to 0}{\simeq} A\left(\frac{1}{r_{ij}}-\frac{1}{a}\right). \tag{2.13}$$

3. **Three-particle contact condition:** when $R\to 0$:

$$\psi(R,\boldsymbol{\Omega}) \underset{R\to 0}{\simeq} A_1^{\mathrm{out}}\frac{\phi_{i\,s_0}}{R^{-5/2}}\left[e^{-i\,s_0\ln R/R_\mathrm{t}} - e^{+i\,s_0\ln R/R_\mathrm{t}}\right] \tag{2.14}$$

   For simplicity, the last condition can also be written as $\psi = A_1^{\mathrm{out}}\left[\varphi_1^{\mathrm{out}} + \mathcal{A}_\mathrm{el}\varphi_1^{\mathrm{in}}\right]$, where $\mathcal{A}_\mathrm{el} = -(kR_\mathrm{t})^{-2is_0}$.

[2] a_- is related to R_t via $R_\mathrm{t} = a_-\exp(-(\delta_0-\pi/2)/s_0)\approx 0.983a_-$, where $\delta_0 = 1.588$ [170]
[3] $\bar{a}$ is related to R_vdW via $\bar{a} = \left[4\pi/\Gamma(1/4)^2\right]R_\mathrm{vdW}$

From now on, the scattering will be considered in the ZRM, meaning that we work under the conditions above. The result of the scattering problem is summarized by the following: If the amplitude and phase of the incoming wave are known, the full wavefunction in the short-range (Regime II) is known.

2.2.3. Long-Distance Scattering

In Section 2.2.2, the short-distance scattering was considered (Regime II). The result of that section is a boundary condition at $R = 0$. This boundary condition determines the wavefunction in the short-range, with the only degree of freedom the amplitude A_1^{out} of the wave going into the short-range, according to Equation (2.7).

In the following, we will describe Regime III and find the solutions of the Schrödinger Equation in this regime. These solutions are then coupled to Regime II, through an s-matrix formalism, which will provide us with a relation between A_1^{out} and the amplitude of the incoming wave in Regime III ($R \gg R_{\text{m}}$).

2.2.3.1. Long-Range Wavefunction

In the long-range, with resonant interactions, the system is correctly described by the hyperradial Schrödinger Equation given in Equation (2.5), with the solutions being the hyperradial wavefunctions given by Equation (2.6). However, the Bessel functions in the limit $kR \to \infty$ are different and the long-distance wavefunctions are given by the linear superposition

$$F_{i\,s_0}(R) \underset{R\to\infty}{\simeq} \frac{1}{\sqrt{kR}} \left[A_3^{\text{out}}\ e^{+ikR} + A_3^{\text{in}}\ e^{-ikR} \right], \tag{2.15}$$

where A_3^{out} and A_3^{in} are the amplitudes of, respectively, the incoming and outgoing waves[4]. These terms are incoming and outgoing hyperspherical waves with relative momentum $k = |\boldsymbol{k}|$ in the long-distance. In terms of the wavefunction, we can write this as

$$\psi(R, \boldsymbol{\Omega}) \underset{R\to\infty}{=} A_3^{\text{out}}\ \varphi_3^{\text{out}} + A_3^{\text{in}}\ \varphi_3^{\text{out}}, \tag{2.16}$$

[4] The index 3 is used to indicate that we use these in the long-range (Regime III)

where we have introduced the incoming and outgoing waves by,

$$\varphi_3^{\text{in}} \equiv \phi_{i\,s_0} \frac{e^{-ikR}}{R^2\sqrt{kR}}$$
$$\varphi_3^{\text{out}} \equiv \phi_{i\,s_0} \frac{e^{+ikR}}{R^2\sqrt{kR}} = \left(\varphi_3^{\text{in}}\right)^* . \tag{2.17}$$

In the following, we will show how these waves couple to the short-range in Regime II.

2.2.3.2. Coupling of the Long-Range to the Short-Range

To describe the coupling between the long-range and the short-range, we will employ an s-matrix technique. In order to do so, we need to define the channels that are available for the scattering. In the short-range, there is only the Efimov Channel (Channel 1) with incoming and outgoing waves, which are given by Equation (2.9). For unitary interactions in the long-range, there is also only one channel with an incoming and an outgoing wave, which are given by Equation (2.17), this is Channel 3.

In order to define the s-matrix and obtain information about the system, we will describe the stationary flow of atoms which are injected at the origin $R = 0$ (see Figure 2.2) and see how it evolves into the system. The wavefunction describing this is given by

$$\psi_1 \begin{cases} \underset{R\to 0}{\simeq} \varphi_1^{\text{in}} + s_{11}\varphi_1^{\text{out}} \\ \underset{R\to\infty}{\simeq} s_{31}\varphi_3^{\text{out}} \end{cases} . \tag{2.18}$$

The short-range wavefunction shows a wave going away from the center and part of it being reflected back into the short-range. The parameter s_{11} indicates the reflection from Channel 1 back into Channel 1. The long-range part of the wavefunction shows that a part of the wavefunction is transmitted from the short-range into the long-range. The transmission is given by the parameter s_{31}. The full s-matrix is given by,

$$s = \begin{pmatrix} s_{11} & s_{13} \\ s_{31} & s_{33} \end{pmatrix} . \tag{2.19}$$

The s-matrix was shown to be unitary [143], meaning that the total flux is conserved. Physically, the system has time reversal symmetry, which means that the

matrix is symmetrical, $s_{13} = s_{31}$.

Using our knowledge about the s-matrix, we can write down the relations between the amplitudes of all the waves:

$$\begin{aligned} A_1^{\text{out}} &= s_{11} A_1^{\text{in}} + s_{13} A_3^{\text{in}}, \\ A_3^{\text{out}} &= s_{31} A_1^{\text{in}} + s_{33} A_3^{\text{in}}. \end{aligned} \tag{2.20}$$

We can use this to obtain the following relation, between the incoming and outgoing waves

$$\begin{aligned} A_3^{\text{out}} &= \left[s_{33} + \frac{(s_{13})^2 \mathcal{A}_{\text{el}}}{1 - s_{11}\mathcal{A}_{\text{el}}} \right] A_3^{\text{in}}, \\ A_3^{\text{out}} &= s' A_3^{\text{in}} \end{aligned} \tag{2.21}$$

This is a direct relation, in Regime III, between the amplitude of the incoming wave and the amplitude of the outgoing wave.

2.3. Finite-a - Hyperspherical Channels

On the positive-a side, there exists a weakly bound dimer with energy $\propto 1/a^2$. The three-particle scattering must then include atom-dimer scattering, which complicates the derivation. To circumvent this, we will only consider the negative-a side, where this dimer is absent. The three-particle recombination rate that we derive now, thus describes direct recombination into deeply-bound dimer states. In Section 2.5.1, we will briefly touch upon the case where this weakly bound dimer is present.

2.3.1. Long-Distance Scattering

In general, the solution of Equation (2.1) is not factorizable, but for the following it suffices to only know the short- and long-range limits ($R \ll a$ and $R \gg a$, respectively). In the short-range, we already found the solutions (see Section 2.2.2). Hence, it only remains to connect the long-range to the short-range. In other words, we will consider Regime III and connect that to Regime II (see Figure 2.1.3 for the regimes).

2.3.1.1. Long-Range Wavefunction

In the long-range limit $R \gg a$, the hyperspherical harmonics are the solutions of Equation (2.3), with $V(R, \mathbf{\Omega}) = 0$. They only depend on the hyperangles $\mathbf{\Omega}$, *i.e.* $\Phi_n(R, \mathbf{\Omega}) \to \Phi_n(\mathbf{\Omega})$ (see Appendix A.1.4). In this limit, the wavefunction can be factorized into a hyperradial and hyperangular part. The resulting wavefunction is given by

$$\psi(\boldsymbol{R}) \underset{R\to\infty}{\simeq} \sum_{n\in\mathcal{C}_\infty} \left(A_n^{\text{out}}\varphi_n^{\text{in}} + A_n^{\text{in}}\varphi_n^{\text{out}}\right). \tag{2.22}$$

Here we have introduced the incoming and outgoing waves

$$\begin{aligned} \varphi_n^{\text{in}} &\equiv \Phi_n^*(\mathbf{\Omega})\frac{e^{-ikR}}{R^2\sqrt{kR}}, \\ \varphi_n^{\text{out}} &\equiv \Phi_n(\mathbf{\Omega})\frac{e^{+ikR}}{R^2\sqrt{kR}} = (\varphi_n^{\text{in}})^*. \end{aligned}$$

The wavefunction above is projected onto the basis of hyperspherical harmonics, given by $\{\Phi_n(\mathbf{\Omega})\}_{n\in\mathcal{C}_\infty}$. The set of integer numbers $\mathcal{C}_\infty = \{3, 4, \ldots\}$ was defined to identify the long-range channels. The hyperspherical harmonics have the following properties: they are an orthonormal complete set of functions, with respect to the inner product given by $(\phi_1|\phi_2) \equiv \int d\mathbf{\Omega}\, \phi_1^*(\mathbf{\Omega})\, \phi_2(\mathbf{\Omega})$. A_n^{out} and A_n^{in} are the amplitudes of the outgoing and incoming waves in the long-range Channel n. Having defined the wavefunction in the long-range, the next step is to connect the long-range to the short-range.

2.3.1.2. Coupling of the Long-Range to the Short-Range

In order to couple the long-range to the short-range, we will use the s-matrix technique (see Section 2.3.1.2). In the short-range, the waves in Channel 1 are given by Equation (2.9). In the long-range, the waves are given by Equation (2.22). There are infinitely many channels in the long-range, which are all coupled to the Channel 1 in the short-range. The set $\mathcal{C} \equiv \{1; 3, 4, \ldots\}$ is a list of integers defining all the channels. To define the s-matrix and obtain information about the system, we have to look at the system by injecting a stationary flow of particles and see how the system evolves.

Consider a stationary flow of particles that is injected into Channel 1. In the short-range, there is a wave going towards the long-range regime and a wave reflected back into the short-range with phase s_{11}. In the long-range, part of the

wave in Channel 1 will be transmitted into Channel n, with an amplitude given by s_{n1}.

On the other hand, when a stationary flow of particles is injected into the long-range Channel $n \in \mathcal{C}_\infty$, there will be a wave traveling towards the short-range and a part that has been reflected back into the long-range Channel $m \in \mathcal{C}_\infty$. The projection of this reflected wave is given by s_{mn}. The part of the wave that is transmitted into Channel 1 will have the projection s_{1n}.

Let us summarize these rules with a wavefunction describing the injection of a stationary flow of particles in Channel $n \in \mathcal{C}$:

$$\psi_n \begin{cases} \underset{R\to 0}{\simeq} \delta_{n,1}\varphi_1^{\text{in}} + s_{1n}\varphi_1^{\text{out}} \\ \underset{R\to\infty}{\simeq} (1-\delta_{n,1})\varphi_n^{\text{in}} + \sum_{m\in\mathcal{C}_\infty} s_{mn}\varphi_m^{\text{out}}. \end{cases} \tag{2.23}$$

The transmission and reflection coefficients form the s-matrix given by

$$s = \begin{pmatrix} s_{11} & s_{13} & s_{14} & \cdots \\ s_{31} & s_{33} & \cdots & \cdots \\ s_{41} & \vdots & s_{44} & \\ \vdots & \vdots & & \ddots \end{pmatrix}. \tag{2.24}$$

By definition, there is only coupling from the long-range states into the short-range states. Also important to notice is that due to the conservation of flux between the short- and long-range the matrix is unitary, and the sum of the amplitudes squared $\sum_{n\in\mathcal{C}} |s_{n1}|^2 = 1$. The matrix has time-reversal symmetry, which implies that it is symmetrical with $s_{1n} = s_{n1}$ for $n \in \mathcal{C}$.

The relations between the amplitudes of the different waves are also described by the s-matrix. Let us combine the knowledge of the wavefunctions in the short-range for Equation (2.8) and in the long-range from Equation (2.22):

$$\psi_n \begin{cases} \underset{R\to 0}{\simeq} A_1^{\text{in}}\varphi_1^{\text{in}} + A_1^{\text{out}}\varphi_1^{\text{out}} \\ \underset{R\to\infty}{\simeq} A_n^{\text{in}}\varphi_n^{\text{in}} + \sum_{m\in\mathcal{C}_\infty} A_m^{\text{out}}\varphi_m^{\text{out}} \end{cases}. \tag{2.25}$$

Comparing Equation (2.23) with Equation (2.25) gives the following relation between the amplitude A_n^{out} and A_n^{in} ($n \in \mathcal{C}$):

$$A_n^{\text{out}} = \sum_{m\in\mathcal{C}} s_{nm} A_m^{\text{in}}. \tag{2.26}$$

It is straight-forward to combine these relations with the boundary condition in the short-range limit and obtain in an "industrial way" the solution to the scattering problem. However, in the following we will introduce a basis change which simplifies the problem to a two-channel problem, which is a direct analog to the unitary case (see Section 2.2).

2.3.1.3. Effective Two-Channel System

Equation (2.26) includes the coupling of the long-range channels $n \in \mathcal{C}_\infty$ to the short-range Efimov channel. This suggests that it should be possible to use a different basis, where, instead of looking at all the long-range channels and calculating how they couple to the short-range, we instead consider an effective Channel $\tilde{3}$, with a hyperangular wavefunction given by $\tilde{\Phi}_3$. This channel will have an effective coupling to the short-range given by $\tilde{s}_{31}$. This effective channel can be defined by

$$\tilde{s}_{31}\tilde{\Phi}_3(\mathbf{\Omega}) = \sum_{m\in\mathcal{C}_\infty} s_{m1}\Phi_m(\mathbf{\Omega}).$$

The effective coupling can then be defined by imposing that the scalar product $(\tilde{\Phi}_3|\tilde{\Phi}_3) = 1$,

$$|\tilde{s}_{31}|^2 = \sum_{m\in\mathcal{C}_\infty} |s_{m1}|^2.$$

The incoming and outgoing waves at $R \to \infty$ are in this case defined by

$$\tilde{\varphi}_n^{\text{in}} \equiv \tilde{\Phi}_n^*(\mathbf{\Omega})\frac{e^{-ikR}}{R^2\sqrt{kR}},$$
$$\tilde{\varphi}_n^{\text{out}} \equiv \tilde{\Phi}_n(\mathbf{\Omega})\frac{e^{+ikR}}{R^2\sqrt{kR}} = \left(\tilde{\varphi}_n^{\text{in}}\right)^*.$$

The $\tilde{s}$-matrix now becomes

$$\tilde{s} = \begin{pmatrix} \boxed{\begin{matrix}\tilde{s}_{11} & \tilde{s}_{13}\\ \tilde{s}_{13} & \tilde{s}_{33}\end{matrix}} & \begin{matrix}0\\0\end{matrix} & \cdots \\ \begin{matrix}0 & 0\end{matrix} & \tilde{s}_{44} & \\ \vdots & \vdots & & \ddots \end{pmatrix}. \tag{2.27}$$

This matrix has only coupling between Channel 1 and Channel $\tilde{3}$, hence, it suffices to only consider the 2×2-matrix in the upper left corner. Since, Channel 1 is still given by the Efimov channel the reflection $\tilde{s}_{11}$ is the same as s_{11}.

In order to calculate the ratio of the incoming and outgoing amplitudes we use the $\tilde{s}$-matrix relations between the amplitudes:

$$\tilde{A}_1^{\text{out}} = s_{11}\tilde{A}_1^{\text{in}} + \tilde{s}_{13}\tilde{A}_3^{\text{in}}$$
$$\tilde{A}_3^{\text{out}} = \tilde{s}_{31}\tilde{A}_1^{\text{in}} + \tilde{s}_{33}\tilde{A}_3^{\text{in}}$$

and the boundary condition given by Equation (2.14). These equations have exactly the same form as the Equations (2.20). Thus the result of the scattering is analogous to the resonant case Equation (2.21)

$$\tilde{A}_3^{\text{out}} = \underbrace{\left[\tilde{s}_{33} + \frac{(\tilde{s}_{13})^2 \mathcal{A}_{\text{el}}}{1 - s_{11}\mathcal{A}_{\text{el}}}\right]}_{\tilde{s}'} \tilde{A}_3^{\text{in}}, \tag{2.28}$$

but now $\tilde{s}$ is a function of ka.

2.4. Inelastic Three-Particle Processus

In Sections 2.1 - 2.3, we considered the three-particle problem under the influence of elastic scattering. The next step is to introduce inelastic scattering. We will start this section by describing an inelastic scattering process common to the three-particle problem and introduce this into the analysis of the short-range physics. The losses occur in the lowest Efimov channel and we will use this knowledge to derive the three-particle loss coefficient.

2.4.1. Elastic versus Inelastic Scattering

In Figure 2.6b, the formation of a bound state of two particles (dimer) is sketched. During this process, the bound state energy is transferred to kinetic energy of the atom-dimer pair. However, since the total momentum needs to be conserved, both the atom and dimer will carry away equal but oppositely directed momenta.

The decay can only happen into two-types of bound-dimer states: a deeply bound dimer state or a weakly bound (shallow) dimer state (when it exists). In the simple two-channel Feshbach resonance picture, as presented in Section 1.2, the weakly bound dimer is the molecular state in the closed channel with coupling

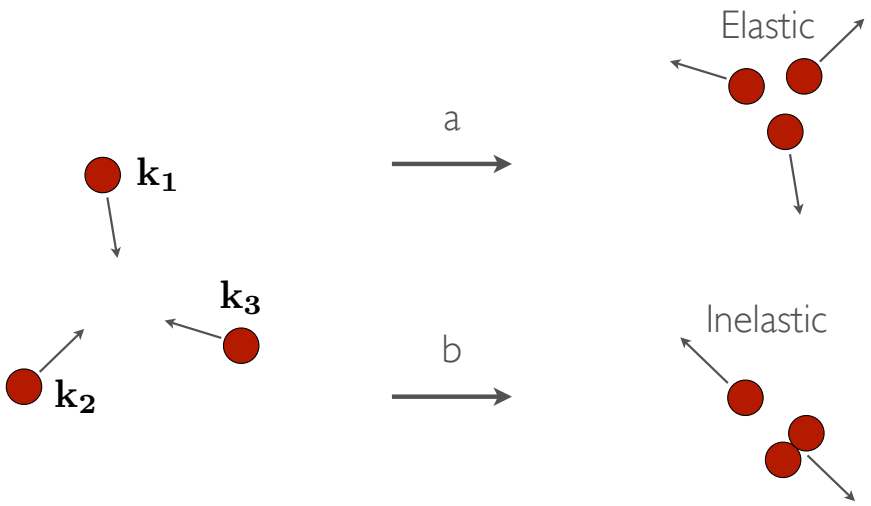

Figure 2.6.: Three-particle scattering. There are two possible processes denoted by **a** and **b**. **a. Elastic scattering**. The total kinetic energy and total momentum are conserved. The incoming and outgoing wavefunctions differ only by a phase factor. **b. Inelastic scattering**. Two of the three particles form a bound-state. The bound state energy is transferred to kinetic energy of the particle-dimer pair.

to the continuum (threshold). This state is a non-virtual state on the positive-a (molecular) side of the Feshbach resonance, with energy $E_\mathrm{b} \propto 1/a^2$. Close to the resonance or on the negative-a side of the resonance, the energy of the state vanishes, rendering the state virtual. The deeply bound dimers are all the lower lying bound states, that are not (directly) involved in the appearance of a Feshbach resonance.

This results in decay into weakly and deeply bound dimers, on the positive-a side, whereas, on the negative side and at resonance, only recombination into the deeply bound dimers is present. In the following, we will focus on the negative-a side.

The change of density due to three-particle recombination into deeply bound dimers in a homogeneous gas is given by

$$\frac{dn}{dt} = -L_3 n^3, \tag{2.29}$$

where n is the density and L_3 is the three-particle loss coefficient. In the following, we will derive L_3 for a cloud with scattering length a and temperature T.

2.4.2. Short-Range

We will now introduce inelastic scattering into the three-particle scattering formalism, which was derived in Section 2.2. The short-range physics will be modified by changing the boundary condition at $R = 0$.

2.4.2.1. Elastic $\rightarrow$ Inelastic Scattering

In Section 2.2.2, elastic scattering of three particles was examined. It was introduced by considering the incoming and outgoing wavefunction outside the range of the potential and arguing how the outgoing wavefunction is modified with respect to the incoming. The modification was done by introducing a phase shift $\delta(k) = -s_0 \ln(kR_t) + \pi/2$ to the outgoing wavefunction. In this section, we will proceed analogously, but in addition to a phase shift we will also reduce the amplitude of the outgoing wavefunction. Following the convention of Braaten and Hammer [168], the reduction of the amplitude is given by $e^{-2\eta_*}$. The limit $\eta_* = 0$, corresponds to no three-particle losses. The limit $\eta_* \rightarrow \infty$ on the other hand causes all particles reaching $R = 0$ to be lost. In other words, it creates an absorbing wall at $R = 0$.

The resulting effect on the hyperradial wavefunction is given by

$$F_{i\,s_0}(R) \underset{R\rightarrow 0}{\propto} e^{-i\,s_0 \ln R/R_t} - e^{-2\eta_*}\, e^{+i\,s_0 \ln R/R_t}. \tag{2.30}$$

The resulting outgoing hyperradial wavefunction has log-periodic behavior in R and its amplitude is reduced by an amount of $e^{-2\eta_*}$ per scattering event.

2.4.2.2. Inelastic Zero-Range Model (ZRM)

In Section 2.2.2.3, we now replace in Condition 3 $\mathcal{A}_{\text{el}}$ by $\mathcal{A}_{\text{inel}}$

3. **Three-particle contact condition:** when $R \rightarrow 0$:

$$\psi(R, \boldsymbol{\Omega}) \underset{R\rightarrow 0}{\simeq} A \frac{\phi_{i\,s_0}}{R^{-5/2}} \left[e^{-i\,s_0 \ln R/R_t} - e^{-2\eta_*}\, e^{+i\,s_0 \ln R/R_t} \right] \tag{2.31}$$

For simplicity, the last condition can also be written as $\psi = A_1^{\text{out}} \left[\varphi_1^{\text{out}} + \mathcal{A}_{\text{inel}} \varphi_1^{\text{in}} \right]$, where $\mathcal{A}_{\text{inel}} = -e^{-2\eta_*} (kR_t)^{-2is_0}$.

2.4.3. Long-Range

In the previous section, we have described the behavior of the three-particle inelastic scattering in the short-range. In this section, we will use the results from Section 2.3.1, in which the short-range was coupled to the long-range, for both resonant (Section 2.4.3.1) and finite elastic scattering (Section 2.4.3.2).

In the short-range, we have seen that it suffices to change from $\mathcal{A}_{\text{el}}$ to $\mathcal{A}_{\text{inel}}$ to introduce losses. In the long-range, since nothing has changed about the coupling between the short- and the long-range, the same replacement will be employed.

2.4.3.1. Resonant Interactions: Efimov Physics

The changes of the long-range resonant interactions case ($a \to \infty$) are summarized by the replacement of $\mathcal{A}_{\text{el}}$ by $\mathcal{A}_{\text{inel}}$ in Equation (2.21) for the relation between the incoming and outgoing waves

$$\begin{aligned} A_3^{\text{out}} &= \left[s_{33} + \frac{(s_{13})^2 \mathcal{A}_{\text{inel}}}{1 - s_{11}\mathcal{A}_{\text{inel}}} \right] A_3^{\text{in}}, \\ A_3^{\text{out}} &= s' A_3^{\text{in}}. \end{aligned} \tag{2.32}$$

2.4.3.2. Finite Interactions

Extending the inelastic scattering problem to finite interactions is also straightforward. We start with the relation between the incoming and outgoing waves in the long-range (see Section 2.3.1.2) and replace $\mathcal{A}_{\text{el}}$ by $\mathcal{A}_{\text{inel}}$

$$\begin{aligned} \tilde{A}_3^{\text{out}} &= \left[\tilde{s}_{33} + \frac{(\tilde{s}_{13})^2 \mathcal{A}_{\text{inel}}}{1 - s_{11}\mathcal{A}_{\text{inel}}} \right] \tilde{A}_3^{\text{in}}, \\ \tilde{A}_3^{\text{out}} &= \tilde{s}' \tilde{A}_3^{\text{in}}. \end{aligned} \tag{2.33}$$

Other quantities are obtained by simply using this relation.

2.4.4. Flux and Recombination

Above, we have derived the relation between the amplitude of the incoming and outgoing waves in the long-range limit for inelastic scattering (see Sections 2.4.3.1 and 2.4.3.2). These amplitudes can be used to calculate the losses at $R = 0$ by looking at the flux through a hypersphere $\mathcal{S}$ centered at $R = 0$.

Let us first define the flux density vector for an arbitrary wavefunction ψ

$$\boldsymbol{j}[\psi] \equiv \frac{\hbar}{m} \operatorname{Im}(\psi^* \boldsymbol{\nabla}_{\boldsymbol{R}} \psi). \tag{2.34}$$

The flux φ_{loss} can then be written as

$$\begin{aligned} \varphi_{\text{loss}} &= -\oint_{\mathcal{S}} \boldsymbol{j}[\psi] \cdot d^5\boldsymbol{S}, \\ &= \frac{\hbar}{m} \left|A_3^{\text{in}}\right|^2 \left(1 - \left|\frac{A_3^{\text{out}}}{A_3^{\text{in}}}\right|^2\right) \\ &= \frac{\hbar}{m} \left|(A_3^{\text{in}})_0\right|^2 \left(1 - |s'|^2\right), \end{aligned} \tag{2.35}$$

where $\mathcal{S}$ is the surface of a hypersphere and $d^5\boldsymbol{S} \equiv \hat{\boldsymbol{n}}\, d^5S$ is an infinitesimal surface area on the hypersphere $\mathcal{S}$ with normal vector $\hat{\boldsymbol{n}}$ pointing away from the center (see a 2d representation in Figure 1.3). Note that the result is also valid for finite interactions by replacing A_3^{in} by $\tilde{A}_3^{\text{in}}$ and s' by $\tilde{s}'$. Here we see an important result: if we know the amplitude of the incoming wave $(A_3^{\text{in}})_0$ (or $(\tilde{A}_3^{\text{in}})_0$ in the case of finite interactions), we can calculate the flux. Thus, in the end, all we need to do is connect the initial conditions given by the plane wave $\psi^{(0)}$ in the long-range limit to the incoming wave φ_3^{in} (or in the case of finite interactions to $\tilde{\varphi}_3^{\text{in}}$). The amplitudes of the initial incoming waves are obtained with the Saddle Point Method (see Appendix A.3):

$$\begin{aligned} (A_3^{\text{in}})_0 &= \frac{(2\pi)^{5/2} e^{+i5\pi/4}}{k^2} \phi_{i\, s_0}(-\hat{\boldsymbol{k}}), \\ (\tilde{A}_3^{\text{in}})_0 &= \frac{(2\pi)^{5/2} e^{+i5\pi/4}}{k^2} \tilde{\Phi}_3(-\hat{\boldsymbol{k}}). \end{aligned}$$

We have to relate the loss coefficient $L_3(k)$ to the lost flux φ_{loss}

$$L_3(a, k) = \frac{3\sqrt{3}}{2} \langle \varphi_{\text{loss}} \rangle_{\hat{\boldsymbol{k}}}, \tag{2.36}$$

where $\langle . \rangle_{\hat{\boldsymbol{k}}}$ is given by the average over the hyperangle $\hat{\boldsymbol{k}}$. The term $3\sqrt{3}/2$ comes from the Jacobian, when the coordinate system is transformed into the center of mass frame.

2.4.5. Temperature Average

As mentioned earlier, our derivation focusses on a thermal non-degenerate gas of atoms. In this case, the particles momenta are distributed over a Boltzmann distribution for a given temperature T. This will relate the loss coefficient for a specific momentum $L_3(a,k)$ with relative energy $\epsilon_k = \hbar^2 k^2/m$ to the thermally averaged $L_3(a,T)$

$$L_3(a,T) = \frac{\int_0^\infty dk\ k\ e^{-\beta\epsilon_k}\ L_3(a,k)}{\int_0^\infty dk\ k\ e^{-\beta\epsilon_k}}. \tag{2.37}$$

To summarize, let us write the full formula for the three-particle losses using the knowledge about the amplitudes

$$\boxed{L_3(a,T) = L_3^{\max}(T)\left(1-e^{-4\eta_*}\right)\frac{2}{k_{\rm th}^2}\int_0^\infty \frac{(1-|s_{11}|^2)ke^{-k^2/k_{\rm th}^2}}{|1-e^{-2\eta_*}(kR_{\rm t})^{-2is_0}s_{11}|^2}dk,} \tag{2.38}$$

This is the central formula of this chapter.

The maximum value, as defined by [140], is given by

$$L_3^{\max}(T) = 36\sqrt{3}\pi^2\frac{\hbar^5}{m^3}\frac{1}{(k_{\rm B}T)^2}. \tag{2.39}$$

Around unitarity, the three-particle loss constant is well approximated by

$$L_3(T) \equiv L_3(\infty,T) = L_3^{\max}(T)\left(1-e^{-4\eta_*}\right), \tag{2.40}$$

because $|s_{11}(\infty)| \approx 0.04$ becomes negligible.

For weak interactions, the three-particle loss coefficient recovers the zero-temperature model [114–117]

$$L_3(a) = \lim_{k_{\rm th}|a|\to 0} L_3(a,T). \tag{2.41}$$

Important properties of Equation (2.38):

- The result is valid for the direct calculation of the resonant ($a\to\infty$) and the finite-a interactions cases, with the only parameter being $s_{11}(ka)$.

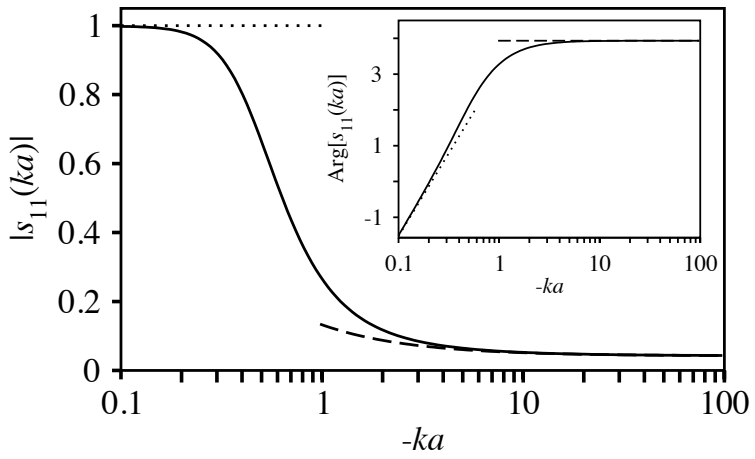

Figure 2.7.: Graphical representation of $|s_{11}(ka)|$ for three identical bosons. For small values of ka, $s_{11}(ka)$ reaches $s_{11}(ka) \approx (k|a|)^{2is_0} e^{-2i\delta_0}$ (dotted lines), with $\delta_0 \approx 1.588$ [170]. For large values of ka, $s_{11}(ka)$ is approximated by $s_{11}(ka) \approx s_{11}(\infty)(1 - Cs_0/ka)$ (dashed lines), with $C \approx 2.1126716\ldots$ [171]. At unitarity, the modulus $|s_{11}(\infty)| = 0.04$. The inset shows $\arg[s_{11}(ka)]$.

- The unitarity limited value scales as $\propto 1/k_{\mathrm{th}}^4 \propto 1/T^2$
- The unitarity limited value is different by a factor $(1 - e^{-4\eta_*})$ compared to the prediction of Mehta *et al.* [140] and this factor is due to Efimov physics.
- At unitarity log-periodic behavior shows itself through the term $(kR_{\mathrm{t}})^{-2is_0}$ in the form of oscillations (see Section 2.4.7).
- For $\eta_* = 0$, there would be no losses.
- For $\eta_* \to \infty$, the unitarity limited value $L_3^{\max}(T)$ has the same form as the formula by Mehta *et al.* [140], although their result is only valid in the weakly interacting limit ($a \to 0$).

2.4.6. Optical Resonator Analogy

Let us reconsider the scattering matrix s'. The quantity has the mathematical form of an optical resonator, because when we look at the absolute square of s', the following equation is found, which resembles the equation of an optical resonator:

$$\left| \frac{A_3^{\mathrm{out}}}{A_3^{\mathrm{in}}} \right|^2 = \left| s_{33} + \frac{(s_{13})^2 \mathcal{A}_{\mathrm{inel}}}{1 - s_{11}\mathcal{A}_{\mathrm{inel}}} \right|^2 .$$

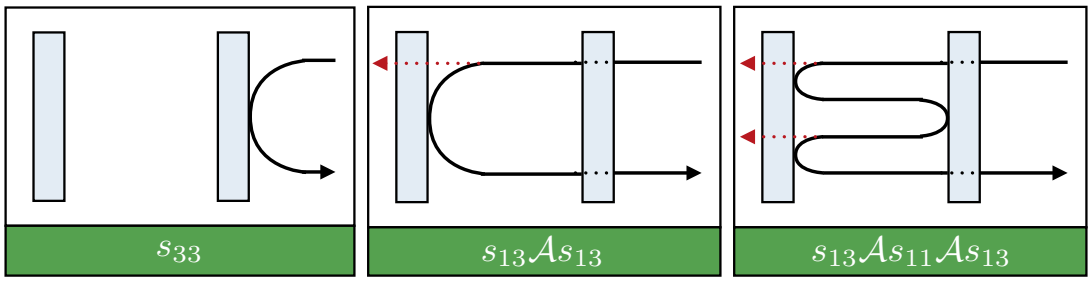

Figure 2.8.: The terms in Equation (2.42) are pictorially represented here. The mirror on the left corresponds to the range of interaction typically $R_c \sim R_{vdW}$. The right mirror is given by the region around $R_m = \min(|a|, 1/k)$. The outer left image shows the scattering at the outer mirror, with s_{33} being the reflection term. The middle image represents transmission into the inner region, given by s_{13}. Followed by, reflection and transmission at the $R = 0$ mirror that are given by $\mathcal{A} \equiv \mathcal{A}_{inel}$. Finally, transmission back into the outer region given by s_{13}. The last image is the same as the middle one, except for an extra term $\mathcal{A}\, s_{11}$, which corresponds to the reflection and transmission on the $R = 0$ mirror and a reflection on the outer mirror, respectively.

To see the analogy with the optical resonator equation, let us expand it

$$\left|\frac{A_3^{out}}{A_3^{in}}\right|^2 = |s_{33} + s_{13}\,\mathcal{A}_{inel}\,s_{13} + s_{13}\,\mathcal{A}_{inel}\,s_{11}\,\mathcal{A}_{inel}\,s_{13} + \cdots|^2 . \tag{2.42}$$

The result is artistically depicted in Figure 2.8. For a particle view of the scattering, see Figure 2.9.

2.4.7. Oscillations of $L_3(T)$ at Unitarity

In the following, we will show that at resonance $a \to \infty$, apart from the overall $1/T^2$ behavior, the three-particle loss constant $L_3(T)$ is log-periodic in T. This is due to the Efimov effect. To show this behavior, let us start with Equation (2.38) and remove the overall $1/T^2$ and $\zeta \equiv (1 - e^{-4\eta_*})$ behavior

$$\frac{L_3(T)}{L_3^{max}(T)\zeta} = \frac{2}{k_{th}^2}\int_0^\infty \frac{1 - |s_{11}(\infty)|^2}{|1 - e^{-2\eta_*}(kR_t)^{-2is_0}\cdot s_{11}(\infty)|^2}\, k e^{-k^2/k_{th}^2} dk.$$

At unitarity, the value $|s_{11}(\infty)| \approx 0.04$ is negligible. This suggests an expansion to first order in $s_{11}(\infty)$. Using the asymptotic value of $s_{11}(\infty)$, we are able to

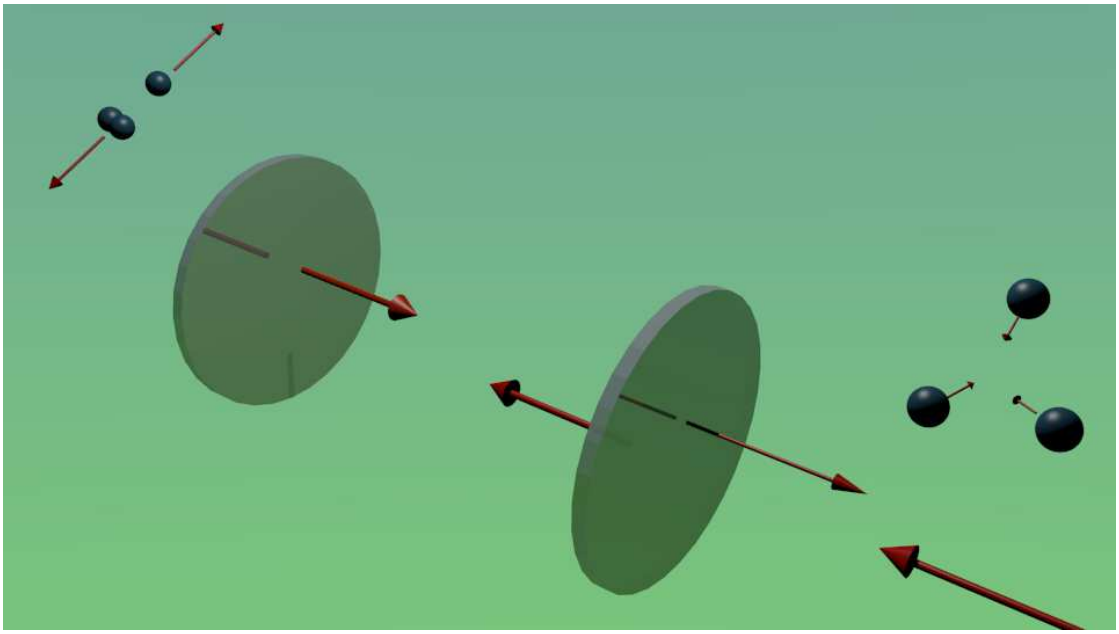

Figure 2.9.: Three-particle losses depicted through the analogy with the optical resonator (see Section 2.4.6). On the right-hand side, we see the three-particle plane wave coming into the $R \sim R_m \equiv \min(|a|, 1/k)$ range. While part of the wave is reflected and obtains a phase shift, some part is transmitted into resonator $R_c < R < R_m$, where R_c is the range of the interactions. On the left side of the resonator, we see that part of the wave inside the resonator is leaking out of the resonator ($R < R_c$), where the particles are lost, and part is reflected back into the resonator. Changing ka corresponds to changing the round-trip phase shift, which in this figure corresponds to changing the position of the mirror at $R = R_m$. For specific values of ka, the resonator becomes resonant and this corresponds to enhanced losses at $R = 0$, corresponding to the Efimov loss resonances for $a < 0$.

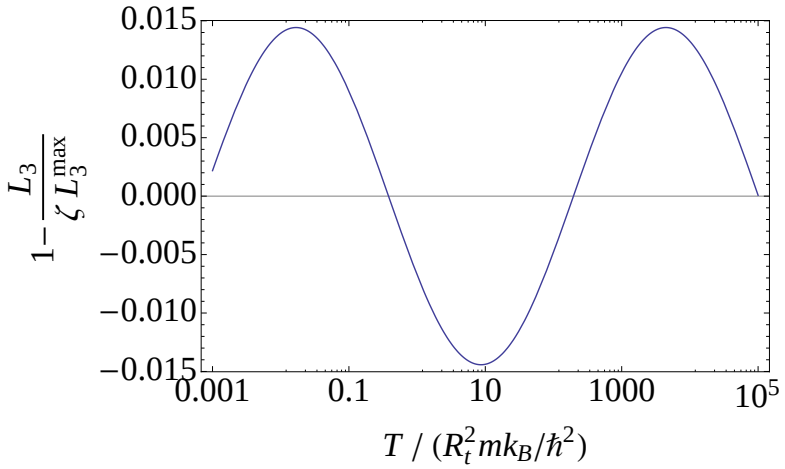

Figure 2.10.: The log-periodic behavior of $L_3(T)$ expressed through $1-\frac{L_3(T)}{\zeta L_3^{\max}(T)}$ to remove the overall $1/T^2$ behavior, for $\eta_* = 0.21$.

analytically solve the integral and the result is

$$\begin{aligned}\frac{L_3(T)}{L_3^{\max}(T)\zeta} &= 1 + \frac{s_{11}(\infty)}{2} e^{-2\eta_*} (k_{\text{th}} R_{\text{t}})^{-2is_0}\ \Gamma(1-is_0) + \frac{s_{11}^*(\infty)}{2} e^{-2\eta_*} (k_{\text{th}} R_{\text{t}})^{+2is_0}\ \Gamma(1+is_0), \\ &= 1 + A_\infty(\eta_*) \cos\left[2s_0 \ln\left(k_{\text{th}} R_{\text{t}}\right) + \varphi\right]\end{aligned}$$

The amplitude $A_\infty(\eta_*)$ and phase φ are given by:

$$\begin{aligned}A_\infty(\eta_*) = e^{-2\eta_*} \big(&[\operatorname{Im} s_{11}(\infty) \operatorname{Re}\Gamma(1-is_0) + \operatorname{Re} s_{11} \operatorname{Im}\Gamma(1-is_0)]^2 \\ &+ [\operatorname{Re} s_{11}(\infty) \operatorname{Re}\Gamma(1-is_0) - \operatorname{Im} s_{11}(\infty) \operatorname{Im}\Gamma(1-is_0)]^2 \big)^{1/2}, \\ \varphi = \arctan &\left[\frac{\operatorname{Im} s_{11}(\infty) \operatorname{Re}\Gamma(1-is_0) + \operatorname{Re} s_{11}(\infty) \operatorname{Im}\Gamma(1-is_0)}{\operatorname{Re} s_{11}(\infty) \operatorname{Re}\Gamma(1-is_0) - \operatorname{Im} s_{11}(\infty) \operatorname{Im}\Gamma(1-is_0)} \right].\end{aligned}$$

The result is shown in Figure 2.10. The oscillations are log-periodic in k_{th}, hence in T. The amplitude of the oscillation is $A_\infty(\eta_*) \simeq 0.022 e^{-2\eta_*}$, which gives for ^{7}Li, $A_\infty(0.21) \approx 0.014$, for ^{39}K [172], $A_\infty(0.09) \approx 0.018$ and for ^{133}Cs [173], $A_\infty(0.04) \approx 0.020$. Thus these oscillations as a function of T are small and constitute a real challenge for their experimental observation. Another possibility for having larger oscillations is the value of $s_{11}(\infty)$ or s_0, which are different for heteronuclear systems.

2.4.8. Numerical Analysis of $L_3(T, a)$

The numerical calculator, discussed in this section, was first developed by Dmitry Petrov for the publication in [143]. We have further optimized it for usage.

To calculate $L_3(a, T)$ (see Equation (2.38)) and the excess heat (see Equation (3.7)), we need to do some numerical calculations. For convenience, we introduce a new index d, which lets us write generic form for Equations (2.38) and (3.7)

$$\mathcal{E}_d(a, T, R_t, \eta_*) \equiv L_3^{\max}\left(1 - e^{-4\eta_*}\right)\frac{2}{k_{th}^2}\int_0^\infty \frac{1-|s_{11}(ka)|^2}{\left|1+(kR_t)^{-2is_0}e^{-2\eta_*}s_{11}(ka)\right|^2}k^{1+d}e^{-k^2/k_{th}^2}dk.$$

Three-particle loss constant L_3 is obtained by $L_3(a, T) = \mathcal{E}_0(a, T, R_t, \eta_*)$.

The scattering matrix $s_{11}(ka)$ was numerically calculated by Dmitry Petrov (see Supplemental Material of [143]) and the result is shown in Figure 2.7. It is a function of the dimensionless parameter ka, so let us replace this by $z \equiv ka$ and write the integral in dimensionless form,

$$\mathcal{E}_d(a, T, R_t, \eta_*) = \frac{72\sqrt{3}\pi^2\hbar}{m}\zeta_{\frac{1}{k_{th}^{6+d}}}\int_0^\infty \frac{1-|s_{11}(z)|^2}{|1+(kR_t)^{-2is_0}e^{-2\eta_*}s_{11}(z)|^2}\left(\frac{z}{a}\right)^{1+d}e^{-z^2/(k_{th}a)^2}\frac{dz}{a}.$$

This function depends on four variables: a, T, R_t, and η_*. The parameter η_* is dimensionless and independent of the others. The others, however, can be cast into two dimensionless parameters, which describe the full behavior: $x \equiv k_{th}a$ and $y \equiv k_{th}R_t$. With these variables we can cast $\mathcal{E}_d$ into

$$\mathcal{E}_d(x, y, \eta_*) = \frac{72\sqrt{3}\pi^2\hbar}{mk_{th}^4}\zeta_{\frac{1}{x^{2+d}}}\int_0^\infty \frac{1-|s_{11}(z)|^2}{\left|1+(z\frac{y}{x})^{-2is_0}e^{-2\eta_*}s_{11}(z)\right|^2}z^{1+d}e^{-z^2/x^2}dz.$$

Normalizing this function to the maximum attainable value $L_3^{\max}(T) = \frac{36\sqrt{3}\pi^2\hbar}{mk_{th}^4}$, will help to show the saturation behavior of L_3,

$$\frac{\mathcal{E}_d(x, y, \eta_*)}{L_3^{\max}(T)} = \zeta_{\frac{2}{x^{2+d}}}\int_0^\infty \frac{1-|s_{11}(z)|^2}{\left|1+(z\frac{y}{x})^{-2is_0}e^{-2\eta_*}s_{11}(z)\right|^2}z^{1+d}e^{-z^2/x^2}dz. \tag{2.43}$$

To give an example, we have taken the case ^{7}Li in the state $|F = 1, m_F = 1\rangle$, with the Efimov parameters from [128].

In Figure 2.11a, we have fixed the inelasticity parameter $\eta_* = 0.21$ governing the width of the Efimov resonance and varied R_t through
$R_t = a_- \exp\left(-(\delta_0 - \pi/2)/s_0\right) \approx 0.983a_-$, $\delta_0 = 1.588$ [170]. In the figure, the log-periodicity is shown by the appearance of four different Efimov resonances. At a

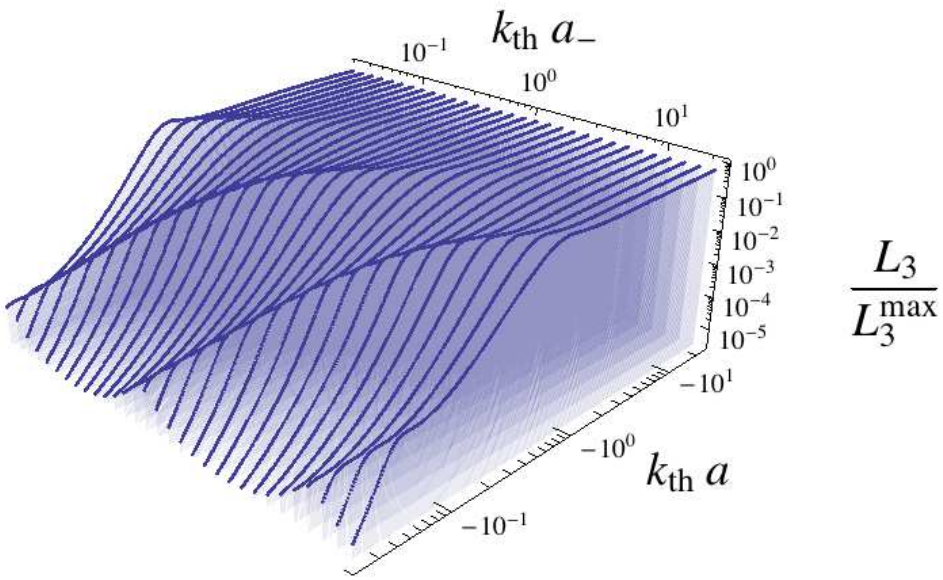

(a)

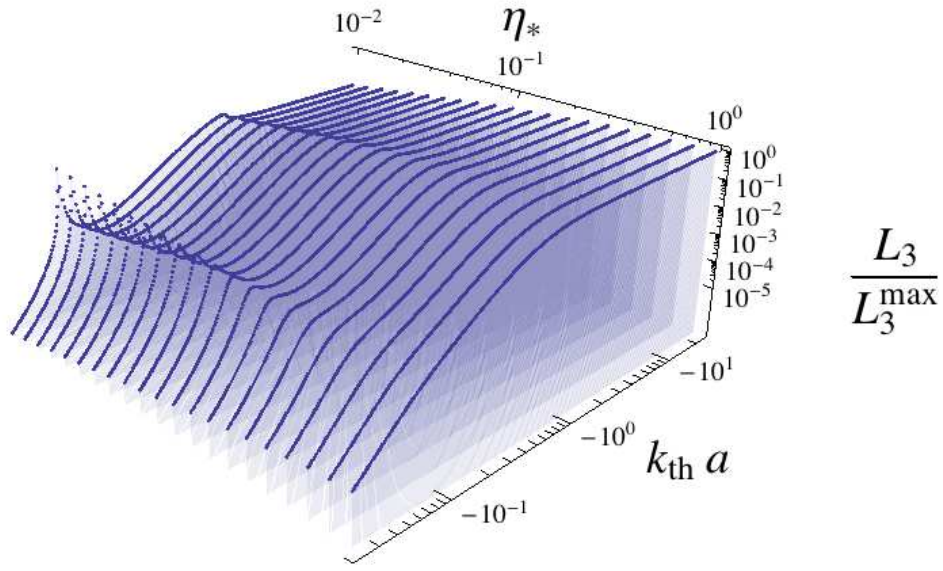

(b)

Figure 2.11.: To give an example, the numerical calculations of $L_3(a,T)$ of ^{7}Li. For weak interactions, both figures show the behavior of $L_3(a) \propto C(a)a^4$ and for unitary interactions ($a \to \infty$) the saturation of $L_3(a)$ to $L_3(T)$ is shown. **(a)** Fixing the elasticity parameter $\eta_* = 0.21$, while varying the position of the Efimov resonance through $k_{\rm th}a_-$ and the scattering length through $k_{\rm th}a$. Four Efimov resonances are showing the log-periodicity. **(b)** Fixing the Efimov resonance $a_- = -274a_0$, varying the width parameter η_*. At resonance, the three-particle loss coefficient saturates to the value $L_3(T)$, which varies with $1 - e^{-4\eta_*}$. For smaller η_*, the Efimov resonance becomes more pronounced and a second resonance becomes visible. For larger η_*, the Efimov resonance is fully washed out ($\eta_* \simeq 1$).

given $k_{\mathrm{th}}a_-$, there are maximally two Efimov resonances on the curve. For weak interactions, the $L_3(a)$ is found with a slope of a^4 and oscillations given $C(a)$. For unitary interactions ($a \to \infty$), $L_3(a)$ saturates to the value $L_3(T)$.

In Figure 2.11b, we fixed the Efimov resonance position $a_- = -274\ a_0$ and varied the inelasticity parameter η_*. For weak interactions, we recover $L_3(a)$ and for increasing interactions $L_3(a)$ saturates to $L_3(T)$. However, at resonance, we see that $L_3(T)$ decreases with $(1 - e^{-4\eta_*})$ and the second Efimov resonance becomes more pronounced for smaller η_*. For large η_*, the Efimov resonance is fully washed out and $L_3(a)$ saturates to $L_3^{\max}(T)$.

2.5. Three-Particle Losses on the Positive-a Side

2.5.1. Weakly Bound Dimer

The analysis of the positive-a side is more complicated, because there appears a (weakly) bound state under the scattering threshold with bound state energy $E_{\mathrm{b}} = -\hbar^2/(ma^2)$. In this case, losses are not only due to direct recombination into deeply bound dimers. We have to also consider the possible loss channel of a weakly bound dimer being formed and directly lost from the trap. As well as, the weakly bound dimer being formed and decaying into a deeply bound dimer.

The kinetic energy that a weakly bound dimer acquires in a recombination event has to be compared with the trap parameters in order to argue whether it is lost or not. In Section 3.1.2, we will explain in detail this comparison using the knowledge of the trap. Let us now focus on the limit of strong interactions ($a \to \infty$). In this case the direct loss of the weakly bound dimer vanishes, because the bound state energy vanishes. In the following, we will show that the decay to deeply bound dimers through the weakly bound dimer state vanishes.

2.5.2. Weakly Bound Dimers and the Efimov Channel

The wavefunction of the weakly bound dimer is given by

$$\Psi_2(\boldsymbol{R}) = \frac{e^{-|\boldsymbol{r}_2 - \boldsymbol{r}_1|/a}}{\sqrt{2\pi a}} \frac{e^{ip_0 R}}{\sqrt{24\pi p_0} R}, \tag{2.44}$$

where the index 2 to the dimer-atom channel and $p_0 = \sqrt{k^2 + 1/a^2} > k$ is the relative momentum of the atom and dimer.

The coupling of the atom-dimer channel to the Efimov channel is given by s_{12}.

The strongly interacting limit ($ka \to \infty$) of $s_{12}(ka)$ was calculated in the Supplemental Material of [143]. The modulus square is given by

$$|s_{12}|^2 \underset{ka\to\infty}{\simeq} 2Cs_0 \frac{1+e^{-2\pi s_0}}{ka}, \tag{2.45}$$

which show that $|s_{12}| \to 0$, as one approaches the resonance.

2.5.3. Atom-Dimer Decay with Chemical Equilibrium

Let us assume that there is chemical equilibrium between atoms and weakly bound dimers. The weakly bound dimer density n_D is related to the atomic density through

$$n_\mathrm{D} = n^2\lambda_\mathrm{th}^3 2\sqrt{2}e^{\beta E_\mathrm{b}} \underset{a\to\infty}{\simeq} n^2\lambda_\mathrm{th}^3 2\sqrt{2}. \tag{2.46}$$

Since there is chemical equilibrium (see the Supplemental Material of [143]), the process of three atoms forming an atom-dimer pair exactly balances the inverse process. Hence, the change of atom number is given by the sum of three-particle losses to deeply bound dimers L_3 and the formation of a deeply bound dimer through the weakly bound dimer state L_2^AD

$$\frac{dn}{dt} = -L_3 n^3 - L_2^\mathrm{AD} n\, n_\mathrm{D}. \tag{2.47}$$

The expression for $L_3(T)$ for $a>0$ is obtained using the energy dependent result from [174] and doing a thermal average. For the positive-a side, we need to change $1-|s_{11}|^2$ to $1-|s_{11}|^2-|s_{12}|^2$ in Equation 2.38. The atom-dimer loss coefficient L_2^AD is given by

$$L_2^\mathrm{AD}(T) = \frac{3\sqrt{3}\hbar^2\,(1-e^{-4\eta_*})}{2(mk_\mathrm{B}T)^{3/2}} e^{-\beta E_\mathrm{b}} \int_{-E_\mathrm{b}}^{\infty} \frac{|s_{12}|^2}{|1+(|k|R_\mathrm{t})^{-2is_0}e^{-2\eta_*}s_{11}|} e^{\beta\epsilon} d\epsilon, \tag{2.48}$$

where $\epsilon_k = \hbar^2k^2/m$ is the total relative energy of the three atom system. For $\epsilon_k > 0$, we have seen that $|s_{12}|$ vanishes as $\propto 1/a$ (see Section 2.5.2), hence L_2^AD vanishes as $\propto 1/a$ close to resonance. For $\epsilon_k < 0$, the integrant gives a contribution $\propto 1/a^2$ to L_2^AD. Therefore, L_2^AD can be neglected in Equation (2.47) and the equation simplifies to Equation (2.29), for direct decay into deeply bound dimers. Hence, only deeply bound dimers are probed.

2.6. Summary

In this chapter, we have treated the quantum-mechanical three-particle problem. We have started by introducing the problem and transforming it to hyperspherical coordinates. We considered the case of resonant interactions and this allowed us to write down the solutions of the problem. These solutions were identified as incoming and outgoing waves, which were used to introduce scattering due to the interactions at $R=0$. In close proximity of the scattering center the scattering can be described by a Zero-Range model using the boundary conditions from the two-particle scattering in addition to a three-particle boundary condition

$$\psi(\boldsymbol{R}) = A_3^{\text{in}} \left[\varphi_3^{\text{in}} + \mathcal{A}_{\text{el}}\varphi_3^{\text{out}}\right]$$

Using this result we were able to find the energy spectrum of the problem and show that there is an infinite number of trimer bound states with a log-periodic energy behavior characterize by the factor $e^{2\pi/s_0}$.

Furthermore, we added inelastic scattering to the problem. This was simply done by changing the boundary condition at $R=0$ to allow for losses at the center ($\mathcal{A}_{\text{el}} \to \mathcal{A}_{\text{inel}}$). Afterwards, the difference in amplitude between the incoming and outgoing waves in the long-range was used to quantify the losses caused by inelastic scattering. This enabled us to write down the three-particle loss coefficient

$$\boxed{L_3(a,T) = L_3^{\max}(T)\left(1-e^{-4\eta_*}\right)\frac{2}{k_{\text{th}}^2}\int_0^\infty \frac{(1-|s_{11}|^2)ke^{-k^2/k_{\text{th}}^2}}{|1-e^{-2\eta_*}(kR_{\text{t}})^{-2is_0}s_{11}|^2}dk,} \tag{2.38}$$

$$L_3^{\max}(T) = 36\sqrt{3}\pi^2\frac{\hbar^5}{m^3}\frac{1}{(k_{\text{B}}T)^2}. \tag{2.39}$$

The result has some remarkable features: The unitarity limited value $L_3(T)$ scales as $\propto 1/T^2(1-e^{-4\eta_*})$. This factor $(1-e^{-4\eta_*})$, comes from Efimov physics at short distances. The term $(kR_{\text{t}})^{-2is_0}$ gives the characteristic log-periodic behavior associated with Efimov physics.

In Section 2.4.6, we have seen that the three-particle loss coefficient has mathematical analogous behavior to the optical resonator. With a mirror at $R=0$ and $R=R_{\text{m}} \equiv \min(|a|, 1/k)$. Changing s_{11}, changes the position of the mirror at $R=R_{\text{m}}$ and changing R_{t} effectively changes the position of the mirror at $R=0$. Furthermore, changing η_* changes the transmission of the mirror at $R=0$. For $\eta_* \to 0$ the losses vanish and for $\eta_* \to \infty$ the point $R=0$ acts as an absorbing wall.

Afterwards, we have shown the log-periodic behavior of the three-particle losses

at unitarity

$$\frac{L_3(T)}{L_3^{\max}(T)\zeta} = 1 + A_\infty(\eta_*)\cos\left[2s_0\ln\left(kR_t\right) + \varphi\right],$$

where $\zeta \equiv (1 - e^{-4\eta_*})$ and $A_\infty(\eta_*) \approx 0.022e^{-4\eta_*}$.

Finally, we have discussed the three-particle losses on the positive-a side of the Feshbach resonance. Close to the resonance the three-particle loss coefficient is given by the coefficient at unitarity, hence the three-particle loss coefficient is smooth across the resonance.

In the following chapter, we will extend these results for a homogeneous gas to the trapped gas.

3. Three-Particle Recombination in a Harmonic Trap

The theory in Chap 2 derives the three-particle loss coefficient as a function of k and a for a homogeneous density (free space). In this chapter, we will discuss the considerations for three-particle losses in a trapped gas.

First, the properties of a typical trap in a quantum gas system is discussed. These properties are then used to derive an equation for the change of total particle number in the trap. Second, we will study the heating effects due to three-particle recombination in a trap. These effects will then be combined into an equation that describes the change of temperature of a trapped cloud. Finally, these heating effects will be compared to evaporation effects and the result will be used to estimate the effect of evaporation on the measurements of the three-particle losses. We will also show the results of simulations on the combined heating and evaporation effects.

3.1. Three-Particle Losses in a Trap

In an ultracold quantum gas system, inelastic scattering can be probed by monitoring the number of particles in a cloud as a function of time. However, to probe the scattering product through loss measurements, the products need to leave the trap. This introduces a new energy scale to the system, the trap depth U. Let us, in the following, discuss the trapping potential.

3.1.1. Trapping Potential

A common trapping potential used in ultracold gases (see for example Section 4.1.7) can be characterized by two properties: a harmonic potential in the center and a finite depth.

The harmonic potential in the center is given by

$$U(x, y, z) = \frac{1}{2} m \left(\omega_x^2 x^2 + \omega_y^2 y^2 + \omega_z^2 z^2 \right), \tag{3.1}$$

where m is the mass of a particle and ω_i is the angular frequency in the direction

$i \in \{x, y, z\}$. The finite depth of the trap is given by the truncation parameter $\eta = U/k_B T$. As an example, for our experiments a trap with a Gaussian shape and cylindrical symmetry is used (see Section 4.1.7).

3.1.2. Weakly and Deeply Bound Dimers in a Trap

The trap depth needs to be much smaller then the kinetic energy T of the scattering products ($U \ll T$), otherwise the products are not lost from the trap and the number probing technique does not work.

In general, having enough kinetic energy is not a problem for the scattering product after recombination into deeply bound dimer states[1], because the bound state energy is much larger than the trap depth.

For weakly bound dimers the kinetic energy scales as $E_b \propto 1/a^2$, this means that there are different regimes. For weak interactions, $E_b \gg U$, hence all the weakly bound dimers are directly lost and the zero-temperature model for $L_3(a)$ is valid. In the strongly interaction limit ($a \to \infty$), the decay through the weakly-bound dimer state vanishes, hence for $k|a| \gg 1$ the unitarity prediction $L_3(T)$ is valid (see Section 2.5). The difficult regimes is when $E_b \simeq U$ (or since U is on the order of $k_B T$: $E_b \simeq k_B T$), because then there is decay through the weakly-bound dimer, however the reaction product stays trapped.

In the weakly interacting limit ($a \to 0$), there have been numerous studies of the three-particle losses (see Introduction). Therefore, we will focus on the full negative-a side of the resonance and around unitarity, with on the positive-a side the condition $a \gg \lambda_{th}$.

3.1.3. Number Decay

In a homogeneous density system, three-particle losses are described by an equation for the change of density

$$\frac{dn(t)}{dt} = -L_3 n^3(t), \tag{3.2}$$

where $n(t)$ is the density and L_3 the three-particle loss coefficient as discussed in Section 2.4. If the cloud is in a thermal equilibrium, we can integrate Equation (3.2) over the space of the cloud. This gives an equation for the change of total particle

[1] In a recent work by Härter *et al.*, the decay product was ionized depending on its molecular state energy, and then trapped in a linear Paul trap. This allowed the authors to study the occupation of the product states [175].

number in the cloud

$$\frac{dN(t)}{dt} = -L_3\langle n^2(t)\rangle N(t),$$

where $\langle . \rangle$ is the mean value integrated over space and $N(t)$ the total number of particles in the cloud at time t. For a non-degenerate gas with temperature T, the equilibrium density distribution for a harmonic potential $U(x, y, z)$ (see Equation (3.1)) is given by

$$n(x, y, z) = n_0 e^{-\frac{m}{2k_B T}\left(\omega_x^2 x^2 + \omega_y^2 y^2 + \omega_z^2 z^2\right)},$$

where n_0 is the central density given by $n_0 = N\bar{\omega}/(2\pi k_B T/m)^{3/2}$, with $\bar{\omega} = (\omega_x\omega_y\omega_z)^{1/3}$, the mean angular frequency. We can use this result to relate the mean density squared to the total number squared

$$\langle n^2(t)\rangle = A/T^3\, N(t)^2,$$

where $A = (m\bar{\omega}^2/2\pi k_B)^3/\sqrt{27}$. The change of total number is then described by

$$\boxed{\frac{dN(t)}{dt} = -A\, L_3 \frac{N^3(t)}{T^3}.} \tag{3.3}$$

This differential equation describes the change of total particle number for a trapped gas. In the following, we will look at temperature effects due to three-particle losses in a trap.

3.2. Heating Effects

In the following, we will study heating of the cloud due to three-particle losses. To do this, the changes in energy, caused by the loss processes, need to be analyzed.

We will start by deriving a heating model in the weakly-interacting limit introduced by Weber *et al.* [56]. Afterwards, we will extend this model to include the temperature dependence of L_3, which we will then study in the limit strong interacting limit ($k|a| \to \infty$).

3.2.1. Weakly-Interaction Limit

In the weakly-interacting limit ($|a| \to 0$), the three-particle losses are described by $L_3(a)$, which is calculated using a zero-temperature model [114–117]. In order to

describe the heating due to three-particle recombination, we will closely follow the model introduced in [56]. In this model, the three-particle recombination is described by Equation (3.3), where the three-particle loss coefficient L_3 only depends on a and not on T (neglecting density independent loss effects)[2]:

$$\frac{dN}{dt} = -A\,L_3(a)\frac{N^3}{T^3}, \tag{3.4}$$

where a non-degenerate gas in an harmonic trap was assumed.

The mean amount of potential energy lost per atom can be calculated by integrating over a thermal distribution with a weight proportional to n^3. This gives a mean potential energy lost per particle of $\frac{1}{2}k_\mathrm{B}T$ and, since the ensemble average is $\frac{3}{2}k_\mathrm{B}T$, an effective $k_\mathrm{B}T$ of excess energy remains in the cloud. Phenomenologically, the heating comes from the fact that atoms that are trapped in a harmonic trap are lost in the region of highest density, because the recombination rate is the highest in this region ($\gamma_3 = L_3(a)\langle n^2\rangle \propto n^2$). This process is "anti-evaporation" and induces heating, because atoms that experience the highest three-particle loss rate are located near the trap center and have a potential energy less then the average potential energy of $\frac{3}{2}k_\mathrm{B}T$. Hence, increasing the average energy per particle in the trap.

In the model from [56], an *ad hoc* parameter to describe recombination heating is added. Recombination heating is caused by the reaction products colliding with the cloud after the loss process, with $k_\mathrm{B}T_\mathrm{h}$ being the energy deposited after the collisions. The change of temperature is then described by $\dot{T}/T = -(\dot{N}/N)(T + T_\mathrm{h})/3T$.

Finally, this allows us to write down a differential equation describing the change of temperature:

$$\frac{\dot{T}}{T} = A\;L_3(a)\frac{N^2}{T^3}\frac{T+T_\mathrm{h}}{3T} \underset{T_\mathrm{h}\to 0}{\simeq} \frac{A\;L_3(a)}{3}\frac{N^2}{T^3}. \tag{3.5}$$

The recombination heating was measured for three-particle losses in ^{133}Cs in [56] by using T_h as a fitting parameter in the fit procedure of the temperature changes. In the following, we will assume that the scattering product directly leaves the trap, such that the recombination heating can be neglected, *e.g.* $T_\mathrm{h} = 0$. Equations (3.4) and (3.5) are coupled should be solved consistently.

[2] Note that in [56], the authors used the definition $\gamma = A\;L_3$. We have chosen a different notation to be consistent throughout this thesis.

3.2.2. Extending the Model to Include Strong Interactions

In the formalism of Weber *et al.* [56] (see Section 3.2.1), the assumption was made that the collisions are in the low-temperature limit. This makes the recombination independent of the kinetic energy. Extending this to include kinetic energy effects is straightforward, with the theory from Chapter 2.

Let us start by calculating the energy lost from the system per particle:

$$\frac{\dot{E}_{3\mathrm{P}}}{\dot{N}_{3\mathrm{P}}} = \frac{\int \left[\prod_{i=1}^{3}\ d^3r_i\ d^3k_i\ n(\boldsymbol{r}_i)\ \exp\left(-\beta\frac{\hbar^2k_i^2}{2m}\right)\right] \sum_{i=0}^{3}\left(\frac{\hbar^2k_i^2}{2m}+V(\boldsymbol{r}_i)\right) L_3(k)}{\int \left[\prod_{i=1}^{3}\ d^3r_i\ d^3k_i\ n(\boldsymbol{r}_i)\ \exp\left(-\beta\frac{\hbar^2k_i^2}{2m}\right)\right] 3\ L_3(k)},$$

where $\boldsymbol{r}_i$ is the position and $\boldsymbol{k}_i$ is the momentum vector of particle i, $\beta \equiv 1/(k_{\mathrm{B}}T)$, and $L_3(k)$ is the loss coefficient for the relative momentum of the three particles k (see Equation (2.36)). The next step is to switch from momentum to energy and separate the center of mass motion from the relative motion via $\int d^3k_i = \int dE\, d\epsilon_k\, D_{\mathrm{CoM}}(E)\, D_{\mathrm{rel}}(\epsilon_k)$,

$$\frac{\dot{E}_{3\mathrm{P}}}{\dot{N}_{3\mathrm{P}}} = \frac{\int d^3r\ dE\ d\epsilon_k\ \epsilon_k^2\ e^{-\beta\epsilon_k}\ \sqrt{E}\ e^{-\beta E}\left[E+\epsilon_k+3V(\boldsymbol{r})\right] L_3(\epsilon_k)\ n^3(\boldsymbol{r})}{\int d^3r\ dE\ d\epsilon_k\ \epsilon_k^2\ e^{-\beta\epsilon_k}\ \sqrt{E}\ e^{-\beta E}\ 3\ L_3(\epsilon_k)\ n^3(\boldsymbol{r})},$$

where we have introduced the center of mass energy $E \equiv \sum_i \hbar^2k_i^2/2M$ and the relative energy $\epsilon_k \equiv \hbar^2k^2/m$. M is the total mass. Solving this equation yields,

$$\frac{\dot{E}_{3\mathrm{P}}}{\dot{N}_{3\mathrm{P}}} = k_{\mathrm{B}}T\left[1+\frac{1}{3}\mathcal{B}(k_{\mathrm{th}})\right] \tag{3.6}$$

The first part comes from the potential energy and kinetic energy of the center of mass motion. The second part comes from the kinetic energy of the relative motion, where we have introduced

$$\begin{aligned}\mathcal{B}(k_{\mathrm{th}}) &= \frac{1}{k_{\mathrm{th}}^2}\left(\int dk \frac{(1-|s_{11}|^2)}{\left|1+(kR_{\mathrm{t}})^{-2\,i\,s_0}e^{-2\eta_*}\cdot s_{11}\right|^2}k^3e^{-k^2/k_{\mathrm{th}}^2}\right), \\ &\quad \Big/\left(\int dk \frac{(1-|s_{11}|^2)}{\left|1+(kR_{\mathrm{t}})^{-2\,i\,s_0}e^{-2\eta_*}\cdot s_{11}\right|^2}ke^{-k^2/k_{\mathrm{th}}^2}\right), \\ &= \begin{cases}3 & \text{if } k|a| \to 0 \\ \approx 1 & \text{if } k|a| \to \infty.\end{cases}\end{aligned} \tag{3.7}$$

In Equation (3.6), the amount of energy lost per particle in a three-particle

recombination event is introduced. This energy has to be compared to the average total energy per particle in the trap of $3k_BT$. This gives the excess heat created per particle in a three-particle recombination event

$$E^{ex} = 3k_BT - \frac{\dot{E}_{3P}}{\dot{N}_{3P}} = k_BT\left(2 - \frac{1}{3}\mathcal{B}(k_{th})\right) \equiv \delta(a,T)k_BT \tag{3.8}$$

$$\delta(a,T) = \begin{cases} 1 & \text{if } k|a| \to 0 \quad \text{we find the same as in Section 3.2.1} \\ 5/3 & \text{if } k|a| \to \infty, \end{cases}$$

This is a more generalized form of the excess heat $\delta(a,T)$ in units of k_BT. In Section 3.2.1, the excess heat was $1k_BT$ and this corresponds to the weakly-interacting limit. As an illustration, we plot in Figure 3.1 the case of ^{7}Li close to a Feshbach resonance.

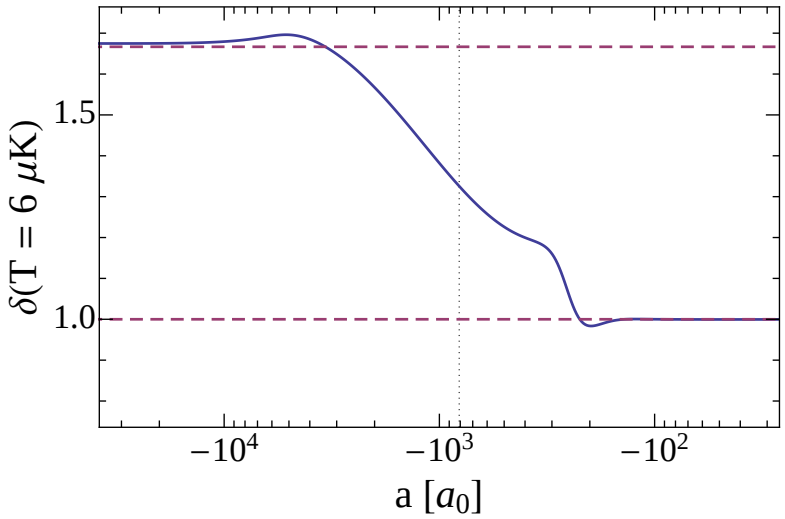

Figure 3.1.: Illustration of Equation (3.8) for the particular case of ^{7}Li. Shown is the excess heat δ in units of k_BT (blue line). The red dashed lines correspond to the limits $|a| \to 0$ with $\delta = 1$ and $|a| \to \infty$ with $\delta = 5/3$. The gray dotted line indicates the position of $-1/k_{th} = -810\ a_0$ for $T = 6\ \mu$K. The heating maxima around $a = -200\ a_0$ and $a = -5.0 \times 10^3\ a_0$ are due to the Efimov resonances.

Finally, casting this into a differential equation for the change of temperature,

we find

$$\begin{aligned}\frac{\dot{T}}{T} &= -\frac{\dot{N}}{N}\frac{\delta(a,T)T + T_\mathrm{h}}{3T}, \\ &= A\ L_3(a,T)\frac{N^2}{T^3}\frac{\delta(a,T)T + T_\mathrm{h}}{3T}. \end{aligned} \tag{3.9}$$

This form together with Equation (3.4) contains, in principle, all the temperature dependence of the losses, but in order to measure L_3, we have to assume a relation between L_3 and T.

The first obvious case is the weakly-interacting case given by $L_3(a)$, with $L_3(a)$ being independent of T.

However, to find a temperature dependence of L_3, we devised a new experimental technique, in which L_3 is measured at constant temperature. Then, repeating the measurement for different temperatures, we will reveal $L_3(a,T)$, see Section 5.2.

Keeping the temperature constant induces evaporative losses, which are relatively small, because the energy lost per evaporation event is larger then the energy gained per loss event. As we will see, this ratio is determined by the trap depth.

3.3. Evaporation

First, we will use the condition of approximate constant temperature during a measurement, and then use an energy balance to estimate the correction of L_3. Secondly, we will model the evaporation process and use the result in Section 5.2.2 to reanalyze the data. We find a "magic" trap depth that holds the temperature constant, which confirms the validity of our assumption of constant temperature. The evaporative model is studied in detail in [176, 177].

3.3.1. A Simple Evaporation Model

Experimentally, we will see that by choosing the right barrier height, it is possible to keep the temperature constant during the relevant time scales in our experiment (see Section 5.1.5). This suggests that there should be an energy balance between the excess heat of the recombination processes and the heat removed by evaporation processes,

$$\boxed{E^\mathrm{ex}_\mathrm{3Body}\dot{N}_\mathrm{3Body} = E^\mathrm{ex}_\mathrm{evap}\dot{N}_\mathrm{evap}.} \tag{3.10}$$

The left hand side is given by Equation (3.8). To obtain the energy lost per

evaporation event on the right hand side, we need to consider evaporative cooling processes. Let us determine the amount of excess heat taken away by evaporative cooling. Evaporative cooling was treated in full detail using kinetic theory in [178]. In the paper, it was shown that the mean energy lost per particle lost through an evaporation process is given by

$$\frac{\dot{E}_{\mathrm{evap}}}{\dot{N}_{\mathrm{evap}}} = \frac{\int_{\eta k_{\mathrm{B}}T}^{\infty} E\, e^{-E/k_{\mathrm{B}}T}}{\int_{\eta k_{\mathrm{B}}T}^{\infty} e^{-E/k_{\mathrm{B}}T}} = (\eta+\kappa)\, k_{\mathrm{B}}T,$$
$$E_{\mathrm{evap}}^{\mathrm{ex}} = \frac{\dot{E}_{\mathrm{evap}}}{\dot{N}_{\mathrm{evap}}} - 3k_{\mathrm{B}}T = (\eta+\kappa-3)k_{\mathrm{B}}T, \tag{3.11}$$

where κ denotes the difference between the average energy of an evaporated particle and the trap depth $\eta \equiv U/k_{\mathrm{B}}T$. The κ, for 3d evaporation in a harmonic trap, is given in [178] by[3] [4]

$$\kappa = 1 - \frac{P(5,\eta)}{\eta P(3,\eta) - 4P(4,\eta)}. \tag{3.12}$$

The $P(a,\eta)$ introduced here is the regularized lower incomplete gamma function[5]. The behavior of κ is shown in Figure 3.2.

In a paper by Luo *et al.* [180], the authors reasoned that for a Boltzmann gas with unitary interactions the energy lost per evaporation event is the same as in the case of weakly interacting gases, hence Equations (3.11) and (3.11) are generally valid. In their model, only the rethermalization rate is changed. Two-particle collisions leading to evaporative loss occur mainly in the cloud center where the trap is harmonic, and the relative momentum for such a collision is approximately fixed by the trap depth so that the result for κ above is applicable.

Since we are making the assumption in Equation 3.10 the rethermalization rate is directly used. In Section 3.3.2, we will give a more elaborate model and consider the rethermalization rate.

At this point, let us write the energy conservation in Equation (3.10) in terms

[3] Note that $\kappa \equiv W_{\mathrm{ev}}/V_{\mathrm{ev}}$, with $\delta = 3/2$ for a harmonic trap in the notation of [178].

[4] The evaporation in our trap is actually a 2d process, because the trap is, practically infinitely deep along the magnetic field curvature (see Section 4.1.7), this would give a small correction to κ.

[5] This regularized lower incomplete gamma function is defined by $P(a,\eta) \equiv \frac{1}{\Gamma(a)} \int_0^{\eta} t^{a-1} e^{-t} dt$, see [179].

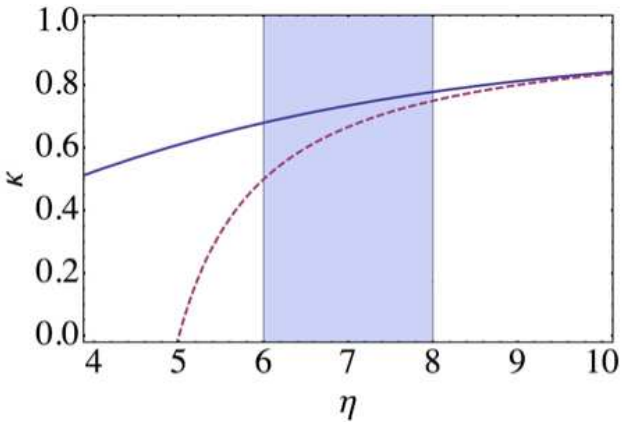

Figure 3.2.: The relation between additional energy taken away during an evaporation event κ (see Equation (3.11)) and the trap depth η, calculated using Equation (3.12), which is taken from [178]. In [180], the authors used the approximation $\kappa \simeq (\eta - 5)/(\eta - 4)$, which is true for $\eta \gg 6$, shown by the dashed red line. In the limit $\eta \to \infty$, the value of κ reaches 1. The blue shaded area shows our working range of η. This κ is calculated for a 3d evaporation process

of change of atom number, using Equations (3.8) and (3.11).

$$\begin{aligned} \delta\, k_B T\, \dot{N}_{3\text{Body}} &= (\eta + \kappa - 3)\, k_B T\, \dot{N}_{\text{evap}} \\ \frac{\dot{N}_{\text{evap}}}{\dot{N}_{3\text{Body}}} &= \frac{\delta(a,T)}{\eta + \kappa - 3}. \end{aligned} \tag{3.13}$$

In other words: each particle lost in a three-particle recombination event is followed by an amount $\delta(a,T)/(\eta+\kappa-3)$ of particles lost through evaporation, in order to keep the temperature constant. To translate this into the total change of atoms we have,

$$\dot{N}_{\text{tot}} = \dot{N}_{3\text{Body}} + \dot{N}_{\text{evap}} = \dot{N}_{3\text{Body}} \left[1 + \frac{\delta(a,T)}{\eta + \kappa - 3}\right], \tag{3.14}$$

which we can directly use to correct the measured L_3^{exp} and obtain the real L_3,

$$\boxed{L_3(a,T) = L_3^{\text{exp}}(a,T) \frac{1}{1 + \frac{\delta(a,T)}{\eta+\kappa-3}}.} \tag{3.15}$$

We arrive at a general formula for predicting a corrected value of L_3 for evaporative losses.

In order to derive this correction, we had to assume constant temperature. This assumption allowed us to use the energy balance in Equation (3.10). This enabled us to derive the correction in Equation (3.15).

3.3.2. More Advanced Model of Evaporation Effects

In the following, we will relax the constant temperature condition and solve the coupled equations for change of atom number and temperature.

The evaporation model is based on the models introduced in [178, 180, 181]. We will closely follow the derivation in [176, 177].

The model requires the following conditions:

1. Resonant scattering ($a \gg \lambda_{\mathrm{th}}$).
2. The temperature dependence of the three-particle loss coefficient is given by $L_3(T) \propto 1/T^2$.
3. The temperature is always much smaller than the trap depth ($U \gg k_{\mathrm{B}}T$ or $\eta \gg 1$)
4. The evaporative process is 3d, *i.e.* the trap depth is given by $\eta_{3\mathrm{d}}$ (this condition is relaxed at the end to include 2d evaporation).

To describe the evaporation, let us consider the total energy of N particles in a harmonic trap,

$$E = 3Nk_{\mathrm{B}}T.$$

Differentiation of this equation makes it possible to derive $\dot{E}/\dot{N}$. If we relate this to Equation (3.11), we find

$$\begin{aligned} 3T + 3N\frac{\dot{T}}{\dot{N}} &= (\eta_{3\mathrm{d}} + \kappa)\, T, \\ \left(\frac{\dot{T}}{T}\right)_{\mathrm{ev}} &= \frac{\eta_{3\mathrm{d}} + \kappa - 3}{3} \left(\frac{\dot{N}}{N}\right)_{\mathrm{ev}}. \end{aligned}$$

The number of particles lost through the evaporation process is given by [181]

$$\left(\frac{\dot{N}}{N}\right)_{\mathrm{ev}} = -\Gamma_{\mathrm{ev}}, \tag{3.16}$$

with $\Gamma_{ev} = n_0\,\sigma\,\bar{v}\,e^{-\eta_{3d}}\,V_{ev}/V_e$, where η_{3d} is the barrier height for a 3d evaporation event, $n_0 = N(m\bar{\omega}^2/2\pi k_B T)^{3/2}$ is the peak density for a non-degenerate gas, $\bar{v} = (8k_B T/\pi m)^{1/2}$ is the average thermal velocity, σ is the collisional cross section $\sigma = 8\pi a^2$ in the limit of $a \ll \lambda_{th}$. In the limit $a \gg \lambda_{th}$, the scattering cross section is bounded by the relative momentum of the collision particles. Since the collisions will happen in the center of the potential, the relative momenta of the collision partners are bounded by the trap height, the cross section is given by $\sigma = 16\pi\hbar^2/(m\,U)$ [180]. V_{ev}/V_e is the ratio of the effective evaporation volume and the cloud volume, which is related to κ

$$\frac{V_{ev}}{V_e} = \frac{P(3,\eta_{3d})}{P(5,\eta_{3d})}\,(1-\kappa).$$

This allows us to write

$$\left(\frac{\dot{T}}{T}\right)_{ev} = -\Gamma_{ev}\,\frac{\eta_{3d}+\kappa-3}{3}.$$

The full differential equations for number and temperature, using both the three-particle recombination and evaporative cooling, are

$$\frac{\dot{N}}{N} = -A\,L_3(T)\,\frac{N^2}{T^3} - A_{ev}\,\left(e^{-\eta_{3d}}\,(1-\kappa)\right)\frac{N}{T}, \tag{3.17}$$

$$\frac{\dot{T}}{T} = \frac{1}{3}\left[\delta(a,T)\,A\,L_3(T)\frac{N^2}{T^3} - A_{ev}\left(e^{-\eta_{3d}}\,(1-\kappa)\right)(\eta_{3d}+\kappa-3)\,\frac{N}{T}\right]. \tag{3.18}$$

Here A_{ev} was introduced to include all the geometrical effects. This A_{ev} can be calculated in two limiting regimes:

$$A_{ev} = \begin{cases} 8a^2\ \hbar^2\bar{\omega}^3/(\pi k_B)\ P(3,\eta_{3d})/P(5,\eta_{3d}) & \text{when } a \ll \lambda_{th}, \\ 16\ \hbar^2\bar{\omega}^3/(k_B U)\ P(3,\eta_{3d})/P(5,\eta_{3d}) & \text{when } a \gg \lambda_{th}. \end{cases}$$

This means that the fitting with the full heating model can only be done at resonance or far away, because it is hard to calculate the specific geometric effects over the whole range. For now, we will restrict ourselves to the resonant interactions case.

We remark that this formulation is done for a 3d evaporative process. In order to go from 3d to 2d, it was shown that it suffices to use the equality $\eta_{3d} = \eta_{real} + 1$, where η_{real} is the parameter that needs to be compared to the experimental values, see [177, 182] for more information about 1d- and 2d-evaporation. The next step

is to fit the data to these two coupled non-linear differential equations.

3.3.3. "Magic" η

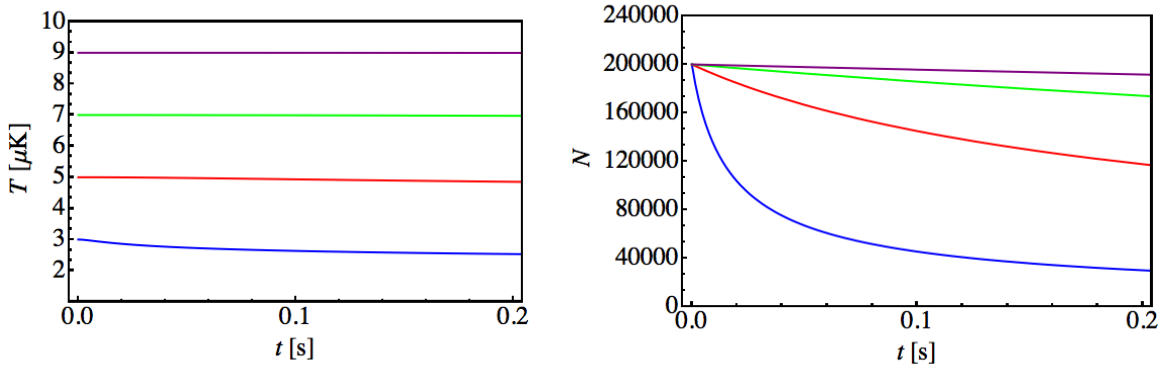

(a) Temperature evolution **(b)** Number decay

Figure 3.3.: The curves shown each correspond to a specific initial temperature and η_m: (blue) $T = 3\ \mu$K, $\eta_m = 7.4$; (red) $T = 5\ \mu$K, $\eta_m = 9.4$; (green) $T = 7\ \mu$K, $\eta_m = 10.5$; (purple) $T = 9\ \mu$K, $\eta_m = 11.4$. These η_ms are found by numerically solving the differential Equations (3.17) and (3.18), for different initial ηs, while minimizing the dT/dt at $t = 0$. For an initial particle number of 2×10^5.

This section treats the result of numerical simulations as described in [176], which were done for ^{7}Li. Numerically solving the differential Equations (3.17) and (3.18) shows us that the choice of a specific barrier height is a good approximation to keep a constant temperature during the measurements, see Figure 3.3a. In Figure 3.3a, we have plotted the temperature behavior for four specific initial temperatures $T = 3\ \mu$K, $T = 5\ \mu$K, $T = 7\ \mu$K, and $T = 9\ \mu$K, where for each initial temperature, we have numerically found a "magic" barrier height η_m, that minimizes the change of temperature at $t = 0$. In Figure 3.3b, we have shown the change of atom number as a function of time. In Figure 3.4, we have plotted the numerically found η_m as a function of initial temperature T. Each η_m corresponds to a curve that minimizes the initial change of temperature.

There is also some work in progress on the losses for a gas of ^{133}Cs with unitary interactions, where these simulation have been used and show promising results [173].

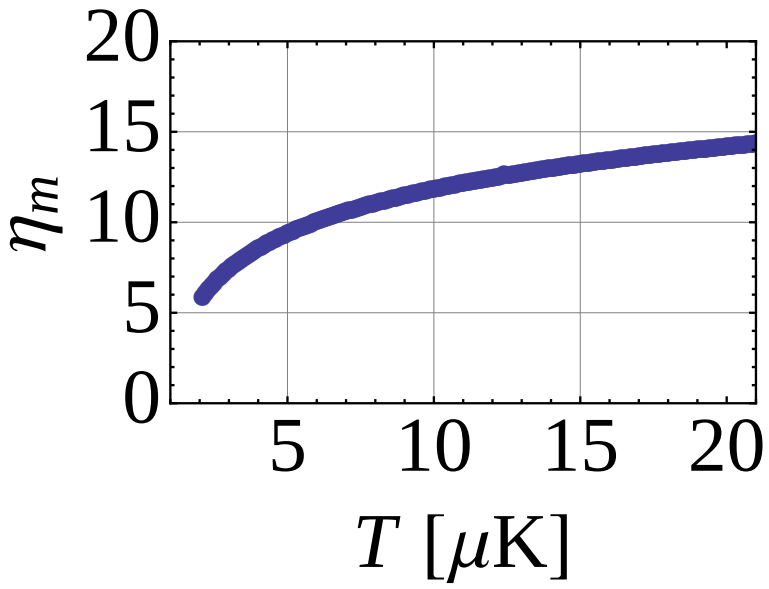

Figure 3.4.: The η_m found for a specific initial temperature T. These η_ms are found by minimizing dT/dt at $t=0$. For an initial particle number of 2×10^5.

3.4. Summary

This chapter was dedicated to three-particle recombination in a trap.

In the first part, we have introduced the characteristics of a commonly used trap in quantum gases. This trap was then used to explain the change of atom number for a non-degenerate cloud. The result is given by Equation (3.3)

$$\boxed{\frac{dN(t)}{dt} = -A\,L_3\frac{N^3(t)}{T^3},} \tag{3.3}$$

where A includes the effects of the trap and the non-degeneracy of the cloud.

In the second part, we studied the evolution of the temperature during three-particle loss events. Initially, we considered the model for weak interactions introduced by Weber *et al.* [56]. Then we extended this model using a temperature dependent $L_3(a,T)$ and considered the limit of strong interactions ($|a|\to\infty$). The change of temperature was described by Equation (3.9)

$$\boxed{\frac{\dot{T}}{T} = A\;L_3(a,T)\frac{N^2}{T^3}\frac{(\delta(a,T)T+T_\mathrm{h})}{3T},} \tag{3.9}$$

where A includes the effects from the trap and non-degeneracy of the cloud and

T_h is the recombination heating.

In the last part, we considered evaporation effects. First, the evaporation effects were estimated using the assumption of constant temperature. The result is a correction formula to account for evaporative losses in the three-particle loss coefficient

$$\boxed{L_3(a,T) = L_3^{\exp}(a,T)\frac{1}{1+\frac{\delta(a,T)}{\eta+\kappa-3}},} \tag{3.15}$$

where $L_3^{\exp}(a,T)$ is the uncorrected value. The correction factor contains the excess heat $\delta(a,T)$ in units of $k_B T$, the trap depth parameter η and the average extra amount of heat taken away per evaporation event κ.

Second, we relaxed the constant temperature condition and modeled the evaporation effects. The result of this is a more accurate correction of the three-particle loss coefficient. We have also shown that there is a "magic" η_m that can be used to keep the temperature approximately constant.

Part II.

Experiments

4. The Road to Strongly Interacting Bose Gases

In the following, we will describe the experimental sequence to create ultracold Bose gases of ^{7}Li and discuss the tunability of this system. With this tunable system, we will test three-particle physics. For references containing a more elaborate description of the experimental setup, the reader is referred to the theses of F. Schreck [59], L. Tarruell [183], S. Nascimbène [184], and N. Navon [185]. We will concentrate on a detailed description of the setup for ^{7}Li.

4.1. Experimental sequence

In this section, we will describe the different stages of cooling and trapping of ^{7}Li.

4.1.1. Lithium-7

Lithium is the lightest alkaline element and the third element in the periodic table after Hydrogen and Helium. There are two stable isotopes, the bosonic ^{7}Li and the fermionic ^{6}Li, which have a natural abundance of 92.4% and 7.6%, respectively [186]. The mass of ^{7}Li is 7.016 m_u, with $m_u = 1.661 \times 10^{-27}$ kg [187]. Alkaline atoms have one electron occupying the outer shell. For lithium, this is a $2s$-state and the excitation of the electron to the $2p$-state is an optical transition, with a wavelength of ≈ 671 nm. Lithium is a soft light metal with its melting point at 181 °C. ^{7}Li has three protons and four neutrons with nuclear spin $I = 3/2$ and electron spin $S = 1/2$, in the ground state.

4.1.2. Laser System

The laser system consists of commercially available diodes[1] that have a maximum output of 135 mW in addition to several Tapered Amplifiers (TA)[2][3].

[1] Hitachi HL6545MG

[2] Eagleyard TPA-0670-0500 Tapered Amplifier Diode

[3] In a future modification, we will use a newly developed solid state laser operating at a wavelength of 1342 nm is doubled to 671 nm, putting out a maximum power of 800 mW [188]. A second version of this laser has already achieved a maximum of >3 W of red light [189].

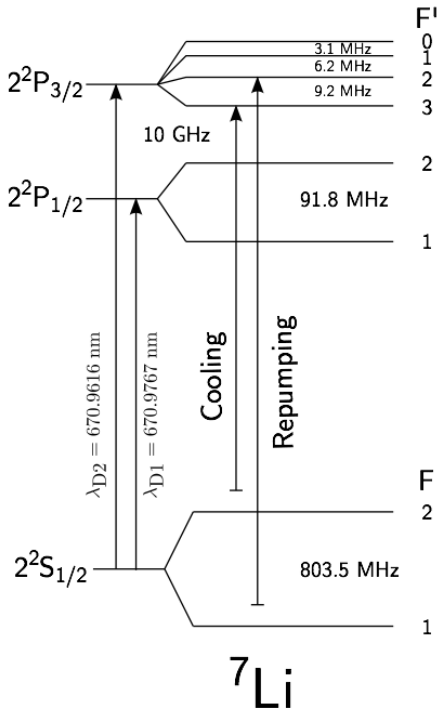

Figure 4.1.: The energy spectrum of ^{7}Li.

In Figure 4.1, the energy spectrum of ^{7}Li is shown, both the cooling and repumping is done on the D_2-line. The ground-state hyperfine splitting is 803.5 MHz, whereas the excited state hyperfine splitting is only 9.2 MHz between the states $|F' = 2\rangle$ and $|F' = 3\rangle$. The line-width of the D-transitions is $\Gamma = 5.9$ MHz, which means that the hyperfine states in $2^2P_{3/2}$-manifold are not optically resolved.

For lithium 7, we use one master laser, which is frequency locked using saturated absorption spectroscopy on the D_2-line. For this master laser, we use an Anti-Reflection (AR) coated diode[4]. The diode is used in an External Cavity Diode Laser (ECDL) setup in Littrow configuration. A reflective holographic grating[5] with $\sim 20\%$ reflectivity is used to create the external cavity, which is used to tune the wavelength. The current versus power output of the ECDL is given in Figure 4.2.

4.1.3. Zeeman slower

The saturated vapor pressure of lithium is the lowest of all the alkali atoms (4.4×10^{-19} Torr at 300 K) and in order to create an atomic beam with sufficient

[4]Eagleyard EYP-RWE-0670-00703-2000-SOT02-0000
[5]Thorlabs GH13-18V perpendicular polarization

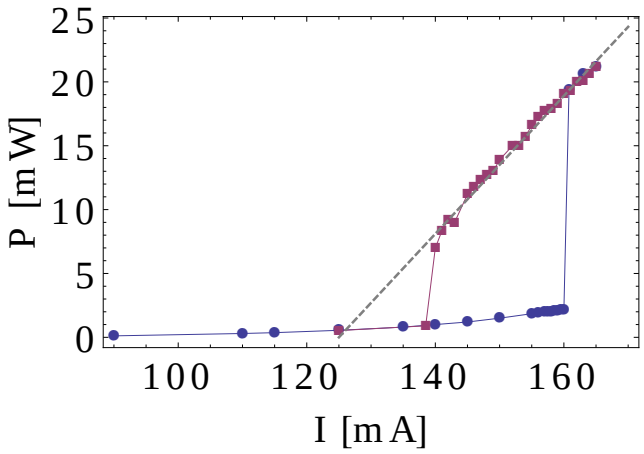

Figure 4.2.: The threshold for the used AR coated diode. We shown the behavior of the AR coated diodes for power versus current. The blue curve is the path going up in current and in red is the curve for going down in current. The difference between the two curves is caused by hysteresis. The measurement is done in an ECDL setup with $\sim 20\%$ reflectivity of the grating and a wavelength around the transition for lithium: 671 nm.

flux, an oven operating around 500 °C is required (7.3×10^{-3} Torr at 800 K). The oven consists of one reservoir tube, with lithium, and a small collimation tube creating the atomic beam. There is a temperature gradient across the length of the collimation tube, which goes from 500 °C in the oven down to $\sim$ 180 °C at the end of the tube. Together with a titanium mesh on the inside of the tube, this temperature gradient will recycle liquid lithium back into the oven. However, it is really important that the mesh is well placed inside the tube, with nothing sticking out, because otherwise the mesh might be colder than the tube and blocking of the oven can occur, due to the formation of solid lithium.

The atomic beam is directed through a spin-flip Zeeman slower[6], which uses a magnetic field to compensate the Doppler shift, occurring due to the slowing down of the atoms by resonant laser light. To slow the atoms down, two lasers are required. First, cooling light detuned by $\delta = -350$ MHz from the D_2-line on the transition between the stretched states $|F = 2, m_F = 2\rangle \rightarrow |F' = 3, m_{F'} = 3\rangle$. Second, a repumping laser on the $|F = 1, m_F = 1\rangle \rightarrow |F' = 2, m_{F'} = 2\rangle$-transition is used to prepare atoms in the oven in the $|F = 2, m_F = 2\rangle$ ground state and to pump atoms, that were lost in the spin-flip region, back into this state. The Zeeman

[6]For more information about the operation of a Zeeman Slower [190]

Slower has a capture velocity of 1100 m/s and the captured atoms are slowed down by the Zeeman slower to a nominal speed of 50 m/s. At this point, the atoms are slow enough to be captured by the MOT.

4.1.4. Magneto-Optical Trap (MOT)

The slow atomic beam is captured in a MOT created by a linear magnetic field gradient together with six circularly polarized laser beams, as is shown in Figure 4.3a. The laser beams consist of cooling light detuned by $\delta \approx -6.7\ \Gamma$ from the stretched state transition $|F=2, m_F=2\rangle \rightarrow |F'=3, m_{F'}=3\rangle$ with an intensity $I/I_{\text{sat}} \approx 0.79$, where $I_{\text{sat}} = 2.54\ \text{mW/cm}^2$. However, since the hyperfine states cannot be optically resolved, the manifolds $|F'=1\rangle$, $|F'=2\rangle$ and $|F'=3\rangle$ in $2^2\text{P}_{3/2}$ are all excited. This means that there is no closed cycling transition and there is an equal chance of either falling back into the $|F=1\rangle$ or $|F=2\rangle$ manifold. In order to keep cycling, a repumper laser detuned by $\delta \approx -5.9\ \Gamma$ from the $|F=1, m_F=1\rangle \rightarrow |F'=2, m_{F'}=2\rangle$-transition with, in practice, the same power as the cooling light ($I/I_{\text{sat}} \approx 0.79$), is needed.

After the MOT cooling stage, the cloud contains $\approx 10^9$ atoms at a temperature of ≈ 1 mK. To decrease the temperature further it is then compressed (CMOT) in 8 ms by detuning the cooling and repumper lasers closer to resonance $\delta \approx -3.5\ \Gamma$ and $\delta \approx -3.5\ \Gamma$, respectively. During the CMOT, the power in the repumping laser beam is reduced to zero, this pumps all the atoms into the $|F=1\rangle$ manifold. This manifold only has three m_F states, compared to the five m_F states in the $|F=2\rangle$ manifold. The cloud will end up in an equal mix of m_F states in the $|F=1\rangle$ manifold, which has a lower entropy than an equal mix of m_F states in the $|F=2\rangle$ manifold, because there are fewer state to occupy. Afterwards, fewer optical pumping transition cycles are required to spin-polarize the cloud into the state $|F=2, m_F=2\rangle$, hence less heating. After the CMOT stage, the cloud consists of $\approx 4 \times 10^8$ atoms at a temperature of $\approx 600\ \mu$K, which is roughly four times the Doppler temperature $T_{\text{D}} = \hbar\Gamma/2k_B \approx 150\ \mu$K for the D_2-line of ^{7}Li.

4.1.5. Optical Pumping

In order to magnetically trap the atoms, the cloud needs to be spin-polarized into a low-field seeking state, because no static magnetic field maxima are allowed by the Maxwell equations [191]. The spin-polarization is achieved using two circularly σ_+-polarized laser beams: a D_2 pumping beam resonant on the transition $|F=1, m_F\rangle \rightarrow |F'=2, m_{F'}=m_F+1\rangle$-transition and a D_1 pumping beam far red

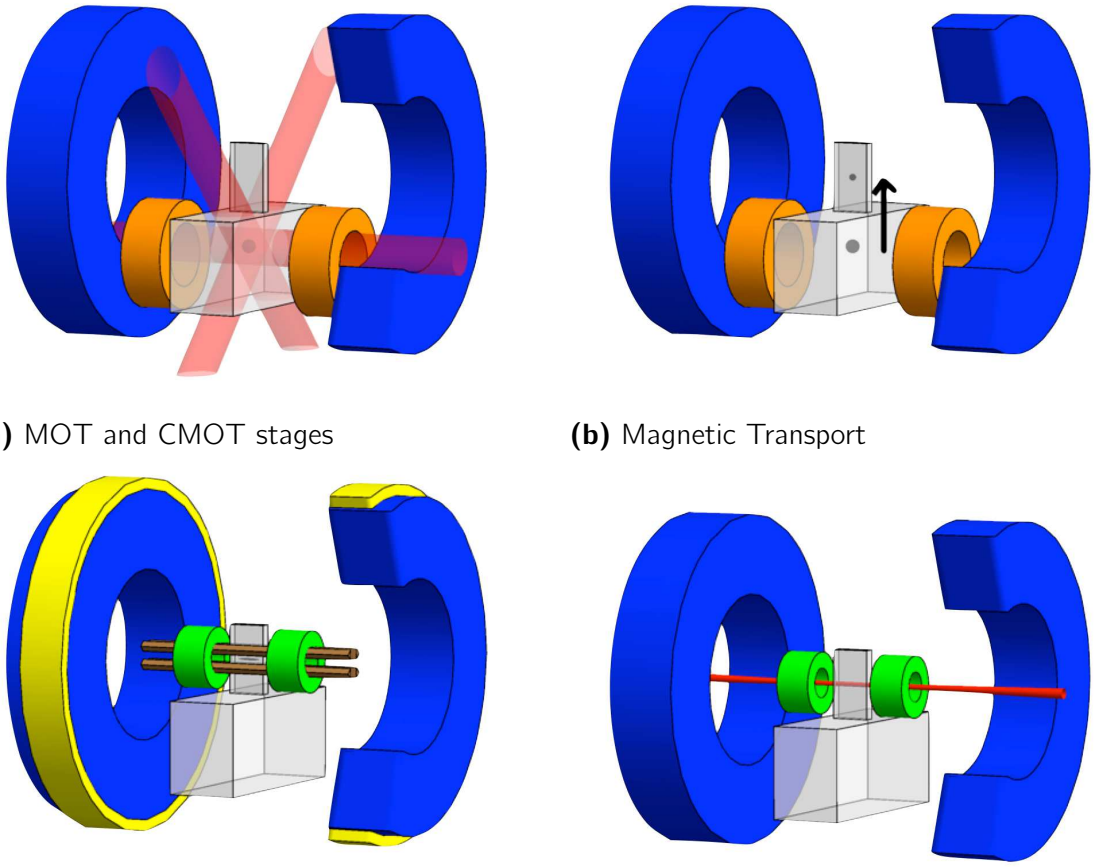

(a) MOT and CMOT stages

(b) Magnetic Transport

(c) Magnetic trapping and Radio-Frequency evaporation

(d) Optical trapping

Figure 4.3.: The experimental sequence
Light gray is the glass cell; **Dark gray** the atoms; **Red** are the laser beams (in **(a)** the MOT beams and in **(d)** the optical dipole trap); **Orange** are the coils which create the MOT trapping field; **Blue** are the coils, which create the Transfer quadrupole and Feshbach bias field; **Green** are the coils which create the curvature field during both the Ioffe-Pritchard and in the optical trapping stage. **Brown** are the Ioffe bars which create a radial quadrupole field; **Yellow** are the precision offset coils which create a small field with high speed.

detuned from the $|F=2, m_F\rangle \rightarrow |F'=2, m_{F'}=m_F+1\rangle$-transition. This makes the state $|F=2, m_F=2\rangle$ a dark state, hence, after several pumping cycles all the atoms end up in the dark state. As mentioned before, having all the atoms initially in the $|F=1\rangle$ manifold reduces the entropy and less cycles of optical pumping (heating) are necessary. The next step in the cooling process is magnetic trapping and evaporation.

4.1.6. Magnetic Trapping and Evaporation

The magnetic trapping stage consists of three steps: a magnetic quadrupole trap [192], a magnetic transport and a Ioffe-Pritchard (IP) trap [193], these stages are shown in Figures 4.3b and 4.3c.

After the atoms are spin-polarized in the state $|F=2, m_F=2\rangle$, they are captured in a quadrupole trap formed by the two coils in anti-Helmholtz configuration, which are used for the MOT, see Figure 4.3a. The field created by the coils is linear along the axis of the coils (we take this to be the z-axis) $Bz\hat{\boldsymbol{z}}$ and leads to a potential $U(\boldsymbol{r}) = -\boldsymbol{\mu} \cdot \boldsymbol{B}(\boldsymbol{r})$, which traps low-field seeking states.

This trap is not suitable to further cool down the atoms because, first of all, at $B=0$ Majorana spin-flips, that lead to trap losses, become more severe at lower temperatures, because the atoms will on average spent more time in the center of the trap. Second, the scattering rate of ^{7}Li is extremely small at low magnetic field [59] and the quadrupole trap is not confining enough to have a sufficiently high collision rate. In this experiment, the choice was made to use a IP trap. To get a confinement that is as strong as possible, the coils need to be as close to the atoms as possible (in the current setup, the distance from the Ioffe-bars to the atoms is 10 mm [183]), which is why a special small sized glass appendage is placed above the MOT area, see Figure 4.3c. This allows for good optical access to the MOT region and tight confinement in the IP region.

To bring the atoms into this appendage, they are magnetically transported over a distance of 5.65 cm, see Figure 4.3b. At the highest gradients possible, the cloud is still too large to fit into the appendage and about 50% of the atoms are lost during the transport. This loss of atoms is caused by the fact that the cloud is too hot and, therefore too large. After the transport, the cloud is loaded into the IP trap, see Figure 4.3c. The base IP trap consists of four Ioffe-bars (brown bars), for radial trapping, and two pinch coils (green coils), for axial trapping. In addition, two compensation coils (blue coils) are added to undo the bias created by the pinch coils.

At this point, the temperature of the cloud is on the order of a few mK, which

corresponds to the minimum in the scattering cross section for lithium. In order to start the evaporation with a more favorable scattering cross section, an extra stage of *in situ* Doppler cooling is applied. This technique was developed in the lithium group at the ENS during the theses of F. Schreck and G. Ferrari [59, 194, 195]. The cooling technique is based on the fact that with a strong magnetic field (in this case 505 G), the transition $|F=2, m_F=2\rangle \rightarrow |F'=3, m_{F'}=3\rangle$ becomes a closed cycling transition, allowing for a more efficient cooling. Also, only a single beam is necessary for the cooling, due to the strong anharmonicity of the trap. After two stages of cooling, the final temperature of 110 μK in the axial and 370 μK in the radial direction, is reached. These results are obtained in a highly compressed trap ($\omega_z = 2\pi \times 122$ Hz and $\Omega_R = 2\pi \times 353$ Hz). After the Doppler cooling stage the bias field is removed and the cloud is further compressed ($\omega_z = 2\pi \times 70$ Hz and $\Omega_R = 2\pi \times 3.1$ kHz). Empirically, this is found to be a good starting point for evaporative cooling.

The evaporative cooling technique is based on spin-flipping the atoms from the state $|F=2, m_F=2\rangle$ (a low field seeking state) into the state $|F=1, m_F=1\rangle$ (a high field seeking state) using Radio-Frequency (RF) radiation. The evaporation is started by dressing state $|F=2, m_F=2\rangle$ with the state $|F=1, m_F=1\rangle$, using a RF photon blue detuned from the hyperfine transition in the cloud, meaning that for a specific magnetic field, outside of the cloud, the potential is, effectively, cut off. When an atom has enough energy to reach this cutoff, its spin is flipped and the atom is pushed out of the trap. By slowly reducing the detuning of the RF-radiation, the cutoff energy is lowered and starts to cut away atoms with lower energies. This process is continued until a temperature below 20 μK is reached and we are left with 2×10^6 atoms. The next step will be to load the atoms into an optical dipole trap.

4.1.7. Optical Dipole Trap (ODT)

The ODT uses the dipole force to create a conservative potential on the atoms [16]. The dipole force, for a two-level atom and a single frequency laser beam, with wavelength λ and detuning Δ from the resonance ω_0, is given by

$$U_{\text{dip}}(\boldsymbol{r}) \underset{\text{RWA}}{\simeq} \frac{3\pi c^2}{2\omega_0^3} \frac{\Gamma}{\Delta} I(\boldsymbol{r}),$$

where c is the speed of light, Γ the natural line width of the resonance, and $I(\boldsymbol{r})$ is the intensity profile given by the laser beam. The detuning determines whether

the potential is attractive $\Delta < 0$ (red-detuned) or repulsive $\Delta > 0$ (blue-detuned). A laser beam around its focus, is given by a Gaussian (*cf.* [196]), with $1/e^2$-radius $w(z)$ and power P:

$$I(r,z) = \frac{2P}{\pi w^2(z)} e^{-2\frac{r^2}{w^2(z)}},$$

where $w_z^2 = w_0^2(1 + z^2/z_R^2)$ is the axial waist, w_0 is the waist and $z_R = \pi w_0^2/\lambda$ is the Rayleigh range. Close to the center of the focus, the potential can be approximated by a harmonic potential

$$U(r,z) \simeq -U_0 \left[1 - 2\left(\frac{r}{w_0}\right)^2 - \left(\frac{z}{z_R}\right)^2\right],$$

We are using a commercial fiber laser[7] at a wavelength of 1071 nm and a maximum rated power of 120 W. During the studies on Bose gases the maximum power used was about 15 W, with a waist[8] of 43(1) μm. The reason for this is that ^{7}Li in the state $|F = 2, m_F = 2\rangle$ experiences strong dipolar losses when the density becomes to high [197]. The axial confinement is rather small. To increase it, we add an axial magnetic curvature.

Before the ODT loading, the axial confinement of the IP trap is changed from strongly confining with a small bias field to only a small curvature field. Afterwards, the current in the Ioffe-bars is turned off and, at the same time, the dipole trap is turned on, in 50 ms. There are no Feshbach resonances in the state $|F = 2, m_F = 2\rangle$. In order to have Feshbach resonances, the atoms are transferred into one of the high-field seeking states. The atoms are transferred from the state $|F = 2, m_F = 2\rangle$ into the state $|F = 1, m_F = 1\rangle$ via a RF induced Landau-Zener sweep [198, 199]. Note that the transfer is done from a low-field to a high-field seeking state, meaning that the axial curvature needs to be inverted after the transfer [185].

We use a Feshbach resonance in the $|F = 1, m_F = 1\rangle$-state of ^{7}Li around $B_0 = 737.8(3)$ G (see Section 4.2) to tune the scattering length for evaporation. The bias magnetic field is increased to ~ 718 G, where the scattering length is $\approx 200\ a_0$, which was empirically found to be the optimum for evaporation. In an

[7] IPG YLR-120-LP

[8] Note that we measured the waist using the beam profile directly, but also via power and trap frequency measurement. Between these measurements we found, at that time, a discrepancy of $\approx \sqrt{2}$, which is probably due to the profiling camera not being at the focus. In the following of this thesis, we have used the more accurate measure, from the power and trapping frequencies, when necessary.

optical trap, in principle, all hyperfine states are trapped, which means that it is not possible to use the spin-flipping to untrappable states technique for evaporation. An optical trap, however, has the advantage that the potential depth is comparable to the thermal energy. This means that by tuning the power of the laser, we can tune the depth of the trap, hence force the evaporation. The disadvantage of this process is that while reducing the power in the trap, the confinement is also reduced, which makes the trapping frequency in the axial direction especially small. This will reduce the elastic scattering processes that are necessary for rethermalisation. To overcome this, it is common to use a crossed dipole trap. In that case, the trapping frequencies in all three-directions become comparable. In our experiment, however, the already existing magnetic curvature along the axial direction (coming from the IP trap) is used to add extra confinement. This, though, implies that the evaporation becomes 2d (see [200] for more information about dimensionality in evaporation), because the magnetic trap is deeper than the ODT.

We first evaporatively cool the cloud to $\sim 1\ \mu$K in ~ 5 seconds. Afterwards, we can recompress the trap to the desired depth or trapping frequency.

In Section 5.1.3, we will describe the specific measurement procedure.

4.1.8. Radio-Frequency (RF) Transitions

In the current setup, we are able to create any possible combination of (in)coherent spin mixtures. We have two methods at hand: Rabi oscillations or Landau-Zener sweeps. Both methods use RF-photons to couple one hyperfine state to another.

Rabi oscillations are coherent oscillations of the population, between two states that are coupled via a coupling Ω_R. On resonance, the population of the final state is given by

$$P_{|m\rangle\to|m\pm1\rangle} = \sin^2\left(\frac{\Omega_\mathrm{R}\ t}{2}\right).$$

Changing the pulse duration t, allows the creation of any superposition of states.

Landau-Zener sweeps [198, 199] are induced by adiabatically sweeping the frequency of the RF radiation over the resonance. The transition probability for Landau-Zener sweeps is given by:

$$P_{|m\rangle\to|m\pm1\rangle} = 1 - e^{-2\pi\frac{\Omega_\mathrm{R}^2}{\dot{\omega}}},$$

where Ω_R is the Rabi-frequency, $\dot{\omega}$ the sweep rate and $|m\rangle$ either $|m_F\rangle$ at low-field or $|m_I + m_J\rangle$ at high-field. As we can see, for diabatic passage $\dot{\omega}\to\infty$ the probability

$P = 0$, so no atoms are transferred, for adiabatic sweeps $\dot{\omega} \to 0$, on the other hand, the probability $P = 1$, so for sufficiently high Ω_R the full population is transferred. Note that these sweeps are coherent single particle processes, which means that any superposition of the two states can be created. However, due to waiting in a trap with inhomogeneous magnetic fields these coherent states will decay (for our trap in about 10 ms) into an incoherent mixture.

The advantage of Rabi oscillations is that the method is, in general, fast (typically < ms), however also sensitive to detuning, magnetic field and power fluctuations. The Landau-Zener sweep method on the other hand is slower (typically 50 - 500 ms), though, the method is less sensitive to detuning, magnetic field and power fluctuations.

In Figure 4.4, the different hyperfine states in the ground and excited $2^2P_{3/2}$ state are depicted up to a 1000 G. The different hyperfine-transitions of interest are:

- **Low-field (around 0 G):**
  - $|F = 2, m_F\rangle \to |F = 1, m_F \pm 1\rangle$: which at low-field has a transition frequency around 803.5 MHz (the hyperfine splitting). This transition is both used for evaporation (see Section 4.1.6) and preparation of the atoms in the ODT (see Section 4.1.7).

- **High-field (around 737.8 G):**
  - $|1\rangle \to |2\rangle$: typical frequency: ~ 170 MHz
  - $|2\rangle \to |3\rangle$: typical frequency: ~ 210 MHz
  - $|3\rangle \to |4\rangle$: typical frequency: ~ 270 MHz
  - $|1\rangle \to |5\rangle$: the transition from an high-field seeking to a low-field seeking state. This transition is sensitive to magnetic field changes and useful for the characterization of the magnetic field strength. Typical frequency: ~ 2.7 GHz.
  - $|1\rangle \to |E_b\rangle$: the transition, on the positive-a side of the Feshbach resonance, into the weakly bound dimer dressed state. Typical frequency range: $0 - 10$ MHz.

These frequencies can be roughly classified into three categories: low-frequency ($0-50$ MHz), mid-frequency ($50-500$ MHz) and high-frequency ($500-3500$ MHz).

We have, for each of these frequency ranges, synthesizers[9], amplifiers[10] and antennas[11].

4.1.9. Imaging

To do a measurement, the resulting cloud needs to be analyzed. This is done by taking an image of the cloud. There are several imaging techniques, *e.g.*, phase-contrast imaging, fluorescence imaging, ionization and absorption imaging. In our experiment, we use the latter. The idea behind absorption imaging is to shine resonant laser light through the cloud and image the shadow cast by the cloud on a CCD camera (let us say that the propagation direction is the y-axis). The cloud will absorb an amount of light proportional to the density in a certain region. The camera will in that case provide us with an image $I(x,z)$. When this image is compared to a reference image $I_0(x,z)$ without atoms, we obtain the optical density profile of the cloud integrated along the propagation direction of the laser, which is directly related to the integrated density in the following way

$$\mathrm{OD}(x,z) = -\ln\left(\frac{I(x,z)}{I_0(x,z)}\right) = \sigma_\mathrm{A}\int dy\, n(x,y,z), \tag{4.1}$$

where σ_A is the absorption cross section. Equation (4.1) only holds if the Lambert-Beer law holds, which means that the images need to be taken in the linear absorption regime ($I \ll I_\mathrm{sat}$ the saturation intensity). The intensity for imaging is $I/I_\mathrm{sat} \simeq 0.01$, with $I_\mathrm{sat} = 2.54$ mW/cm^2.

Figure 4.4 shows the energy dependence of the ^{7}Li energy state in the D2-line system. The red arrows, in the Figure, are indicating the imaging transitions used for imaging at both low- and high-field. The low-field probe cycles on the $|F=2, m_F=2\rangle \rightarrow |F'=3, m_{F'}=3\rangle$ transition using σ_+-polarized light. The three high-field probes cycle on the following three transitions: $|1\rangle \rightarrow |9\rangle$, $|2\rangle \rightarrow |10\rangle$ and

[9] Rohde Schwarz SMT 03 (5 kHz - 3 GHz);
Rohde Schwarz SML 01 (9 kHz - 1.1 GHz);
Marconi 2030 (10 kHz - 1.35 GHz)

[10] MiniCircuits ZHL-30W (30 W 700 - 2500 MHz);
MiniCircuits ZHL-50W (50W 50-500 MHz);
MiniCircuits ZHL-42W (10-4200 MHz);
Nucletudes ALP 6050 (10 W 1 - 500 MHz)

[11] 1x 1 turns - 10 mm diameter;
1x 10 turns - 10 mm diameter;
1x 100 turns - 10 mm diameter;
1x wire for linear-polarization

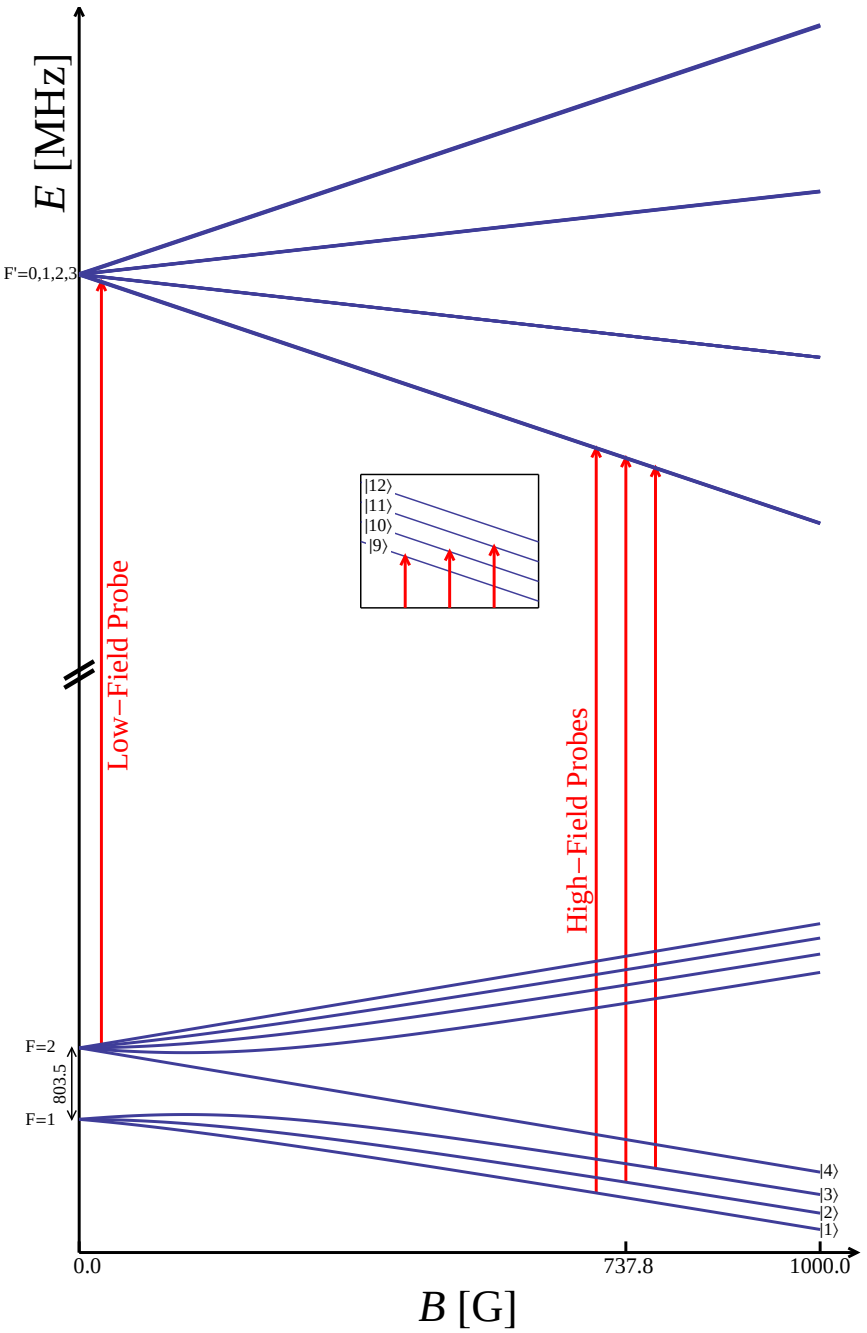

Figure 4.4.: The energy spectrum E of the D2-line of ^{7}Li for a magnetic field of 0 to 1000 G. The red arrows indicate the transitions used for the imaging. The outermost left arrow indicates the low-field imaging on the transition $|F=2, m_F=2\rangle \rightarrow |F'=3, m_{F'}=3\rangle$. The other three arrows indicate the high-field imaging transitions, which are from left-to-right: $|1\rangle \rightarrow |9\rangle$, $|2\rangle \rightarrow |10\rangle$ and $|3\rangle \rightarrow |11\rangle$. For most of the measurements, the imaging transition $|1\rangle \rightarrow |9\rangle$ was used. Inset: the different Zeeman states used in the high-field imaging.

$|3\rangle \rightarrow |11\rangle$. In the following, we will only use the $|1\rangle \rightarrow |9\rangle$-transition.

A recurring problem in ultracold gases is the determination of σ_A. The absorption cross section σ_A is given by

$$\sigma_A = \frac{C^2\lambda^2}{2\pi\left[1+\left(\frac{4\pi\Delta}{\Gamma}\right)^2\right]} \underset{\Delta=0}{=} \frac{C^2\lambda^2}{2\pi}, \tag{4.2}$$

where C is the Clebsch-Gordan (CG) coefficient. The imaging is perpendicular to the magnetic field axis. Hence, for linear polarization perpendicular to the magnetic field direction the CG coefficient equals 1/2. The determination of σ_A is, in general, rather difficult (*e.g.* due to the laser frequency linewidth and precise knowledge of the magnification factor of the imaging system), so a calibration of the atom number is needed. Our calibration method is extensively described in Section 5.1.4 and [95].

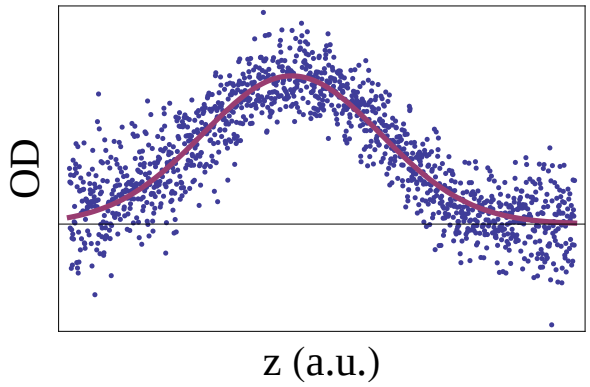

Figure 4.5.: A typical integrated optical density profile, for a non-degenerate gas of $\sim 1.5\times10^5$ ^{7}Li atoms at $T = 10$ μK. The total number is obtained by integrating along the z-axis and the temperature by fitting a Gaussian (red line). Extracting the width and using Equation (4.3) gives the temperature.

Using this, each image provides us with information about the cloud. The number of atoms can be extracted by simply integrating over the OD of the cloud. Because the cloud is non-degenerate, the width of the cloud is obtained by a Gaussian fit. In a non-degenerate gas in equilibrium the temperature is related to the width of the cloud via

$$T = \frac{m\omega_z^2\sigma_z^2}{k_B}, \tag{4.3}$$

where σ_z is the width obtained from the fit.

As an example, we have shown a typical integrated absorption profile in Figure 4.5. The blue dots correspond to the integrated density profile along the y-axis and the red line to the fitted Gaussian.

4.2. Feshbach Resonance in ^{7}Li

In this section, we will discuss the Feshbach resonance specific to ^{7}Li. For more information about Feshbach resonances in general, the reader is referred to Section 1.2 or, for a detailed review of the subject, to [48].

Around a Feshbach resonance, the scattering length behaves as

$$a = a_{\text{bg}} \left(1 - \frac{\Delta}{B - B_0}\right), \tag{4.4}$$

where a_{bg} is the background scattering length, Δ is the width and B_0 is the position of the Feshbach resonance.

Predicting the position and width of a Feshbach resonance is difficult, because the calculation of the scattering length is very sensitive to the details of the atom-atom potential. Usually, the fine tuning of these parameters is performed using the input of experimental measurements.

There are several methods to experimentally detect Feshbach resonances. The fastest and most popular method is to do inelastic loss spectroscopy. However, the disadvantage is that it is rather inaccurate. We have used this method to roughly determine the position of the resonance. Afterwards, binding energy measurements were used to characterize the full resonance.

We use the Feshbach resonance in the state $|F = 1, m_F = 1\rangle_{\text{LF}}$ or $|1\rangle_{\text{HF}}$ of ^{7}Li. Before the measurements were done in our group [95, 185], there were two independent measurements of this resonance, which were disagreeing in resonance position by ≈ 1.5 G. The first measurement was done in Rice [61]. They fitted a Thomas-Fermi profile to an *in situ* BEC to determine the scattering length as a function of the magnetic field, thus characterizing the resonance position and width. They found the resonance position $B_0 = 736.8(2)$ G and width $\Delta = -192.3(3)$ G. The second measurement was done in Bar-Ilan [128], using RF-spectroscopy on the weakly bound dimer state to determine a, close to the Feshbach resonance, as a function of the magnetic field. They found the resonance position $B_0 = 738.3(3)$ G.

In our group, we used the latter method and found a result similar to one obtained by the Bar-Ilan group [95, 185]. After our measurements, the group in Rice remea-

sured the Feshbach resonance position using weakly bound state RF-spectroscopy and found a matching position [125]. The most accurate determination of the Feshbach resonances in ^{7}Li was done in [201]. The authors used spectroscopic data of three Feshbach resonances in the two lowest hyperfine states of ^{7}Li to fit to a coupled channel calculation. The resonance position is $B_0 = 737.88(2)$G, the background scattering length $a_{bg} = -20.98\ a_0$ and resonance width $\Delta = -171.0$ G.

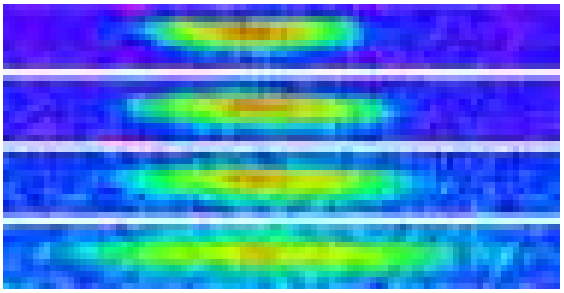

Figure 4.6.: Absorption images of interacting BECs, with from top to bottom increasing interactions. ^{7}Li in the state $|F = 1, m_F = 1\rangle$, on the positive-a side of the Feshbach resonance at $B_0 = 737.88(2)$G. The images have a scattering length a of 200, 520, 1420 and 2940 a_0, respectively. With increasing interactions the size of the cloud increases. Red corresponds to high and blue to low density regions.

At the original resonance position of the Rice group, the scattering length corresponds to $a(736.8\text{G}) = 3300\ a_0$. Hence, the resonance was remeasured [125] and the results from [202] corrected.

In Figure 4.6, we have shown the result of increasing interactions on a BEC of ^{7}Li.

4.3. Summary

In this chapter, we have discussed the different stages of the experiment, which are schematically depicted in Figure 4.3. Let us here summarize the different stages:

1. **Zeeman Slower:** An atomic beam coming from an oven at 500 °C is slowed down from 1100 m/s to 50 m/s.

2. **MOT:** The atomic beam is captured using laser light and magnetic field gradients and cooled to $\approx 600\ \mu$K.

3. **Magnetic trapping and Evaporative cooling:** The atoms are spin-polarized, magnetically trapped and cooled using RF-evaporation. The final temperature is $\approx 20\ \mu$K.

4. **Hybrid Magnetic and Optical Trapping:** A dipole trap together with a magnetic field curvature is used to trap the atoms. A bias magnetic field is used to change the collision properties and forced spilling of atoms evaporatively cools the cloud further down to $\approx$ 1-15 μK.

5. **Measurements:** The measurement is done at and around the Feshbach resonance described in Section 4.2.

6. **Imaging:** An absorption image is taken after a sequence and the atom number and temperature of the cloud are extracted.

In Chapter 5, we will describe in detail the results of measurements that were done at and around the Feshbach resonance.

5. Lifetime of the Resonant Bose Gas

This chapter is dedicated to the experimental study of the lifetime of Bose gases with resonant interactions. This study will focus on the dominating three-particle losses in the non-degenerate regime ($T \gg T_c$). In Chapter 2, a theoretical model for three-particle losses was derived. In order to test the predictions arising from this model, we will consider two situations.

In the first situation, we will focus on the limit of unitary interactions ($a \to \infty$) and study the temperature behavior of the three-particle losses. In this experimental study, we will for the first time quantitatively test the $1/T^2$ law expected for three-particle losses at unitarity.

In the second situation, we will consider finite-a and study the saturation behavior around $|a| \sim 1/k_{\mathrm{th}}$ of the three-particle losses. We will measure the three-particle losses while varying the scattering length at a fixed temperature and give a quantitative comparison of the results with the theory.

Furthermore, we use the theory from Chapter 2 to quantitatively explain results in previous studies. A group in Innsbruck [122, 203] did quantitative measurements on the change of the position of a Efimov resonance due to saturation of the three-particle losses. We will compare these measurements with the theory presented in Chapter 2. The result is a remarkable quantitative agreement between, on the one hand, the temperature effects seen in the experiments and, on the other, the theoretical explanation of these effects.

After our publication [143], a second study of the three-particle losses in a system with resonant interactions was performed in Cambridge [172]. In this study, the $1/T^2$ behavior was verified using a different method. We will discuss these measurements and show that the theory quantitatively explains their results.

We will start by explaining the experimental setup specific to our measurements. More precisely, we will describe the quasi-thermal and constant temperature conditions and explain the atom number calibration.

5.1. Recombination Rate Measurements and Assumptions

In the following, we will explain under which conditions our measurements were done and how we calibrate the measurements. We will start by introducing the quasi-thermal equilibrium condition. This condition will be important to extract the density and temperature from an *in situ* density profile. Moreover, the quantitative $1/T^2$ behavior is derived under the condition of quasi-equilibrium. Afterwards, we will talk about the different time scales of N-particle processes. We will discuss the specific experimental procedure for the loss measurements. Thereafter, the number calibration is described. Finally, we will discuss the constant temperature condition and explain the data analysis procedure.

5.1.1. Quasi-Thermal Equilibrium Condition

In order to describe the losses, we need to compare the time scales of elastic and inelastic collisions. The reason for this is that the elastic collisions determine the reaction time of the cloud to reach its equilibrium state, whereas inelastic collisions

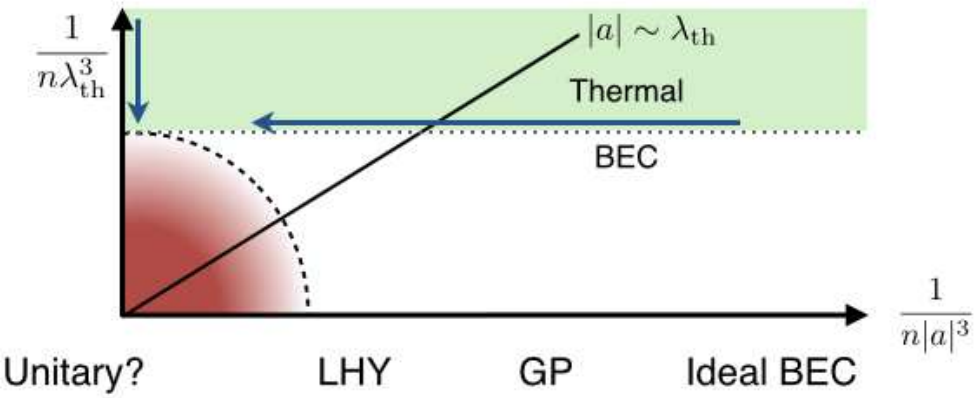

Figure 5.1.: The quasi-thermal equilibrium condition diagram, which is based on the quasi-thermal equilibrium conditions, see Equation (5.1), at resonance (y-axis), and Equation (5.2), at zero-temperature (x-axis). On the x-axis the interaction parameter is plotted and on the y-axis the degeneracy parameter. The origin corresponds to the unitary Bose gas and the red region to the regime, where the gas is unstable and theories for $L_3(T)$ and $L_3(a)$ are not valid. The shaded green area corresponds to the validity region of the theory in Chapter 2, the blue arrows correspond to our loss measurement at resonance and at finite interactions. The dashed quarter circle corresponds to $\gamma_3/\gamma_2 \simeq 1$ and sets limits to the quasi-thermal equilibrium condition.

are driving the cloud away from equilibrium. Hence, elastic collisions need to occur much faster than the inelastic collisions in order to have equilibration. If this would not be the case, and the inelastic collisions would be dominating over the elastic collisions, then inelastic processes would trigger dynamic macroscopic processes, which are, in general, difficult to describe without doing a full dynamical simulation. Operating under these conditions can be considered as working in a **quasi-thermal equilibrium**. The word quasi marks the important fact that there are still losses.

Assuming that we have a non-degenerate cloud ($n\lambda_{\mathrm{th}}^3 \ll 1$), with unitary interactions. The ratio of interest is given by the elastic two-particle scattering rate $\gamma_2 = n\sigma v_{\mathrm{th}}$ and the inelastic three-particle scattering rate $\gamma_3 = L_3 n^2$. Here σ is the scattering cross section and v the thermal velocity of the atoms. Neglecting the log-periodic term in γ_3, the quasi-thermal equilibrium condition reads (using Equation (2.38) for L_3):

$$\gamma_3/\gamma_2 \underset{a\to\infty}{\propto} n\lambda_{\mathrm{th}}^3 \left(1 - e^{-4\eta_*}\right) \ll 1. \tag{5.1}$$

In the zero-temperature weakly-interacting limit ($k|a| \to 0$), a similar condition is derived. The three-particle loss coefficient is given $L_3 \propto \hbar/m\, a^4$ [56, 113–115, 117] and for the elastic scattering the characteristic reaction time of a BEC is given by $\gamma_2 \propto \mu/h \underset{a\to 0}{\simeq} ng/h = 4\pi(\hbar/m)na$. Hence, the condition becomes

$$\gamma_3/\gamma_2 \underset{k_{\mathrm{th}}\to 0}{\propto} na^3 \ll 1. \tag{5.2}$$

In Figure 0.1 of the Introduction, we have plotted the different regimes of the scattering problem as a function of both interactions (na^3) and temperature ($n\lambda_{\mathrm{th}}^3$). The quasi-thermal equilibrium conditions Equations (5.1) and (5.2) allow us to graphically depicted the regions of stability (see Figure 5.1). The dashed quarter circle corresponds to $\gamma_3/\gamma_2 = 1$ and inside this circle ($\gamma_3/\gamma_2 \gg 1$) is the unstable region and outside this circle ($\gamma_3/\gamma_2 \ll 1$) is the stable region. The horizontal dotted line corresponds to the critical temperature T_c, the solid black line is the condition $\lambda_{\mathrm{th}} = |a|$.

The general expectation, in the limit $T \to 0$ and $a \to \infty$, is that the losses will be limited by the bosonic Fermi energy $E_F \propto n^{2/3}$ (see for example [204]). However, we will limit ourselves to the measurement of the losses in the non-degenerate gas, see the shaded green region in Figure 5.1.

5.1.2. Separation of Time Scales

As we have seen in Section 5.1.1, for the non-degenerate gas with unitary interactions, the time scales of the two- and three-particle processes are separated by the degeneracy parameter $n\lambda_{\mathrm{th}}^3$. In the non-degenerate gas, $n\lambda_{\mathrm{th}}^3$ can be considered as a small parameter and allows for the separation of the time scales between different order processes.

Since N-particle losses provide us with interesting information about the N-particle inelastic scattering problem, let us consider the expansion of many-particle recombination into N-particle recombination problems. Then, N-particle losses are, in general, well described by the following differential equations:

$$\dot{n}(t) = -\sum_{k\in\mathbb{N}} L_k n^k(t)$$
$$\frac{\dot{N}(t)}{N(t)} = -\sum_{k\in\mathbb{N}} L_k \langle n^{k-1}(t)\rangle,$$

where $N(t)$ is the total number of atoms after a wait time t, $\langle n^{k-1}\rangle$ is the average density to the power $(k-1)$, describing the average probability to have $(k-1)$-particles together. The conditions that we work under are the following:

- **Negligible density-independent loss processes.**
- **Internal ground-state:** negligible spin-changing (inelastic two-particle) collisions.
- **Non-degenerate gases:** negligible higher-order, *e.g.* $N>3$, inelastic collisions.

Finally, in a harmonic trap there is another time-scale determined by the trapping frequencies ω_r and ω_z. In our trap configuration the most stringent trap time-scale is given by the axial trapping frequency, which is in the worst case $\omega_z = 2\pi \times 18$ Hz, so the three-particle loss rate needs to be slower than this: $\gamma_3/\omega_z \ll 1$ (see Section 5.1.3 for the other trap parameters).

5.1.3. Starting Point for the Measurements

The experimental setup is described in Chapter 4. The initial condition for the experiments is a spin-polarized (in state $|1\rangle$) non-degenerate gas, which we load

into the optical dipole trap (ODT). At this point, we have $\simeq 2\times10^6$ atoms at $\simeq 30$ μK.

Using the Feshbach resonance at $B_0 = 737.8(4)$ G (see Section 4.2) the scattering length can be tuned to the desired value. For evaporative cooling of bosons, an empirical optimum is found near 200 a_0, which corresponds to a magnetic field of $B \simeq 718$ G. Evaporative cooling is then forced by reducing the power in the laser beam of the ODT. By choosing the appropriate final power, the potential depth U' and thus the final temperature can be controlled. When the cloud is thermalized the ODT is recompressed to the height $U = \eta k_B T > U'$ with $6 \leq \eta \leq 8$. At a specific T the height U is chosen such that the temperature is kept constant during the three-particle loss measurement, as we have shown to be possible in Section 3.3.3.

The typical trapping frequencies lie in the range of $0.87 < \omega_r/(2\pi) < 3.07$ kHz with an error of ~ 5 % and $18 < \omega_z/(2\pi) < 49$Hz with an error of < 1 %, which we have measured both with parametric heating and center of mass oscillations. After recompression, the temperature varies between 1 and 10 μK, with an atom number between 0.5 and 3.0×10^5. In this range of parameters, the phase-space density (PSD) varies between 7×10^{-4} and 1.1×10^{-2}. Since the PSD is $\ll 1$, we stay in a regime where a quasi-thermal equilibrium can be maintained and where 4-particle or higher-order particle losses are negligible.

The next step in the measurement procedure, is to ramp the magnetic field to its final value B in 100-500 ms. At this point the scattering length is given by $a(B)$ (see Equation (4.4)). For the measurements at resonance the magnetic field is $B = B_0$, while the temperature is varied. For the measurements away from the resonance, the temperature is kept around $T \simeq 5.9(6)$ μK and the scattering length $a(B)$ is changed using B.

The ramp to a specific a always starts at the positive a side of the resonance and then sweeps across the resonance to the final value of a. This is to avoid the adiabatic formation of weakly-bound dimers, when scanning from the negative- to the positive-a side [205–207]. The magnetic field ramp time is much longer than the characteristic times associated to the trapping frequencies and elastic scattering. This condition needs to hold in order to avoid fast variations of the density profile that induce strong particle currents in the trap making the loss process difficult to analyze.

After the ramp, the cloud is kept at a magnetic field B for a variable hold time t after which an *in situ* image is taken to extract both atom number and temperature from a Gaussian fit to the density profile. A typical decay curve is shown in Figure 5.3.

To check for independence of the preparation procedure, we have prepared the gas in a non-interacting state (state $|2\rangle$ of ^{7}Li) at the magnetic field corresponding to unitary interactions in the state $|1\rangle$. Afterwards the atoms are transferred into the interacting state using an RF-pulse. This method gave the same result as the other preparation method.

5.1.4. Number Calibration

This section is based on unpublished notes of Andrew Grier [208]. Accurately determining the number of atoms is a difficult problem and usually the associated error is quite large. We have overcome this problem by calibrating our system using a weakly interacting BEC, as introduced in [95]. The method is based on measurements of the equation of state [84, 85, 87] of a BEC in the zero-temperature limit using *in situ* imaging techniques to extract the pressure as a function of the interaction parameter. The pressure can be written as

$$P(\mu, a) = \frac{\hbar^2}{m a^5} \cdot h\left(\nu \equiv \frac{\mu}{g} a^3\right), \tag{5.3}$$

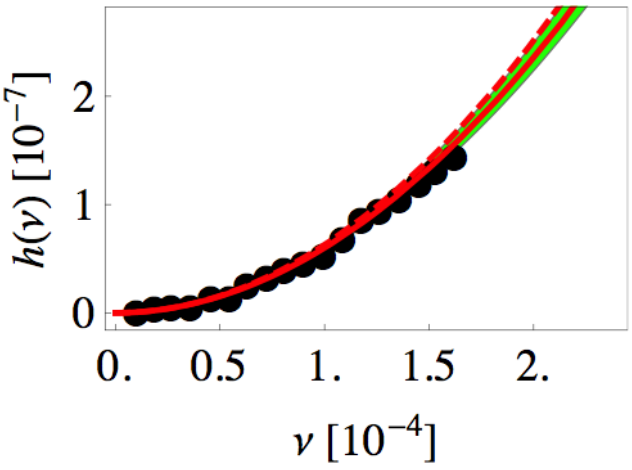

Figure 5.2.: The pressure measurement of $h(\nu)$ as defined by Equation (5.3). The black dots are the result of the pressure measurement. The red dashed line corresponds to the mean field prediction. A scaling factor ξ was used to overlap the data with the mean-field prediction for $a \to 0$, we find $\xi = 2.45(60)$. The red solid line includes the first order corrections (LHY) measured in [95]. We have only used the range $0 \leq \nu \leq 1 \times 10^{-4}$ for the calibration.

where we have introduced the dimensionless pressure h, the grand canonical interaction parameter ν, which becomes na^3 in the limit of weak interactions, and the coupling constant $g = 4\pi\hbar^2 a/m$. In the mean field limit ($a \to 0$), the normalized pressure is given by $h(\nu) = 2\pi\nu^2$ and this result is used to calibrate the number of atoms. The pressure is then written as

$$P(\mu) \underset{a\to 0}{\simeq} \frac{\mu^2}{2g}.$$

Let us use this to calibrate the system and analyze potential error sources in the determination of the loss coefficient L_3.

5.1.4.1. Pressure calibration

Let us introduce the experimentally measured pressure P_{exp} and chemical potential μ_{exp}, which are related to the real pressure and chemical potential through the calibration factor ξ,

$$\frac{P(\mu, a)}{\mu^2} = \xi \, \frac{P_{\text{exp}}(\mu_{\text{exp}}, a)}{\mu_{\text{exp}}^2}.$$

The starting point for the determination of the calibration quantities is the relation between the pressure and the doubly-integrated density $n(z)$ [84, 85, 87],

$$P(\mu_z) = \frac{m\omega_r^2}{2\pi}\bar{n}(z),$$

where ω_r is the radial frequency of the trap and $\bar{n}(z) = \int dx\, dy\, n(x, y, z)$ is the integrated density. The two quantities prone to errors in this formulae are ω_r and $\bar{n}(z)$. ω_r is a known quantity with a known error (see Section 4.1.7). The doubly-integrated density depends on several parameters and in order to find its dependence on the experimental observables, we need to look at the imaging process.

The imaging was described in Section 4.1.9. We can directly relate the number of missing photons on a pixel of the imaging system to the number of particles in the region that the imaging beam passes through. Let OD_{ij} be the optical density measured in pixel (i, j). Using the Lambert-Beer law, the relation between the

density of particles and the number of missing photons can be written as,

$$\begin{aligned} \sigma_{\mathrm{A}} N_{ij} &= (l_{\mathrm{px}})^2 \ \mathrm{OD}_{ij} \\ N = \sum_{ij} N_{ij} &= \frac{(l_{\mathrm{px}})^2}{\sigma_{\mathrm{A}}} \ \sum_{ij} \mathrm{OD}_{ij}, \end{aligned} \tag{5.4}$$

where σ_{A} is the absorption cross section of a particle, N_{ij} is the number of particles in the imaged region corresponding to pixel (i, j), and l_{px} being the pixel size.

In order to understand the calibration, let us introduce a notation to signify the calibration factors: $C[X]$. Let X be some quantity to be measured and X_{exp} the experimentally measured value, then

$$C[X] = \frac{X}{X_{\mathrm{exp}}} \tag{5.5}$$

is the calibration factor between the measured value of X and the real value.

Let us have a look at the total number calibration factor and relate this to calibration factor for the doubly integrated density $\bar{n}(z)$. In Equation (5.4), the OD_{ij} is a measured quantity and the calibration and errors of the relation are only in the pre-factor. From this it follows that the calibration factor in N is given by

$$C[N] = \frac{C[l_{\mathrm{px}}]^2}{C[\sigma_{\mathrm{A}}]}.$$

Following a similar reasoning, the doubly integrated density $\bar{n}(z)$ is related to the number of atoms per pixel through,

$$\begin{aligned} \bar{n}(z) = \frac{1}{l_{\mathrm{px}}} \sum_j N_{ij} &= \frac{l_{\mathrm{px}}}{\sigma_{\mathrm{A}}} \sum_j \mathrm{OD}_{ij} \\ C[\bar{n}(z)] &= \frac{C[l_{\mathrm{px}}]}{C[\sigma_{\mathrm{A}}]}. \end{aligned}$$

So the two quantities here that are prone to errors are l_{px} and σ_{A} (see Section 4.1.9). Translating this into the pressure relation and using the calibration-notation gives,

$$C[P(\mu_z)] = C[\omega_r]^2 \ \frac{C[l_{\mathrm{px}}]}{C[\sigma_{\mathrm{A}}]}.$$

In the local density approximation the chemical potential is given by $\mu_z = \mu_0 - \frac{1}{2} m \omega_z^2 z^2 \rightarrow C[\mu_z] = C[\omega_z]^2 \, C[l_{\mathrm{px}}]^2$. Putting everything together the cal-

ibration parameter of the pressure is given by,

$$C\left[\frac{P(\mu_z)}{\mu_z^2}\right] = \frac{C\left[\omega_r\right]^2}{C\left[\omega_z\right]^4}\,\frac{1}{C\left[l_{\mathrm{px}}\right]^3\;C\left[\sigma_{\mathrm{A}}\right]}. \tag{5.6}$$

The temperature for a non-degenerate gas in a harmonic trap is directly related to the size of the cloud (here along the z-axis):

$$\begin{aligned}\frac{1}{2}k_{\mathrm{B}}T &= \frac{1}{2}m\omega_z^2\sigma_z^2\\ \rightarrow C\left[T\right] &= C\left[\omega_z\right]^2 C\left[\sigma_z\right]^2.\end{aligned}$$

In the following, we will use this result and compare it to the calibration factor of the pressure.

5.1.4.2. Recombination and Temperature calibration

A similar procedure can be followed to estimate the calibration error in L_3, thus allowing the derivation of the calibration factor of L_3T^2. When taking the solution of the number of particles as a function of time $N(t)/N_0 = (2\tilde{A}N_0^2L_3t+1)^{-1/2}$, where $\langle n^2\rangle = \tilde{A}\,N^2$ defines $\tilde{A}$ and $C\left[\tilde{A}\right] = \left(C\left[\omega_r\right]/C\left[\omega_z\right]\right)^4 \times 1/C\left[l_{\mathrm{px}}\right]^6$. The fit will be done on $L_3^{\mathrm{fit}} = \tilde{A}\,N_0^2\,L_3$ so in order to get the real L_3 we need several quantities. In the calibration notation this becomes

$$\begin{aligned}C\left[L_3\right] = \frac{1}{C\left[A(T)\right]C\left[N_0\right]^2} &= \left(\frac{C\left[\omega_z\right]}{C\left[\omega_r\right]}\right)^4 \left(C\left[l_{\mathrm{px}}\right]C\left[\sigma_{\mathrm{A}}\right]\right)^2\\ C\left[L_3T^2\right] &= \frac{C\left[\omega_z\right]^8}{C\left[\omega_r\right]^4}\;C\left[l_{\mathrm{px}}\right]^6 C\left[\sigma_{\mathrm{A}}\right]^2.\end{aligned} \tag{5.7}$$

Finally, comparing Equations (5.7) and (5.6), we arrive at the remarkable property

$$\boxed{\left(C\left[\frac{P(\mu_z)}{\mu_z^2}\right]\right)^{-2} = C\left[L_3T^2\right].} \tag{5.8}$$

We will use the factor ξ which calibrates the relation between the pressure and the chemical potential and use it directly to calibrate the recombination constant times the temperature squared. In the experiment, we can measure the trap frequencies with great accuracy. This means that the calibration is likely related to the absorption cross section and the magnification factor of the imaging system. For unitary interactions the calibration can be applied to the L_3 versus T behavior. However,

away from the resonance, we will assume that the calibration comes from the number counting. This means that we will use the calibration in the recombination coefficient

$$L_3 = \xi^{-2} L_3^{\text{exp}}. \tag{5.9}$$

Here L_3^{exp} is taken to be the uncalibrated L_3 measurement.

Using the mean-field fit of $h(\nu)$ to the data in Figure 5.2, we find $\xi = 2.45(60)$. When the necessity of the calibration is only due to the number calibration this gives an extra 20 % uncertainty, arising on $L_3 T^2$ from the T^2 scaling with l_{px}^4.

Let us note here that for the unitarity measurements of L_3, in principle, we do not have to assume anything about where the error comes from, because the error is directly related to $L_3 T^2$. Which means that λ_3 can be directly given and corrected for each point. This also means that the fitted value of λ_3 will not change depending on where the error comes from. This reduces the error on λ_3.

5.1.5. Constant Temperature

In Section 3.2, we have seen that three-particle losses intrinsically heat the cloud (see Equation (3.9)). So in order to predict the dynamics, one would have to solve and fit the two coupled Equations (5.10) (number) and (3.9) (temperature). For this we would have to assume that the three-particle losses follow the model derived in Chapter 2. To avoid this assumption, we have experimentally kept the temperature constant[1], by allowing relatively small evaporative losses. These losses will add to the uncertainty of the result, but an estimation of the losses due to evaporation can be made based on the comparison of the amount of heat added per particle in a recombination event with the amount of heat taken away per particle in an evaporation event. Doing this reduces the systematical effects and allows us to measure the loss coefficient, while making relatively small model dependent assumptions, for more details we refer the reader to Section 3.3.1. Afterwards, we have also modeled the evaporation using the theory from Section 3.3.2.

5.1.6. Data Analysis

In Section 4.1.9, we have discussed how to obtain the temperature and number of a cloud from an absorption image. In Figure 5.3, these results have been plotted for different wait times t. In Figure 5.3a, the number of particles is plotted (blue

[1] we have also reproduced this in simulations (see Section 3.3.3)

dots) as a function of wait time and we see a clear decrease of atom number with time. In Figure 5.3b, the temperature is plotted as a function of wait time. The temperature is kept approximately constant with an increase in the temperature spread over time due to the difficulty of doing a fit to an image with a low number of particles. The red line corresponds to a fit of a constant to the temperature.

In Figure 5.3a, the theory that was fitted to the data (red line) is described by three-particle recombination losses under a quasi-thermal equilibrium. The change of particle number is given by

$$\frac{\dot{N}}{N} = -L_3(a, T)\langle n^2(t)\rangle.$$

The only other loss process present is induced by evaporative losses, which will

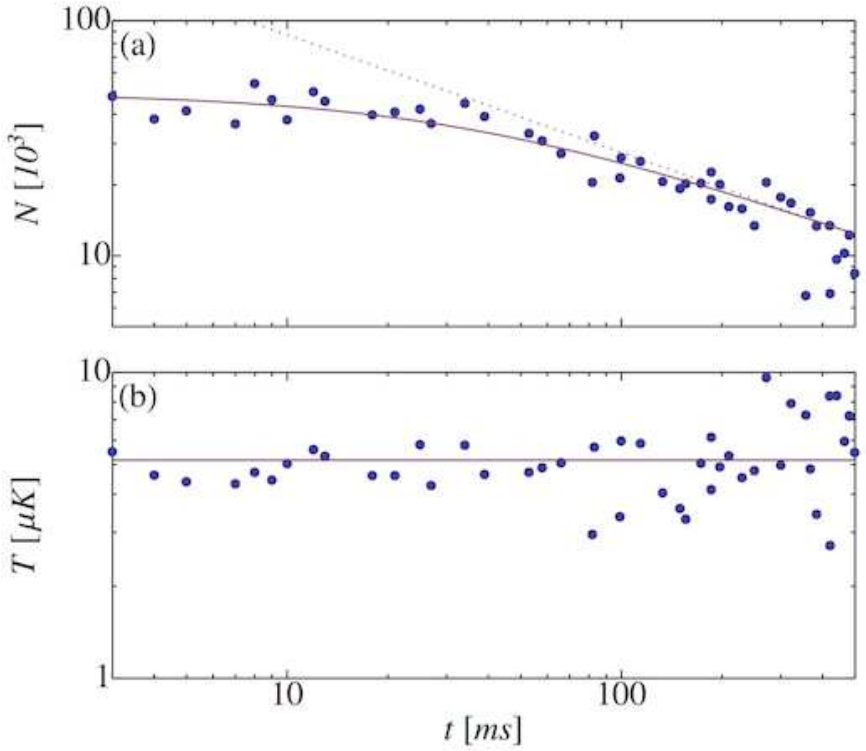

Figure 5.3.: Time-dependence of the atom number (a) and temperature (b) of a non-degenerate cloud at unitarity. The fitted temperature corresponds to $T = 5.2(4)$ μK, for potential $U = \eta k_B T$ with $\eta = 7.4$. The fitted $L_3^{\text{meas}} = 1.2(2)_{\text{stat}} \times 10^{-21}$ cm^{6}s^{-1}. The dotted line in (a) shows the long time $t^{-1/2}$ behavior of the number of atoms.

depend on the trap depth. In Section 3.2, we have both estimated and modeled these losses and we will take the corrections due to evaporation into account in Sections 5.2 and 5.3, respectively.

The fact that we use dilute non-degenerate gases further simplifies the problem in the sense that $\langle n^2 \rangle$ is proportional to N^2 and the geometrical effects are easily calculated. The differential equation for the losses becomes

$$\frac{\dot{N}}{N} = -A\ L_3(T)\ \frac{N^2}{T^3}, \tag{5.10}$$

where $A = (m\bar{\omega}^2/2\pi k_B)^3/\sqrt{27}$, with $\bar{\omega} = (\omega_r^2\omega_z)^{1/3}$, was introduced to include the temperature independent geometrical effects.

Keeping the temperature constant during the measurement allows us to simplify the Equation (5.10) and solve it exactly

$$\begin{aligned} \frac{\dot{N}}{N} &= -\tilde{A}\ L_3\ N^2, \\ \frac{N}{N_0} &= \left(2\ \tilde{A}\ L_3\ N_0^2\ t + 1\right)^{-1/2}, \\ &\underset{t\to\infty}{\propto} t^{-1/2} \end{aligned}$$

where we have introduced the constant $\tilde{A} = A/T^3$ and N_0 to be the total atom number at time $t = 0$. Fitting this to the data gives L_3^{exp} for a specific temperature T, the result of which is shown in Figure 5.3a (red line). In the limit of long waits times, the number decay scales as $t^{-1/2}$, which is shown in Figure 5.3a (red dotted line). We have included all the other fits in Appendix C.1.

Next, the calibration correction is applied to the measured L_3^{exp},

$$L_3^{\xi} = \xi^{-2} L_3^{\text{exp}}, \tag{5.9}$$

where ξ is the calibration factor obtained in Section 5.1.4.2.

Afterwards, we apply the correction due to evaporation effect (see Equation (3.15))

$$L_3 = L_3^{\xi}\left[\frac{1}{1+\frac{\delta(a,T)}{\eta+\kappa-3}}\right], \tag{3.15}$$

where η is the depth of the potential, κ the additional heat lost per evaporation event given by Equation (3.12) and $\delta(a,T)$ the excess heat in units of $k_B T$, given by Equation 3.8.

As an example the systematic overestimation of L_3, due to evaporation effects, for typical trap depths of $\eta = 6$ and $\eta = 8$ are 50% and 30%, respectively. Finally, we have a method to obtain L_3 for any value of the temperature T and scattering length a.

5.2. Results - Unitary Interactions

5.2.1. Temperature Dependence of L_3 at Unitarity

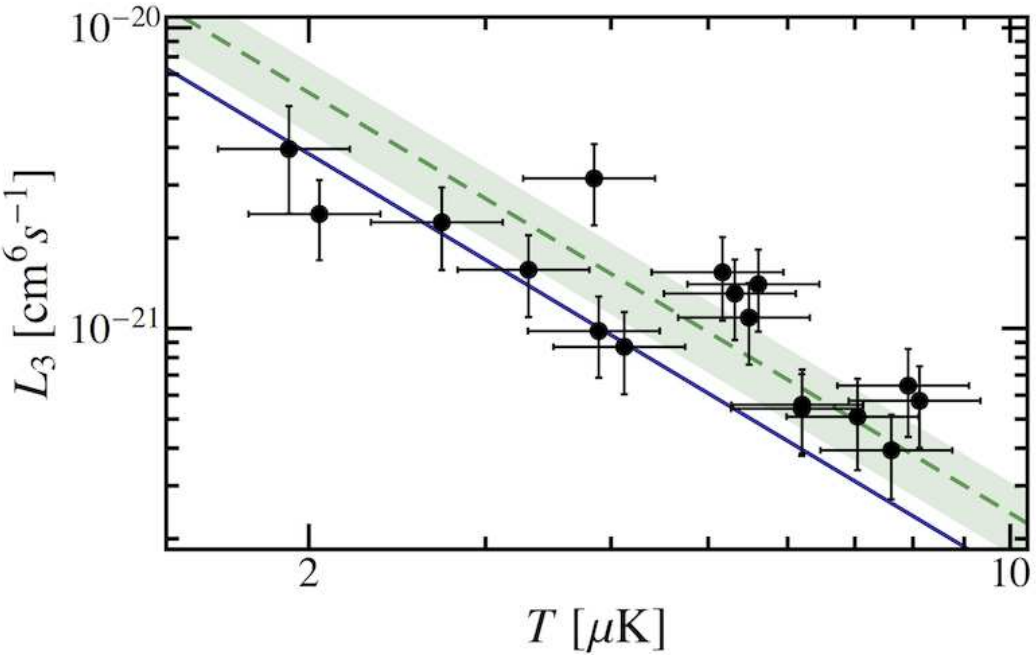

Figure 5.4.: The green dashed line shows a fit to the functional form $L_3(T) = \lambda_3/T^2$, with the experimentally determined value $\lambda_3 = 2.5(3)_{\text{stat}}(6)_{\text{syst}} \times 10^{-20}(\mu\text{K})^2\text{cm}^6\text{s}^{-1}$. The shaded green band shows the $1-\sigma$ uncertainty (which is given by a quadrature sum of both the statistical and systematical uncertainty). The solid blue line corresponds to the theory prediction of $\lambda_3 = 1.52 \times 10^{-20}(\mu\text{K})^2\text{cm}^6\text{s}^{-1}$, where we have taken $\eta_* = 0.21$ from [127, 128, 201].

In these first measurements the scattering length diverges ($a \to \infty$), while the temperature is varied. Then for each temperature we have done a loss measurement as shown in Figure 5.3. For each temperature T, we obtain the three-particle loss coefficient $L_3(T)$. This measured value is then corrected using the calibration

factor for L_3T^2 (see Section 5.1.4.2) and for evaporation (see Section 3.3.1). The result is plotted in Figure 5.4 (black dots with error bars).

The green dashed line is the result of a fit, on the logarithmic scale, of the data to the functional from $L_3(T) = \lambda_3/T^2$. The result is:
$\lambda_3 = 2.5(3)_{\text{stat}}(6)_{\text{syst}} \times 10^{-20}(\mu\text{K})^2\text{cm}^6\text{s}^{-1}$. We have taken into account both statistical errors, which are due to the fitting procedure of $N(t)$ (12 %) and systematic errors (due to finite-range corrections (14 %), trap-frequency (16 %) and uncertainty in the density profile fit (10 %), giving a total error of 25 %), due to uncertainty in the number calibration and temperature measurement. When we compare the measured result with the theory prediction $\lambda_3 = 1.52 \times 10^{-20}(\mu\text{K})^2\text{cm}^6\text{s}^{-1}$, we find that the theory is slightly outside the $1-\sigma$ confidence interval of the result of the fit. We consider this result, without any adjustable parameter and considering the difficulty of exact quantitative measurements of the loss coefficient, as satisfactory.

5.2.2. Reanalysis using the Advanced Evaporation Model

In the previous section, we have estimated the effects of evaporation by assuming that the heating due to three-particle losses is directly compensated by evaporation. This gives an estimate of the extra losses due to evaporation (see Section 5.1.6). However, we have also introduced a full heating and evaporation model (see Section 3.3.2). In the following, we will show the results of the fits using this model and compare that with our results that were obtained by estimating the evaporative losses.

Using the model from Section 3.3.2, we have refitted all the data points on both atom number and temperature change, with the only free parameter being the depth of the trapping potential. The full description of the procedure is discussed in [176]. The results of the fitting are presented in Figure 5.5, indicated by the black dots. These results are then fitted to the functional form $L_3(T) = \lambda_3/T^2$ with the result given by $\lambda_3 = 2.6 \times 10^{-20}(\mu\text{K})^2\text{cm}^6\text{s}^{-1}$. Comparing this to the result obtained by estimating the evaporative losses, $\lambda_3 = 2.5(3)_{\text{stat}}(6)_{\text{syst}} \times 10^{-20}(\mu\text{K})^2\text{cm}^6\text{s}^{-1}$, we find that both results agree within the error bars.

To calculate the spread of the loss coefficient, let us calculate $\lambda_3 = L_3(T)T^2$ for each point and then compute the mean value and standard deviation. The results from Section 5.2.1 have a mean value of $\langle\lambda_3\rangle = 2.7 \times 10^{-20}(\mu\text{K})^2\text{cm}^6\text{s}^{-1}$ and a standard deviation of $\sigma_{\lambda_3} = 1.21 \times 10^{-20}(\mu\text{K})^2\text{cm}^6\text{s}^{-1}$. The results from this section have a mean value of $\langle\lambda_3\rangle = 2.8 \times 10^{-20}(\mu\text{K})^2\text{cm}^6\text{s}^{-1}$ and a standard deviation of $\sigma_{\lambda_3} = 1.23 \times 10^{-20}(\mu\text{K})^2\text{cm}^6\text{s}^{-1}$. We find that both agree extremely

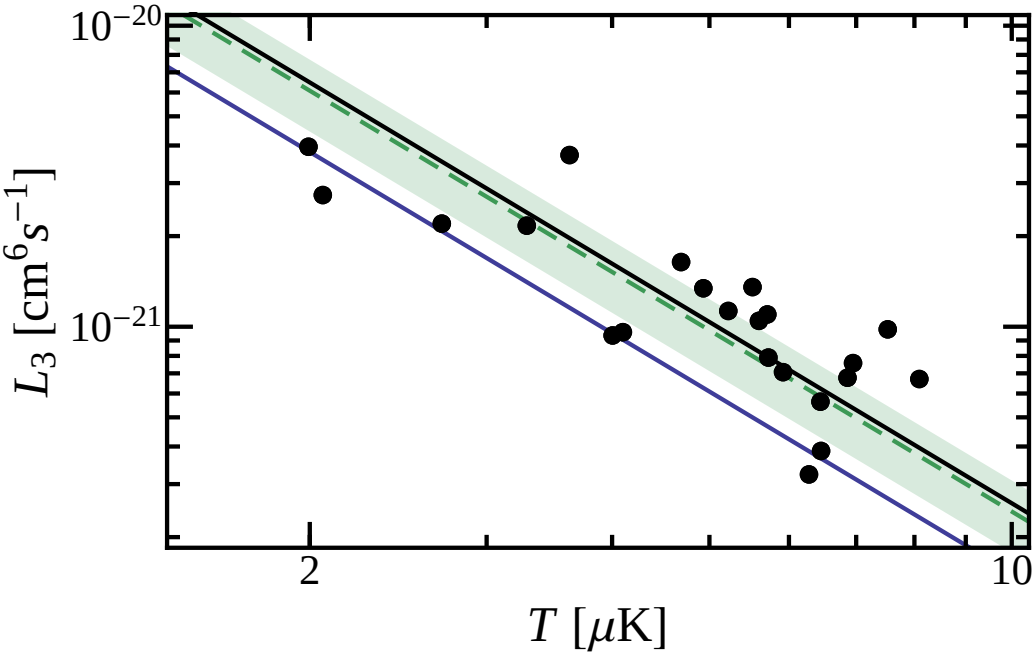

Figure 5.5.: The results of fitting with the full temperature model (see Section 3.3.2 and [176]). The results are given by the black dots and a fit to the data points is shown by the black line. A fit was done to the functional form $L_3(T) = \lambda_3/T^2$. The fitted value is $\lambda_3 = 2.6 \times 10^{-20}(\mu\text{K})^2\text{cm}^6\text{s}^{-1}$, which is in good agreement with the value obtained by estimating the evaporation effects, which is depicted by the green dashed line with error bars given by the shaded green area. The original result was $\lambda_3 = 2.5(3)_{\text{stat}}(6)_{\text{syst}} \times 10^{-20}(\mu\text{K})^2\text{cm}^6\text{s}^{-1}$. The solid blue line corresponds to the theory prediction of $\lambda_3 = 1.52 \times 10^{-20}(\mu\text{K})^2\text{cm}^6\text{s}^{-1}$, where we have taken $\eta_* = 0.21$ from [127, 128, 201].

well within error bars.

In the end, we can conclude that the estimation of the evaporative losses is justified and can also be used for the measurements performed away from resonance. In the intermediate regime $k|a| \approx 1$, the usage of this full model is complicated, because the scattering cross section in the intermediate regime is, to our knowledge, unknown. Therefore, we will rely on our estimation method in this interaction regime.

5.3. Results - Finite Interactions

5.3.1. Saturation of L_3 for Resonant Interactions

For these measurements, we have varied the scattering length a and kept the temperature T the same for each measurement of L_3. In Figure 5.6, the results of the measurements are shown. Each point corresponds to a measurement as depicted in Figure 5.3 and gives a point $\{a, L_3\}$. The result of the fits for all the points are given in Appendix C.2.

The red dashed line is the zero-temperature theory with the Efimov parameters from [201][2]. For weak interactions ($|a| \ll 1/k_{\text{th}}$), the zero-temperature is valid. However, when the scattering length becomes on the order of the thermal wavelength ($|a| \sim 1/k_{\text{th}}$) the data points deviate from zero-temperature $L_3(a)$. In the resonant interactions limit ($|a| \gg 1/k_{\text{th}}$), the data shows a maximum attainable value. This behavior is called saturation and it occurs when $|a| \gg 1/k_{\text{th}}$. The maximum value is given by $L_3(T)$, whose temperature dependence we have tested at unitarity in Section 5.2.

These are the two limiting cases of $L_3(a, T)$, however, the theory developed in Chapter 2 is smooth across the resonance and holds for the full negative-a side and in the regime $a \gg 1/k_{\text{th}}$ on the positive-a side. The result of the theory is shown by the blue solid line for a temperature of $T = 5.9$ μK and the Efimov parameters from [201]. The shaded blue area corresponds to the $1-\sigma$ temperature spread of the data points. As we can see there is a excellent agreement between theory and experiment, with no adjustable parameter.

There are some interesting features to be seen in the theory curve for $L_3(a, T)$. For weak-interactions the theory connects to the zero-temperature theory. Close to the point $a \approx -300$ a_0, there is a Efimov resonance, which shows a reduced loss

[2]Note that we used $\eta_* = 0.21$, which is the average value of η_* on the negative and positive side. Since we are interested in the saturation regime and there is a priori no difference in this regime between positive- or negative-a side we have taken the mean value.

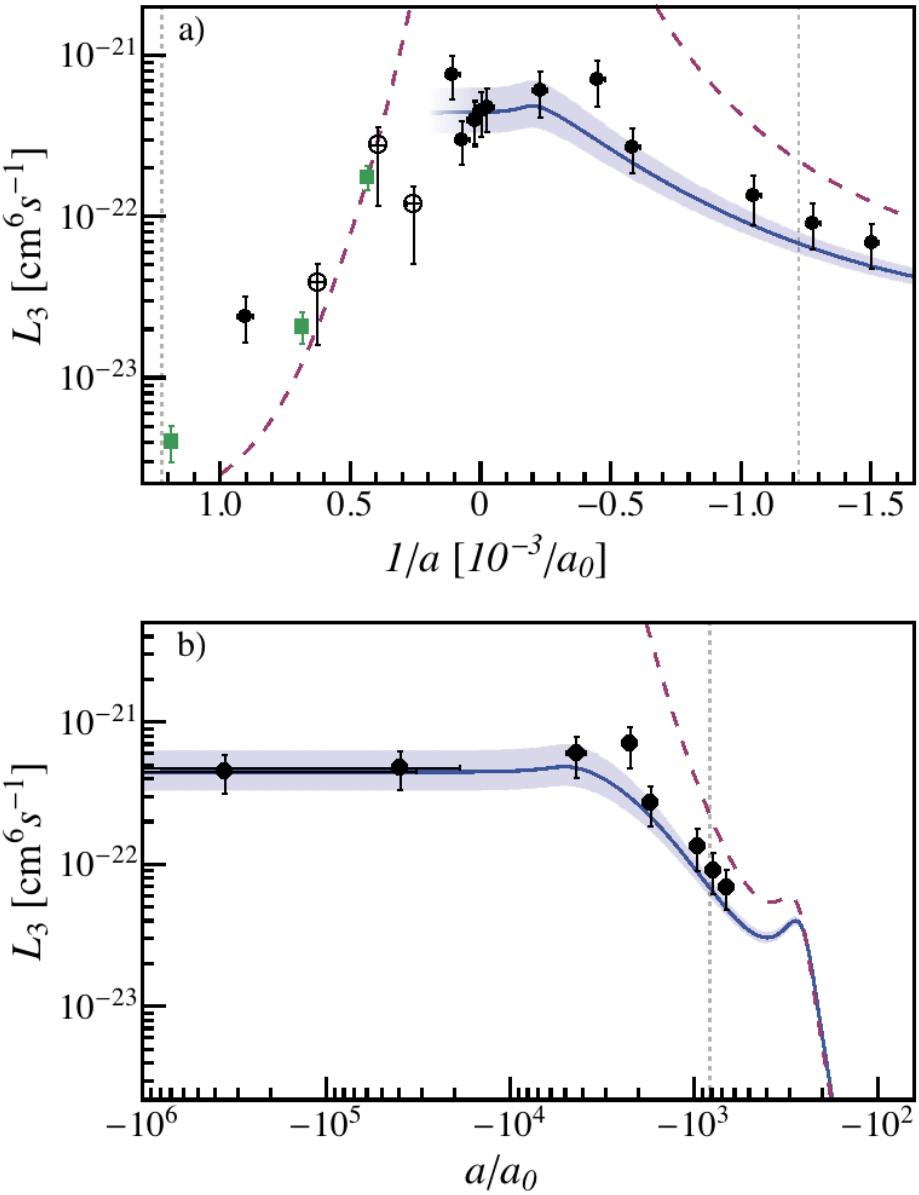

Figure 5.6.: a) ^{7}Li scattering-length dependence of the three-particle loss coefficient $L_3(a)$ for constant $T = 5.9(6)$ μK (filled and open circles). For small positive a, $L_3(a)$ for a low temperature condensate is also shown (green squares). The solid blue line corresponds to the theoretical prediction in Equation (2.38) for $T = 5.9$ μK. The blue shaded region is the same theory for 5.3 to 6.5 μK. The dashed lines show the zero-temperature prediction for $L_3(a)$ [168] fitted to the measurements in [127, 128, 201] with the parameters $\eta_* = 0.21$ and $a_- = -274\,a_0$. The vertical dotted lines correspond to $k_{\text{th}}|a| = 1$. The open circles in the range $1500\,a_0 < a < 5000\,a_0$ are not corrected for residual evaporation as our model is not applicable. b) Logarithmic plot of the $a < 0$ side, displaying the two Efimov loss resonances.

coefficient with respect to zero-temperature (saturation), even though $|a| < 1/k_{\text{th}}$. The first indication of a second Efimov resonance around $a \approx -5000\ a_0$ (the expected position is at $a_-^{(2)} = a_-^{(1)} e^{\pi/s_0} \approx -6218\ a_0$). Across the resonance, the $L_3(a, T)$ varies smoothly. On the positive-a side, for weak interactions, we used a BEC at zero-temperature (see green squares) to confirm the zero-temperature theory for $L_3(a)$ and we have also used thermal gases to show the smooth connection from unitary to weak interactions (black open circles).

The saturation behavior of the Efimov resonance brings us to the next section, where we will quantitatively describe the movement of the position of the Efimov resonance with temperature as was observed in ^{133}Cs.

5.3.2. Comparison with Previous Data - ^{133}Cs

In the following, we will look at some specific experiments done on Efimov resonances. We will compare the experimental results to the theory, described in Chapter 2, and see the effect of temperature on both the saturation of L_3 and the position of the Efimov resonances.

5.3.2.1. The First Efimov Resonance

The first direct evidence for a universal three-particle bound state was found in three-particle recombination losses in cold-atomic gases by a group in Innsbruck [122]. They used a Feshbach resonance to vary the interactions between the particles, and characterized the losses as a function of the scattering length a. Doing so revealed a clear resonance signature at $a = a_- = -872\ a_0$ [3]. The data from that paper is shown in Figure 5.7, for different temperatures. At that time, the same measurement was done for different temperatures, however, only a zero-temperature theory was available. The coldest data ($T = 10$ nK the blue points) was used to fit the theory and the following parameters were found (which is already taking into account the newly determined Feshbach resonance position [209]): $a_- = -872\ a_0$, and $\eta_* = 0.10$.

Furthermore, the higher temperature data, $T = 200$ nK and $T = 250$ nK (shown in Figure 5.7 by the red and yellow points respectively), was used to show the reduction of the loss coefficient (saturation), due to temperature, but no quantitative theory was available at that time. The saturation data was used to show the importance of having cold enough temperatures. We can now compare the data

[3] In [122] the Efimov resonance parameters were determined to be $a_- = -850 a_0$ and $\eta_* = 0.06$. We show the newer calibration from [129] using the parameters $a_- = -872 a_0$ and $\eta_* = 0.10$.

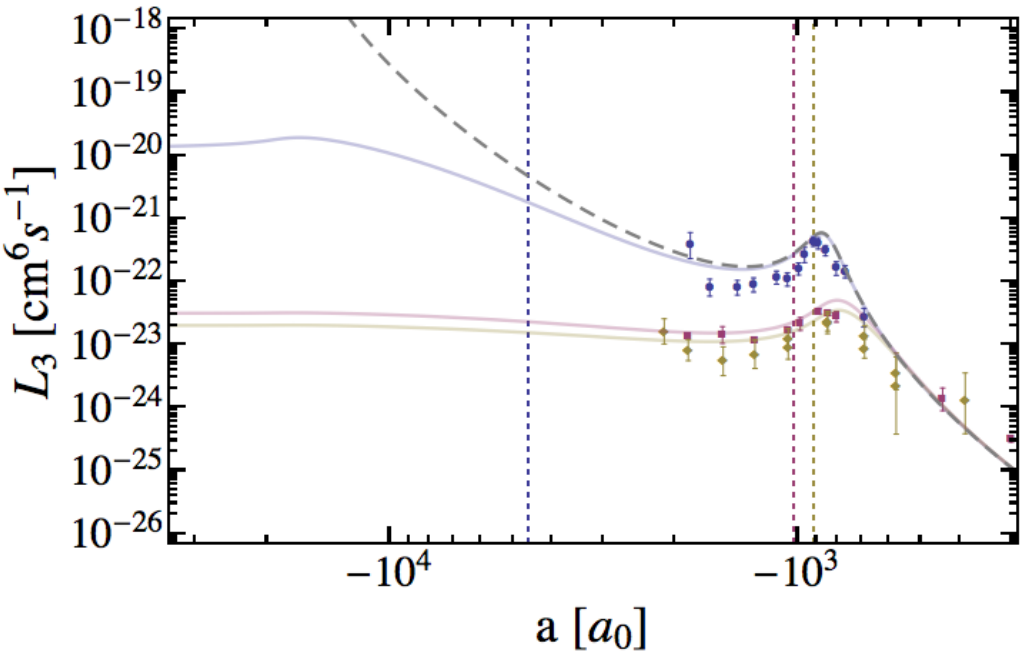

Figure 5.7.: $L_3(a, T)$ for three different temperatures taken from [122]. The different colors correspond to $L_3(a, T)$ for different temperatures, which are $T = 10$ nK (blue dots), $T = 200$ nK (red squares), and $T = 250$ nK (gold diamonds). The solid curves with corresponding color, are the theory curves for the respective temperatures. We have used the new calibration for $a_- = -872\ a_0$ and $\eta_* = 0.10$ [129]. The gray dashed line is the zero-temperature curve with the same parameters. The three vertical lines indicate the position of λ_{th} for the three temperatures. The values are: $\lambda_{\text{th}} = 4.6 \times 10^3\ a_0$ for $T = 10$ nK, $\lambda_{\text{th}} = 1.0 \times 10^3\ a_0$ for $T = 200$ nK, and $\lambda_{\text{th}} = 9.1 \times 10^2\ a_0$ for $T = 250$ nK.

to the theory in Equation (2.38), for $L_3(T, a)$ using the fit parameters from the $T = 10$ nK data and the resulting curves are plotted as solid lines in Figure 5.7. The light blue curve corresponds to the $T = 10$ nK data and one clearly sees an excellent agreement and also nearly no saturation of the Efimov resonance due to temperature. The light red curve corresponds to the theory for $T = 200$ nK and the light yellow curve to $T = 250$ nK. These curves show strong saturation of the Efimov resonances, due to temperature. However, the quantitative agreement, without any adjustable parameter, is excellent.

Next, let us use the theory from Chapter 2 to quantify a "cold enough temperature".

5.3.2.2. Resonance Position

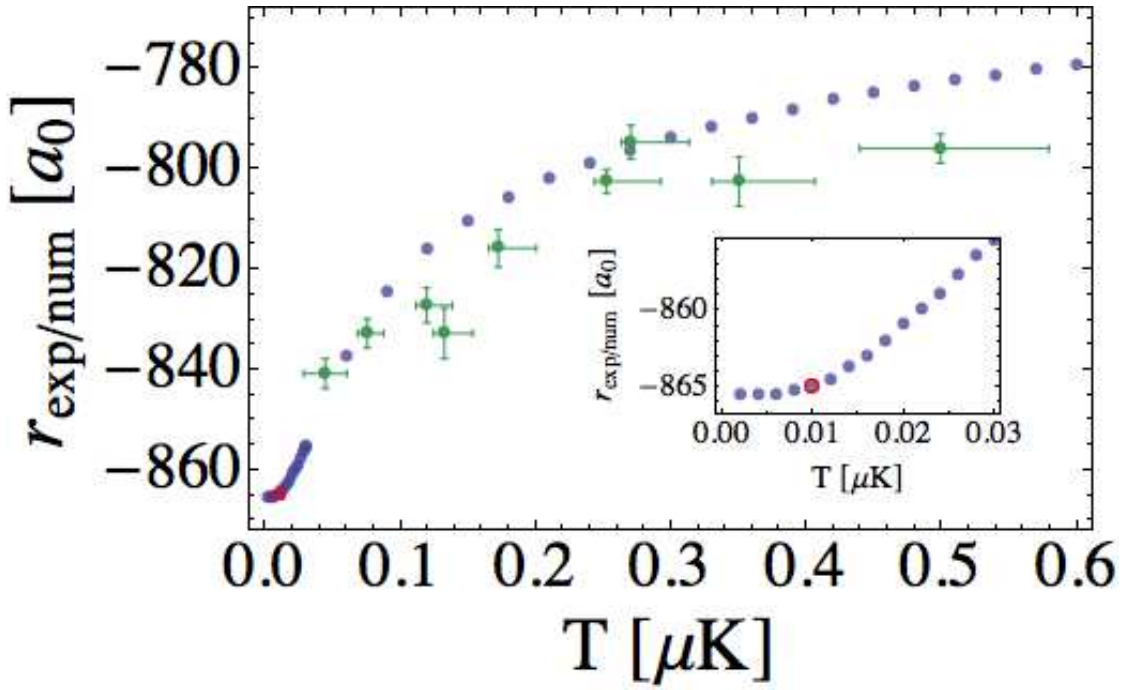

Figure 5.8.: The position of the Efimov resonance as a function of temperature for ^{133}Cs. The green dots correspond to the data from [203]. The red circle corresponds to the point that was used, for calibrating the experimental data and the numerical results. The parameters that were used for the numerical calculations are $a_- = -872\ a_0$ and $\eta_* = 0.10$. As can be seen the temperature behavior seems to be in good agreement. The inset shows the small T behavior and marks when the asymptotic zero-temperate regime is reached.

The authors of 5.7 have noted a temperature dependence of the Efimov resonance position, which was quantitatively studied in [203]. Using the theory from Chapter 2, we will quantitatively reproduce this dependence.

In Figure 5.8, we have plotted the position of the Efimov resonance determined experimentally in [203] (green dots, corrected using [209]) and compared that to the finite temperature theory. The resonance position is determined by numerically calculating the theory around the Efimov peak and then finding the local maximum. For the numerical calculations, we used the Efimov parameters: $a_- = -872\ a_0$ and $\eta_* = 0.10$. Let us call the experimentally found position of the Efimov resonance r_{exp} and the numerically calculated maximum r_{num}.

To given an example, let us look at the data for 10 nK from Figure 5.7. The

experimentally found maximum in that curve is at $r_{exp} = -896.7\ a_0$, whereas the numerically calculated value $r_{num} = -865\ a_0$. The difference between the two we will consider as a systematical effect due to the method of maxima finding and we will use this to shift the experimental data points for r_{exp}. The result of this is shown in Figure 5.8. The green dots are the values of r_{exp} for different temperatures and the blue dots are the numerically calculated points r_{num}. The red dot corresponds to the calibrating point at $T = 10$ nK, from the example above. The shift of these points is due to the slight saturation of the Efimov resonance, as can be seen in Figure 5.7. The shifting factor is 1.04, which corresponds to a magnetic field shift of 0.27 G.

The agreement is remarkable. The numerical resolution used to calculate the maxima is 1 a_0. In the inset the small temperature range was studied with a higher resolution of 0.25 a_0 to see the asymptotic behavior of the Efimov resonance position. The red circle corresponds to the 10 nK data in Figure 5.7. Here one clearly sees that the temperature at which the resonance was measured was sufficiently cold, with a calculated correction on a_- of less than 1 %. It is safe to assume that the fitted values correspond to the asymptotic zero-temperature parameters.

Refitting existing Efimov resonance data, using the theory for $L_3(a, T)$ from Chapter 2, will lead to improved values for both Efimov resonance position and width. This is interesting for future studies.

The thermal wavelength corresponding to 10 nK is around $1/k_{th} \simeq 4.6 \times 10^3\ a_0$, so it seems at least in the case of ^{133}Cs that with an $a_- = -872\ a_0$ and an $\eta_* = 0.06$ the saturation starts to already set in when $k_{th} a_- \simeq 0.19$. An interesting remark to make here is that for $a_- = -872\ a_0$ the highest point of the Efimov peak saturates when $T < 10$ nK at a value around $r_{num} = -860.5\ a_0$. This shift is probably due to the overall a^4 slope of the L_3 measurement.

Recently, a second Efimov peak on the negative-a side of the resonance in ^{133}Cs has been seen [126] and verified with the theory as presented in Chapter 2.

5.3.3. Temperature Behavior of L_3 - ^{39}K

In a recent work at Cambridge [172], the authors studied the stability of a non-degenerate resonant Bose gas of ^{39}K atoms. The measurements were done in a tight and deep trap, where evaporative losses could be neglected (trap parameters: geometric mean trap frequency $\omega = 2\pi \times 185$ Hz and trap depth $U \approx k_B \times 30\ \mu K$ with a temperature of 1 to 2 μK.). The Feshbach resonance that was used, is in the state $|F = 1, m_F = 1\rangle$ with $B_0 = 403.4(7)$ G and $\Delta \simeq 52$ G [210]. They have studied the behavior of three-particle losses and heating due to these losses on both

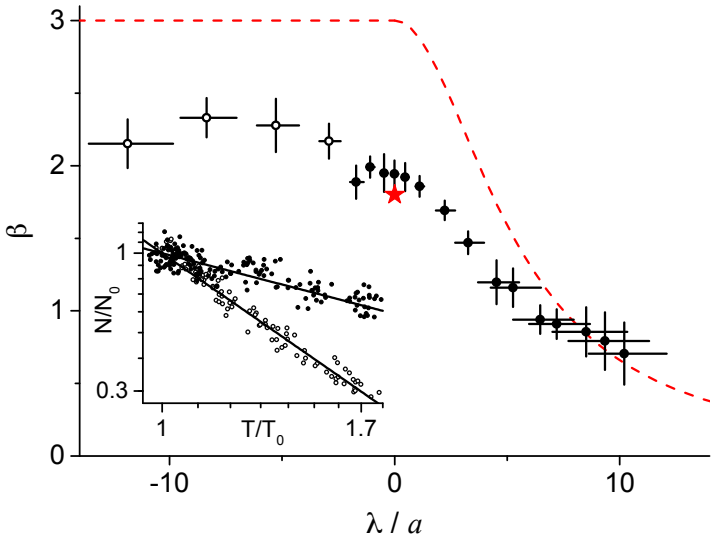

Figure 5.9.: The exponent β, as defined by Equation (5.11). The black dots and circles correspond to the measurement of the β, using N versus T curves of which two are depicted by the plot, on log scale, in the inset. We will limit ourselves to the negative side, for information about the positive side, see [172]. The red dashed line corresponds to the limit of $k|a| \to 0$. The red star is our prediction of $\beta = 9/5$ at the unitary value, see Equation (5.13). In the paper the thermal wavelength is $\lambda_{\text{th}} \approx 5 \times 10^3 a_0$, which is assumed to only vary weakly during the measurement and the horizontal error bars on the data points correspond to its variation.

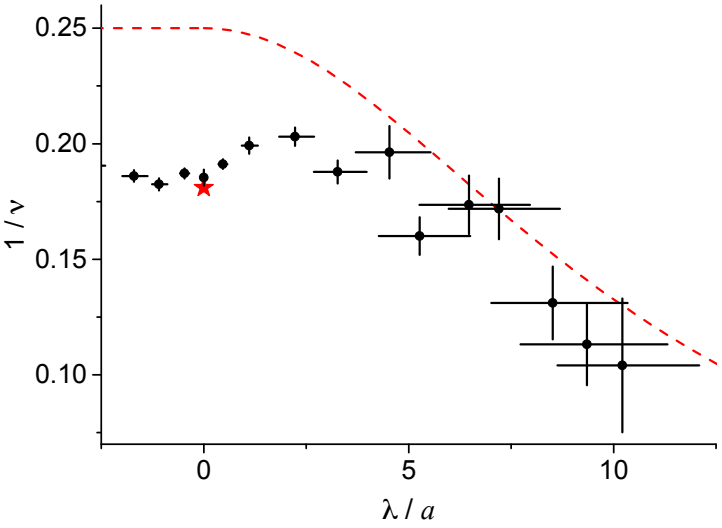

Figure 5.10.: The exponent ν, as defined by Equation (5.15), versus λ/a, which is a direct measure of the exponent of the N dependence. The black dots are the result of the fits of their data. If we just concentrate on the point $\lambda/a = 0$, see the red star indicating the theory prediction $\nu = 3 + 5/\beta$, taking the measured β. There is an excellent agreement between the theory prediction and the measured value.

sides of the Feshbach resonance. From these measurements, at unitarity, they were able to extract the temperature behavior of the three-particle loss coefficient.

In their measurements the main experimental observable is

$$\beta = -\frac{d\left[\ln(N)\right]}{d\left[\ln(T)\right]}, \tag{5.11}$$

which corresponds to the slope of a plot of N versus T on log-scale (see for example the inset of Figure 5.9). To compare this with our theory we look at the equation that describes the change of temperature in three-particle loss events (see Equation (3.9)),

$$\begin{aligned} \frac{\dot{T}}{T} &= \frac{d\left[\ln(T)\right]}{dt} = -\frac{\dot{N}}{N}\frac{1}{3}\left[\delta(a,T) + \frac{T_\mathrm{h}}{T}\right], \\ \frac{\dot{N}}{N} &= \frac{d\left[\ln(N)\right]}{dt}, \end{aligned} \tag{3.9}$$

where T_h is the ad hoc parameter to describe recombination heating due to the collisions of the recombination products with the rest of the cloud. Taking the ratio of both equations directly leads to an equation for β,

$$\beta = \frac{3}{\delta(a,T) + T_\mathrm{h}/T} \simeq \frac{3}{\delta(a,T)}. \tag{5.12}$$

In the paper, they are forced to make the assumption that there is no recombination heating T_h, which can be justified somewhat on the negative-a side, where there is no shallow dimer state. It needs to be noted that, since their trap is rather deep, there might still be some recombination heating effect, as was shown in [56] for caesium, due to deeply bound dimers colliding with the cloud before leaving the trap. Let us assume that they are small.

Equation (5.12) has the two limiting cases (see Equation 3.8)

$$\beta = \begin{cases} 3 & \text{if } k|a| \ll 1 \\ 9/5 & \text{if } k|a| \to \infty. \end{cases} \tag{5.13}$$

This means that β can be considered as a constant at unitarity and far away from the resonance. Then we expect a simple scaling law

$$NT^\beta = \text{const.} \tag{5.14}$$

It is relatively easy to see that this holds at unitarity, because in the case $|a| \to \infty$ a temperature increase only strengthens the $k|a| \to \infty$ requirement. The cloud will always be in the high-temperature limit $k|a| \to \infty$. In the cold temperature regime, the condition $k|a| \ll 1$ needs to stay valid when the temperature changes.

In Figure 5.9 the results of the measurements are shown. At resonance the red star depicts the prediction in Equation (5.13) of $\beta = 9/5 = 1.8$. The measured value $\beta = 1.94(9)$ is in excellent agreement with theory. Providing another strong test for the theory in Chapter 2, using a different system and a different experimental method.

5.3.3.1. Validating the $1/T^2$ Law for $L_3(T)$

The other observable in their experiments is ν (see Figure 5.10), which is defined by the equation describing the change of the atom number

$$\dot{N} = -C\ N^{\nu}, \tag{5.15}$$

where C is some constant that does not change during the decay.

Together with β, ν gives a direct measure of the temperature dependence of L_3. In order to see this, let us consider the equation describing the change of atom number during three-particle losses (see Equation (5.10)

$$\frac{\dot{N}}{N} = -A\ L_3(T)\ \frac{N^2}{T^3}. \tag{5.10}$$

In the limiting cases ($a \to 0$ and $a \to \infty$), the temperature behavior of $L_3(T)$ can be written as $L_3(T) = C/T^{\alpha}$, with C some constant and $\alpha = 0$ for $a \to 0$ or $\alpha = 2$ for $a \to \infty$.

Let us restrict ourselves to unitarity ($a \to \infty$). Assuming the validity of Equation (5.14) and ignoring the constants, we can write

$$\begin{aligned} \dot{N} &\propto -\frac{N^3}{T^{3+\alpha}}, \\ &\propto -N^{3+\frac{3+\alpha}{\beta}}, \end{aligned}$$

hence $\nu = 3 + \frac{3+\alpha}{\beta}$. When ν and β are directly measured this should give the value of α and hence test the $1/T^2$ prediction.

The measured values are $\beta = 1.94(9)$ and $\nu = 5.4(2)$, which gives the value $\alpha = 1.7(3)$. The result at unitarity is in excellent agreement without any adjustable

parameter. In the following, we will release the unitarity condition and study the negative-a side.

5.3.3.2. Excess Heat Measurements

Let us now restrict ourself to the negative-a side and compare that with the theory described in Chapter 2.

In the intermediate regime, with $a \simeq \lambda_{\mathrm{th}}$, the assumption for Equation (5.14) that $\beta = \text{const.}$ is not necessarily true, however empirically this seems to be true.

Let us, in the following, show that the scaling law in Equation (5.14) approximately holds even when β changes with temperature. The scaling law implies that the derivative of Equation (5.14) equals zero, so let us write this, using the log-derivative:

$$\begin{aligned} \frac{(N\dot{T}^{\beta})}{NT^{\beta}} &= \frac{\dot{N}}{N} + \beta\frac{\dot{T}}{T} + \dot{\beta}\ln T \\ &= \dot{\beta}\ln T \to 0. \end{aligned} \tag{5.16}$$

From this equation it becomes clear that, for the scaling law in Equation (5.14) to hold, $\dot{\beta}$ needs to vanish.

In Figure 5.11 the behavior of β while varying T for 1 to 2 μK is shown for different values of a around the Efimov resonance a_{-}. The parameters here are taken such that it mimics the experiments done in [172]. The results of Figure 5.11 are summarized in Figure 5.12. Here the mean value of β in the temperature range 1 to 2 μK is shown (blue dots). The bars around the mean value indicate the minimum and maximum value of β in this temperature range. As expected for $a \to 0$, $\beta = 3$ and does not vary, which is also true for the other limit $a \to \infty$, for which $\beta = 9/5$.

The numerically calculated trajectory with the biggest change of β, has a β that changes from 2.5 to 2.9. The change of β (indicated by the bars around the blue dots) is biggest in the region $|a| \sim 1/k_{\mathrm{th}}$. The result of the numerical analysis is compared to the measured data from [172] (purple dots). The theory seems to be in good agreement with the data.

However, there are situations where β varies considerably. In Figure 5.13 the temperature varies from 1 to 10 μK and it shows large changes of β, which violates the condition in Equation (5.16).

In conclusion, the numerical results show that the variation of β for a temperature variation of 1 to 2 μK is small compared to the experimental error bars.

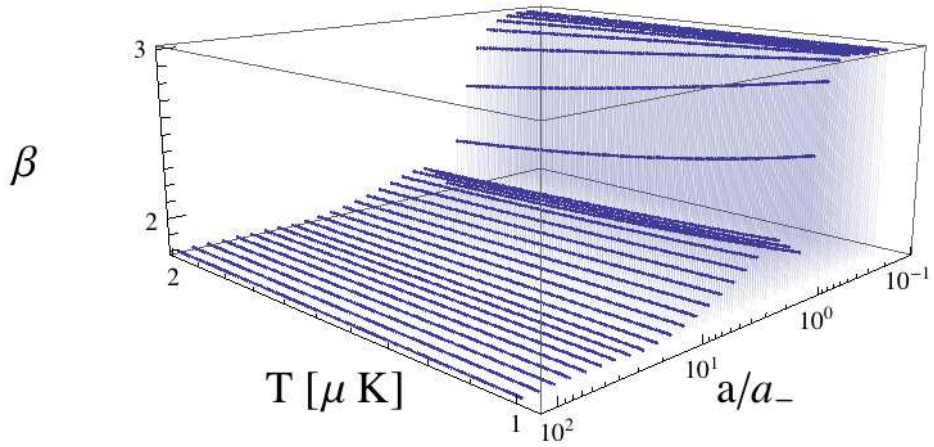

Figure 5.11.: The slope β as given by Equation (5.12). The blue lines are the values for $\beta(a, T)$, for a heating event from 1 to 2 μK, and a specific value of the scattering length a. The a_- indicates the position of the Efimov resonance. The Efimov resonance parameters used are: $a_- = -690 a_0$ [130] and $\eta_* = 0.09$ [172].

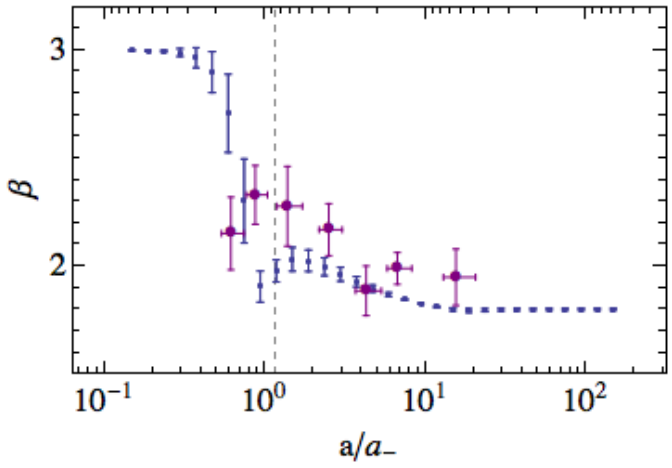

(a)

Figure 5.12.: The average value of β for the temperature range 1 to 2 μK from [172] (blue dots). Using the Efimov parameters $a_- = -690\ a_0$ [130] and $\eta_* = 0.09$ [172]. The bars correspond to the change of β in the 1 to 2 μK range of temperature, as depicted in Figure 5.11. The purple dots are the data from [172]. The minimum at $a/a_- = 1$ is due to the Efimov resonance. The increase of β from 1.8 to 3 happens in the range where $|a| \sim 1/k_{\text{th}} \approx 8 \times 10^2\ a_0$ (see gray dashed line).

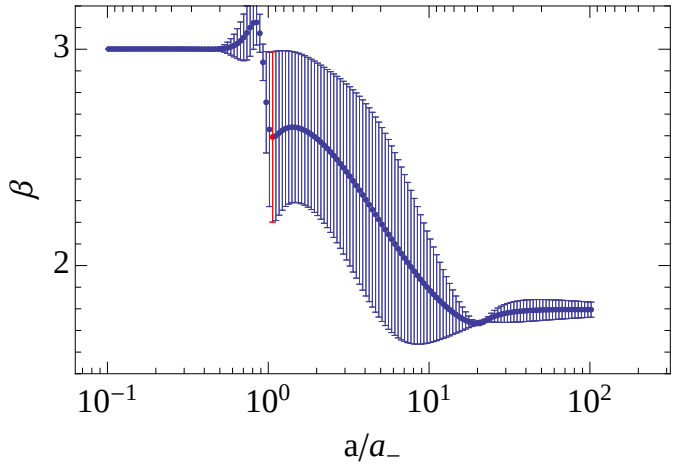

Figure 5.13.: Based on Figure 5.12a, but for a temperature range of 1 to 10 μK. The red point corresponds to the maximum change of β and it changes from 2.3 to 3, which is a change of 23%.

This validates the usage of the scaling law in Equation (5.14). For larger temperature changes β changes considerably and the condition $\dot{\beta} = 0$, coming from Equation (5.16), is violated. Hence, the scaling law in Equation (5.14) is valid for the measurements in [172], however, this is not generally the case.

Finally, let us note that in the paper the authors claim that, in the negative-a range, four-particle losses were seen. As a next step, it is interesting to use the knowledge of the three-particle loss theory to extract a more accurate measure of four-particle losses.

5.4. Summary

This chapter is dedicated to the saturation of three-particle losses in a finite temperature system near a Feshbach resonance.

We have shown measurements for two specific scattering cases.

- **Unitary interactions:**
  - We have shown that there is good agreement between the theory prediction of $L_3 \propto 1/T^2$ and the measurements.
  - A full analysis of the losses using simulations for the evaporative losses was used to determine the three-particle loss coefficient.

- **Finite interactions:**
  - The three-particle recombination shows that for resonant interactions the three-particle loss coefficient saturates to it unitarity limited value $L_3(T)$.
  - We have used the theory from Chapter 2 to explain temperature saturation effects of three-particle loss coefficient L_3 as measured in [122].
  - We have used the theory from Chapter 2 to explain the shift of a Efimov resonance due to temperature as measured in [203].
  - We have compared our theory with N versus T measurements done in [172] and concluded that the measurements are in good agreement with the theory.

In Appendix D, we discuss the saturation effects seen by other experiments.

Concluding remarks

This work was dedicated to the theoretical and experimental study of the lifetime of the Bose gas with resonant interactions in the non-degenerate regime. We started by recalling two-particle scattering and extended it to three-particle scattering. The richness of the three-particle scattering exhibits itself not only in Efimov trimer bound states, but also in three-particle recombination. In the limit of weak interactions and zero-temperature, varying the scattering length a revealed three-particle loss resonances, which marked the first direct observation of Efimov physics. However, in the strongly interacting limit, no quantitative prediction nor quantitative experimental study was dedicated to three-particle losses.

In this thesis, we have performed the first quantitative comparison between theory and experiment as a function of both scattering length a and temperature T for the three-particle loss coefficient $L_3(a,T)$. We have discussed the theoretical derivation of $L_3(a,T)$, which is given by

$$\boxed{L_3(a,T) = L_3^{\max}(T)\left(1-e^{-4\eta_*}\right)\frac{2}{k_{\text{th}}^2}\int_0^\infty \frac{(1-|s_{11}|^2)ke^{-k^2/k_{\text{th}}^2}}{|1-e^{-2\eta_*}(kR_{\text{t}})^{-2is_0}s_{11}|^2}dk,} \tag{2.38}$$

$$L_3^{\max}(T) = 36\sqrt{3}\pi^2\frac{\hbar^5}{m^3}\frac{1}{(k_{\text{B}}T)^2}. \tag{2.39}$$

This formula accommodates some interesting properties.

The unitarity limited value $L_3^{\max}(T)$ is proportional to $\propto 1/T^2(1-e^{-4\eta_*})$ and we have directly measured this behavior using a non-degenerate gas of ^{7}Li atoms. For the quantitative prediction of the temperature behavior we used $L_3(T) = \lambda_3/T^2$. The experimentally measured value of $\lambda_3 = 2.5(3)_{\text{stat}}(6)_{\text{syst}} \times 10^{-20}(\mu\text{K})^2\text{cm}^6\text{s}^{-1}$ is, without any adjustable parameter, in good agreement with the theory prediction $\lambda_3^{\text{th}} = 1.52\times 10^{-20}(\mu\text{K})^2\text{cm}^6\text{s}^{-1}$. We have used a special trapping situation in which the temperature was kept constant in order to test the $1/T^2$ law.

Furthermore, we extended our measurements to arbitrary values of the scattering length a. In the weakly interacting limit, we recover the zero-temperature prediction $L_3(a)$. In the strongly interacting limit, we observed saturation of three-particle recombination to the unitarity limited $L_3(T)$. These limiting cases are

smoothly connected in the range $|a| \sim 1/k_{\text{th}}$. A measurement of the loss coefficient at $T = 6\ \mu$K for varying scattering length a tested the prediction and excellent quantitative agreement between the theory prediction and experimental measurements was found. Furthermore, for weak interactions we have experimentally verified the zero-temperature model with non-degenerate gases on both sides of the resonance and with BECs, on the positive-a side.

Apart from the comparison of the theory with measurements obtained by our group, we also compared it with measurements done by other groups. Highlighting two interesting results from Innsbruck and Cambridge, we used the theory to show the observed temperature dependence of three-particle losses. In Innsbruck, the effects of the temperature on the first Efimov resonance position on the negative-a side in ^{133}Cs were measured, but never quantitatively explained. The theory enabled us to explain the observed temperature dependence on the resonance position.

In Cambridge, an independent quantitative test of the temperature behavior of $L_3(T)$ was performed with ^{39}K and they found the theory to be in remarkable agreement with the experiment. Furthermore, the heating per loss event was directly measured for different values of the scattering length. We demonstrated that on the negative-a side of the resonance, these measurements are in good agreement with the theory.

Overall, the theory in Chapter 2 is found to be in good agreement with experiment, both according to measurements done at the ENS and elsewhere. These lifetime measurements open up the possibility to explore new regimes in the quest for the unitary Bose gas. Let us finish by reconsidering Figure 5.1. The theory that we explained in Chapter 2 is valid in the green region. The zero-temperature theory is valid close to the x-axis and far away from the strongly interacting region ($k|a| \to 0$). The open question remains, what happens in the strongly interacting zero-temperature "unstable" region.

Perspectives

The Lithium experiment at ENS

With the results discussed in this thesis in hand, the next step would be to try to measure the corrections to the equation of state of an ideal gas due to resonant interactions. In the introduction, we have already shown the virial expansion of the

pressure P ($\beta \equiv 1/(k_B T)$)

$$P = \frac{1}{\beta \lambda_{\mathrm{th}}^3} \sum_{k=1}^{\infty} \tilde{b}_k e^{k\beta\mu},$$

where $\tilde{b}_k$ is the k-th virial coefficient described by the k-particle problem. An interesting direction of research would be to measure the 2nd and 3rd virial coefficients using the pressure measurement technique [87, 95]. Preliminary results have been discussed in [211]. The result $\tilde{b}_2 = 1.8(2.7)$ therein agrees, within error bars, with both $\tilde{b}_2 = 0$ and the theoretical prediction of $\tilde{b}_2 = 9\sqrt{2}/8 \approx 1.59$ [98], so the error bar has to be reduced to get a significant measurement of $\tilde{b}_2$ and $\tilde{b}_3$. During the writing of this thesis, a theoretical study on calculating the influence of the three-particle losses on both the coefficients $\tilde{b}_2$ and $\tilde{b}_3$ was started [176].

In the theory curve for $T = 6\ \mu$K, a second Efimov resonance starts to be visible. Hence, another possible direction would be the study of the second Efimov resonance at the negative-a side, which should be observable for a temperature around $T \simeq 1\ \mu$K, in ^{7}Li. It would then be interesting to see if the universal Efimov scaling ($a_-^{(n)} = (22.7)^n a_-$) is valid for lithium. Preliminary results on the second Efimov resonance in ^{133}Cs have been presented [126].

General Trends in the Study of Unitary Bose gases

After our publication [143], the interest in the unitary Bose gas steadily increased. Several theoretical papers predicted equilibrium properties of the unitary Bose gas [112, 212]. Notably, in [213] the authors used Quantum Monte Carlo simulations to predict the existence of a first-order Quantum Phase Transition (QPT) to a superfluid Efimov liquid, however a stable system with unitary two-particle interactions is required to explore this phase. On the experimental side of research, there were the excess heat measurements [172] in ^{39}K (which were discussed in Chapter 5), showing interesting properties (the Efimov parameter $\eta_* = 0.09(4)$ being small) for studying equilibrium effects. In combination with a flat box potential [17], in which BEC occurs without condensation in position space [18], this system might be favorable to study the onset of degeneracy in unitary Bose gases. In this experiment it would also be interesting to use the theory of Chapter 2 to fix L_3 and extract a more accurate value of the four-particle loss coefficient L_4. It would be also interesting to study Efimov physics in heteronuclear systems with either comparable masses like ^{6}Li-^{7}Li or very different masses ^{6}Li-^{133}Cs.

In recent experiments at JILA [214], the interactions in an ultracold BEC of ^{85}Rb

were quenched to resonance. At resonance, the density in momentum space $n(k)$ was measured as a function of time. In an equilibrium situation, the high-k tail of the distribution is proportional to $1/k^4$ [110, 215, 216]. This high momentum tail is associated with Tan's two-particle contact, which is a thermodynamic measure of two-particle correlations. The results of the measurements on the unitary Bose gas show a build up of this high momentum tail on a shorter timescale than the timescale of the losses [214].

The question, whether the unitary Bose gas exists and can be made stable, remains. In all the situations studied so far, the three-particle losses are the limiting factor. Could there be a more favorable situation, in an atom with a very small η_*? To our knowledge, the smallest measured η_* has a numerical value of $\eta_* \approx 0.057(2)$ in ^{85}Rb [96]. Are there interesting elements that have Feshbach resonances with an even smaller η_*? For example Erbium, which seems to exhibit a rich structure of Feshbach resonances [217]. A different approach would be to try and use narrow ($s_{\mathrm{res}} \ll 1$) Feshbach resonances, which are expected to have reduced losses [131]. Finally, there might also be the possibility of artificially engineering η_*, with ideas similar to the blue shielding technique. This technique has so far been used to avoid inelastic collisions [218]. The populations of different deeply-bound dimer states after three-particle recombination were measured. The result of this study is that many molecular states are occupied after inelastic three-particle scattering [175].

Finally, to get back to the experiment at the ENS, mixtures of ^{6}Li and ^{7}Li also offer interesting possibilities, because there are some candidates for overlapping Feshbach resonances in both isotopes. A possible situation would be to use the resonance in the mixture $|1\rangle - |2\rangle$ (with $B_0 = 832.18(8)$ G) of ^{6}Li and the resonance in the state $|2\rangle$ (with $B_0 = 893.95(5)$ G) in ^{7}Li. In this situation, the possibility of creating a mixture of strongly interacting degenerate Fermi gases in combination with an interacting Bose gas opens up. This mixture can, for example, be used to simulate QCD [219]. Another interesting possibility would be the use of the Bose gas to create a homogeneous potential for a unitary Fermi gas [220], which is based on a study of mixed Bose gases [221].

Acknowledgements

This work is the result of a team effort and it would have not been possible without the devotion an hard work of every single member. I would like to thank everyone that was directly or indirectly involved in this project. I would like to specifically mention the following:

- Let me start with Christophe Salomon and Frédéric Chevy, who have given me the opportunity to work in such an inspiring environment. Christophe is a perfectionist. I really appreciate his eye for detail, his optimism and his never ending energy. Fred never ceased to astonish me with his experimental and theoretical knowledge making him a great source of inspiration. Together, Christophe and Frédéric have had a great influence on my understanding of physics and research and I would like to thank them for everything they did.

- After working closely together on an experiment for three years you know A LOT about your collegues. I am really pleased to have worked this intensively with both Andrew Grier and Igor Ferrier-Barbut. Andrew has been such an inspiring colleague and I am still amazed he made the French national Lacrosse team!!! Igor is a really strong experimentalist and while discussing with him we always found the best (middle) way to solve our experimental problems (although shouting "allez petit!" still worked best). I thank Ulrich Eismann for all the stimulating discussions. The new generation is already up to speed on the experiment and I thank them for the new input they brought and wish Marion Delehaye and Sébastien Laurent good luck on this very special experiment.

- When I arrived in the lithium group, Nir Navon and Kenneth Günter (Dude!) introduced me to the experiment and especially Nir has helped me a lot in understanding and mastering all the subtleties of the experiment. I am really happy to have worked with these two excellent scientists.

- I thank Tim Langen, who joined the group as a visitor for a couple of months. Lev Khaykovich, who joined as a visiting professor for a year in Paris, was an

infinite source of information about three-body losses and I thank him for our many fruitful discussions.

- During my studies in Amsterdam, Gora Shlyapnikov has introduced me to the subject of superfluidity. His courses were extremely challenging and triggered my interest in the subject. He invited me to Paris to talk with several experimental groups in and around Paris. Furthermore, he inspired our efforts to find a stable unitary Bose gas. I am really grateful to Gora for all of his support.

- The theory guys Dima Petrov and Felix Werner have been so dedicated to understanding three-body losses and to providing such a beautiful theory. Let me especially thank Felix for checking every single step and assumption we have made in our experiment as well as having the enormous patience to explain to me every small detail of the theory.

- The external jury members Zoran Hadzibabic, Philippe Lecheminant, Rudi Grimm, Klaus Sengstock and Roland Combescot have created an inspiring atmosphere for discussion during and after the defense and I am thankful to them for making this possible.

- Let me thank the people from the other cold atom groups at the LKB: Jean, Rémi, Tarik, Laura, Laurianne, Katharina, Christof, David, Tom, Franz(le), Norman (Norbert), Diogo, Penn, Mikhail, Vincent, Tilman, David, Fabrice, Jerome, Sylvain, Davide, Bruno, Theo, Matthias (Jonguh!), Alexandre, Daniel. Thank you all for creating such a stimulating research atmosphere.

- Furthermore, let me thank all the people from the administration, atelier mécanique, service électronique, service informatique. Merci beaucoup!

- I would also like to thank Robert Smith, Zoran Hadzibabic, Rudi Grimm, Lev Khaykovich, Philip Makotyn, Sanjukta Roy, Paul Dyke and Randy Hulet for kindly providing me their data.

Apart from my colleagues, I would like to also thank family and friends, who have helped me through the last three years, who are always there to support me.

- My flatmates, with whom I've spend so many nice evenings and weekends enjoying inspiring discussions: Lynn & Ralf, Sara & Will, Jasper. Thanks!

- Katinka, Agaath, Ulli & René, Linda & Uli, Farina, Natas, Kim & Charlotte, Bob, Bea, Rogier, Judith, Kasper, Siri, Floor, Jeroen, Kilian, Anna, Steffen, Claudia. Dankjewel! Vielen Dank! Thanks!
- My mom and dad, who have always been there for me no matter how difficult the challenge. I am really grateful for all the opportunities you have given me.
- And of course Lana. It is really remarkable how you have been able to help me through such a stressful period. Dankjewel!

Thank you for reading this thesis!

A. Technical Details - Theory

A.1. Jacobian and Hyperspherical Coordinates

A.1.1. Jacobian Coordinates

For three-particle with positions $\boldsymbol{r}_1$, $\boldsymbol{r}_2$ and $\boldsymbol{r}_3$ the center of mass and relative motion can be separated. The center of mass motion is described by the vector $\boldsymbol{C}$

$$\boldsymbol{C} = \tfrac{1}{3}\left(\boldsymbol{r}_1 + \boldsymbol{r}_2 + \boldsymbol{r}_3\right).$$

The relative motion of the particles is described by the Jacobian coordinates,

$$\begin{aligned} \boldsymbol{r}_{ij} &= \boldsymbol{r}_i - \boldsymbol{r}_j \\ \rho_k &= \tfrac{2}{\sqrt{3}}\left(\boldsymbol{r}_k - \frac{\boldsymbol{r}_i + \boldsymbol{r}_j}{2}\right). \end{aligned}$$

In Figure A.1, the different permutations of the Jacobi coordinates for the three-particle problem are shown. All the information about the relative motion in this system is given by the two distances r_{ij} and ρ_k and the four angles given by $\hat{\boldsymbol{r}}_{ij}$ and $\hat{\boldsymbol{\rho}}_k$.

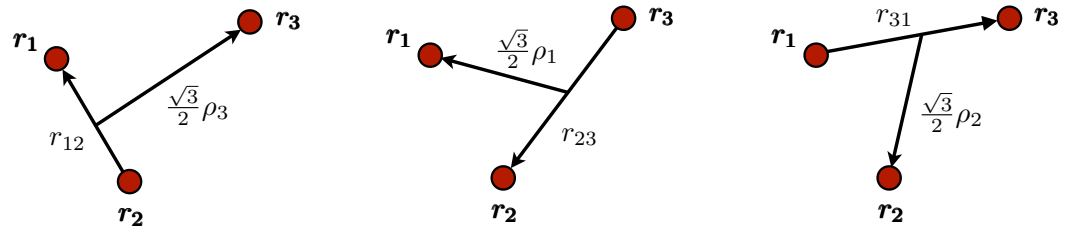

(a) Jacobi coordinates 1 **(b)** Jacobi coordinates 2 **(c)** Jacobi coordinates 3

Figure A.1.: The three Jacobi coordinate systems used for the permutations of the three-particle problem. The coordinate vectors are defined by the cyclic permutations the vectors $\boldsymbol{r}_{ij} = \boldsymbol{r}_i - \boldsymbol{r}_j$ and $\rho_k = \frac{2}{\sqrt{3}}\left(\boldsymbol{r}_k - \frac{\boldsymbol{r}_i + \boldsymbol{r}_j}{2}\right)$.

The position transformation matrix is given by

$$\begin{pmatrix} \boldsymbol{C} \\ \boldsymbol{r}_{ij} \\ \boldsymbol{\rho}_k \end{pmatrix} = \underbrace{\begin{pmatrix} \frac{1}{3} & \frac{1}{3} & \frac{1}{3} \\ 1 & -1 & 0 \\ -\frac{1}{\sqrt{3}} & -\frac{1}{\sqrt{3}} & \frac{2}{\sqrt{3}} \end{pmatrix}}_{\mathcal{M}} . \begin{pmatrix} \boldsymbol{r}_i \\ \boldsymbol{r}_j \\ \boldsymbol{r}_k \end{pmatrix},$$

with the Jacobian given by $\det(\mathcal{M}) = -\frac{2}{\sqrt{3}}$. The three-particle vector for the relative motion is given by

$$\boldsymbol{R} = \tfrac{1}{\sqrt{2}} \{\boldsymbol{r}_{ij}, \boldsymbol{\rho}_k\} = \left\{ \tfrac{1}{\sqrt{2}} r_{ij}, \tfrac{1}{\sqrt{2}} \rho_k, \hat{\boldsymbol{r}}_{ij}, \hat{\boldsymbol{\rho}}_k \right\}$$

The result can be used to define the momentum operators of the three-particle system. Let us define the momentum operator for the center of mass motion $\boldsymbol{P} \equiv -i\hbar\boldsymbol{\nabla}_{\boldsymbol{C}}$ and the Jacobi momenta $\boldsymbol{\Pi}_{\boldsymbol{r}_{ij}} \equiv -i\hbar\boldsymbol{\nabla}_{\boldsymbol{r}_{ij}}$ and $\boldsymbol{\Pi}_{\boldsymbol{\rho}_k} \equiv -i\hbar\boldsymbol{\nabla}_{\boldsymbol{\rho}_k}$. The transformation from the momenta of the three-particle $\boldsymbol{p}_1$, $\boldsymbol{p}_2$ and $\boldsymbol{p}_3$ can be transformed to the center of mass and relative momenta using

$$\boldsymbol{p} \equiv \begin{pmatrix} \boldsymbol{p}_i \\ \boldsymbol{p}_j \\ \boldsymbol{p}_k \end{pmatrix} = \mathcal{M}^{\top} . \begin{pmatrix} \boldsymbol{P} \\ \boldsymbol{\Pi}_{\boldsymbol{r}_{ij}} \\ \boldsymbol{\Pi}_{\boldsymbol{\rho}_k} \end{pmatrix}.$$

The matrix above allows us to directly write the kinetic energy operator

$$T = \frac{p_1^2 + p_2^2 + p_3^2}{2m} = \underbrace{\frac{P^2}{2(3m)}}_{T_{\text{com}}} + \underbrace{\frac{\Pi_{\boldsymbol{r}_{ij}}^2 + \Pi_{\boldsymbol{\rho}_k}^2}{m}}_{T_{\text{rel}}}.$$

The relative motion of the system is given by the kinetic energy operator T_{rel} and the interaction potential $V(r_{ij}, \rho_k)$ in the for of the Hamiltonian of the relative motion

$$\begin{aligned} H_{\text{rel}} &= \frac{\Pi_{\boldsymbol{r}_{ij}}^2 + \Pi_{\boldsymbol{\rho}_k}^2}{m} + V(r_{ij}, \rho_k), \\ &= -\tfrac{\hbar^2}{m} \left(\boldsymbol{\Delta}_{\boldsymbol{r}_{ij}} + \boldsymbol{\Delta}_{\boldsymbol{\rho}_k} \right) + V(r_{ij}, \rho_k). \end{aligned}$$

As in the case of the two-particle Hamiltonian, the radial and angular motion in

both $\boldsymbol{r}_{ij}$ and $\boldsymbol{\rho}_k$ can be separated

$$H_{\text{rel}} = -\frac{1}{m}\left(p^2_{r_{ij}} + \frac{\boldsymbol{L}_{r_{ij}}}{r^2_{ij}} + p^2_{\boldsymbol{\rho}_k} + \frac{\boldsymbol{L}_{\boldsymbol{\rho}_k}}{\rho^2_k}\right) + V(r_{ij}, \rho_k), \tag{A.1}$$

where $p^2_x = \left(\frac{\partial^2}{\partial x^2} + \frac{2}{x}\frac{\partial}{\partial x}\right)$.

A.1.2. Jacobian → Hyperspherical Coordinates

Translating this into hyperspherical coordinates is done via

$$R^2 = \tfrac{1}{3}\left(r^2_{ij} + r^2_{jk} + r^2_{ki}\right) = \tfrac{1}{2}\left(r^2_{ij} + \rho^2_k\right)$$
$$\alpha_i = \arctan\left(\frac{r_{ij}}{\rho_k}\right).$$

The inverse transformation is given by

$$r_{ij} = \sqrt{2}R\sin\alpha_i$$
$$\rho_k = \sqrt{2}R\cos\alpha_i.$$

The hyperspherical radius R does not depend on the permutations and is fixed for the three-particle system. The hyperangle α_i, on the other hand, does depend on the exact configuration, because it relates the lengths of r_{ij} and ρ_k. The three-particle vector $\boldsymbol{R}$ can be translated into hypersherical coordinates, the result is

$$\boldsymbol{R} = \{R, \alpha_i, \hat{\boldsymbol{r}}_{ij}, \hat{\boldsymbol{\rho}}_k\}.$$

The next step is to transform the Hamiltonian into these coordinates.

A.1.3. Jacobian → Hyperspherical Hamiltonian

In Equation A.1, we have seen the Hamiltonian in Jacobian coordinates. The next step is to transform the Hamiltonian into hyperspherical coordinates. The radial

part of the kinetic energy is given by

$$\begin{aligned} T_{r_{ij},\rho_k} &= -\frac{\hbar^2}{m}\left[\frac{\partial^2}{\partial r_{ij}^2}+\frac{\partial^2}{\partial \rho_k^2}+\frac{2}{r_{ij}}\frac{\partial}{\partial r_{ij}}+\frac{2}{\rho_k}\frac{\partial}{\partial \rho_k}\right], \\ &= -\frac{\hbar^2}{2m}\left[\frac{\partial^2}{\partial R^2}+\frac{5}{R}\frac{\partial}{\partial R}+\frac{1}{R^2}\left(4\cot 2\alpha_i\frac{\partial}{\partial \alpha_i}+\frac{\partial^2}{\partial \alpha_i^2}\right)\right], \\ &= T_R + T_{\alpha_i}, \end{aligned}$$

where we have introduced the kinetic energy operators associated to the hyperradius through $T_R \equiv -\frac{\hbar^2}{2m}\left[\frac{\partial^2}{\partial R^2}+\frac{5}{R}\frac{\partial}{\partial R}\right]$ and to the relative distance of the three-particles through $T_{\alpha_i} \equiv -\frac{\hbar^2}{2mR^2}\left[4\cot 2\alpha_i\frac{\partial}{\partial \alpha_i}+\frac{\partial^2}{\partial \alpha_i^2}\right]$. The hyperspherical Hamiltonian is given by

$$H = T_R + \underbrace{T_{\alpha_i}+\frac{1}{2mR^2}\Lambda^2}_{T_{\mathbf{\Omega}}/R^2} + V(r_{ij},\rho_k)$$

with $\Lambda^2 \equiv \frac{L_{r_{ij}}^2}{\sin^2\alpha_i}+\frac{L_{\rho_k}^2}{\cos^2\alpha_i}$.

A.1.4. Hyperradial and Hyperangular Schrödinger Equations

To separate the hyperradial from the hyperangular part of the wavefunction we will insert the adiabatic hyperspherical representation of the wavefunction into the Schrödinger Equation. The adiabatic hyperspherical representation is given by

$$\psi(R,\mathbf{\Omega}) = R^{-5/2}\sum_n f_n(R)\Phi_n(R,\mathbf{\Omega}).$$

Using this representation the solutions of $\Phi_n(R,\mathbf{\Omega})$ for a specific value of R are given by the hyperangular equation

$$\left[\frac{T_{\mathbf{\Omega}}}{R^2}+V(R,\mathbf{\Omega})\right]\Phi_n(R,\mathbf{\Omega}) = V_n(R)\Phi_n(R,\mathbf{\Omega}),$$

where the term $V_n(R)$ is the eigenvalue depending on R. Far away from the scattering center (for $R\to\infty$ we have $V(R,\mathbf{\Omega})=0$) the equation becomes the equation of the hyperspherical harmonics

$$\frac{T_{\mathbf{\Omega}}}{R^2}\Phi_n(\mathbf{\Omega}) = V_n(R)\Phi_n(\mathbf{\Omega}).$$

In the other limit, $R \ll a$, the equation turns into the equation that defines the Efimov channels

$$\frac{T_{\mathbf{\Omega}}}{R^2}\phi_n(\mathbf{\Omega}) = s_n\phi_n(\mathbf{\Omega}).$$

The Ansatz for this limit is shown to be valid in Appendix A.4.

These function have the property that they are orthonormal under hyperangular integral

$$(\Phi_n|\Phi_m) \equiv \int d^5\mathbf{\Omega}\, \Phi_n^*\, \Phi_m = \delta_{nm}.$$

The Efimov channel are given by the functions

$$\phi_n(\mathbf{\Omega}) = (1+\hat{Q})\frac{\varphi_n(\alpha)}{\sin(2\alpha)}Y_l^m(\hat{\boldsymbol{\rho}}),$$

where $\hat{Q} = \hat{P}_{13} + \hat{P}_{23}$ is the exchange operator giving all the different possible permutations of the Jacobian coordinates (See Section A.1.1). We have also used to notation $\alpha \equiv \alpha_1$ and $\hat{\boldsymbol{\rho}} \equiv \hat{\boldsymbol{\rho}}_3$ and the permutation operator takes care of the different possibilities. The functions $\varphi_n(\alpha)$ are given by

$$\left[-\frac{\partial^2}{\partial\alpha^2} + \frac{l(l+1)}{\cos^2\alpha}\right]\varphi_n(\alpha) = s_n^2\varphi_n(\alpha).$$

We have used the results of this section in the main text.

A.2. Incoming and Outgoing waves

Let us consider the incoming and outgoing waves in the three-particle problem:

$$\psi^{\text{in/out}} \underset{R\to 0}{\simeq} \frac{1}{R^2}\frac{1}{\Gamma(1\mp is_0)}\left(\frac{kR}{2}\right)^{\mp is_0}\phi_{is_0}.$$

To see that these are incoming and outgoing waves let us consider the flux through a sphere around the origin (see Figure 1.3):

$$\begin{aligned}\varphi^{\text{in/out}} &= -\frac{\hbar}{m}\oint \text{Im}((\psi^{\text{in/out}})^*\frac{\partial}{\partial R}\psi^{\text{in/out}})\; d^5S,\\ &\propto \frac{\hbar}{m}(\mp s_0) \quad \text{in the limit } R\to 0.\end{aligned}$$

Here we can clearly see that the incoming wave has a flux towards $R = 0$ and the outgoing wave a flux away from the center.

A.3. Saddle Point Method

To project the hyper spherical plane wave onto the basis of either hyperspherical harmonics or the Efimov waves, we need to calculate the inner product $(f(\mathbf{\Omega})|\Psi_{\boldsymbol{k}}(\boldsymbol{R}))$, where $f(\mathbf{\Omega})$ is one of these channels or some other function that is not to singular. The hyperspherical plane wave is given by

$$\Psi_{\boldsymbol{k}}(\mathbf{\Omega}) = e^{i\boldsymbol{k}\cdot\boldsymbol{R}},$$

where $\boldsymbol{k}$ is the relative momentum vector of the three-particle problem and $\boldsymbol{R}$ is the hyper spherical position vector. The projection of $(f(\mathbf{\Omega})|\Psi_{\boldsymbol{k}}(\boldsymbol{R}))$ is given by:

$$(f(\mathbf{\Omega})|\Psi_{\boldsymbol{k}}(\boldsymbol{R})) = \int d^5\mathbf{\Omega} f(\mathbf{\Omega}) e^{i\boldsymbol{k}\cdot\boldsymbol{R}}.$$

This integral is the integral over a sphere $\mathcal{S}$ and the main contribution of the integral comes from the poles, where $\boldsymbol{k}$ is parallel with the vector $d^5\mathbf{\Omega}$. This region is indicated by $\mathbf{\Omega} = \pm\hat{\boldsymbol{k}} + \delta\Omega$. So let us write $\boldsymbol{k}\cdot\boldsymbol{R}$ and $f(\mathbf{\Omega})$ as:

$$\begin{aligned}\boldsymbol{k}\cdot\boldsymbol{R} = \pm kR\cos|\delta\Omega| &\approx \pm(kR - \tfrac{kR}{2}\delta^2\Omega)\\ f(\mathbf{\Omega}) &\approx f(\pm\hat{\boldsymbol{k}}).\end{aligned}$$

Using these results the projection can be written as:

$$\begin{aligned}(f(\mathbf{\Omega})|\Psi_{\boldsymbol{k}}(\boldsymbol{R})) &= f(\pm\hat{\boldsymbol{k}})e^{\pm ikR}\int d^5\delta\Omega\ e^{\mp i\frac{kR}{2}(\delta\Omega)^2}\\ &= f(+\hat{\boldsymbol{k}})\frac{e^{+ikR}}{R^2\sqrt{kR}}\frac{(2\pi)^{5/2}}{k^2}e^{-i5\pi/4} + f(-\hat{\boldsymbol{k}})\frac{e^{-ikR}}{R^2\sqrt{kR}}\frac{(2\pi)^{5/2}}{k^2}e^{+i5\pi/4}.\end{aligned}$$

Giving the amplitudes of the waves:

$$A^{\text{in}} = f(-\hat{\boldsymbol{k}})\frac{e^{-ikR}}{R^2\sqrt{kR}}\frac{(2\pi)^{5/2}}{k^2}e^{+i5\pi/4}, \tag{A.2}$$

$$A^{\text{in}} = f(+\hat{\boldsymbol{k}})\frac{e^{+ikR}}{R^2\sqrt{kR}}\frac{(2\pi)^{5/2}}{k^2}e^{-i5\pi/4}. \tag{A.3}$$

This result can be used for the initial conditions.

A.4. Efimov's Ansatz

The wavefunction Ψ for the three-particle problem is given by the sum of all the possible permutations of the problem in Jacobian coordinates:

$$\Psi = \chi(\boldsymbol{r}_{12}, \boldsymbol{\rho}_3) + \chi(\boldsymbol{r}_{23}, \boldsymbol{\rho}_1) + \chi(\boldsymbol{r}_{31}, \boldsymbol{\rho}_2) \equiv (1 + \hat{Q})\chi(\boldsymbol{r}, \boldsymbol{\rho}), \tag{A.4}$$

with $\boldsymbol{r}_{ij} = \boldsymbol{r}_i - \boldsymbol{r}_j$, $\boldsymbol{\rho}_k = 2/\sqrt{3}(\boldsymbol{r}_k - (\boldsymbol{r}_i + \boldsymbol{r}_j)/2)$, $i, j, k \in \{1, 2, 3\}$ and $\boldsymbol{r} = \boldsymbol{r}_{12}$ and $\boldsymbol{\rho} = \boldsymbol{\rho}_3$. The operator $\hat{Q}$ is the permutation operator given by $\hat{Q} = \hat{P}_{13} + \hat{P}_{23}$. The function χ can be written in terms of the hyper spherical coordinates, but to do this we need to introduce $\chi_0(\boldsymbol{r}, \boldsymbol{\rho}) = r\rho\,\chi(\boldsymbol{r}, \boldsymbol{\rho})$. This wave function can be written as $\chi_0(\boldsymbol{r}, \boldsymbol{\rho}) = F(R)\varphi(\alpha)$, which is the Efimov Ansatz [118].

In order to fulfill the two-particle scattering condition the Bethe-Peierls boundary condition [152] needs to valid. The Bethe-Peierls condition reads:

$$\left.\frac{\partial(r_{ij}\Psi)}{\partial r_{ij}}\right|_{r_{ij}\to 0} = -\frac{1}{a}\left. r_{ij}\Psi\right|_{r_{ij}\to 0} \qquad \forall i, j \in \{1, 2, 3\}.$$

Using the permutation notation in Equation (A.4) gives,

$$\begin{aligned}
\left.\frac{\partial(r_{ij}(1+\hat{Q})\chi)}{\partial r_{ij}}\right|_{r_{ij}\to 0} &= -\frac{1}{a}\left. r_{ij}(1+\hat{Q})\chi\right|_{r_{ij}\to 0} \\
(1+\hat{Q})\chi\big|_{r_{ij}\to 0} + \left. r_{ij}\frac{\partial((1+\hat{Q})\chi)}{\partial r_{ij}}\right|_{r_{ij}\to 0} &= -\frac{1}{a}\left. r_{ij}(1+\hat{Q})\chi\right|_{r_{ij}\to 0} \\
(1+\hat{Q})\chi\big|_{r_{ij}\to 0} + \left. r_{ij}\frac{\partial\chi(\boldsymbol{r}_{ij}, \boldsymbol{\rho}_k)}{\partial r_{ij}}\right|_{r_{ij}\to 0} &= -\frac{1}{a}\left. r_{ij}\chi(\boldsymbol{r}_{ij}, \boldsymbol{\rho}_k)\right|_{r_{ij}\to 0}
\end{aligned}$$

The χ terms that have dropped out of the equation above are regular in the origin $r_{ij} \to 0$ and thus becomes zero. The Bethe-Peierls condition then can be written is terms of χ_0 as

$$\begin{aligned}
&\left.\tfrac{\chi_0}{r_{ij}}\right|_{r_{ij}\to 0} + \left.\tfrac{\rho_k}{\rho_i}\tfrac{\chi_0}{r_{jk}}\right|_{r_{ij}\to 0} + \left.\tfrac{\rho_k}{\rho_j}\tfrac{\chi_0}{r_{ki}}\right|_{r_{ij}\to 0} + \left.\tfrac{\partial}{\partial r_{ij}}\left(\chi_0(\boldsymbol{r}_{ij}, \boldsymbol{\rho}_k)\right)\right|_{r_{ij}\to 0} - \left.\tfrac{1}{r_{ij}}\left(\chi_0(\boldsymbol{r}_{ij}, \boldsymbol{\rho}_k)\right)\right|_{r_{ij}\to 0} \\
&\qquad = -\tfrac{1}{a}\chi_0(\boldsymbol{r}_{ij}, \boldsymbol{\rho}_k)\big|_{r_{ij}\to 0}
\end{aligned}$$

Replacing χ_0 by $F(R)\varphi(\alpha)$ and using $r_{ij} \to 0$ gives

$$\frac{\rho_k}{\rho_i}\frac{F(R)\varphi(\pi/3)}{r_{jk}}\Big|_{r_{ij}\to 0} + \frac{\rho_k}{\rho_j}\frac{F(R)\varphi(\pi/3)}{r_{ki}}\Big|_{r_{ij}\to 0} + \frac{\partial\alpha}{\partial r_{ij}}F(R)\varphi'(0)\Big|_{r_{ij}\to 0} = -\frac{1}{a}F(R)\varphi(0)$$
$$\frac{8}{\sqrt{3}}\varphi(\pi/3)+\varphi'(0) = -\frac{R}{a}\varphi(0). \quad \text{(A.5)}$$

This equation is only true for all R if $R \ll a$, hence the Efimov Ansatz $\chi_0(\boldsymbol{r}, \boldsymbol{\rho}) = F(R)\varphi(\alpha)$ is only valid when $R \ll a$.

When $R \ll a$ is validated, then Equation (A.5) becomes a boundary condition for $\varphi(\alpha)$

$$\frac{\varphi'(0)}{\varphi(\pi/3)} = -\frac{8}{\sqrt{3}}. \quad \text{(A.6)}$$

This is a boundary condition for three-particle scattering, due to the Bethe-Peierls condition.

A.5. The s-matrix at Unitarity

To find $s_{11}(\infty)$, let us start with the general result at unitarity for the three-particle problem:

$$F_{is_0}(R) = AJ_{+is_0}(kR) + BJ_{-is_0}(kR). \quad \text{(A.7)}$$

The two-limiting cases of the Besselfunction are given by

$$J_\nu(x) \begin{cases} \underset{x\to 0}{\simeq} \frac{1}{\Gamma(1+\nu)}\left(\frac{x}{2}\right)^\nu \\ \underset{x\to\infty}{\simeq} \sqrt{\frac{2}{\pi x}}\cos\left(x - \frac{\nu\pi}{2} - \frac{\pi}{4}\right) = \sqrt{\frac{1}{2\pi x}}\left(e^{+i(x-\nu\pi/2-\pi/4)} + e^{-i(x-\nu\pi/2-\pi/4)}\right) \end{cases}.$$

Let us take the wave function for an outgoing particle $(kR)^{is_0}$ and write Equation (A.7) using this form for $R \to 0$ (we will forget about the normalization factor):

$$F_{is_0}(R) \underset{R\to 0}{\simeq} (kR)^{is_0} + \frac{B}{A}\frac{\Gamma(1+is_0)}{\Gamma(1-is_0)}2^{2is_0}(kR)^{-is_0},$$
$$\underset{R\to 0}{\simeq} (kR)^{is_0} + s_{11}(\infty)\,(kR)^{-is_0}.$$

When a particle is added to the center of the problem we have the boundary condition that there should be no incoming wave ($e^{-ikR}/\sqrt{kR}$) at large distance. This will determine the ratio of A and B. Using the large-x behavior of the Bessel

function the radial wave function becomes (again forgetting about the normalization factor):

$$F_{is_0}(R) \underset{R\to\infty}{\simeq} \frac{1}{\sqrt{kR}}\left[(Ae^{+s_0\pi}+B)e^{ikR}+i(A+Be^{+s_0\pi})e^{-ikR}\right]$$

$$\downarrow$$

$$(A+Be^{+s_0\pi}) \;=\; 0 \rightarrow \frac{B}{A} = -e^{-s_0\pi}$$

Finally, the result for $s_{11}(\infty)$ is given by

$$s_{11}(\infty) = -e^{-s_0\pi}\frac{\Gamma(1+is_0)}{\Gamma(1-is_0)}2^{2is_0}. \tag{A.8}$$

For completeness, these are the values of s_{13} and s_{33}

$$s_{13} = s_{31} = 2^{is_0}\sqrt{2/\pi s_0}\Gamma(1+is_0)\sinh(\pi s_0)e^{-\pi s_0/2-i\pi/4},$$
$$s_{33} = -\frac{s_{13}}{s_{13}^*}s_{11}^* =$$

B. Peer-reviewed papers

B.1. Dynamics and Thermodynamics of the Low-Temperature Strongly Interacting Bose Gas

Dynamics and Thermodynamics of the Low-Temperature Strongly Interacting Bose Gas

Nir Navon,[1,*] Swann Piatecki,[2,†] Kenneth Günter,[1] Benno Rem,[1] Trong Canh Nguyen,[1] Frédéric Chevy,[1] Werner Krauth,[2] and Christophe Salomon[1]

[1]*Laboratoire Kastler Brossel, CNRS, UPMC, École Normale Supérieure, 24 rue Lhomond, 75005 Paris, France*
[2]*Laboratoire de Physique Statistique, École Normale Supérieure, UPMC, Université Paris Diderot, CNRS, 24 rue Lhomond, 75005 Paris, France*

(Received 15 March 2011; revised manuscript received 21 June 2011; published 19 September 2011)

We measure the zero-temperature equation of state of a homogeneous Bose gas of ^{7}Li atoms by analyzing the *in situ* density distributions of trapped samples. For increasing repulsive interactions our data show a clear departure from mean-field theory and provide a quantitative test of the many-body corrections first predicted in 1957 by Lee, Huang, and Yang [Phys. Rev. **106**, 1135 (1957).]. We further probe the dynamic response of the Bose gas to a varying interaction strength and compare it to simple theoretical models. We deduce a lower bound for the value of the universal constant $\xi > 0.44(8)$ that would characterize the universal Bose gas at the unitary limit.

DOI: 10.1103/PhysRevLett.107.135301 PACS numbers: 67.85.−d, 05.30.Jp, 32.30.Bv, 67.60.Fp

From sandpiles to neuronal networks, electrons in metals, and quantum liquids, one of the greatest challenges in modern physics is to understand the behavior of strongly interacting systems. A paradigmatic example is superfluid ^{4}He, the understanding of which has resisted theoretical analysis for decades. Early attempts to address the problem of the strongly interacting Bose liquid focused on the dilute limit. A seminal result for the thermodynamics of the dilute Bose gas was the expansion of the ground state energy (per volume V), first obtained in the late 1950s [1]:

$$\frac{E}{V} = \frac{gn^2}{2}\left(1 + \frac{128}{15\sqrt{\pi}}\sqrt{na^3} + \cdots\right), \tag{1}$$

where n is the density of the gas, $g = 4\pi\hbar^2 a/m$ is the coupling constant for particles with mass m, and a is the s-wave scattering length, which characterizes the low-energy interactions. The first term in Eq. (1) is the mean-field energy, while the Lee-Huang-Yang (LHY) correction, proportional to $\sqrt{na^3}$, is due to quantum fluctuations [1]. Up to this order, the expansion is *universal*, in the sense that it depends solely on the gas parameter na^3 and not on microscopic details of the interaction potential [2–4].

Despite its fundamental importance, this expansion was never checked experimentally before the advent of ultracold quantum gases, where it became possible to tune the value of the scattering length using magnetic Feshbach resonances [5,6]. A first check of the LHY prediction was provided by recent experiments on strongly correlated Fermi gases [7–9] that behave as a gas of tightly bound dimers in the limit of small and positive values of a [10–12]. By contrast, early studies of Bose gases in the strongly interacting regime were plagued by severe inelastic atom loss [13], but recent experiments at JILA and Rice have revived interest in these systems and showed the onset of beyond mean-field effects [14,15]. Here we report on a quantitative measurement of the thermodynamic equation of state (EOS) of a strongly interacting atomic Bose gas in the low-temperature limit. We show that the EOS follows the expansion (1), and the comparison with fermionic systems illustrates the universality of the LHY correction.

In the first part, we restrict ourselves to a moderately interacting gas with negligible 3-body atom loss: $a/a_0 \sim 2000$, a_0 being the Bohr radius. In this regime our EOS reveals the Lee-Huang-Yang correction due to quantum fluctuations. We perform quantum Monte Carlo (QMC) simulations to support our zero-temperature approximation. We then test our assumption of thermal equilibrium by dynamically bringing the gas into a more strongly interacting regime where atom loss is no longer negligible. Finally, we explore the unitary regime where the scattering length is infinite.

Our experimental setup was described in [16]. Starting from a ^{7}Li cloud in a magneto-optical trap, we optically pump the atoms into the $|F = 2, m_F = 2\rangle$ hyperfine state and transfer them into a magnetic Ioffe trap. After evaporative cooling to a temperature of ~ 4 μK, the atoms are loaded into a hybrid magnetic/optical trap and then transferred to the $|F = 1, m_F = 1\rangle$ state. The radial optical confinement of the trap is provided by a single laser beam of 35 μm waist operating at a wavelength of 1073 nm, while the weak axial confinement is enhanced by an additional magnetic-field curvature. We apply a homogeneous magnetic field to tune the interaction strength by means of a wide Feshbach resonance that we locate at 737.8(2) G. The final stage of evaporation in the optical trap is carried out at a bias field of 717 G, where the scattering length has a value of about $200a_0$, and results in a Bose-Einstein condensate of $\sim 6 \times 10^4$ atoms with no discernible thermal part. In the final configuration the trapping frequencies are given by $\omega_r = 2\pi \times 345(20)$ Hz in the radial and $\omega_z = 2\pi \times 18.5(1)$ Hz in the axial direction. The magnetic bias field is then adiabatically ramped

to the vicinity of the Feshbach resonance in 150 ms and the density distribution is recorded using *in situ* absorption imaging (Fig. 1). As the EOS critically depends on the scattering length, a precise knowledge of the latter close to the Feshbach resonance is essential. In view of the discrepancy between two recent works [15,17], we have independently calibrated the scattering length $a(B)$ as a function of magnetic field B by radio-frequency molecule association spectroscopy [18], as described in the Supplemental Material [19].

For the measurement of the EOS, we follow the method of [9,20–23]. Accordingly, the local pressure $P(z)$ along the symmetry axis of a harmonically trapped gas is related to the doubly integrated *in situ* density profile $\bar{n}(z) = \int dxdyn(x, y, z)$:

$$P(\mu_z) = \frac{m\omega_r^2}{2\pi}\bar{n}(z). \tag{2}$$

This formula relies on the local-density approximation in which the local chemical potential is defined as $\mu_z = \mu_0 - \frac{1}{2}m\omega_z^2 z^2$, where μ_0 is the global chemical potential of the gas.

To measure the pressure at different interaction strengths we have selected images with atom numbers in the range of 3–4 $\times 10^4$ in order to avoid high optical densities during absorption imaging while keeping a good signal-to-noise ratio. A total of 50 images are used, spanning values of a/a_0 from 700 to 2150. We calibrate the relation between the integrated optical density and the pressure of the gas at weak interaction, well described by mean-field theory (inset of Fig. 2). The density profiles then generate the EOS (2). The global chemical potential μ_0 remains to be determined. For this work, we infer μ_0 self-consistently in a model-independent way from the density profiles (see the Supplemental Material [19]).

In the dilute limit $na^3 \ll 1$, where the EOS is universal, dimensional analysis can be used to write the grand canonical EOS of the homogeneous Bose gas at zero temperature in the form

$$P(\mu, a) = \frac{\hbar^2}{ma^5}h(\nu), \tag{3}$$

where $\nu \equiv \mu a^3/g$ is the (grand canonical) gas parameter and $h(\nu)$ is the normalized pressure. This EOS contains all thermodynamic macroscopic properties of the system. For example, the energy can be deduced from the pressure using a Legendre transform detailed in the Supplemental Material [19], and in particular, its LHY asymptotic expansion (1). According to the above definition of h, the mean-field EOS simply reads $h(\nu) = 2\pi\nu^2$. These predictions for $h(\nu)$ are compared to the experimental data points in Fig. 2, and to our QMC calculation. We observe a clear departure of the EOS from the mean-field prediction [dashed gray line (dashed red online)]. At the largest measured value of $\nu = 2.8 \times 10^{-3}$ our data show a reduction of 20% of the pressure with respect to the mean-field result.

We observe that LHY theory accurately describes our experimental data and is hardly distinguishable from the

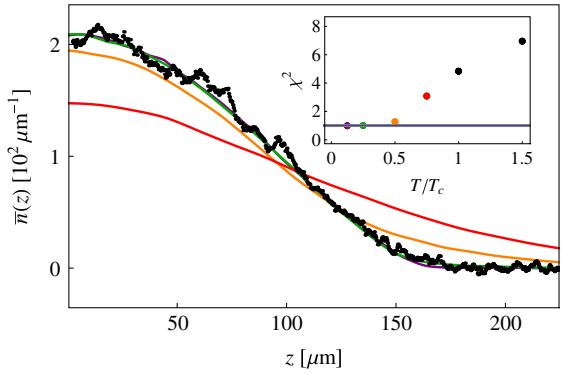

FIG. 1 (color online). Doubly integrated density profile of a trapped Bose gas at a scattering length $a/a_0 = 2150$, used to measure the LHY expansion (1). The average over 5 experimental images is shown in black points. The QMC predictions for 3.9×10^4 atoms are plotted in a solid line for $T/T_c = 0.75$ in red, 0.5 in orange, 0.25 in green, and 0.125 in purple (solid lines from bottom to top). Inset: χ^2 deviation per degree of freedom of a single experimental density profile with QMC results at different temperatures. The excellent agreement between experimental profiles and QMC validates the zero-temperature assumption for the EOS measurement.

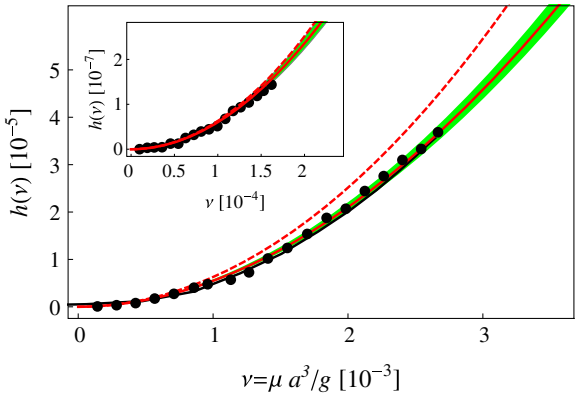

FIG. 2 (color online). Equation of state of the homogeneous Bose gas expressed as the normalized pressure h as a function of the gas parameter ν. The gas samples for the data shown in the main panel (inset) have been prepared at scattering lengths of $a/a_0 = 1450$ and 2150 ($a/a_0 = 700$). The gray (red online) solid line corresponds to the LHY prediction, and the gray (red online) dashed line to the mean-field EOS $h(\nu) = 2\pi\nu^2$. In the weakly interacting regime the data are well described by mean-field theory (inset), in opposition to stronger interactions where beyond-mean-field effects are important (main panel). The QMC EOS at $T/T_c = 0.25$ (solid black line) is nearly indistinguishable from the LHY EOS. The shaded (green online) area delimits the uncertainty of 5% on the value of a.

QMC in the studied range of interaction strength, a point already put forward in a diffusion Monte Carlo simulation at even higher values of the gas parameter [24]. We can quantify the deviation of our data from mean-field theory by fitting the measured EOS with a function that includes a correction of order $\sqrt{na^3}$. For this purpose we convert the energy $E/N = [2\pi\hbar^2/(ma^2)]na^3[1 + \alpha(na^3)^{1/2}]$ to the grand canonical EOS (see the Supplemental Material [19]) and use α as a fit parameter in the resulting pressure $P(\mu)$. The fit yields the value $\alpha = 4.5(7)$, which is in excellent agreement with the theoretical result $128/(15\sqrt{\pi}) \approx 4.81$ in Eq. (1). Together with the measurement with composite bosons of [9], this provides a striking check of the universality predicted by the expansion (1) up to order $\sqrt{na^3}$ [11].

In the above interpretation we assumed that the zero-temperature regime has effectively been reached. To check this crucial assumption, we have performed finite-temperature path-integral quantum Monte Carlo simulations [25] in the anisotropic harmonic trap geometry of the experiment with continuous space variables. The experimental atom number can be reached without difficulty and pair interactions are described by a pseudopotential. All thermodynamic properties of the gas at finite temperature are obtained to high precision and without systematic errors. As seen in Fig. 1, we find good agreement between the experimental density distributions and the QMC profiles at temperatures up to $0.25T_c$, where T_c is the condensation temperature of the ideal Bose gas. This shows that thermal effects are negligible and lead to an error in the EOS much smaller than the statistical error bars in Fig. 2.

We now assess the adiabaticity of the interaction sweep in the measurements described above. A violation of adiabaticity could lead to nonequilibrium density profiles that distort the measured EOS. We study the dynamics of the Bose gas subjected to time-dependent interaction sweeps into increasingly strongly interacting regimes, where the enhanced three-body loss rate limits the practical duration of the sweep. In Fig. 3 we plot the axial cloud size determined by a Thomas-Fermi fit as a function of the sweep duration. The magnetic field is ramped approximately linearly in time, sweeping a/a_0 from an initial value of 200 to different final values. Besides the experimental data we present theoretical results from a mean-field scaling solution [26,27] and from a solution of the hydrodynamic equations incorporating the LHY EOS based on a variational scaling ansatz [28]. The latter shows a remarkable agreement with our experimental data for $a \leq 3000a_0$. For scattering lengths $a/a_0 \leq 840$ the radius is nearly constant for sweep durations $\tau\omega_z/(2\pi) > 1.5$ ($\tau > 80$ ms), indicating that the cloud follows the interaction strength adiabatically. For the largest value used in the EOS study ($a/a_0 = 2150$), the atom loss is less than 4% and the cloud size after the $\tau = 150$ ms sweep [$\tau\omega_z/(2\pi) \gtrsim 2.8$] is 2.5% smaller than the equilibrium value. We have corrected for this systematic effect by rescaling the measured density n_0 for the determination of the EOS, $\bar{n} = \eta^{-1}\bar{n}_0(\eta z)$ (with $\eta = 0.975$ for $a/a_0 = 2150$).

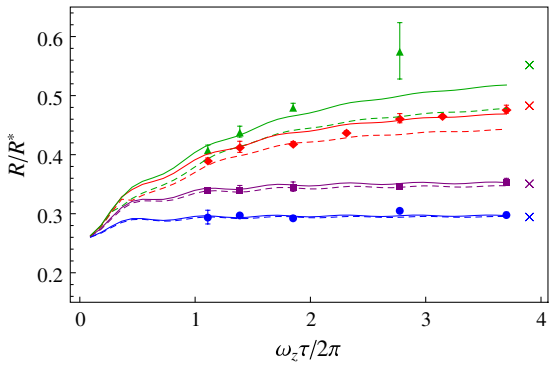

FIG. 3 (color online). Radius R of the Bose gas as a function of the duration τ of the interaction sweep. The radius R is normalized to the radius $R^* = a_{\rm ho}(15\lambda^2 N)^{1/5}$ [where $a_{\rm ho} = (\hbar/m\omega_z)^{1/2}$ and $\lambda = \omega_r/\omega_z$]. N is the measured atom number at the end of each sweep. The final values of a/a_0 are 380 (blue dots), 840 (purple squares), 2940 (red diamonds), and 4580 (green triangles). The solid (dashed) lines show the solution of a variational hydrodynamic approach (mean-field scaling solutions). The crosses show the predicted equilibrium beyond-mean-field radii.

The properties of the Bose gas for very large values of na^3 constitute a challenging open problem. Because of the

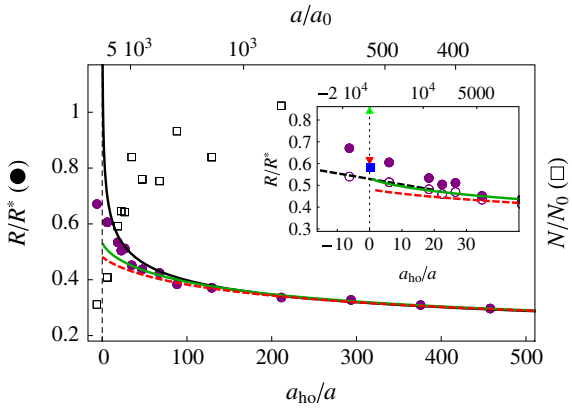

FIG. 4 (color online). Normalized cloud radius $R_{\rm TF}/R^*$ (filled purple circles) and normalized atom number (open black squares) as a function of the inverse scattering length $a_{\rm ho}/a$ at the end of a 75-ms magnetic-field sweep. The static mean-field prediction is plotted in a solid black line, the mean-field scaling solution in a dashed red line, and the beyond mean-field scaling ansatz in a solid gray line (green online). Inset: Zoom around the unitary limit. Predictions for the universal constant ξ are shown in an up triangle [34], down triangle [33], and square [32]. The filled (empty) circles correspond to the radii normalized to the final (initial) atom number (see [31]). The dashed black line is the linear interpolation at unitarity.

experimental limitation imposed by three-body recombination, we access this region with a shorter sweep of duration $\tau\omega_z/(2\pi) = 1.35$ ($\tau \approx 75$ ms). In Fig. 4 we plot the normalized radius of the Bose gas as a function of the inverse scattering length a_{ho}/a. Deep in the mean-field regime ($a \lesssim 800a_0$) the ramp is adiabatic as the data match the equilibrium Thomas-Fermi prediction. As the scattering length is increased, both nonadiabaticity and beyond mean-field effects become important. A departure from the equilibrium result becomes evident above a scattering length of $\simeq 2000a_0$. Taking into account the mean-field dynamics gives an improved description of our data (red dashed line). Even better agreement (up to values of $a/a_0 \simeq 5000$) is obtained with the variational approach incorporating the LHY correction as presented above [gray solid line (green online)] [28]. Probing larger values of the scattering length enables us to gain further insight into the unitary Bose gas, $a = \infty$. Because of the low densities of our samples, only half of the atoms are lost at the end of the sweep to the resonance (see squares in Fig. 4). Universal thermodynamics at unitarity have been conjectured for quantum gases [29] and successfully checked experimentally for Fermi gases [30]. In the case of bosonic atoms the existence of a many-body universal state at unitarity is still unknown. Under the assumption of universality, the only relevant length scale should be the interparticle spacing $n^{-1/3}$ and the EOS would take the form $\mu \propto \frac{\hbar^2}{m} n^{2/3}$. Up to a numerical factor, this EOS is identical to that of an ideal Fermi gas and we can write $\mu = \xi E_F$ [where $E_F = \hbar^2/2m(6\pi^2 n)^{2/3}$]. As we increase the scattering length towards the unitarity regime, the cloud is expected to grow in size. Because of the finite response time of the gas, it is reasonable to assume that the measured radius R is smaller than the equilibrium radius. From this inequality, in the spirit of variational methods, we deduce a lower bound for the value of ξ by interpolating our data at unitarity [black dashed line in the inset of Fig. 4]: $\xi > 0.44(8)$ [31]. This bound is satisfied for the predictions $\xi = 0.66$ [32] and for the upper bounds from variational calculations, 0.80 [33] and 2.93 [34].

Future work could focus on the measurement of the condensate fraction since the quantum depletion is expected to be as large as $\sim$8% for our most strongly interacting samples in equilibrium, and on finite-temperature thermodynamic properties [35]. Our measurements on resonance as well as future theoretical studies should give crucial insights on the unitary Bose gas.

We are grateful to Y. Castin, F. Werner, X. Leyronas, S. Stringari, S. Giorgini, S. Pilati, and A. Grier for discussions and to C. Lancien, I. Lahlou, S. El-Ghazzal, T. Vu, and L. Bernard for experimental assistance. We thank J. Dalibard and S. Nascimbène for useful comments on the manuscript. We acknowledge support from ESF Euroquam (FerMix), ANR FABIOLA, Région Ile de France (IFRAF), ERC, and Institut Universitaire de France.

*navon@ens.fr
†swann.piatecki@ens.fr

[1] T. D. Lee, Kerson Huang, and C. N. Yang, Phys. Rev. **106**, 1135 (1957).
[2] K. Brueckner and K. Sawada, Phys. Rev. **106**, 1117 (1957).
[3] S. Beliaev, JETP **7**, 289 (1958).
[4] E. Lieb, Phys. Rev. **130**, 2518 (1963).
[5] S. Inouye *et al.*, Nature (London) **392**, 151 (1998).
[6] J. Roberts *et al.*, Phys. Rev. Lett. **85**, 728 (2000).
[7] A. Altmeyer *et al.*, Phys. Rev. Lett. **98**, 40 401 (2007).
[8] Y. Shin *et al.*, Phys. Rev. Lett. **101**, 070404 (2008).
[9] N. Navon *et al.*, Science **328**, 729 (2010).
[10] G. Astrakharchik *et al.*, Phys. Rev. Lett. **93**, 200404 (2004).
[11] X. Leyronas and R. Combescot, Phys. Rev. Lett. **99**, 170402 (2007).
[12] H. Hu *et al.*, Europhys. Lett. **74**, 574 (2006).
[13] P. Fedichev *et al.*, Phys. Rev. Lett. **77**, 2921 (1996).
[14] S. Papp *et al.*, Phys. Rev. Lett. **101**, 135301 (2008).
[15] S. Pollack *et al.*, Phys. Rev. Lett. **102**, 90402 (2009).
[16] S. Nascimbene *et al.*, Phys. Rev. Lett. **103**, 170402 (2009).
[17] N. Gross *et al.*, Phys. Rev. Lett. **105**, 103203 (2010).
[18] J. Zirbel *et al.*, Phys. Rev. A **78**, 13 416 (2008).
[19] See Supplemental Material at http://link.aps.org/supplemental/10.1103/PhysRevLett.107.135301 for technical details about the density profiles analysis and Feshbach resonance calibration.
[20] C. H. Cheng and S. K. Yip, Phys. Rev. B **75**, 14 526 (2007).
[21] Y. I. Shin, Phys. Rev. A **77**, 41 603 (2008).
[22] T. Ho and Q. Zhou, Nature Phys. **6**, 131 (2009).
[23] S. Nascimbene *et al.*, Nature (London) **463**, 1057 (2010).
[24] S. Giorgini, J. Boronat, and J. Casulleras, Phys. Rev. A **60**, 5129 (1999).
[25] W. Krauth, Phys. Rev. Lett. **77**, 3695 (1996).
[26] Y. Castin and R. Dum, Phys. Rev. Lett. **77**, 5315 (1996).
[27] Y. Kagan, E. L. Surkov, and G. V. Shlyapnikov, Phys. Rev. Lett. **79**, 2604 (1997).
[28] The details of the time-dependent analysis will be published elsewhere.
[29] T. L. Ho, Phys. Rev. Lett. **92**, 90 402 (2004).
[30] M. Inguscio, W. Ketterle, and C. Salomon, *Proceedings of the International School of Physics Enrico Fermi, Course CLXIV* (IOS Press, Amsterdam, 2006).
[31] At unitarity, the cloud radius R would scale as $N^{1/6}\xi^{1/4}$. The normalization R^* used in Fig. 4 scales as $N^{1/5}$ so that $R/R^* \propto \xi^{1/4}N^{-1/30}$ very slowly depends on the atom number. In order to take into account the changing atom number near unitarity and obtain a safe experimental lower bound on $\xi \propto (R/R^*)^4 N^{2/15}$, we minimize both R/R^* and $N^{2/15}$. This is done by taking for R/R^* the initial atom number (empty circles in the inset of Fig. 4), and the final, for $N^{2/15}$.
[32] Y.-L. Lee and Y.-W. Lee, Phys. Rev. A **81**, 063613 (2010).
[33] J. L. Song and F. Zhou, Phys. Rev. Lett. **103**, 25302 (2009).
[34] S. Cowell *et al.*, Phys. Rev. Lett. **88**, 210403 (2002).
[35] R. Smith, R. Campbell, N. Tammuz, and Z. Hadzibabic, Phys. Rev. Lett. **106**, 250403 (2011).

B.2. Lifetime of the Bose Gas with Resonant Interactions

Lifetime of the Bose Gas with Resonant Interactions

B. S. Rem,[1] A. T. Grier,[1] I. Ferrier-Barbut,[1] U. Eismann,[1] T. Langen,[2] N. Navon,[1] L. Khaykovich,[1,3] F. Werner,[1] D. S. Petrov,[4,5] F. Chevy,[1] and C. Salomon[1]

[1]*Laboratoire Kastler-Brossel, École Normale Supérieure, CNRS and UPMC, 24 rue Lhomond, 75005 Paris, France*
[2]*Vienna Center for Quantum Science and Technology, Atominstitut, TU Wien, Stadionallee 2, 1020 Wien, Austria*
[3]*Department of Physics, Bar-Ilan University, Ramat-Gan, 52900 Israel*
[4]*Université Paris-Sud, CNRS, LPTMS, UMR8626, Orsay F-91405, France*
[5]*Russian Research Center Kurchatov Institute, Kurchatov Square, 123182 Moscow, Russia*

(Received 20 December 2012; published 16 April 2013)

We study the lifetime of a Bose gas at and around unitarity using a Feshbach resonance in lithium 7. At unitarity, we measure the temperature dependence of the three-body decay coefficient L_3. Our data follow a $L_3 = \lambda_3/T^2$ law with $\lambda_3 = 2.5(3)_{\mathrm{stat}}(6)_{\mathrm{syst}} \times 10^{-20}$ $(\mu\mathrm{K})^2\,\mathrm{cm}^6\,\mathrm{s}^{-1}$ and are in good agreement with our analytical result based on zero-range theory. Varying the scattering length a at fixed temperature, we investigate the crossover between the finite-temperature unitary region and the previously studied regime where $|a|$ is smaller than the thermal wavelength. We find that L_3 is continuous across the resonance, and over the whole $a < 0$ range our data quantitatively agree with our calculation.

DOI: 10.1103/PhysRevLett.110.163202 PACS numbers: 34.50.Lf, 03.65.Nk, 31.15.xj, 67.85.−d

Recent advances in manipulating cold atomic vapors have enabled the study of Fermi gases at the unitary limit where the scattering length a describing two-body interactions becomes infinite. It has been demonstrated both experimentally and theoretically that in this limit the system is characterized by a scale invariance leading to remarkably simple scaling laws [1]. In contrast, most experimental results on Bose-Einstein condensates were obtained in the weakly interacting regime. Recent experimental results on bosons near Feshbach resonances have revived the interest in strongly interacting bosons [2]: the development of experimental tools has enabled a precise test of the Lee-Huang-Yang corrections [3,4], and several theoretical papers have studied the hypothetical unitary Bose gas at zero [5–8] or finite [9] temperature. The strongly interacting Bose gas is one of the most fundamental quantum many-body systems, yet many open questions remain. Examples include the prediction of weakly bound Efimovian droplets [10,11], the existence of both atomic and molecular superfluids [12], and the creation of strongly correlated phases through three-body losses [13].

Experimental investigation of ultracold bosons near unitarity has been hampered by the fast increase of the three-body recombination rate close to a Feshbach resonance [14,15]. In this case, the number of trapped atoms $N(t)$ follows the usual three-body law

$$\dot{N} = -L_3\langle n^2\rangle N, \tag{1}$$

where $\langle n^2\rangle = \int d^3r n^3(\boldsymbol{r})/N$ is the mean square density and L_3 is the three-body loss rate constant. In the zero-temperature limit L_3 increases as $\hbar a^4/m$ [16] multiplied by a dimensionless log-periodic function of a revealing Efimov physics [17–26]. At finite temperature, L_3 saturates when a becomes comparable to the thermal wavelength $\lambda_{\mathrm{th}} = h/\sqrt{2\pi m k_B T}$, and $L_3 \sim \hbar a^4/m \sim \hbar^5/m^3(k_B T)^2$ [9,27,28]. This saturation suggests that a non-quantum-degenerate Bose gas near a Feshbach resonance will maintain thermal quasiequilibrium [9]. Indeed, in this regime, $|a| \gtrsim \lambda_{\mathrm{th}}$ and $n\lambda_{\mathrm{th}}^3 \ll 1$. Thus, the elastic collision rate $\gamma_2 \propto \hbar\lambda_{\mathrm{th}} n/m$ is much higher than the three-body loss rate $\gamma_3 = L_3 n^2 \propto \hbar\lambda_{\mathrm{th}}^4 n^2/m$. Experimental and numerical evidence for a saturation of L_3 was reported in Refs. [3,22,27]. A theoretical upper bound compatible with this scaling was derived in Ref. [29] assuming that only the lowest three-body hyperspherical harmonic contributes, an assumption which breaks down when $|a|$ exceeds λ_{th}.

In this Letter, we measure the temperature dependence of the unitary three-body recombination rate and find agreement with a $L_3 \propto 1/T^2$ scaling law. In a second set of measurements performed at constant temperature, we study L_3 versus a. We show how this function smoothly connects to the zero-temperature calculations when $|a| \ll \lambda_{\mathrm{th}}$. These observations are explained by a general theoretical result for $L_3(a, T)$, exact in the zero-range approximation, that we derive in the second part. Our theory allows for a complete analytic description of the unitary case and, in particular, predicts (weak) log-periodic oscillations of the quantity L_3T^2. Our findings quantify the ratio of good-to-bad collisions in the system and provide solid ground for future studies of strongly interacting Bose gases. Furthermore, on the $a < 0$ side, experiments have so far detected a single Efimov trimer [3,23–25,30]. Our analysis predicts that a second Efimov trimer of very large size should be detectable in ^{7}Li at temperatures on the order of a few microkelvins.

Our experimental setup was presented in Ref. [4]. After magneto-optical trapping and evaporation in an Ioffe magnetic trap down to $\simeq 30$ μK, $\simeq 2 \times 10^6$ ^{7}Li atoms are transferred into a hybrid magnetic and dipole trap in

the state $|1, 1\rangle$. The transverse confinement is obtained by a single laser beam of waist 43(1) μm and wavelength 1073 nm, while the longitudinal trapping is enhanced by a magnetic field curvature. The resulting potential has a cylindrical symmetry around the propagation axis of the laser and is characterized by trapping frequencies $0.87 < \omega_\rho/2\pi < 3.07$ kHz and $18 < \omega_z/2\pi < 49$ Hz. Further cooling is achieved by applying a homogeneous magnetic field $B \simeq 718$ G for which the scattering length is $\simeq 200a_0$, and decreasing the depth of the trapping potential down to a variable value U' allowing us to vary the final temperature of the cloud. Afterwards, the dipole trap is recompressed to a value $U > U'$, to prevent significant atom loss due to the enhanced evaporation rate; see below. At each T we choose U so as to maintain the temperature constant during the three-body loss rate measurement. Finally, the magnetic field is ramped in 100–500 ms to $B_0 \simeq 737.8(3)$ G, where the scattering length a diverges [4]. We then measure the total atom number N remaining after a variable waiting time t and the corresponding T, using *in situ* imaging of the thermal gas.

Our data are limited to the range of temperature $1 \leq T \leq 10$ μK. For $T \gtrsim 1$ μK, the rate $\gamma_3 = -\dot{N}/N$ remains small with respect to other characteristic rates in our cloud (elastic scattering rate, trapping frequencies), which guarantees that a thermal quasiequilibrium is maintained. We check that for these parameters the *in situ* integrated density profile is indeed Gaussian, and we use it to extract the temperature of the cloud, found to be in agreement with that of time of flight. The peak phase-space density varies within $0.07 \times 10^{-2} < n_0\lambda_{\rm th}^3 < 1.1 \times 10^{-2}$. A typical time dependence of N and T is shown in Fig. 1. The time dependence of the atom number is fitted using the usual three-body recombination law Eq. (1) [31]. For a nondegenerate gas of temperature T, the density profile is Gaussian,

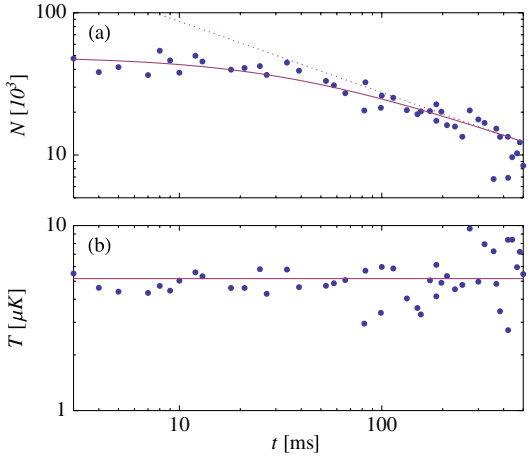

FIG. 1 (color online). Time dependence of the atom number (a) and temperature (b) for $U = \eta k_B T$, with $T = 5.2(4)$ μK, $\eta = 7.4$, and (uncorrected) $L_3 = 1.2(2)_{\rm stat} \times 10^{-21}$ cm^6 s^{-1}. The dotted line shows the long time $t^{-1/2}$ dependence of the number of atoms.

and we have $\langle n^2 \rangle = N^2 A(T) = N^2(m\bar{\omega}^2/2\pi\sqrt{3}k_B T)^3$, with $\bar{\omega} = (\omega_\rho^2\omega_z)^{1/3}$ being the mean trapping frequency. We then have

$$\dot{N} = -L_3(T)A(T)N^3. \tag{2}$$

Assuming constant temperature, integrating Eq. (2) gives

$$N(t) = \frac{N(0)}{\sqrt{1 + 2A(T)L_3(T)N^2(0)t}}, \tag{3}$$

which we use as a fitting function to analyze $N(t)$, and extract $L_3(T)$ as shown in Fig. 1.

Because of their n^3/T^2 dependence, three-body losses preferentially remove atoms of low kinetic energy and those located at the center of the trap where the density is the highest and potential energy is the smallest. As a result, three-body loss events heat up the cloud [16]. We ensure constant temperature by operating with a typical trap depth $U \simeq \eta k_B T$ with $6 \leq \eta \leq 8$, for which the residual evaporation then balances recombination heating; see Fig. 1(b). This ensures that L_3 is time independent, but, as a drawback, evaporation contributes to losses. To quantify the relative importance of evaporative and three-body losses, we first note that an atom expelled by evaporation removes on average an energy $\simeq(\eta + \kappa)k_B T$, where, taking κ from Ref. [32], we follow Ref. [33]. Typically, we have $\kappa \simeq 0.68$ for $\eta = 6$ and $\kappa \simeq 0.78$ for $\eta = 8$ [34]. In comparison, each three-body event leaves on average an excess heat of $\delta k_B T$ per particle. Extending the derivation of Ref. [16] to the case of an energy dependent three-body loss rate $\propto E^{-2}$, we obtain $\delta = 5/3$ [34]. The energy balance required to keep the temperature constant thus implies that the evaporation rate is $\simeq\delta/(\eta + \kappa - 3)$ times smaller than the three-body loss rate. Neglecting this effect would induce a systematic overestimation of L_3 of about 50% for $\eta = 6$ and 30% for $\eta = 8$. Therefore, we apply this systematic correction to our data.

The temperature dependence of L_3 obtained from our measurements at unitarity is shown in Fig. 2. It is well fit by the scaling law $L_3(T) = \lambda_3/T^2$, with $\lambda_3 = 2.5(3)_{\rm stat} \times 10^{-20}$ $(\mu{\rm K})^2\,{\rm cm}^6\,{\rm s}^{-1}$ as the best-fit value. In order to discuss the systematic uncertainty of this measurement, we note that the quantity L_3T^2 scales in all experimental parameters identically to the thermodynamic quantity $(\mu^2/P)^2$ of a zero-temperature Bose-Einstein condensate with chemical potential μ and pressure P [34]. We use this relation to calibrate our experimental parameters [4] and obtain a systematic uncertainty on λ_3 of $\leq 25\%$ resulting in $\lambda_3 = 2.5(3)_{\rm stat}(6)_{\rm syst} \times 10^{-20}$ $(\mu{\rm K})^2\,{\rm cm}^6\,{\rm s}^{-1}$.

We now study the a dependence of L_3 on both sides of the resonance by employing the same experimental procedure as in the unitary case. We tune the scattering length while keeping the temperature within 10% of 5.9 μK; see Fig. 3. The excess heat δ entering in the correction now depends on the value of ka. The correction is applied to all data points (filled circles) except in the range $1500a_0 < a < 5000a_0$ (open circles), where the assumptions of our

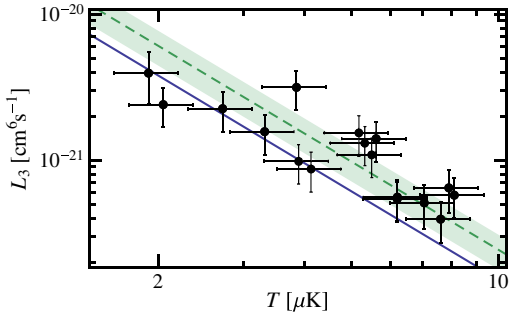

FIG. 2 (color online). Temperature dependence of the three-body loss rate L_3. Filled circles, experimental data; green dashed line, best fit to the data $L_3(T) = \lambda_3/T^2$ with $\lambda_3 = 2.5(3)_{\rm stat}(6)_{\rm syst} \times 10^{-20}\,(\mu{\rm K})^2{\rm cm}^6{\rm s}^{-1}$; the shaded green band shows the 1σ quadrature sum of uncertainties. Solid line, prediction from Eq. (5), $\lambda_3 = 1.52 \times 10^{-20}\ (\mu{\rm K})^2\,{\rm cm}^6\,{\rm s}^{-1}$ with $\eta_* = 0.21$ from Refs. [30,39].

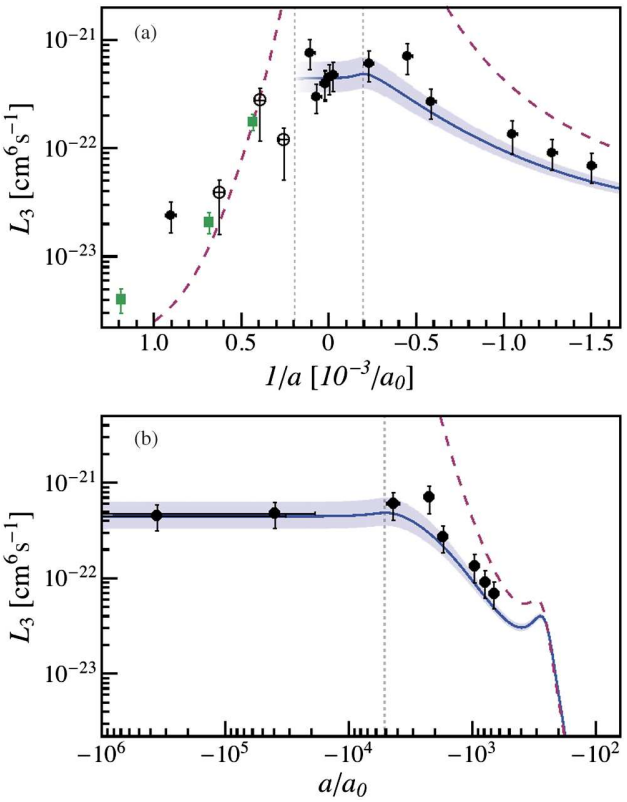

FIG. 3 (color online). (a) ^{7}Li scattering-length dependence of the three-body rate constant $L_3(a)$ for constant $T = 5.9(6)\ \mu$K (filled and open circles). For small positive a, $L_3(a)$ for a low-temperature condensate is also shown (green squares). The solid blue line corresponds to our theoretical prediction Eq. (4) for $T = 5.9\ \mu$K. The blue range is the same theory for 5.3 to 6.5 μK. The dashed lines show the zero-temperature prediction for $L_3(a)$ [20] fitted to the measurements in Refs. [30,39] with the parameters $\eta_* = 0.21$ and $R_0 = 270a_0$. The vertical dotted lines correspond to $|a|/\lambda_{\rm th} = 1$. The open circles in the range $1500a_0 < a < 5000a_0$ are not corrected for residual evaporation as our model is not applicable. (b) Logarithmic plot of the $a < 0$ side, displaying the two Efimov loss resonances.

model are not applicable [34]. In the limit $|a| \gg \lambda_{\rm th}$, we observe that $L_3(a)$ saturates to the same value on both sides of the resonance. In the opposite limit $|a| \ll \lambda_{\rm th}$, our data connect to the zero-temperature behavior [20] studied experimentally in Refs. [22–26]. On the $a < 0$ side, the dashed line is the zero-temperature prediction for L_3 from Ref. [20]. We clearly see that finite temperature reduces the three-body loss rate. On the $a > 0$ side, temperature effects become negligible for $a < 2000a_0$, as testified by our measurements performed on a low-temperature Bose-Einstein condensate (green squares), which agree with the total recombination rate to shallow and deep dimers calculated at $T = 0$ in Ref. [20] (dashed line). The data around unitarity and on the $a < 0$ side are seen to be in excellent agreement with our theory Eq. (4) described below.

In order to understand the dependence $L_3(a, T)$ theoretically, we employ the S-matrix formalism developed in Refs. [20,35,36]. According to the method, at hyperradii $R \gg |a|$ one defines three-atom scattering channels ($i = 3, 4, \ldots$) for which the wave function factorizes into a normalized hyperangular part $\Phi_i(\hat{R})$ and a linear superposition of the incoming, $R^{-5/2}e^{-ikR}$, and outgoing, $R^{-5/2}e^{+ikR}$, hyperradial waves. The channel $i = 2$ is defined for $a > 0$ and describes the motion of an atom relative to a shallow dimer. The recombination or relaxation to deep molecular states (with a size of order the van der Waals range R_e) requires inclusion of other atom-dimer channels. In the zero-range approximation, valid when $R_e \ll R_m \equiv \min(1/k, |a|)$, the overall effect of these channels and all short-range physics in general can be taken into account by introducing a single Efimov channel ($i = 1$) defined for $R_e \ll R \ll R_m$: the wave function at these distances is a linear superposition of the incoming, $\Phi_1(\hat{R})R^{-2+is_0}$, and outgoing, $\Phi_1(\hat{R})R^{-2-is_0}$, Efimov radial waves. Here $s_0 \approx 1.00624$. The notion "incoming" or "outgoing" is defined with respect to the *long-distance* region $R_m \lesssim R \lesssim |a|$, so that, for example, the incoming Efimov wave actually propagates towards larger R whereas incoming waves in all other channels propagate towards smaller hyperradii. The matrix s_{ij} relates the incoming amplitude in the ith channel with the outgoing one in the jth channel and describes the reflection, transmission, and mixing of channels in the long-distance region. This matrix is unitary and independent of the short-range physics. The short-range effects are taken into account by fixing the relative phase and amplitude of the incoming and outgoing Efimov waves $R^2\Psi \propto (R/R_0)^{is_0} - e^{2\eta_*}(R/R_0)^{-is_0}$, where R_0 is the three-body parameter and the short-range inelastic processes are parametrized by $\eta_* > 0$, which implies that the number of triples going towards the region of $R \sim R_e$ is by the factor $e^{4\eta_*}$ larger than the number of triples leaving this region [37]. Braaten *et al.* [36] have shown that for a given incoming channel $i \geq 2$ the probability of recombination to deeply bound states is $P_i = (1 - e^{-4\eta_*})|s_{i1}|^2/|1 + (kR_0)^{-2is_0}e^{-2\eta_*}s_{11}|^2$ [38]. For $a < 0$, by using the fact that s_{11} is unitary ($\sum_{i=1}^{\infty}|s_{1i}|^2 = 1$) and averaging over the

Boltzmann distribution, we then obtain the total loss rate constant

$$L_3 = \frac{72\sqrt{3}\pi^2\hbar(1-e^{-4\eta_*})}{mk_{\rm th}^6} \times \int_0^\infty \frac{(1-|s_{11}|^2)e^{-k^2/k_{\rm th}^2}kdk}{|1+(kR_0)^{-2is_0}e^{-2\eta_*}s_{11}|^2}, \quad (4)$$

where $k_{\rm th} = \sqrt{mk_BT}/\hbar$.

Note that in deriving Eq. (4) we closely followed [36] where the scattering length was assumed to be finite. However, we easily generalize this derivation to the case $a = \infty$, in which the channels become decoupled at distances $R \gg 1/k$ and the long-distance region can now be defined by $R \sim 1/k$. A less trivial result of our analysis is that for any ka there exists a unitary transformation of the matrix s_{ij} which leaves the element s_{11} invariant, but all channels with $i > 3$ become decoupled from the Efimov channel [34]. This transformation constructs a new large-R channel characterized by a certain hyperangular wave function $\tilde{\Phi}_3(\hat{R})$. For negative or infinite a this is the only channel that can "talk" to the lossy short-distance Efimov channel via a unitary 2×2 matrix. Therefore, the three-body loss rate cannot exceed the so-called maximum value $L_3^{\rm max} = 36\sqrt{3}\pi^2\hbar^5(k_BT)^{-2}/m^3$ reached in the case when the outgoing flux in this newly constructed channel vanishes. Previous derivations of $L_3^{\rm max}$ [29] essentially implied that $\tilde{\Phi}_3(\hat{R})$ is the lowest *noninteracting* hyperspherical harmonics. This approximation can be made only for $k|a| \ll 1$. In general, $\tilde{\Phi}_3(\hat{R})$ is *not* an eigenstate of the angular momentum operator. In particular, at unitarity $\tilde{\Phi}_3(\hat{R}) = \Phi_1(\hat{R})$ [34].

The function $s_{11}(ka)$ is calculated in Ref. [34]. At unitarity it equals $s_{11}(\infty) = -e^{-\pi s_0}e^{2i[s_0\ln 2+\arg\Gamma(1+is_0)]}$, and from Eq. (4) one sees that L_3T^2 should be a log-periodic function of T. However, due to the numerically small value of $|s_{11}| \approx 0.04$, in the case of three identical bosons the oscillations are very small and L_3 is well approximated by setting $s_{11} = 0$:

$$L_3 \approx \frac{\hbar^5}{m^3}36\sqrt{3}\pi^2\frac{1-e^{-4\eta_*}}{(k_BT)^2}. \quad (5)$$

This explains the $L_3 \propto T^{-2}$ experimental observation seen in Fig. 2 at unitarity. Taking $\eta_* = 0.21$, which is the average of two measurements made for our ^{7}Li Feshbach resonance in Refs. [30,39], we get $L_3 = \lambda_3/T^2$ with $\lambda_3 = 1.52\times 10^{-20}$ $(\mu{\rm K})^2\,{\rm cm}^6\,{\rm s}^{-1}$. This is 40% below the experimentally determined value without any adjustable parameter and the agreement between theory and experiment is 1.4σ.

We should point out that Eq. (4) can be easily generalized to the case of other three-body systems with smaller s_0. Then, the terms neglected in Eq. (5) can become important. They also become important in our system of three identical bosons when departing from resonance in the direction of $a < 0$. Then $|s_{11}(ka)|$ monotonically increases as a function of $1/k|a|$ reaching 1 in the limit $ka \to 0^-$, the argument of s_{11} also being a monotonic function of $1/k|a|$ [34]. The solid dark gray (blue) line in Fig. 3 is the result obtained from Eq. (4) using the same η_* as above and $R_0 = 270a_0$ also taken from Refs. [30,39]. The shaded blue area reflects our experimental range of temperatures. More or less visible maxima of L_3 appear when the denominator in the integrand of Eq. (4) reaches its minimum, i.e., becomes resonant. The approximate condition for this is $\arg s_{11}(ka) = \pi + 2s_0\ln kR_0$, and the features become increasingly more pronounced for larger $|s_{11}|$ and smaller η_*. Note that from the viewpoint of the visibility of the maxima, decreasing $|a|$ is equivalent to decreasing $\sqrt{T}$. Figure 3(b) shows the pronounced resonance at $a = a_- \approx -274a_0$ observed in Refs. [30,39]. This resonance is associated with the passage of an Efimov trimer through the three-atom threshold. Another Efimov trimer, larger in size by a factor of $e^{\pi/s_0} = 22.7$, is expected to go through the threshold at around $a \approx -6350a_0$, leading to another zero energy resonance. As we deduce from Eq. (4) and show in Fig. 3 for 5.9 μK, the thermally averaged remnants of this predicted resonance lead to a maximum of L_3 at $a \approx -5100a_0$. As seen in Fig. 3(b), the agreement between theory and experiment is very good over the entire $a < 0$ range.

Because of the existence of a shallow dimer state, the case $a > 0$ becomes, in general, a complicated dynamical problem which should take into account the atom-dimer and dimer-dimer relaxation as well as various nonuniversal factors: the finite trap depth, chemical imbalance between trapped shallow dimers and free atoms, and deviations from thermal equilibrium which possibly depend on the preparation sequence. These issues require an extensive discussion beyond the scope of this Letter. The situation obviously simplifies in the case of very small a when the system is purely atomic and the three-body recombination to deep and shallow molecules leads to an immediate loss of three atoms.

Discussing the opposite limit of large $a > 0$, we first note that dimers are well defined when their size $\sim a$ is smaller than $n^{-1/3}$, which we assume in the following (the limit $na^3 \gg 1$ is equivalent to the case $a = \infty$). In the regime $a \gg \lambda_{\rm th}$ we find using the Skorniakov-Ter-Martirosian equation that $s_{12} \to 0$ for $ka \to \infty$, which implies that the atom-dimer relaxation rate vanishes; shallow dimers then remain at chemical quasiequilibrium with the decaying atomic ensemble, with a molecular fraction $\propto n\lambda_{\rm th}^3 \ll 1$ (for the data of Fig. 3 with $a > \lambda_{\rm th}$, the molecular fraction is 0.6%) [34]. Shallow dimer formation and breakup are then balanced, so that the atomic decay is just given by Eq. (1). The expression of L_3 for $a > 0$ was obtained in Ref. [36] and reduces to Eq. (4) for $s_{12} \to 0$. We conclude that the loss rate must be continuous across the resonance, in accordance with our experimental data. Therefore, in Fig. 3(a) the result of Eq. (4) is simply continued to positive a for $a \gg \lambda_{\rm th}$.

In summary, we have systematically studied the dependence of the three-body loss rate on T and a in a Bose gas

near unitarity. Equation (5) shows that, at unitarity, L_3 never reaches $L_3^{\max}$, and one can hope to produce quantum degeneracy in a unitary Bose gas using atomic species with a particularly small η_*. Note that the loss mechanism in our system drastically differs from a chemical reaction with finite activation energy ΔE characterized by the well-known Arrhenius law $L_3 \propto \exp(-\Delta E/k_B T)$. In our case, instead of a potential hill there is an effective three-body R^{-2} attraction leading to $\Psi(R) \propto (\lambda_{\rm th}/R)^2$ at distances $R_e \lesssim R \lesssim \lambda_{\rm th}$, where we normalized the three-body wave function Ψ to unit volume and omitted its log-periodic R dependence. We clearly see that the probability of finding three atoms in the recombination region is enhanced at small temperatures and scales as $|\Psi|^2 \propto \lambda_{\rm th}^4 \propto 1/T^2$. More subtle is a quantum interference effect in Efimov three-body scattering, which leads to an enhanced decay rate at a negative a, suggesting the possibility to observe the signature of a second Efimov trimer of large size. Another future direction is to explore the approach to the quantum-degenerate regime and test whether the virial expansion of the unitary Bose gas [40] can be measured by using quasiequilibrium thermodynamics [9].

We acknowledge fruitful discussions with G. Shlyapnikov and F. Ferlaino, and support from Région Île de France (IFRAF), EU (ERC advanced grant Ferlodim), Institut Universitaire de France, and the Russian Foundation for Fundamental Research. T. L. acknowledges support by the Austrian Science Fund (FWF) through the Doctoral Programme CoQuS (W1210).

[1] *BCS-BEC Crossover and the Unitary Fermi Gas*, Lecture Notes in Physics Vol. 836, edited by W. Zwerger (Springer, Berlin, 2011).
[2] S. E. Pollack, D. Dries, M. Junker, Y. P. Chen, T. A. Corcovilos, and R. G. Hulet, Phys. Rev. Lett. **102**, 090402 (2009).
[3] R. J. Wild, P. Makotyn, J. M. Pino, E. A. Cornell, and D. S. Jin, Phys. Rev. Lett. **108**, 145305 (2012).
[4] N. Navon, S. Piatecki, K. Günter, B. Rem, T.-C. Nguyen, F. Chevy, W. Krauth, and C. Salomon, Phys. Rev. Lett. **107**, 135301 (2011).
[5] S. Cowell, H. Heiselberg, I. E. Mazets, J. Morales, V. R. Pandharipande, and C. J. Pethick, Phys. Rev. Lett. **88**, 210403 (2002).
[6] J.-L. Song and F. Zhou, Phys. Rev. Lett. **103**, 025302 (2009).
[7] Yu-Li Lee and Yu-Wen Lee, Phys. Rev. A **81**, 063613 (2010).
[8] D. Borzov, M. S. Mashayekhi, S. Zhang, J.-L. Song, and F. Zhou, Phys. Rev. A **85**, 023620 (2012).
[9] W. Li and T.-L. Ho, Phys. Rev. Lett. **108**, 195301 (2012).
[10] J. von Stecher, J. Phys. B **43**, 101002 (2010).
[11] J. von Stecher, Phys. Rev. Lett. **107**, 200402 (2011).
[12] S. Basu and E. J. Mueller, Phys. Rev. A **78**, 053603 (2008).
[13] N. Syassen, D. M. Bauer, M. Lettner, T. Volz, D. Dietze, J. J. Garcia-Ripoll, J. I. Cirac, G. Rempe, and S. Durr, Science **320**, 1329 (2008).
[14] S. Inouye, M. R. Andrews, J. Stenger, H.-J. Miesner, D. M. Stamper-Kurn, and W. Ketterle, Nature (London) **392**, 151 (1998).
[15] J. L. Roberts, N. R. Claussen, S. L. Cornish, and C. E. Wieman, Phys. Rev. Lett. **85**, 728 (2000).
[16] T. Weber, J. Herbig, M. Mark, H.-C. Nägerl, and R. Grimm, Phys. Rev. Lett. **91**, 123201 (2003).
[17] E. Nielsen and J. H. Macek, Phys. Rev. Lett. **83**, 1566 (1999).
[18] B. D. Esry, C. H. Greene, and J. P. Burke, Phys. Rev. Lett. **83**, 1751 (1999).
[19] P. F. Bedaque, E. Braaten, and H.-W. Hammer, Phys. Rev. Lett. **85**, 908 (2000).
[20] E. Braaten and H.-W. Hammer, Phys. Rep. **428**, 259 (2006).
[21] D. S. Petrov, in *Proceedings of the Les Houches Summer Schools, Session 94*, edited by C. Salomon, G. V. Shlyapnikov, and L. F. Cugliandolo (Oxford University Press, Oxford, England, 2013).
[22] T. Kraemer, M. Mark, P. Waldburger, J. G. Danzl, C. Chin, B. Engeser, A. D. Lange, K. Pilch, A. Jaakkola, H. C. Nägerl, and R. Grimm, Nature (London) **440**, 315 (2006).
[23] M. Zaccanti, B. Deissler, C. D'Errico, M. Fattori, M. Jona-Lasinio, S. Müller, G. Roati, M. Iguscio, and G. Modugno, Nat. Phys. **5**, 586 (2009).
[24] S. E. Pollack, D. Dries, and R. G. Hulet, Science **326**, 1683 (2009).
[25] N. Gross, Z. Shotan, S. Kokkelmans, and L. Khaykovich, Phys. Rev. Lett. **103**, 163202 (2009).
[26] F. Ferlaino, A. Zenesini, M. Berninger, B. Huang, H. C. Nägerl, and R. Grimm, Few-Body Syst. **51**, 113 (2011).
[27] J. P. D'Incao, H. Suno, and B. D. Esry, Phys. Rev. Lett. **93**, 123201 (2004).
[28] J. P. D'Incao, C. H. Greene, and B. D. Esry, J. Phys. B **42**, 044016 (2009).
[29] N. P. Mehta, S. T. Rittenhouse, J. P. D'Incao, J. von Stecher, and C. H. Greene, Phys. Rev. Lett. **103**, 153201 (2009).
[30] N. Gross, Z. Shotan, S. Kokkelmans, and L. Khaykovich, Phys. Rev. Lett. **105**, 103203 (2010).
[31] We neglect four- and higher-body losses which, dimensionally, are expected to be suppressed by a factor $n_0 \lambda_{\rm th}^3$ [29].
[32] O. Luiten, M. Reynolds, and J. T. M. Walraven, Phys. Rev. A **53**, 381 (1996).
[33] L. Luo, B. Clancy, J. Joseph, J. Kinast, A. Turlapov, and J. E. Thomas, New J. Phys. **8**, 213 (2006).
[34] See Supplemental Material at http://link.aps.org/supplemental/10.1103/PhysRevLett.110.163202 for more information on the calculation of s_{11}; a discussion of s_{12}, atom-dimer relaxation, and chemical equilibrium in the limit $a \to \infty$; a construction of the unitary transformation for the matrix s_{ij}; an interpretation of Eq. (4) in terms of a Fabry-Perot interferometer; and a discussion of evaporation and experimental uncertainties.
[35] V. Efimov, Sov. J. Nucl. Phys. **29**, 546 (1979).
[36] E. Braaten, H.-W. Hammer, D. Kang, and L. Platter, Phys. Rev. A **78**, 043605 (2008).
[37] E. Braaten, H.-W. Hammer, and M. Kusunoki, Phys. Rev. A **67**, 022505 (2003).
[38] Our s_{11} differs by a phase factor from the one defined in Ref. [36]; see Ref. [34].
[39] N. Gross, Z. Shotan, O. Machtey, S. Kokkelmans, and L. Khaykovich, C.R. Physique **12**, 4 (2011).
[40] Y. Castin and F. Werner, arXiv:1212.5512v2.

B.3. Λ-enhanced sub-Doppler cooling of lithium atoms in D_1 gray molasses

Λ-enhanced sub-Doppler cooling of lithium atoms in D_1 gray molasses

Andrew T. Grier,[1,*] Igor Ferrier-Barbut,[1] Benno S. Rem,[1] Marion Delehaye,[1] Lev Khaykovich,[2] Frédéric Chevy,[1] and Christophe Salomon[1]

[1]*Laboratoire Kastler-Brossel, École Normale Supérieure, CNRS and UPMC, 24 rue Lhomond, 75005 Paris, France*

[2]*Department of Physics, Bar-Ilan University, Ramat-Gan 52900, Israel*

(Received 26 April 2013; published 12 June 2013)

Following the bichromatic sub-Doppler cooling scheme on the D_1 line of ^{40}K recently demonstrated in Fernandes *et al.* [Europhys. Lett. **100**, 63001 (2012)], we introduce a similar technique for ^{7}Li atoms and obtain temperatures of 60 μK while capturing all of the 5×10^8 atoms present from the previous stage. We investigate the influence of the detuning between the the two cooling frequencies and observe a threefold decrease of the temperature when the Raman condition is fulfilled. We interpret this effect as arising from extra cooling due to long-lived coherences between hyperfine states. Solving the optical Bloch equations for a simplified Λ-type three-level system we identify the presence of an efficient cooling force near the Raman condition. After transfer into a quadrupole magnetic trap, we measure a phase space density of $\sim 10^{-5}$. This laser cooling offers a promising route for fast evaporation of lithium atoms to quantum degeneracy in optical or magnetic traps.

DOI: 10.1103/PhysRevA.87.063411 PACS number(s): 37.10.De, 32.80.Wr, 67.85.−d

I. INTRODUCTION

Lithium is enjoying widespread popularity in the cold-atom trapping community thanks to the tunability of its two-body interactions and its lightness. Both the fermionic and the bosonic isotopes of lithium feature broad, magnetically tunable Feshbach resonances in a number of hyperfine states [1]. The presence of these broad resonances makes lithium an attractive candidate for studies of both the Fermi- and Bose-Hubbard models [2] and the strongly correlated regime for bulk dilute gases of Fermi [3] or Bose [4–6] character. Its small mass and correspondingly large photon-recoil energy are favorable factors for large area atom interferometers [7] and precision frequency measurements of the recoil energy and fine structure constant [8]. Under the tight-binding lattice model, lithium's large photon-recoil energy leads to a larger tunneling rate and faster time scale for superexchange processes, allowing for easier access to spin-dominated regimes [9]. Finally, lithium's small mass reduces the heating due to nonadiabatic parts of the collision between ultracold atoms and Paul-trapped ions. This feature, together with Pauli suppression of atom-ion three-body recombination events involving ^{6}Li [10], potentially allows one to reach the s-wave regime of ion-atom collisions [11].

However, lithium, like potassium, is harder to cool using optical transitions than the other alkali-metal atoms. The excited-state structure of the D_2 transition in lithium lacks the separation between hyperfine states for standard sub-Doppler cooling techniques such as polarization gradient cooling [12–14] to work efficiently. Recently, it has been shown by the Rice group that cooling on the narrow $2S_{1/2} \rightarrow 3P_{3/2}$ transition produces lithium clouds near 60 μK, about half the D_2-line Doppler cooling limit [15], and can be used for fast all-optical production of a ^{6}Li quantum degenerate Fermi gas. However, this approach requires special optics and a coherent source at 323 nm, a wavelength range where power is still limited. Another route is to use the three-level structure of the atom as implemented previously in neutral atoms and trapped ions [16–22]. The three-level structure offers the possibility of using dark states to achieve temperatures below the standard Doppler limit, as evidenced by the use of velocity-selective coherent population trapping (VSCPT) to produce atomic clouds with subrecoil temperatures [23]. In another application, electromagnetically induced transparency has been used to demonstrate robust cooling of a single ion to its motional ground state [19,24].

In this paper, we implement three-dimensional bichromatic sub-Doppler laser cooling of ^{7}Li atoms on the D_1 transition. Figure 1 presents the ^{7}Li level scheme and the detunings of the two cooling lasers that are applied to the atoms after the magneto-optical trapping phase. Our method combines a gray molasses cooling scheme on the $|F = 2\rangle \rightarrow |F' = 2\rangle$ transition [25,26] with phase-coherent addressing of the $|F = 1\rangle \rightarrow |F' = 2\rangle$ transition, creating VSCPT-like dark states at the two-photon resonance. Instead of UV laser sources, the method uses laser light that is conveniently produced at 671 nm by semiconductor laser sources or solid-state lasers [27,28] with sufficient power. This enables us to capture all of the $\simeq 5 \times 10^8$ atoms from a MOT and cool them to 60 μK in a duration of 2 ms.

We investigate the influence of the relative detuning between the two cooling lasers and observe a threefold decrease of the temperature in a narrow frequency range around the exact Raman condition. We show that extra cooling arises due to long-lived coherences between hyperfine states. We develop a simple theoretical model for a sub-Doppler cooling mechanism which occurs in atoms with a Λ-type three-level structure, in this case, the $F = 1$, $F = 2$, and $F' = 2$ manifolds of the D_1 transition in ^{7}Li. The main physical cooling mechanism is contained in a 1D bichromatic lattice model. We first give a perturbative solution to the model and then verify the validity of this approach with a continued fraction solution to the optical Bloch equations (OBEs).

II. EXPERIMENT

The stage preceding D_1 sub-Doppler cooling is a compressed magneto-optical trap (CMOT) in which, starting from a standard MOT optimized for total atom number, the

*Corresponding author: agrier@lkb.ens.fr

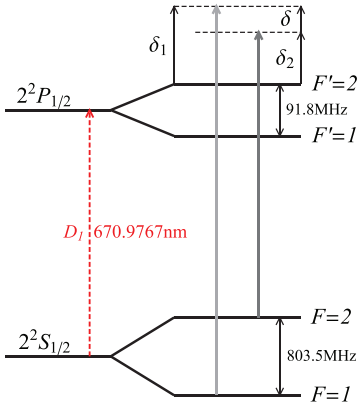

FIG. 1. (Color online) The D_1 line for ^{7}Li. The cooling scheme has a strong coupling laser (principal beam, black solid arrow) δ_2 blue detuned from the $|F=2\rangle \rightarrow |F'=2\rangle$ transition and a weak coupling laser (repumper, gray solid arrow) δ_1 blue detuned from the $|F=1\rangle \rightarrow |F'=2\rangle$ transition. The repumper is generated from the principal beam by an electro-optical modulator operating at a frequency $803.5+\delta/2\pi$ MHz, where $\delta=\delta_1-\delta_2$.

frequency of the cooling laser is quickly brought close to resonance while the repumping laser intensity is diminished in order to increase the sample's phase space density [29]. The CMOT delivers 5×10^8 ^{7}Li atoms at a temperature of 600 μK. The atoms are distributed throughout the $F=1$ manifold in a spatial volume of 800 μm $1/e$ width. Before starting our D_1 molasses cooling, we wait 200 μs to allow any transient magnetic fields to decay to below 0.1 G. The light used for D_1 cooling is generated by a solid-state laser presented in [27]. The laser is locked at frequency ω_2, detuned from the $|F=2\rangle \rightarrow |F'=2\rangle$ D_1 transition in ^{7}Li by δ_2. It is then sent through a resonant electro-optical modulator (EOM) operating at a frequency near the hyperfine splitting in ^{7}Li, $\nu_{\mathrm{EOM}}=803.5\ \mathrm{MHz}+\delta/2\pi$. This generates a small-amplitude sideband, typically a few percent of the carrier, at frequency ω_1. We define the detuning of this frequency from the $|F=1\rangle \rightarrow |F'=2\rangle$ transition as δ_1 (such that $\delta=\delta_1-\delta_2$), as shown in Fig. 1. Using about 150 mW of 671-nm light we perform a three-dimensional D_1 molasses as in [25], with three pairs of $\sigma^+-\sigma^-$ counterpropagating beams. The beams are of 3.4-mm waist and the intensity (I) of each beam is $I\gtrsim 45I_{\mathrm{sat}}$, where $I_{\mathrm{sat}}=2.54\ \mathrm{mW/cm^2}$ is the saturation intensity of the D_2 cycling transition in lithium.

We capture all of the atoms present after the CMOT stage into the D_1 gray molasses. The $1/e$ lifetime of atoms in the molasses is $\geqslant$50 ms. After being cooled for 1.5–2.0 ms, the temperature is as low as 40 μK without optical pumping or 60 μK after optical pumping into the $|F=2,m_F=2\rangle$ state for imaging and subsequent magnetic trapping. In contrast with [25], we find no further reduction in the steady-state temperature by slowly lowering the light intensities after the initial 2.0 ms.

During the molasses phase, we find a very weak dependence on the principal laser detuning for $3\Gamma\leqslant\delta_2\leqslant6\Gamma$. For the remainder of this article, we use a principal laser detuning of $\delta_2=4.5\Gamma=2\pi\times26.4$ MHz. In Fig. 2(a), the temperature dependence upon the repumper detuning is displayed for

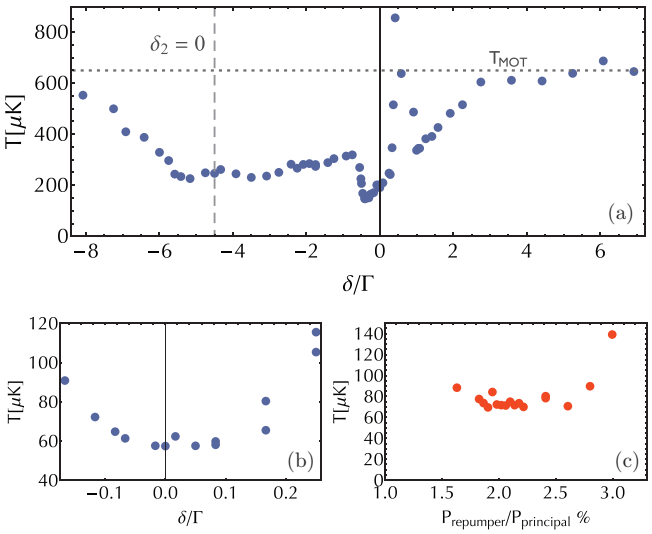

FIG. 2. (Color online) (a) Typical temperature of the cloud as a function of the repumper detuning for a fixed principal beam detuned at $\delta_1=4.5\Gamma=2\pi\times26.4$ MHz. The dashed vertical line indicates the position of the resonance with transition $|F=2\rangle\rightarrow|F'=2\rangle$, the dotted horizontal line shows the typical temperature of a MOT. (b) Magnification of the region near the Raman condition with well-aligned cooling beams and zeroed magnetic offset fields. (c) Minimum cloud temperature as a function of repumper power.

typical conditions. For $-9\leqslant\delta/\Gamma\leqslant-6$, the temperature drops from 600 μK (the CMOT temperature) to 200 μK as gray molasses cooling gains in efficiency when the weak repumper comes closer to resonance. For $-6\leqslant\delta/\Gamma\leqslant-1$, the cloud temperature stays essentially constant but, in a narrow range near the position of the exact Raman condition ($\delta=0$), one notices a sharp drop of the temperature. For δ slightly blue of the Raman condition, a strong heating of the cloud occurs, accompanied by a sharp decrease in the number of cooled atoms. Finally for $\delta\geqslant\Gamma$, the temperature drops again to a level much below the initial MOT temperature until the repumper detuning becomes too large to produce significant cooling below the CMOT temperature.

Figures 2(b) and 2(c) show the sensitivity of the temperature minimum to repumper deviation from the Raman condition and repumper power, respectively. The temperature reaches 60 μK in a $\pm$500-kHz interval around the Raman resonance condition. After taking the data for Fig. 2(a), the magnetic field zeroing and beam alignment were improved, which accounts for the frequency offset and higher temperature shown in Fig. 2(a) relative to Figs. 2(b) and 2(c). The strong influence of the repumper around the Raman condition with a sudden change from cooling to heating for small and positive Raman detunings motivated the study of the bichromatic-lattice effects induced by the Λ-type level configuration which is presented in the next section.

III. MODEL FOR HYPERFINE RAMAN COHERENCE EFFECTS ON THE COOLING EFFICIENCY

In order to understand how the addition of the second manifold of ground states modifies the gray molasses scheme,

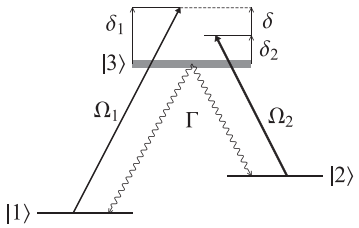

FIG. 3. The Λ level scheme. An intense standing wave with Rabi frequency Ω_2 and a weaker standing wave with Rabi frequency Ω_1, detuning δ_1, illuminate an atom with three levels in a Λ configuration.

we analyze a one-dimensional model based on a Λ-type three-level system schematically represented in Fig. 3.

A. The model

This model includes only the $F = 1,2$ hyperfine ground states and the $F' = 2$ excited state ignoring the Zeeman degeneracy; hence, standard gray molasses cooling [26] does not appear in this model. The states are addressed by two standing waves with nearly the same frequency $\omega_1 \simeq \omega_2 \simeq \omega = kc$ but spatially shifted by a phase ϕ. The principal cooling transition $F = 2 \rightarrow F' = 2$ is labeled here and below as transition 2, between states $|2\rangle$ and $|3\rangle$ with a Rabi frequency $\Omega_2 = \Gamma\sqrt{I/2I_{\rm sat}}$, where I is the laser light intensity and $I_{\rm sat}$ the saturation intensity on this transition. The repumper transition is labeled 1, between states $|1\rangle$ and $|3\rangle$ with Rabi frequency Ω_1 much smaller than Ω_2.

The corresponding Hamiltonian for the light-atom interaction in the rotating wave approximation (at ω) is

$$\begin{aligned}\hat{\mathcal{H}}_{\rm a.l.} &= \hbar\Omega_2\cos(kz)\,(|2\rangle\langle 3| + \text{H.c.})\\ &\quad + \hbar\Omega_1\cos(kz+\phi)\,(|1\rangle\langle 3| + \text{H.c.})\\ &\quad + \hbar\delta_2|2\rangle\langle 2| + \hbar\delta_1|1\rangle\langle 1|. \end{aligned} \tag{1}$$

The usual formalism used to compute the atom's dynamics is to consider the light force as a Langevin force. Its mean value is $\mathcal{F}(v)$, and the fluctuations around this mean will give rise to diffusion in momentum space, characterized by the diffusion coefficient $\mathcal{D}_p(v) \geqslant 0$. In order to calculate an equilibrium temperature, one needs $\mathcal{F}(v)$ and $\mathcal{D}_p(v)$. In the limit of small velocities the force reads

$$\mathcal{F}(v) \simeq -\alpha\, v, \tag{2}$$

with α the friction coefficient. If $\alpha > 0$ the force is a cooling force; in the opposite case it produces heating. For a cooling force the limiting temperature in this regime is given by

$$k_{\rm B}T \simeq \mathcal{D}_p(0)/\alpha. \tag{3}$$

However, since our model (1) is a gross simplification of the physical system, we do not expect to be able to quantitatively predict a steady-state temperature. Instead, in order to reveal the physical mechanisms in action, we only calculate the force $\mathcal{F}(v)$ and the excited state population ρ_{33}. Restricting our analysis to the force and photon scattering rate, $\Gamma\rho_{33}$, suffices to determine whether the action of the weak repumper serves to heat or cool the atomic ensemble.

From (1) the mean light force on the atoms is computed by taking the quantum average of the gradient of the potential, $F = \langle -\nabla\hat{\mathcal{H}}_{\rm a.l.}\rangle = -{\rm Tr}[\,\hat{\rho}\,\hat{\mathcal{H}}_{\rm a.l.}]$, with ρ the density matrix, yielding the wavelength-averaged force $\mathcal{F}$,

$$\mathcal{F}(v) = \frac{k}{2\pi}\int_0^{\frac{2\pi}{k}} dz\, F(z,v), \tag{4}$$

$$\mathcal{F}(v) = \frac{\hbar k^2}{\pi}\int_0^{\frac{2\pi}{k}} dz\,\sin(kz)(\Omega_2 {\rm Re}\rho_{23} + \Omega_1 {\rm Re}\rho_{12}). \tag{5}$$

The spontaneous emission rate averaged over the standing wave is simply given by the linewidth of the excited state multiplied by its population:

$$\Gamma' = \frac{k}{2\pi}\int_0^{\frac{2\pi}{k}} dz\,\Gamma\,\rho_{33}. \tag{6}$$

So, both the force and the spontaneous emission rate are functions of the density matrix ρ, the evolution of which is given by the OBEs,

$$i\frac{d}{dt}\rho = \frac{1}{\hbar}[\hat{\mathcal{H}}_{\rm AL},\rho] + i\left(\frac{d\rho}{dt}\right)_{\text{spont. emis.}}. \tag{7}$$

As we are focusing on the sub-Doppler regime, we assume

$$v \ll \Gamma/k, \tag{8}$$

with v being the velocity. The inequality holds for $T \ll 13$ mK for lithium. This inequality allows us to replace the full time derivative in the left-hand side of (7) by a partial spatial derivative times the atomic velocity,

$$\frac{d}{dt} \rightarrow v\frac{\partial}{\partial z}.$$

Using the notation $\Omega_i(z) = \Omega_i\cos(z+\phi_i)$ and setting $\hbar = k = 1$ from here on,

$$iv\frac{\partial\rho_{22}}{\partial z} = -2i\Omega_2(z)\,{\rm Im}(\rho_{23}) + i\frac{\Gamma}{2}\rho_{33}, \tag{9}$$

$$iv\frac{\partial\rho_{11}}{\partial z} = -2i\Omega_1(z)\,{\rm Im}(\rho_{13}) + i\frac{\Gamma}{2}\rho_{33}, \tag{10}$$

$$iv\frac{\partial\rho_{23}}{\partial z} = \left(\delta_2 - i\frac{\Gamma}{2}\right)\rho_{23} + \Omega_2(z)\,(\rho_{33}-\rho_{22}) - \Omega_1(z)\rho_{21}, \tag{11}$$

$$iv\frac{\partial\rho_{13}}{\partial z} = \left(\delta_1 - i\frac{\Gamma}{2}\right)\rho_{13} + \Omega_1(z)\,(\rho_{33}-\rho_{11}) - \Omega_2(z)\rho_{12}, \tag{12}$$

$$iv\frac{\partial\rho_{21}}{\partial z} = (\delta_2-\delta_1)\rho_{21} + \Omega_2(z)\rho_{31} - \Omega_2(z)\rho_{23}. \tag{13}$$

The solution of these equations yields the expression of $\mathcal{F}(v)$ and Γ'. This semiclassical model is valid only for velocities above the recoil velocity $v_{\rm rec} = \hbar k/m$ (corresponding to a temperature $mv_{\rm rec}/k_B$ of about 6 μK for lithium). Different theoretical studies [17,18,20,22,30,31] as well as experiments [16,32] have been performed on such a Λ configuration in standing waves or similar systems. However, in our ^{7}Li experiment, we have the situation in which the Λ configuration is coupled to a gray molasses scheme which involves a different set of dark states. This fixes the laser light parameters to values that motivate our theoretical exploration. Thus, we

concentrate on the situation corresponding to the conditions of our experiment.

To solve the OBEs (9)–(13), we first introduce a perturbative approach that enables us to point out the relevant physical mechanisms. We further extend the analysis by an exact approach in terms of continued fractions.

B. Perturbative approach

In our perturbative approach we choose a Rabi frequency Ω_2 between 2Γ and 4Γ and $\Omega_1 \ll \Gamma, \Omega_2, \delta_2$ as the ratio of the repumper to principal laser power is very small, typically $(\Omega_1/\Omega_2)^2 \lesssim 0.03$, under our experimental conditions. We further simplify the approach by considering only the in-phase situation $\phi = 0$; any finite phase would lead to divergencies of the perturbative approach at the nodes of wave 1. The validity of these assumptions are discussed in Sec. III C.

We perform an expansion in powers of the Rabi frequency Ω_1 and the atomic velocity such that the complete expansion reads

$$\rho_{ij} = \sum_{n,l} \rho_{i,j}^{(n,l)} (\Omega_1)^n (v)^l. \tag{14}$$

This expansion of ρ allows us to recursively solve the OBEs. Using an expansion similar to Eq. (14) for the force, we find

$$\alpha = -\sum_{n=0}^{\infty} \mathcal{F}^{(n,1)} (\Omega_1)^n. \tag{15}$$

We plug the perturbative solution of the OBEs into Eq. (5) and find, to the lowest order ($n = 2$) in Ω_1,

$$\alpha \simeq -\frac{(\Omega_1)^2}{2\pi} \int_0^{2\pi} dz \sin(z) \left(\Omega_2 \mathrm{Re}\, \rho_{23}^{(2,1)} + \mathrm{Re}\, \rho_{13}^{(1,1)}\right). \tag{16}$$

The spontaneous emission rate to lowest order in v and Ω_1 reads

$$\Gamma' = \Gamma \frac{(\Omega_1)^2}{2\pi} \int_0^{2\pi} dz\, \rho_{33}^{(2,0)}. \tag{17}$$

Figure 4 presents the results from (15) and (17) compared with the experimental data. It shows that indeed a narrow cooling force appears near the Raman resonance condition and that the photon scattering rate vanishes at exact resonance, hinting at an increase of cooling efficiency with respect to the gray molasses Sisyphus cooling mechanism which achieves a temperature near 200 μK over a broad range. The strong heating peak for small, positive repumper detuning is also a consequence of the negative value of α, and the heating peak shifts towards higher frequency and broadens for larger intensities of the principal laser. In contrast, the friction coefficient and scattering rate in the range $-6 \leqslant \delta/\Gamma \leqslant -3$, which correspond to a repumper near resonance, do not seem to significantly affect the measured temperature.

To gain further physical insight into this cooling near the Raman condition, it is useful to work in the dressed-atom picture. Given the weak repumping intensity, we first ignore its effect and consider only the dressing of the states $|2\rangle$ and $|3\rangle$ by the strong pump with Rabi frequency Ω_2. This dressing

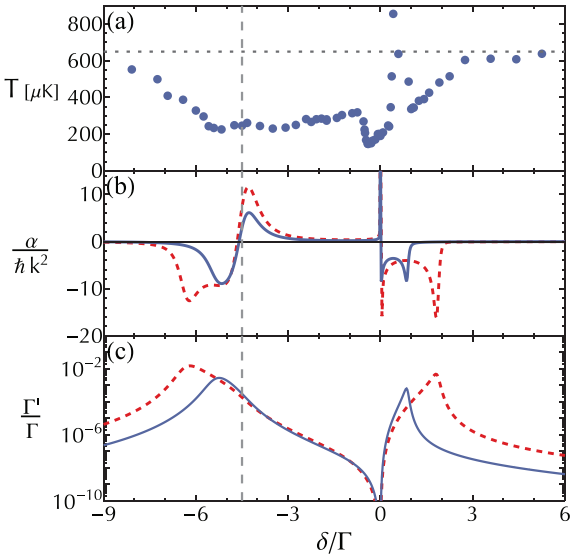

FIG. 4. (Color online) Comparison of experimental data with the perturbative approach results for a detuning of the pump $\delta_2 = 2\pi \times 26.4$ MHz $= 4.5\Gamma$. (a) Temperature versus repumper detuning, experiment; we indicate the MOT temparature by the dotted line. Panels (b) and (c) show, respectively, the friction coefficient α and photon scattering rate Γ' for $\Omega_2 = 3.4\Gamma$ (red dashed curve) and 2.1Γ (blue solid curve). The intensity ratio $(\Omega_1/\Omega_2)^2$ is 0.02. The vertical dashed line indicates the position of $\delta_1 = 0$.

gives rise to an Autler-Townes doublet structure which follows the spatial modulation of the standing wave:

$$|2'\rangle \propto |2\rangle - i\Omega_2(z)/\delta_2 |3\rangle, \tag{18}$$

$$|3'\rangle \propto -i\Omega_2(z)/\delta_2 |2\rangle + |3\rangle. \tag{19}$$

Since the pump is relatively far detuned (in the conditions of Fig. 4 $\Omega_2/\delta_2 \lesssim 0.45$), the broad state $|3'\rangle$ carries little $|2\rangle$ character. Conversely, the narrow state $|2'\rangle$ is mostly state $|2\rangle$. It follows that $|3'\rangle$ has a lifetime $\Gamma^{|3'\rangle} \simeq \Gamma$, while $|2'\rangle$ is relatively long lived with a spatially dependent linewidth $\Gamma^{|2'\rangle} = \Gamma(\Omega_2(z)/\delta_2)^2$, which is always $\leqslant \Gamma/6$ for the parameters chosen here. In order to reintroduce the effects of the repumping radiation, we note that the position in δ of the broad state is $\delta^{|3'\rangle} \simeq -\delta_2 - \Omega_2(z)^2/\delta_2$ and the narrow state $\delta^{|2'\rangle} \simeq \Omega_2(z)^2/\delta_2$. As coherent population transfer between $|1\rangle$ and $|2'\rangle$ does not change the ensemble temperature, we consider only events which couple atoms out of $|2'\rangle$ to $|1\rangle$ through spontaneous decay and therefore scale with $\Gamma_{|2'\rangle}$. The rates of coupling from $|1\rangle$ into the dressed states can be approximated by the two-level absorption rates:

$$\gamma_{|1\rangle\to|2'\rangle} \sim \frac{\Omega_1(z)^2}{2} \frac{\Gamma^{|2'\rangle}(z)}{[\Gamma^{|2'\rangle}(z)/2]^2 + [\delta - \delta^{|2'\rangle}(z)]^2}, \tag{20}$$

$$\gamma_{|1\rangle\to|3'\rangle} \sim \frac{\Omega_1(z)^2}{2} \frac{\Gamma}{(\Gamma/2)^2 + [\delta - \delta^{|3'\rangle}(z)]^2}. \tag{21}$$

Finally, these results are valid only in the limit $|\delta| > \Gamma\Omega_2^2/\delta_2^2$ (see, e.g., [33]) when state $|1\rangle$ is weakly coupled to the radiative cascade. Near the Raman resonance, the dressed state family contains a dark state which bears an infinite lifetime under the assumptions made in this section but is, in reality, limited by

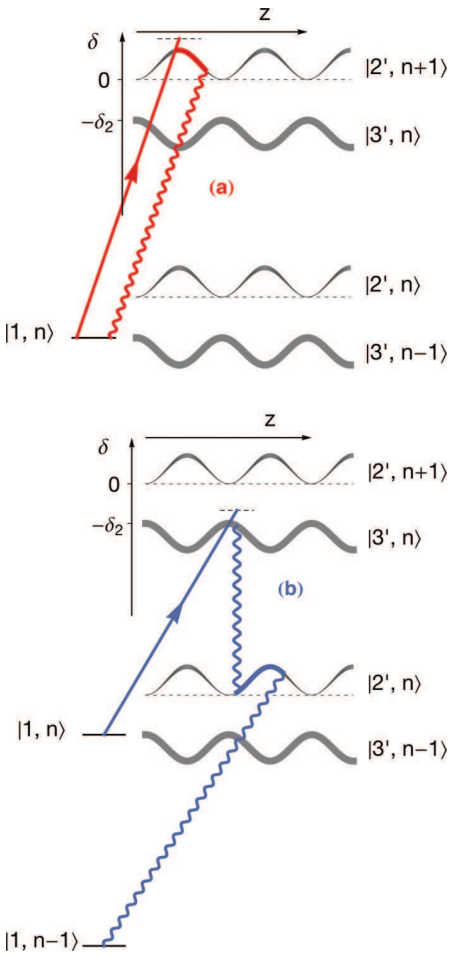

FIG. 5. (Color online) The cascade of levels dressed by transition 2 with a schematical representation of state $|1\rangle$. Traces show typical cycles of atoms pumped from $|1\rangle$ and back depending on the detuning of wave 1. The detuning of the repumper modulates the entry point into the cascade of the dressed states, leading either (a) heating or (b) cooling processes.

off-resonant excitations and motional coupling. This dark state reads

$$|\mathrm{NC}\rangle = (\Omega_2|1\rangle - \Omega_1|2\rangle)/\sqrt{\Omega_1^2 + \Omega_2^2}, \tag{22}$$

which we must add in by hand.

Using this toy model, we now explain the features of Fig. 4 and Fig. 2. Figure 5 represents the cascade of dressed levels where each doublet is separated by one pump photon. It gives rise, for example, to the well-known Mollow triplet. Condition (8) states that if an atom falls in state $|3'\rangle$ it will rapidly decay to $|2'\rangle$ without traveling a significant distance. However, the atom will remain in $|2'\rangle$ long enough to sample the spatial variation of the standing wave and gain or lose energy depending on the difference of light shift between the entry and the departure points, as in most sub-Doppler cooling schemes.

Let us first analyze the spontaneous emission rate shown in Fig. 4(c). It reaches two maxima, the first one for $\delta \sim \delta^{|3'\rangle}$ and the second one for $\delta \sim \delta^{|2'\rangle}$, and it goes to exactly zero at $\delta = 0$. The two maxima are simply due to scattering off the states $|2'\rangle$ and $|3'\rangle$. At $\delta = 0$, Γ' goes to zero due to coherent population trapping in $|\mathrm{NC}\rangle$. It is the presence of this dark state which leads to the reduced scattering rate of photons around $\delta = 0$ and the suppression of the final temperature of the gas in the region around the Raman condition.

The friction coefficient, Fig. 4(b), displays a more complicated structure with variations in δ. It shows a dispersive shape around $\delta^{|3'\rangle}$, remains positive in the range $\delta^{|3'\rangle} < \delta < 0$, diverges at $\delta = 0$, and reaches negative values for $\delta > 0$ up to $\delta^{|2'\rangle}$, where it drops to negligible values. This structure for α can be explained using our toy model. Let us consider the different scenarios corresponding to both sides of δ near 0, they follow formally from Eqs. (20) and (21) and the spatially varying linewidth of $|2'\rangle$.

For the case of the repumper tuned slightly blue of the narrow doublet state, $\delta > \delta^{|2'\rangle}$, shown in Fig. 5(a), the atoms are pumped directly from $|1\rangle$ into $|2'\rangle$. However, this pumping happens preferentially at the antinodes of the standing wave as the repumper intensity is greatest, the linewidth of $|2'\rangle$ is the largest, and the light shift minimizes the detuning of the repumper from the $|1\rangle \rightarrow |2'\rangle$ transition for the $\phi = 0$ case considered here. On average, the atoms exit this state at a point with a smaller light shift through a spontaneous emission process either into the cascade of dressed states or directly back to $|1\rangle$. As a result, we expect heating and $\alpha < 0$ in this region.

For repumper detunings between $\delta^{|3'\rangle}$ and 0, Fig. 5(b), we predict cooling. For this region, the atoms are initially pumped into $|3'\rangle$. Here the light shift modifies the relative detuning, favoring coupling near the nodes of the light. Spontaneous decay drops the atoms near the nodes of the longer-lived $|2'\rangle$, and they travel up the potential hill into regions of larger light shift before decaying, yielding cooling and a positive α. These sign changes of α and the decreased scattering rate due to $|\mathrm{NC}\rangle$ in the vicinity of the Raman condition explain the features of our perturbative model.

We conclude this section by stating that the experimentally observed change of sign of the force close to the Raman condition is well described in our perturbative model. The model further reveals the importance of Raman coherence and the existence of a dark state. The dark state together with the friction coefficient associated with cycles represented in trace 5(b) correspond to a cooling mechanism analogous to that of gray molasses. In this way, the bichromatic system provides an additional gray molasses scheme involving both hyperfine states which complements the gray molasses cooling scheme on the principal transition. On the other hand, when the friction coefficient is negative in the vicinity of the two-photon resonance, it turns into a heating mechanism that overcomes the standard gray molasses operating on the $F = 2 \rightarrow F' = 2$ transition.

The perturbative approach successfully revealed the mechanisms giving rise to the experimentally observed additional cooling. However, it also possesses some shortcomings. First, the divergence of α at $\delta = 0$ is not physical; the assumption that Ω_1 is the smallest scale in the problem breaks down when $\delta \rightarrow 0$. Alternatively, it can be seen as the failure of our model based on nondegenerate perturbative theory in the region where $|1\rangle$ and $|2\rangle$ become degenerate when dressed with ω_1 and ω_2, respectively. Second, we have only addressed the $\phi = 0$ case. Since the experiment was done in three dimensions with three pairs of counterpropagating beams, the relative phase

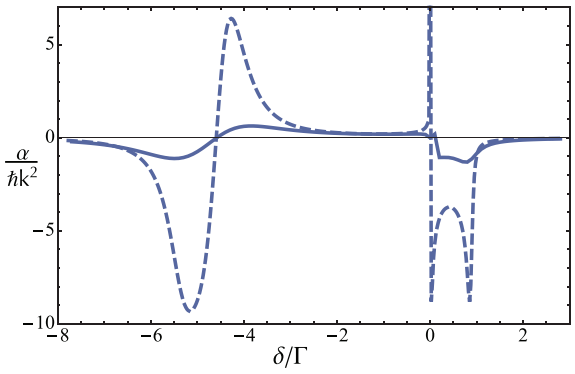

FIG. 6. (Color online) Comparison of results using the perturbative calculation (dashed), and the continued fractions (solid) for the $\phi = 0$ case, with the same parameters as in Fig. 4 and $\Omega_2 = 2.1\Gamma$.

between the two frequencies varies spatially, and we must test if the picture derived at $\phi = 0$ holds when averaging over all phases. In order to address these limitations and confirm the predictions of the perturbative approach, we now present a continued-fractions solution to the OBEs which does not rely on Ω_1 being a small parameter.

C. Continued fractions approach

The limitations listed above can be addressed by using a more general approach, namely, an expansion of the density matrix in Fourier harmonics:

$$\rho_{ij} = \sum_{n=-\infty}^{n=+\infty} \rho_{ij}^{(n)} e^{inkz}. \tag{23}$$

Injecting this expansion in (9)–(13) yields recursive relations between different Fourier components of ρ. Kozachiov *et al.* [17,30] express the solutions of these relations for a generalized Λ system in terms of continued fractions. Here we use their results to numerically solve the Bloch equations. We then compute the force $\mathcal{F}(v)$ to arbitrary order of Ω_1 and extract α by means of a linear fit to the small-v region. We then compute $\mathcal{F}(v)$ and the photon scattering rate Γ' averaged over the phase between the two standing waves.

Figure 6 compares $\alpha(\delta)$ obtained through the continued-fractions approach with the results of the perturbative expansion for the $\phi = 0$ case. The continued-fractions approach has removed the divergence at $\delta = 0$ and α crosses zero linearly. The overall friction coefficient is reduced but the two methods show qualitative agreement in the range of δ considered. At the Raman condition the interaction with light is canceled due to the presence of $|\mathrm{NC}\rangle$; thus, the diffusion coefficient $\mathcal{D}_p$ in momentum space also cancels. To lowest order, the diffusion and friction coefficients scale as

$$\mathcal{D}_p \simeq \delta^2, \tag{24}$$

$$\alpha \simeq \delta; \tag{25}$$

according to (3) the temperature scales as

$$T \simeq \delta. \tag{26}$$

Through this qualitative scaling argument, we show that even though the light action on the atoms is suppressed when approaching the Raman condition, we expect that the temperature will drop when approaching from the $\delta < 0$ side, completing the physical picture derived in the previous section.

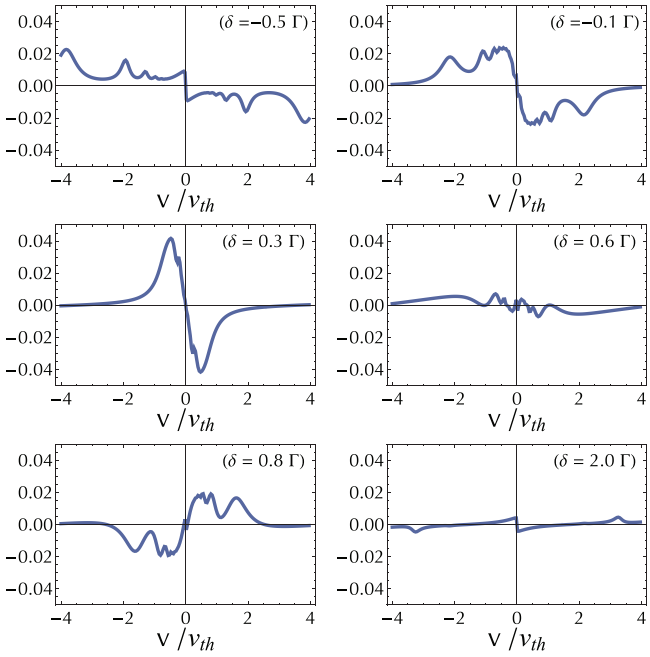

FIG. 7. (Color online) $\langle\mathcal{F}\rangle_\phi$ in units of $1/\hbar k\Gamma$ as a function of v for different values of δ around $\delta = 0$. The horizontal scale is in units of the thermal velocity at $T = 200\,\mu$K, $v_{th} = \sqrt{k_B T/m}$.

Next, we analyze how a randomized phase between the repumping and principal standing waves, ϕ, modifies $\mathcal{F}(v)$. In order to take this into account, we calculate the phase-averaged force:

$$\langle\mathcal{F}(v)\rangle_\phi = \frac{1}{2\pi}\int_0^{2\pi} \mathcal{F}(v,\phi)\,d\phi. \tag{27}$$

In Fig. 7, the phase-averaged force is plotted for various detunings near the Raman condition. It can be seen that a cooling force is present for small detunings, qualitatively in agreement with our perturbative model and with the experimental data. The force, however, changes sign to heating for small blue detuning, close to $\delta = 0.6\,\Gamma$, also in qualitative agreement with the experimental data. We note that the cooling slope very close to zero velocity in the $\delta = 0.8\,\Gamma$ plot corresponds to a velocity on the order of or below the single-photon recoil velocity, i.e., is nonphysical.

Finally, for the $\phi \neq 0$ case, $|\mathrm{NC}\rangle$ varies in space and the motion of the atoms can couple atoms out of $|\mathrm{NC}\rangle$ even at the Raman condition. In Fig. 8 we verify that the rate of photon scattering retains a minimum near the $\delta = 0$ region after averaging over ϕ by plotting $\langle\Gamma'\rangle_\phi = \Gamma\langle\rho_{33}\rangle_\phi$ calculated with the continued fractions approach. Overall, the friction coefficient α and photon scattering rate Γ' confirm the existence of a cooling force associated with a decrease in photon scattering in the vicinity of the Raman condition for the 1D bichromatic standing-wave model. Thus, the continued fractions calculation has confirmed the physical mechanisms revealed by the perturbative expansion and that the lowest

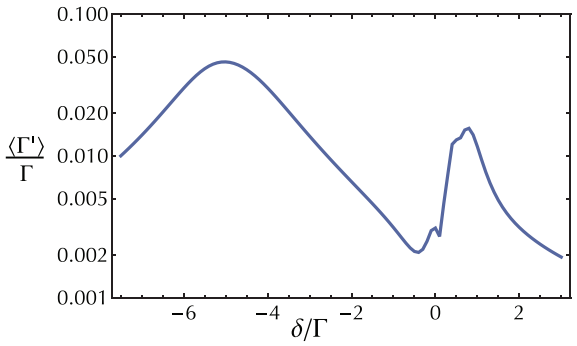

FIG. 8. (Color online) Continued fractions solution of the photon scattering rate $\Gamma' = \Gamma\,\rho_{33}$ averaged over all relative phases of the repumper and principal standing waves as a function of the two-photon detuning δ. Velocity-dependent effects are taken into account here by computing an average of $\langle\Gamma'\rangle_\phi(v)$ weighed by a Maxwell-Boltzmann velocity distribution at 200 μK.

temperatures should be expected close to $\delta = 0$, as seen in the experiment.

IV. CONCLUSION

In this study, using bichromatic laser light near 670 nm, we have demonstrated sub-Doppler cooling of ^{7}Li atoms down to 60 μK with near unity capture efficiency from a magneto-optical trap. Solving the OBEs for a simplified Λ level structure, we have analyzed the detuning dependence of the cooling force and photon scattering rate. Our analysis shows that the lowest temperatures are expected for a detuning of the repumping light near the Raman condition, in agreement with our measurements. There the Λ configuration adds a new set of long-lived dark states that strongly enhance the cooling efficiency. For ^{7}Li, this addition results in a threefold reduction of the steady-state temperature in comparison with an incoherently repumped gray molasses scheme. This atomic cloud at 60 μK is an ideal starting point for direct loading into a dipole trap, where one of the broad Feshbach resonances in the lowest-energy states of ^{7}Li or ^{6}Li could be used to efficiently cool the atoms to quantum degeneracy [15,34]. Alternatively, when the atoms are loaded into a quadrupole magnetic trap, we measure a phase space density of $\simeq 10^{-5}$. This Λ-enhanced sub-Doppler cooling in a D_1 gray molasses is general and should occur in all alkali metals. Notably, we have observed its signature in a number of the alkali-metal isotopes not amenable to polarization gradient cooling: ^{7}Li (this work), ^{40}K [25], and ^{6}Li [35].

ACKNOWLEDGMENTS

We acknowledge fruitful discussions with Y. Castin, J. Dalibard S. Wu, F. Sievers, N. Kretzschmar, D. R. Fernandes, M. Schleier-Smith, and I. Leroux and support from Région Île de France (IFRAF-C'Nano), EU (ERC advanced grant Ferlodim), Institut de France (Louis D. Foundation), and Institut Universitaire de France.

[1] C. Chin, R. Grimm, P. Julienne, and E. Tiesinga, Rev. Mod. Phys. **82**, 1225 (2010).
[2] I. Bloch, J. Dalibard, and W. Zwerger, Rev. Mod. Phys. **80**, 885 (2008).
[3] S. Nascimbène, N. Navon, K. J. Jiang, F. Chevy, and C. Salomon, Nature (London) **463**, 1057 (2010).
[4] N. Navon, S. Piatecki, K. Günter, B. Rem, T. C. Nguyen, F. Chevy, W. Krauth, and C. Salomon, Phys. Rev. Lett. **107**, 135301 (2011).
[5] R. J. Wild, P. Makotyn, J. M. Pino, E. A. Cornell, and D. S. Jin, Phys. Rev. Lett. **108**, 145305 (2012).
[6] B. S. Rem, A. T. Grier, I. Ferrier-Barbut, U. Eismann, T. Langen, N. Navon, L. Khaykovich, F. Werner, D. S. Petrov, F. Chevy *et al.*, Phys. Rev. Lett. **110**, 163202 (2013).
[7] S. Lepoutre, A. Gauguet, G. Trénec, M. Büchner, and J. Vigué, Phys. Rev. Lett. **109**, 120404 (2012).
[8] R. Bouchendira, P. Cladé, S. Guellati-Khélifa, F. Nez, and F. Biraben, Phys. Rev. Lett. **106**, 080801 (2011).
[9] T. Esslinger, Annu. Rev. Condens. Matter Phys. **1**, 129 (2010).
[10] A. Härter, A. Krükow, A. Brunner, W. Schnitzler, S. Schmid, and J. H. Denschlag, Phys. Rev. Lett. **109**, 123201 (2012).
[11] M. Cetina, A. T. Grier, and V. Vuletic, Phys. Rev. Lett. **109**, 253201 (2012).
[12] J. Dalibard and C. Cohen-Tannoudji, J. Opt. Soc. Am. B **6**, 2023 (1989).
[13] P. D. Lett, W. D. Phillips, S. L. Rolston, C. E. Tanner, R. N. Watts, and C. I. Westbrook, J. Opt. Soc. Am. B **6**, 2084 (1989).
[14] D. S. Weiss, E. Riis, Y. Shevy, P. J. Ungar, and S. Chu, J. Opt. Soc. Am. B **6**, 2072 (1989).
[15] P. M. Duarte, R. A. Hart, J. M. Hitchcock, T. A. Corcovilos, T. L. Yang, A. Reed, and R. G. Hulet, Phys. Rev. A **84**, 061406 (2011).
[16] R. Gupta, C. Xie, S. Padua, H. Batelaan, and H. Metcalf, Phys. Rev. Lett. **71**, 3087 (1993).
[17] D. V. Kosachiov, Y. V. Rozhdestvensky, and G. Nienhuis, J. Opt. Soc. Am. B **14**, 535 (1997).
[18] M. Drewsen, Phys. Rev. A **51**, 1407 (1995).
[19] C. F. Roos, D. Leibfried, A. Mundt, F. Schmidt-Kaler, J. Eschner, and R. Blatt, Phys. Rev. Lett. **85**, 5547 (2000).
[20] G. Grynberg and J.-Y. Courtois, Europhys. Lett. **27**, 41 (1994).
[21] G. Morigi and E. Arimondo, Phys. Rev. A **75**, 051404 (2007).
[22] J. W. Dunn, J. W. Thomsen, C. H. Greene, and F. C. Cruz, Phys. Rev. A **76**, 011401 (2007).
[23] A. Aspect, E. Arimondo, R. Kaiser, N. Vansteenkiste, and C. Cohen-Tannoudji, Phys. Rev. Lett. **61**, 826 (1988).
[24] G. Morigi, J. Eschner, and C. H. Keitel, Phys. Rev. Lett. **85**, 4458 (2000).
[25] D. R. Fernandes, F. Sievers, N. Kretzschmar, S. Wu, C. Salomon, and F. Chevy, Europhys. Lett. **100**, 63001 (2012).

[26] M. Weidemüller, T. Esslinger, M. A. Ol'shaniî, A. Hemmerich, and T. W. Hänsch, Europhys. Lett. **27**, 109 (1994).
[27] U. Eismann, F. Gerbier, C. Canalias, A. Zukauskas, G. Trénec, J. Vigué, F. Chevy, and C. Salomon, Appl. Phys. B **106**, 25 (2011).
[28] U. Eismann, A. Bergschneider, F. Sievers, N. Kretzschmar, C. Salomon, and F. Chevy, Opt. Express **21**, 9091 (2013).
[29] M.-O. Mewes, G. Ferrari, F. Schreck, A. Sinatra, and C. Salomon, Phys. Rev. A **61**, 011403 (1999).
[30] D. V. Kosachev and Y. V. Rozhdestvenskii, J. Exp. Theor. Phys. **79**, 856 (1994).
[31] C. Menotti, G. Morigi, J. H. Müller, and E. Arimondo, Phys. Rev. A **56**, 4327 (1997).
[32] N. Malossi, S. Damkjær, P. L. Hansen, L. B. Jacobsen, L. Kindt, S. Sauge, J. W. Thomsen, F. C. Cruz, M. Allegrini, and E. Arimondo, Phys. Rev. A **72**, 051403 (2005).
[33] E. Arimondo, in *Progress in Optics*, Vol. 35 (Elsevier, Amsterdam, 1996), pp. 257–354.
[34] N. Gross and L. Khaykovich, Phys. Rev. A **77**, 023604 (2008).
[35] F. Sievers, N. Kretzschmar, S. Wu, *et al.* (private communication).

C. Data Loss Measurements

C.1. Unitary Interactions

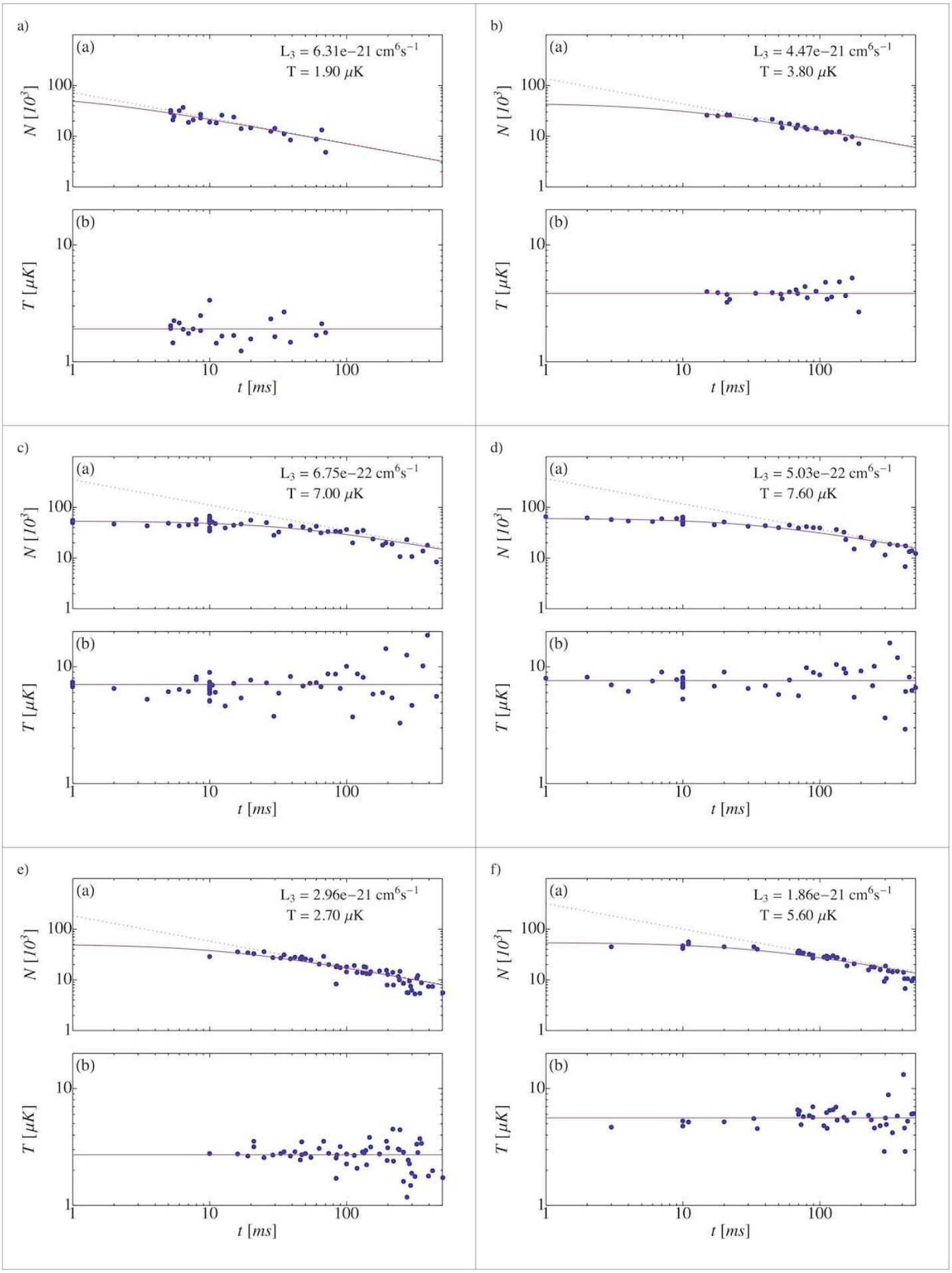
a)
(a)
L_3 = 6.31e−21 cm^{6}s^{-1}
T = 1.90 μK
N [10^3]
100
10
1
(b)
T [μK]
10
1
1
10
100
t [ms]
b)
(a)
L_3 = 4.47e−21 cm^{6}s^{-1}
T = 3.80 μK
N [10^3]
100
10
1
(b)
T [μK]
10
1
1
10
100
t [ms]
c)
(a)
L_3 = 6.75e−22 cm^{6}s^{-1}
T = 7.00 μK
N [10^3]
100
10
1
(b)
T [μK]
10
1
1
10
100
t [ms]
d)
(a)
L_3 = 5.03e−22 cm^{6}s^{-1}
T = 7.60 μK
N [10^3]
100
10
1
(b)
T [μK]
10
1
1
10
100
t [ms]
e)
(a)
L_3 = 2.96e−21 cm^{6}s^{-1}
T = 2.70 μK
N [10^3]
100
10
1
(b)
T [μK]
10
1
1
10
100
t [ms]
f)
(a)
L_3 = 1.86e−21 cm^{6}s^{-1}
T = 5.60 μK
N [10^3]
100
10
1
(b)
T [μK]
10
1
1
10
100
t [ms]

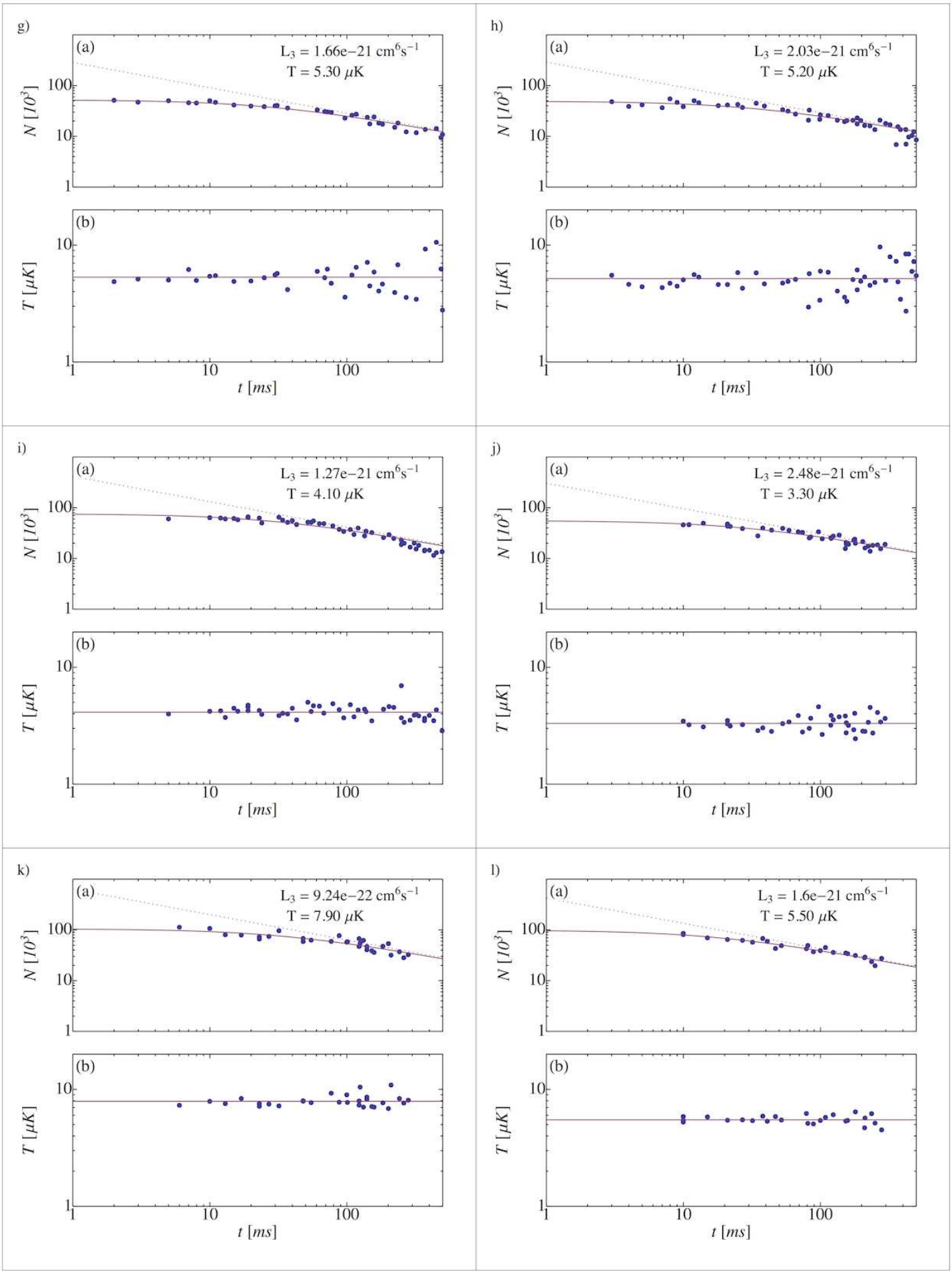
g)
(a)
L_3 = 1.66e−21 cm^{6}s^{-1}
T = 5.30 μK
N [10^3]
100
10
1
(b)
T [μK]
10
1
1
10
100
t [ms]
h)
(a)
L_3 = 2.03e−21 cm^{6}s^{-1}
T = 5.20 μK
N [10^3]
100
10
1
(b)
T [μK]
10
1
1
10
100
t [ms]
i)
(a)
L_3 = 1.27e−21 cm^{6}s^{-1}
T = 4.10 μK
N [10^3]
100
10
1
(b)
T [μK]
10
1
1
10
100
t [ms]
j)
(a)
L_3 = 2.48e−21 cm^{6}s^{-1}
T = 3.30 μK
N [10^3]
100
10
1
(b)
T [μK]
10
1
1
10
100
t [ms]
k)
(a)
L_3 = 9.24e−22 cm^{6}s^{-1}
T = 7.90 μK
N [10^3]
100
10
1
(b)
T [μK]
10
1
1
10
100
t [ms]
l)
(a)
L_3 = 1.6e−21 cm^{6}s^{-1}
T = 5.50 μK
N [10^3]
100
10
1
(b)
T [μK]
10
1
1
10
100
t [ms]

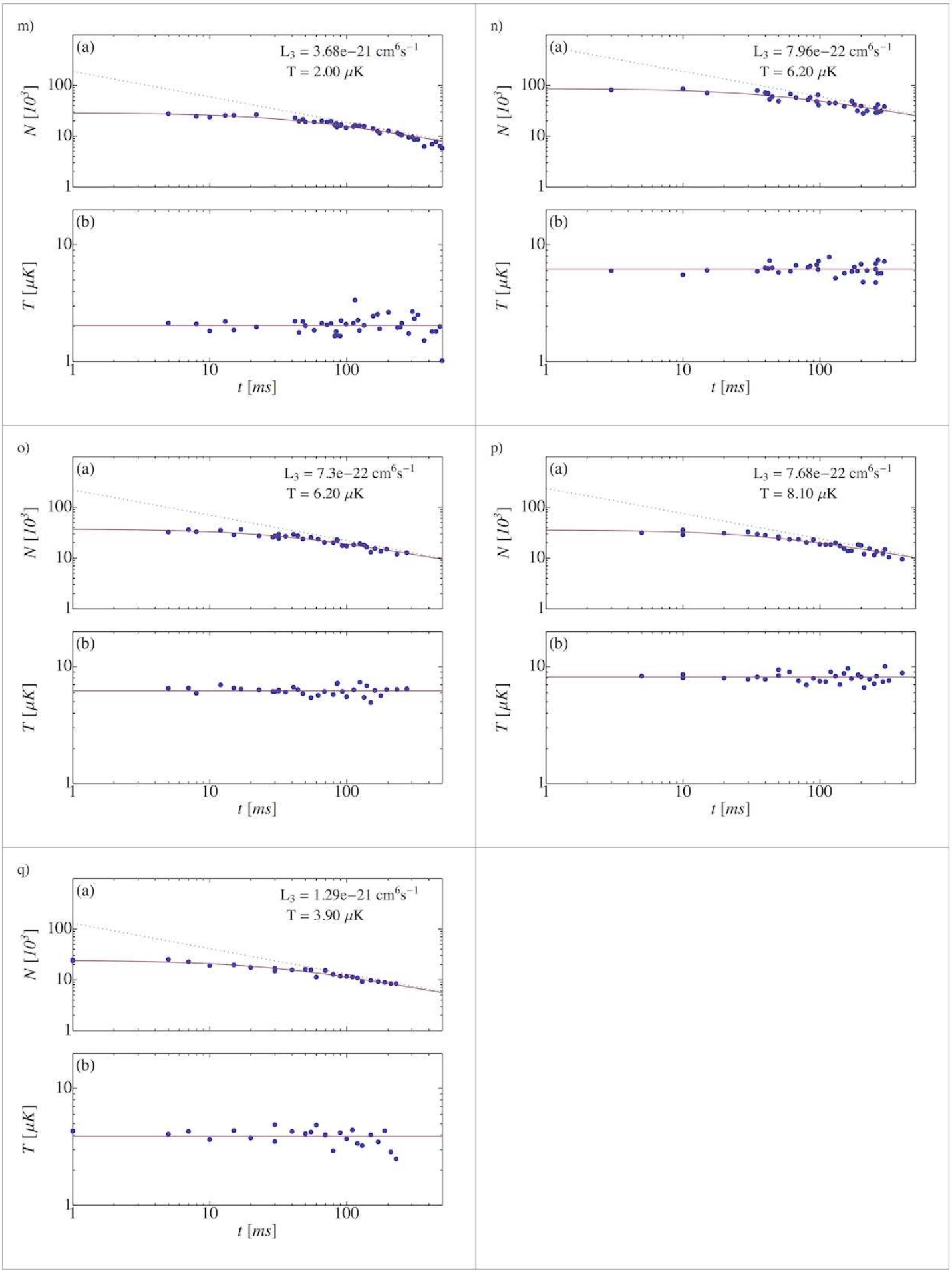
m)
(a)
L_3 = 3.68e−21 cm^{6}s^{-1}
T = 2.00 μK
N [10^3]
100
10
1
(b)
T [μK]
10
1
1
10
100
t [ms]
n)
(a)
L_3 = 7.96e−22 cm^{6}s^{-1}
T = 6.20 μK
N [10^3]
100
10
1
(b)
T [μK]
10
1
1
10
100
t [ms]
o)
(a)
L_3 = 7.3e−22 cm^{6}s^{-1}
T = 6.20 μK
N [10^3]
100
10
1
(b)
T [μK]
10
1
1
10
100
t [ms]
p)
(a)
L_3 = 7.68e−22 cm^{6}s^{-1}
T = 8.10 μK
N [10^3]
100
10
1
(b)
T [μK]
10
1
1
10
100
t [ms]
q)
(a)
L_3 = 1.29e−21 cm^{6}s^{-1}
T = 3.90 μK
N [10^3]
100
10
1
(b)
T [μK]
10
1
1
10
100
t [ms]

C.2. Finite-a Interactions

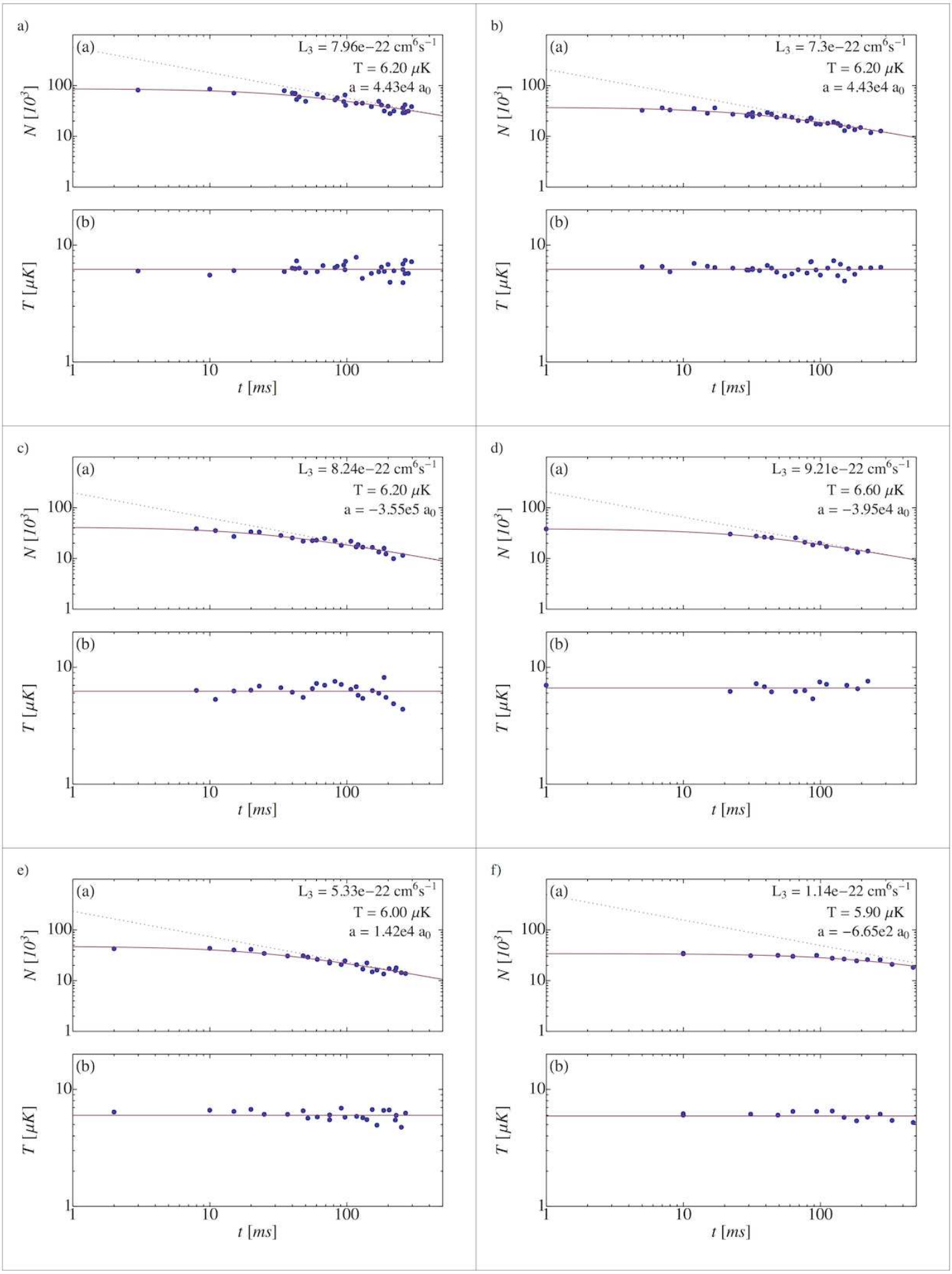
a)
(a)
L_3 = 7.96e−22 cm^{6}s^{-1}
T = 6.20 μK
a = 4.43e4 a$_0$
N [10^3]
100
10
1
(b)
T [μK]
10
1
1
10
100
t [ms]
b)
(a)
L_3 = 7.3e−22 cm^{6}s^{-1}
T = 6.20 μK
a = 4.43e4 a$_0$
N [10^3]
100
10
1
(b)
T [μK]
10
1
1
10
100
t [ms]
c)
(a)
L_3 = 8.24e−22 cm^{6}s^{-1}
T = 6.20 μK
a = −3.55e5 a$_0$
N [10^3]
100
10
1
(b)
T [μK]
10
1
1
10
100
t [ms]
d)
(a)
L_3 = 9.21e−22 cm^{6}s^{-1}
T = 6.60 μK
a = −3.95e4 a$_0$
N [10^3]
100
10
1
(b)
T [μK]
10
1
1
10
100
t [ms]
e)
(a)
L_3 = 5.33e−22 cm^{6}s^{-1}
T = 6.00 μK
a = 1.42e4 a$_0$
N [10^3]
100
10
1
(b)
T [μK]
10
1
1
10
100
t [ms]
f)
(a)
L_3 = 1.14e−22 cm^{6}s^{-1}
T = 5.90 μK
a = −6.65e2 a$_0$
N [10^3]
100
10
1
(b)
T [μK]
10
1
1
10
100
t [ms]

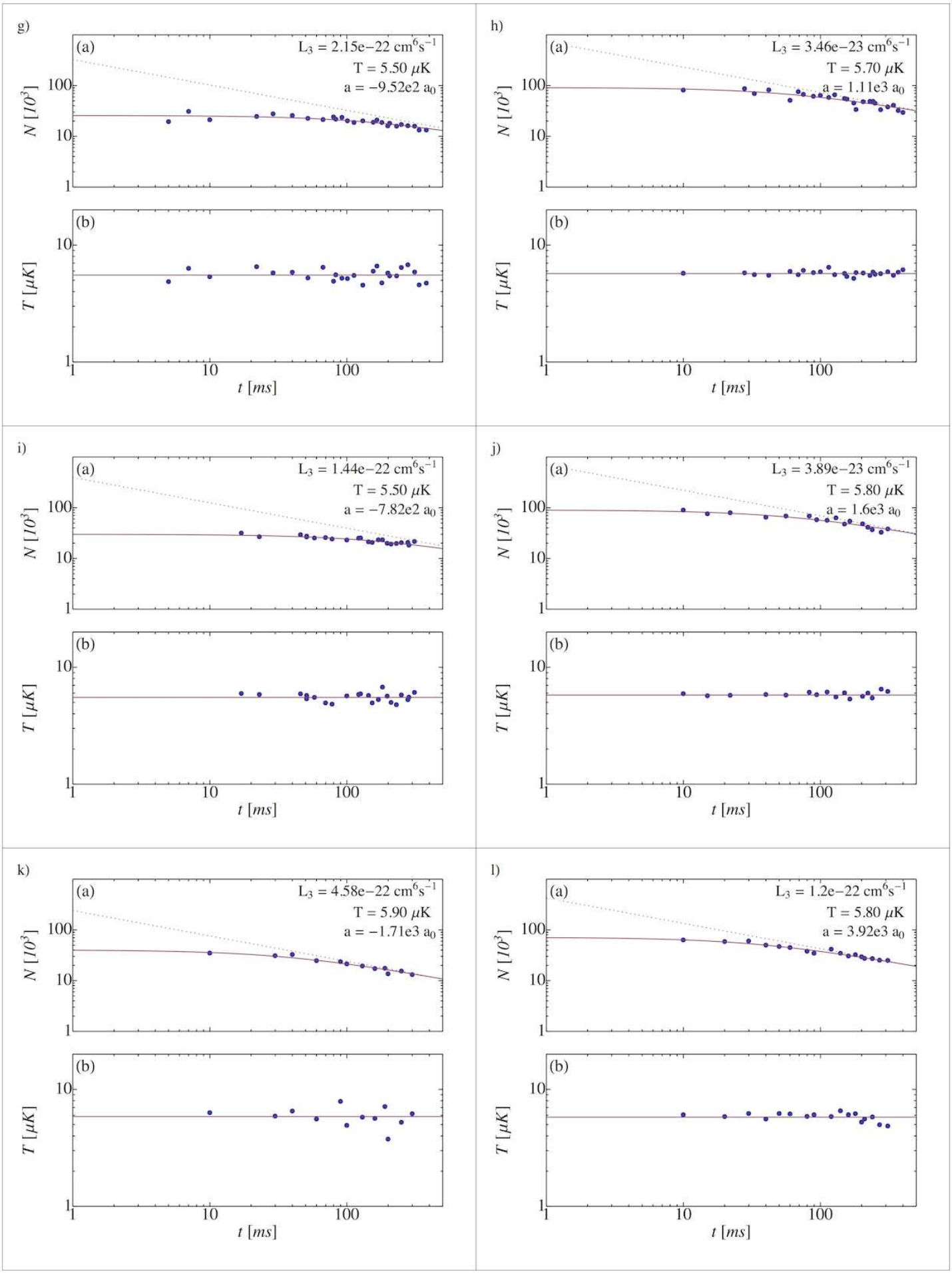
g)
(a)
L3 = 2.15e−22 cm6s−1
T = 5.50 μK
a = −9.52e2 a0
N [10^3]
100
10
1
(b)
T [μK]
10
1
1
10
100
t [ms]
h)
(a)
L3 = 3.46e−23 cm6s−1
T = 5.70 μK
a = 1.11e3 a0
N [10^3]
100
10
1
(b)
T [μK]
10
1
1
10
100
t [ms]
i)
(a)
L3 = 1.44e−22 cm6s−1
T = 5.50 μK
a = −7.82e2 a0
N [10^3]
100
10
1
(b)
T [μK]
10
1
1
10
100
t [ms]
j)
(a)
L3 = 3.89e−23 cm6s−1
T = 5.80 μK
a = 1.6e3 a0
N [10^3]
100
10
1
(b)
T [μK]
10
1
1
10
100
t [ms]
k)
(a)
L3 = 4.58e−22 cm6s−1
T = 5.90 μK
a = −1.71e3 a0
N [10^3]
100
10
1
(b)
T [μK]
10
1
1
10
100
t [ms]
l)
(a)
L3 = 1.2e−22 cm6s−1
T = 5.80 μK
a = 3.92e3 a0
N [10^3]
100
10
1
(b)
T [μK]
10
1
1
10
100
t [ms]

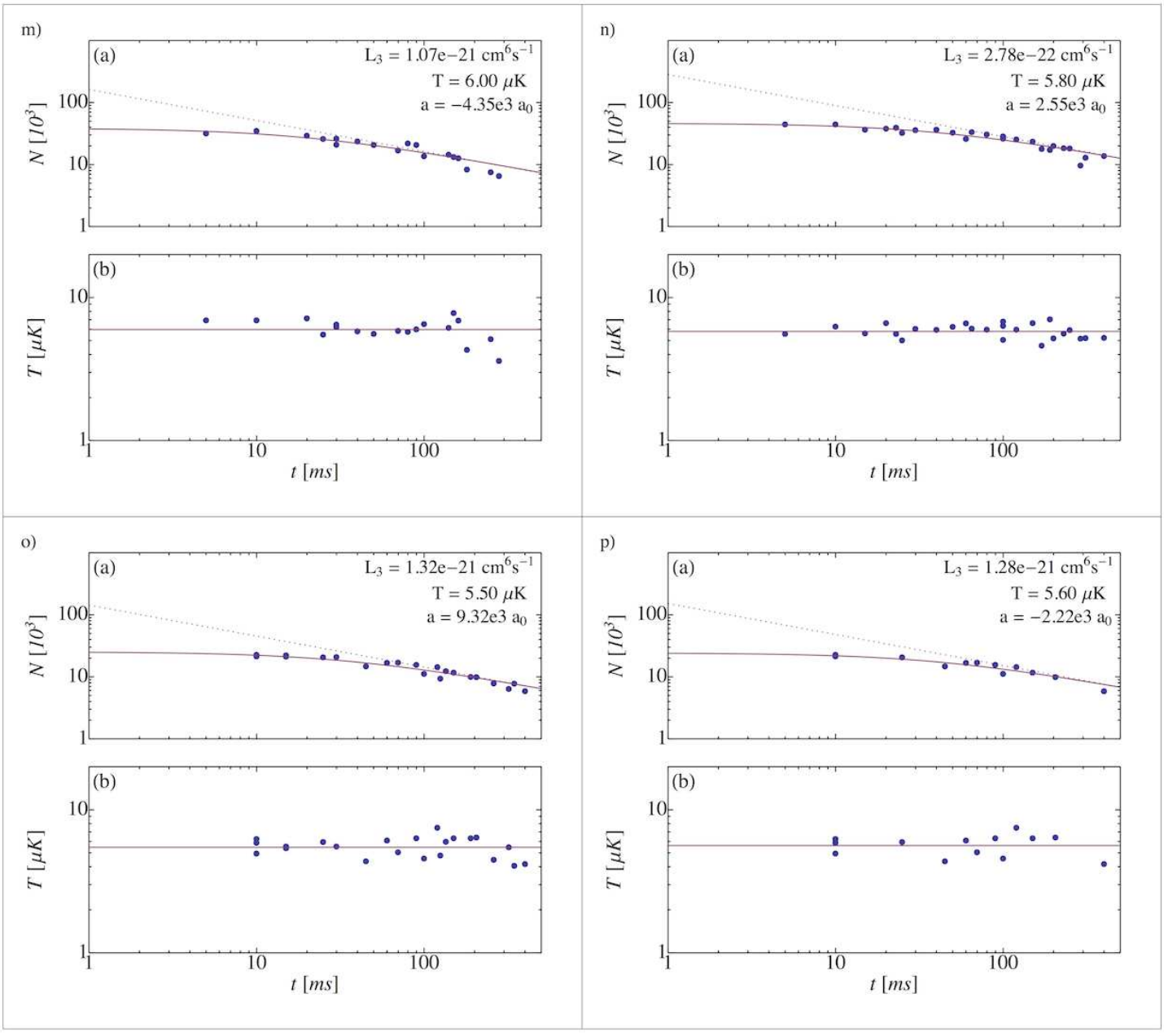
m)
(a)
L_3 = 1.07e−21 cm^{6}s^{-1}
T = 6.00 μK
a = −4.35e3 a$_0$
N [10^3]
100
10
1
(b)
T [μK]
10
1
1
10
100
t [ms]
n)
(a)
L_3 = 2.78e−22 cm^{6}s^{-1}
T = 5.80 μK
a = 2.55e3 a$_0$
N [10^3]
100
10
1
(b)
T [μK]
10
1
1
10
100
t [ms]
o)
(a)
L_3 = 1.32e−21 cm^{6}s^{-1}
T = 5.50 μK
a = 9.32e3 a$_0$
N [10^3]
100
10
1
(b)
T [μK]
10
1
1
10
100
t [ms]
p)
(a)
L_3 = 1.28e−21 cm^{6}s^{-1}
T = 5.60 μK
a = −2.22e3 a$_0$
N [10^3]
100
10
1
(b)
T [μK]
10
1
1
10
100
t [ms]

D. Efimov resonances

In this chapter, we will discuss the results previously obtained by several groups. The data is taken for the following atomic species from (in order of first appearance): ^{133}Cs Kraemer *et. al.* (2006), and Nägerl *et. al.* (2006), and Berninger *et. al.* (2011) [122, 129, 203]; ^{7}Li Pollack *et. al.* (2009) and Dyke *et. al.* (2013) [125, 202]; ^{39}K Zaccanti *et. al.* (2009) and Roy *et. al.* (2013) [124, 130]; ^{7}Li Gross *et. al.* (2009) and Gross *et. al.* (2010) [127, 128], ^{85}Rb Wild *et. al.* (2012) [96]; ^{39}K Fletcher *et. al.* (2013) [172].

The chapter is divided into sections each centered around a specific atom. The sections themselves are again divided by the type of measurements that have been done. These measurements that we performed can roughly be categorized by three themes:

1. **Zero-temperature Efimov resonance position.**
   These measurements were done for all the considered species [61, 96, 122, 124, 125, 127, 128, 130];

2. **Efimov resonance position as a function of temperature**
   These measurements have, in particular, been done for ^{133}Cs [122, 203];

3. **Unitarity saturation effects of the losses**
   Interestingly enough these measurements have not been done explicitly, but several experiments display saturation effects that were not interpreted quantitatively [61, 96, 122, 172].

We will primarily focus on the last two categories, however we will use category 2 to estimate the error caused by finite temperature effects on the determination of the position in category 1.

D.1. Caesium-133

In 2006, the group in Innsbruck for the first time found evidence for an Efimov resonance in ^{133}Cs [122]. Their research opened up a rapidly expanding research field in few-particle systems with cold atoms.

D.1.1. Universality of the Efimov resonances

Fig D.1	m_F	B_0 (G)	s_{res}	$a_-(a_0)$	η_*	$T(nK)$
(a)	+3	-12.3	560	-872(22)	0.10(3)	10
(b)	+3	550	0.9	-1029(58)	0.12(1)	15
(c)	+3	550	170	-957(80)	0.19(2)	15
(d)	+3	820.33	1470	-955(80)	0.08(1)	15

Table D.1.: The measured Efimov resonances in ^{133}Cs from [129]. The actual data with the theory comparison is shown in Figure D.1.

After the measurements on ^{7}Li in two different hyperfine states [127, 128] (see Section D.2), triggered the suggestion of a universal behavior of a_-, the group in Innsbruck started doing measurements on different Feshbach resonances in ^{133}Cs [129]. The results of these measurements are shown in Figure D.1 and Table D.1. In the figure we have again used our finite temperature theory for the specific temperatures of the measurement. As can be seen from the figure the saturation effects are small, when looking at Figure 5.8 (which was taken with the parameters corresponding to Figure D.1(a)) the shift of the position of the Efimov resonance even for $T = 15$ nK is less then $\sim 1\%$. Note that Figure D.1(a) corresponds directly to the same Efimov resonance in Figure 5.7.

D.2. Lithium-7

Lithium-7 is a rather interesting atomic species, because it has several relatively large (considering the width in magnetic field) Feshbach resonances, with the resonant strength parameter $s_{res} \sim 1$, which indicates an intermediately strong resonance. Prior to our work, two experimental groups have characterized the recombination losses as a function of the scattering length.

The first experiment was done by a group in Rice [61], where they looked at the Feshbach resonance in the hyperfine state $|F = 1, m_F = 1\rangle$ at temperatures in the range of $1\ \mu K \leq T \leq 3\ \mu K$. In order to measure the characteristics of the Feshbach resonance, however, they used the size of a BEC and extracted a as a function of magnetic field using the Thomas-Fermi approximation, with beyond-mean-field corrections. This measurement determined the Feshbach resonance to be at 736.97(7) G, but the accuracy of the method was hard to quantify. The result

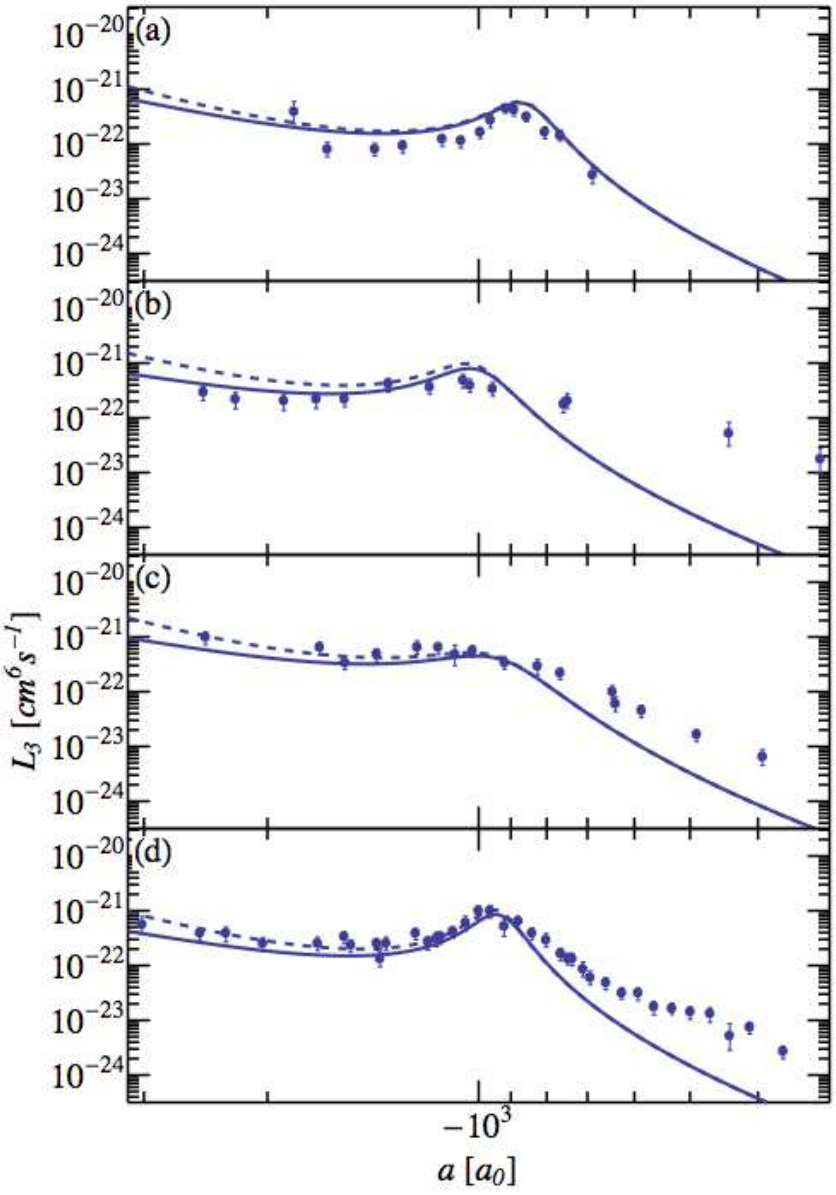

Figure D.1.: The data for four different intermediate and strong resonances in ^{133}Cs from [129].

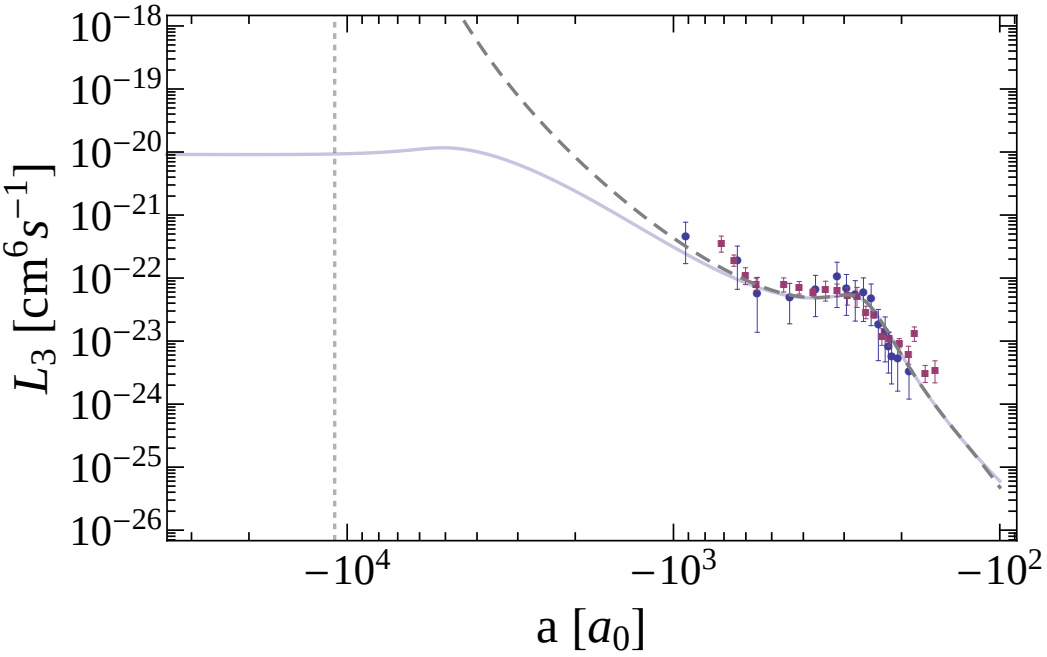

Figure D.2.: L_3 vs. a for two different hyperfine states of ^{7}Li ($|F = 1, m_F = 1\rangle$ red squares [128] and $|F = 1, m_F = 0\rangle$ blue dots [127]). The gray dashed line is the zero temperature theory with the parameters $a_- = -274\ a_0$ and $\eta = 0.25$. The light blue curve is our temperature dependent theory (see Chapter 2) with the same parameters and a temperature of $T = 1.3\ \mu K$. The dotted vertical line indicates the value of $\lambda_{\text{th}} = 1.1 \times 10^4\ a_0$. We have chosen to only show the theory for $|F = 1, m_F = 1\rangle$, this makes the picture clearer and also shows in how close agreement both measurements are.

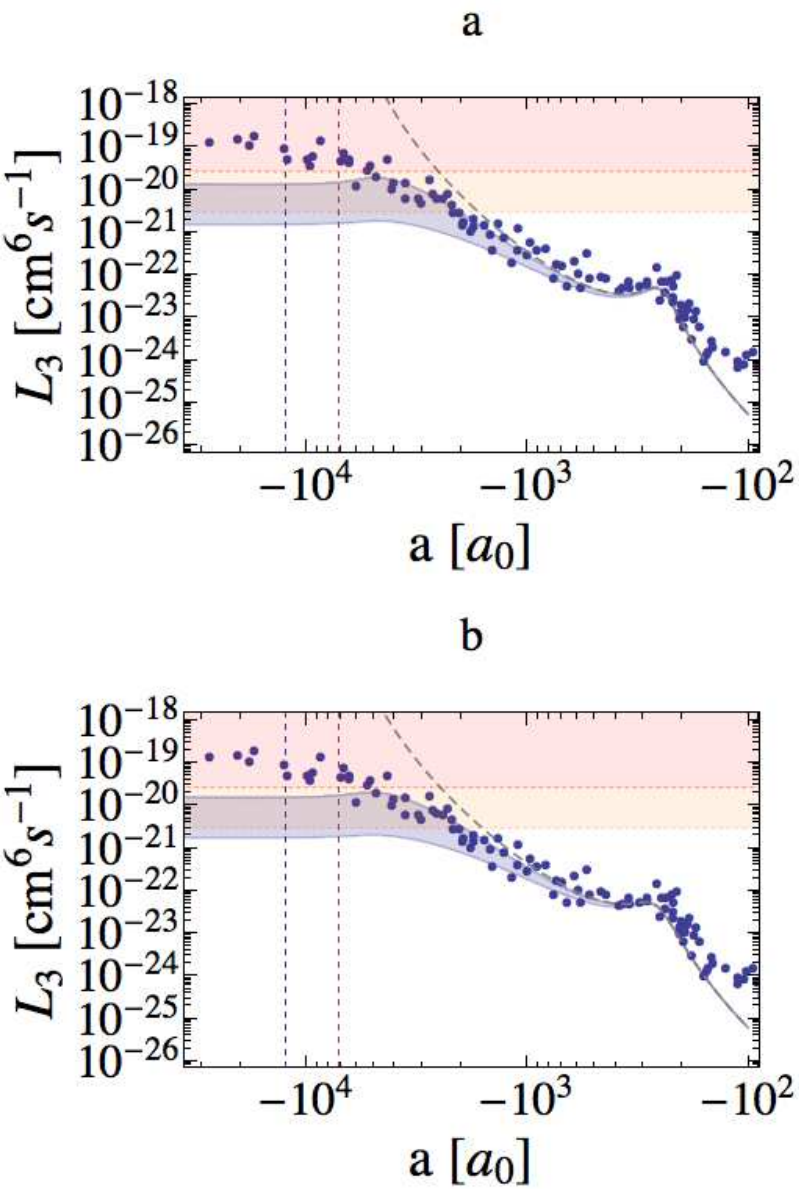

Figure D.3.: L_3 vs. a (negative a side) for one hyperfine state $|F=1, m_F=1\rangle$ for ^{7}Li taken from [61, 125]. In a the fitting parameters found in [61] are used, meaning that $a_- = -252\ a_0$ and $\eta_* = 0.17$. The temperature range in the paper goes from $T = 1\ \mu$K to $T = 3\ \mu$K, which is depicted in the blue band with the upper limit of the band corresponding to 1 μK and the lower band to 3 μK. In b the same data was plotted but the theory parameters were taken from [128], which are $a_- = -274\ a_0$ and $\eta_* = 0.25$. The vertical lines correspond to the values of the thermal wavelengths for $T = 1\ \mu$K (blue dashed) and $T = 3\ \mu$K (red dashed) respectively $\lambda_{\text{th}} = 1.2 \times 10^4\ a_0$ and $\lambda_{\text{th}} = 7.2 \times 10^3\ a_0$. The red and orange marked zones correspond to values above the maximum unitary values ($\eta_* \to \infty$). The $L_3^{\max}$ is these cases correspond to $L_3^{\max}(1\ \mu\text{K}) = 2.7 \times 10^{-20}$ cm^6 s^{-1} (red) and $L_3^{\max}(3\ \mu\text{K}) = 3.0 \times 10^{-21}$ cm^6 s^{-1} (orange), respectively.

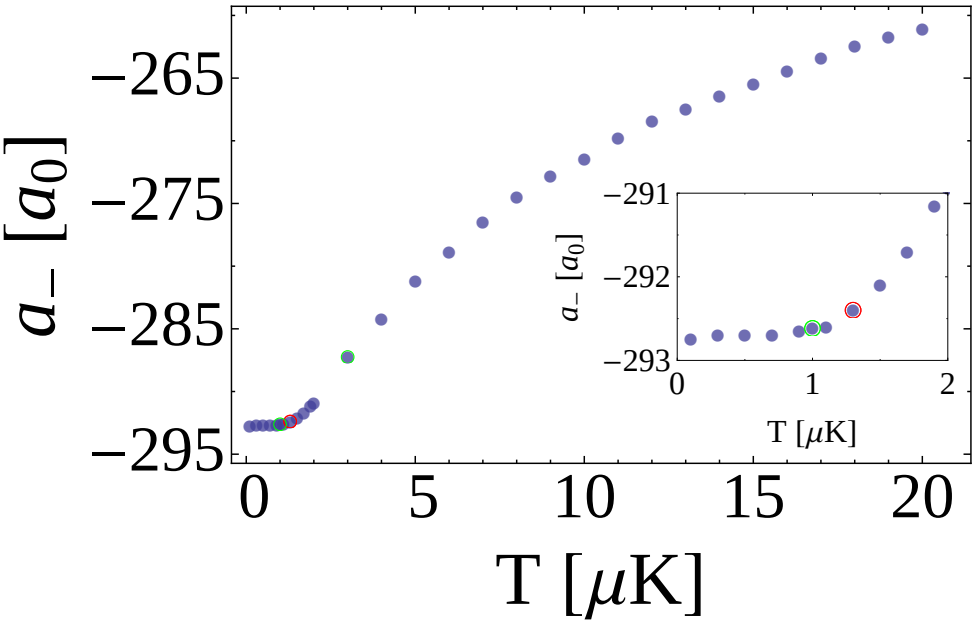

Figure D.4.: The position of the Efimov resonance as a function of temperature for ^{7}Li (We chose to only show the Efimov resonance in $|F=1, m_F=1\rangle$, since both measured Efimov resonances have similar parameters). We have taken the parameters from [127, 128, 201] ($a_- = -274\ a_0$ and $\eta_* = 0.21$, we have used our η_* in order to compare both measurements) and numerically calculated the L_3 vs. a curve for different temperatures T as was done in Figure 5.8 for caesium. The green circle indicates the temperature limits of the measurements in [61, 125], which where $T = 1\ \mu$K and $T = 3\ \mu$K. The red circle corresponds to the temperature in [127, 128, 201], which was $T = 1.3\ \mu$K. The inset shows the low temperature limit.

of the Efimov resonance measurement, is given by $a_- = -298\ a_0$ and $\eta_* = 0.13$. Also in the paper a second Efimov peak was claimed to have been seen with the following parameters: $a_-^2 = -6301\ a_0$ and the same η_* as for the first resonance.

Following these measurements, the Bar-Ilan group did the same measurement on the $|F=1, m_F=0\rangle$-state and found $a_- = -274\ a_0$ and $\eta_* = 0.253(62)$[1]. They were, however, using Radio-Frequency association of molecules [158] as a more precise measurement to determine the position of the Feshbach resonance [127] (the resonance is found at 894.63(24) G). This triggered the group to do the

[1] Note here that we used the results after doing a coupled channel calculation on three resonances in two hyperfine states of ^{7}Li [201]

same measurement on the Feshbach resonance in the $|F=1, m_F=1\rangle$-state and use the new calibration method to determine the position of the Feshbach resonance. Then loss spectroscopy was used to measure the position and width of the Efimov resonance. They found $a_- = -274\ a_0$ and $\eta_* = 0.180(48)$, with the Feshbach resonance at 738.3(3) G. Finally, the group in Bar-Ilan did a fit of the full coupled-channel calculations on the three Feshbach resonances in Lithium-7 [201] (two moderately broad and one narrow). This determined the Feshbach resonances at 845.54 G (narrow resonance in the state $|F=1, m_F=0\rangle$), 893.95(5) G (moderately strong resonance in the state $|F=1, m_F=0\rangle$) and 737.88(2) G (moderately strong resonance in the state $|F=1, m_F=1\rangle$). This last resonance was used in our group in [95] and also found to be at 737.8(2) G [185].

Finally, the initial measurement of the Feshbach resonance in the Rice group [61] has been redone using the molecule association method and they also found the resonance to be at 737.67(10) G. Their measurement of the Efimov resonance gives the following parameters: $a_- = -252\ a_0$ and $\eta_* = 0.17$. In has to also be noted that the observation of the 2nd Efimov resonance was actually an artifact of the wrong calibration and was the real position of the Feshbach resonance.

D.2.1. L_3 vs. a

Next, we will have a look at the data from Rice as given in [125], with the improved resonance position. The result is plotted in Figure D.3. The blue dots correspond to the data from the paper. We have taken the fitting results from the paper $a_- = -241\ a_0$ and $\eta_* = 0.12$ and plotted a band for the temperature range of $1\ \mu K \leq T \leq 3\ \mu K$. If we compare this directly to b, where the parameters from the Bar-Ilan group were taken ($a_- = -274\ a_0$ and $\eta_* = 0.25$), we can see that the data fits very well with the parameters from the Bar-Ilan group and worse with the old parameters.

Another puzzling feature shows up in the saturation regime, when $a \gg 1/k_{\text{th}}$. The red and orange zones in the figure mark the region above the absolute maximum unitary value $L_3^{\max}$ from Equation (2.39), corresponding respectively to $L_3^{\max}(3\mu\text{K}) = 3.0\times10^{-21}\text{cm}^6\text{s}^{-1}$. Close to unitarity the measured L_3 clearly exceeds even the absolute maximum for the lowest temperature. One could argue that when the temperature changes during the measurement the L_3 changes as well. However, three-particle recombination intrinsically heats up the cloud (see Chapter 5), which in itself lowers the L_3 meaning that this process is not very likely to cause the high value.

In Figure D.4 we have also marked (with green circles) the range of temperatures

probed by the Rice group. In the best case $T = 1$ μK their data is in the saturated regime and the correction is less then 1 % also in the worst case $T = 3$ μK the correction is less then 3 %, which is within the error bars of the determination of their Efimov resonance position.

We can clearly see that the data overshoots the unitary limit by more than a factor 10. This overshoot is not well understood, but it might be due to effect of four-particle losses. The phase-space density measured in those experiments is in the range $0.02 < n\lambda_{\mathrm{th}}^3 < 0.54$, which is rather high and close to unity and might already cause some four-particle inelastic scattering to show up. In [124], using ^{39}K, probably similar effects close to resonance have been seen. More recently, in [172] also evidence for four-particle scattering has been seen (see Section 5.3.3). For their lowest temperatures, quasi-equilibrium might already be violated.

D.3. Rubidium-85

Rubidium-85 has a rather large and negative scattering length at zero field ($a \simeq -470$ a_0[222]), this initially hampered the efforts to obtain a BEC. In 2000, however, the group in Boulder used a Feshbach resonance to stabilize the BEC [55]. This Feshbach resonance, in the state $|F = 2, m_F = 2\rangle$, is now well characterized [222], with the following parameters: $a_{\mathrm{bg}} = -443(3)$ a_0, $\Delta = 10.71(2)$ G and $B_0 = 155.041(18)$ G, where we have used the notation for the Feshbach resonance from equation (4.4).

The knowledge about the Feshbach resonance has been used in [96] to measure the three-particle recombination losses as a function of scattering length. We have taken the data from that paper and plotted these in Figure D.5 (the blue dots) and compared it with the zero-temperature theory (gray dashed curve) and our temperature dependent theory. In the paper they found the following parameters for this specific Efimov resonance: $a_- = -759$ a_0, $\eta_* = 0.06$ and the measurements were done at temperatures starting from $T = 80$ nK. Our theory does fit correctly in the zero-temperature limit $ka \to 0$, but around the Efimov resonance already clear saturation effects are appearing. This shows that the condition $a \ll \lambda_{\mathrm{th}}$ is somewhat violated, but we should note that the correction to the position of the Efimov resonance position are rather small ~ 2 % as shown in Figure D.6. In this figure the shift of the Efimov resonance maximum value is plotted as a function of temperature (blue dots). The measurements of the Boulder group correspond to the red circle.

Note that the saturation regime seems to follow the shape of curve quite well, and

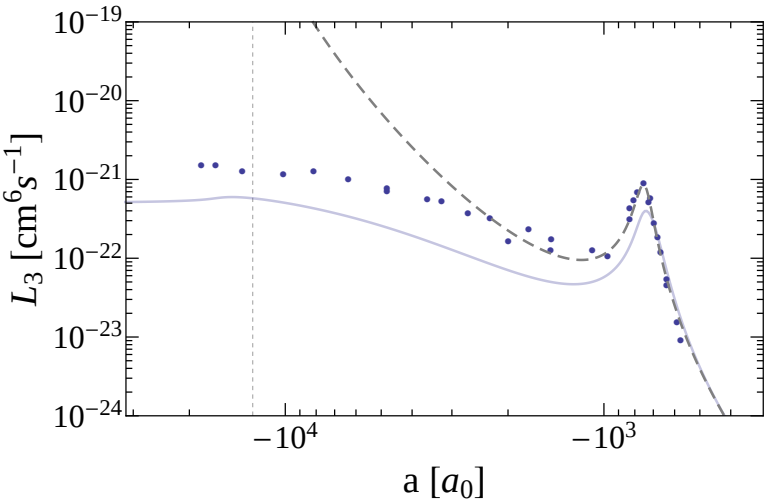

Figure D.5.: We have plotted recombination the data from [96] in the form of L_3 vs. a. The blue dots are the data taken from that paper. The measurements were done at $T = 80\ nK$ and fitted to the zero-temperature theory to determine the parameters of the Efimov resonance ($a_- = -759\ a_0$ and $\eta_* = 0.06$). We have used this information and calculated the expected theory curve for L_3 at a temperature of $T = 80\ nK$, which is shown as the light blue solid line. The vertical dashed light gray line indicates the thermal wavelength $\lambda_{\mathrm{th}} = 1.3 \times 10^4$.

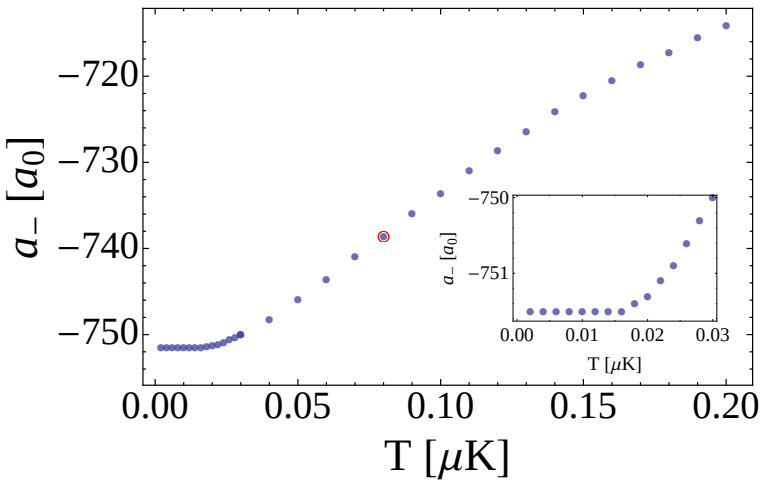

Figure D.6.: The position of the local maximum of the Efimov resonance as a function of temperature. We have used the theory (see Chapter 2), with the parameters from [96]: $a_- = -759\ a_0$ and $\eta_* = 0.06$, to determine the local maximum of the curve at the Efimov resonance as a function of temperature, which are indicated by the blue dots. The red circle corresponds to the temperature at which the measurements in Figure D.5 were done. The point corresponds to $\{80\ nK, -738.6\ a_0\}$, whereas the saturation value for $T \to 0$ goes to $a_- = -751.5\ a_0$ which is a correction of less than 2 %.

since the data was probably shifted by some offset to match the zero-temperature data, this might be the reason why the finite temperature theory does not fully describe the data.

D.4. Potassium-39

D.4.1. Efimov resonance

In 2009, the group in Florence for the first time saw two Efimov resonances on the positive-a side [124]. Their data on the negative side however showed two peaks, which were interpreted as an Efimov feature and a related four-body resonance. The position of the Efimov feature seemed to be somewhat away from the expected position and also raised a lot of questions. To overcome all the questions and issues the same group again did measurements, in 2013, on the negative-a side of several Efimov resonances [130], where they argued that the features they initially saw might have been some artifacts of their measurement, although this could also be due to different regimes for $n\lambda_{\text{th}}^3$ in the two experiments.

In the later paper they have measured the Efimov resonances for five intermediately strong Feshbach resonances which we will consider in the following.

D.4.2. Universality of the Efimov resonances in ^{39}K

Fig D.7	m_F	B_0 (G)	s_{res}	$a_-(a_0)$	η_*	$T(nK)$
(a)	+1	402.6(2)	2.8	690(40)	0.145(12)	90(6)
(b)	0	471.0(4)	2.8	640(100)	0.065(11)	50(5)
(c)	-1	33.64(15)	2.6	830(140)	0.204(10)	120(10)
(d)	-1	560.72(20)	2.5	640(90)	0.22(2)	20(7)
(e)	-1	162.35(18)	1.1	730(120)	0.26(5)	40(5)

Table D.2.: The measured Efimov resonances in ^{39}K from [130]. The actual data with the theory comparison is shown in Figure D.7.

In [130] the authors have looked at a total of 7 resonances: five moderately strong resonances $1.1 < s_{\text{res}} < 2.8$ and two weak resonances $s_{\text{res}} = 0.11$ and $s_{\text{res}} = 0.14$. In Figure D.7 the five intermediately strong resonances are shown. In the plots we have compared the data (blue dots) with both zero temperature theory (dashed

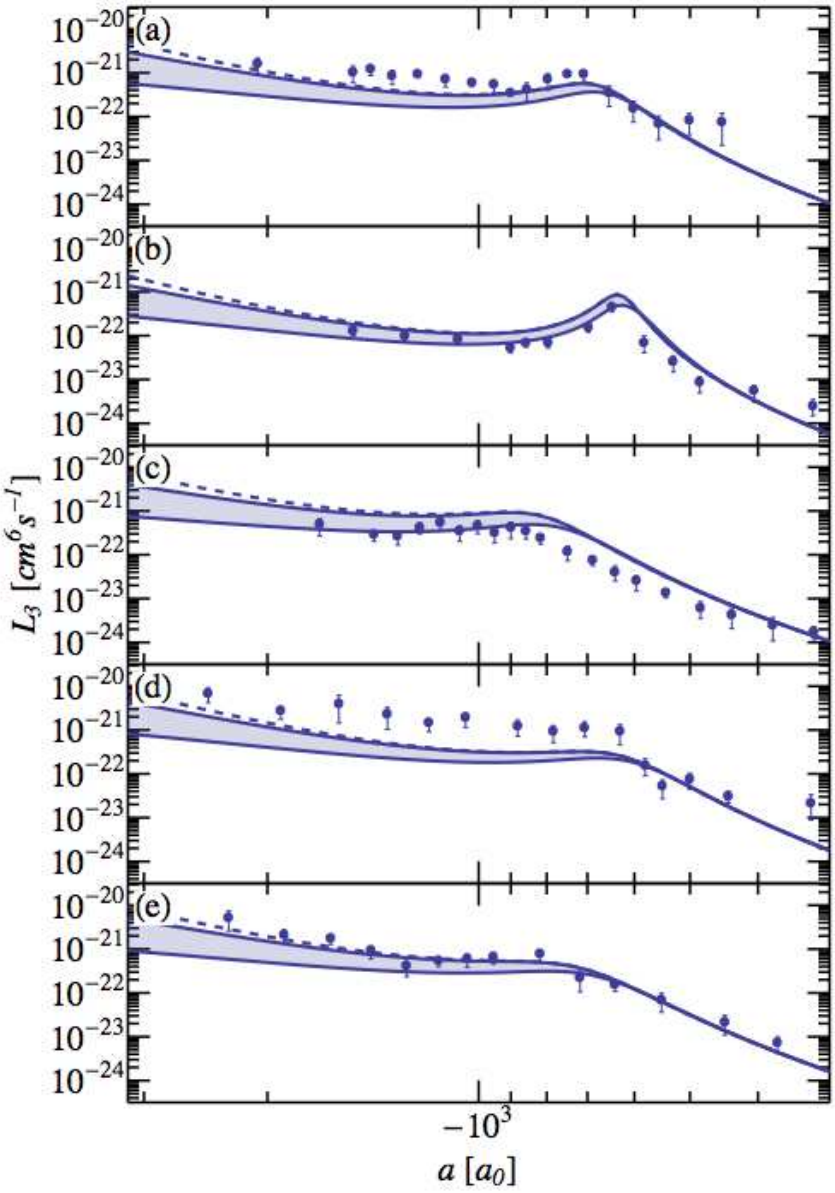

Figure D.7.: The data for five different intermediate resonances taken from [130]. The details about the measurements in the individual figure (a) - (e) are given in Table D.2. In all the blue dots correspond to the measurements. The dashed blue line to the zero-temperature theory and solid blue lines with the shaded region to the finite temperature theory with $40 < T < 200$ nK.

blue line) and finite temperature theory for the temperature range $40 < T < 200$ nK (solid blue lines and blue shaded region). The exact parameters for each figure can be found in Table D.2. We can clearly see that the finite temperature saturation effects are rather small, meaning that a_- is only very slightly modified by the finite temperature, which is within their error bars.

D.5. How to determine the Efimov parameters

First of all, and most trivially, when measuring the position of the Efimov resonance one has to be far away from the inset of unitarity, in practice this means $|a| \ll 1/k_{\text{th}}$. Quite often it might be even more practical to do the measurements for different temperatures and determine the exact saturation value (for $T \to 0$) of a_-. The finite temperature theory should then be used to calculate the shift of the Efimov peak with temperature and fit this result. This procedure should give an accurate value of a_- and an initial value for η_*.

Secondly, a second way of determining η_* is through the unitarity limited value of L_3, when measurements are done for different temperatures at unitarity, one should be able to determine η_* with great accuracy. In [172] they where even able to completely remove evaporative losses (but not have constant temperature) and use the exponents β and ν to find the value of η_* for ^{39}K at unitarity.

Together these methods should improve both the accuracy on a_- and η_*.

D.6. Summary

In this chapter, we have been comparing previous experiments with the theory developed in our group (see Chapter 2). This was done for different atomic species, each corresponding to a section:

- ^{133}Cs in the state $|F = 3, m_F = 3\rangle$
- ^{7}Li in the states $|F = 1, m_F = 1\rangle$ and $|F = 1, m_F = 0\rangle$
- ^{85}Rb in the state $|F = 2, m_F = -2\rangle$
- ^{39}K in the states $|F = 1, m_F = +1\rangle$, $|F = 1, m_F = 0\rangle$, and $|F = 1, m_F = -1\rangle$.

The type of measurements that have been done could be classified into three categories:

- Zero-temperature Efimov resonance position

- Efimov resonance position as a function of temperature, which has in particular been done for ^{133}Cs
- Unitarity saturation effects on the losses.

Bibliography

[1] I. Bloch, J. Dalibard, and W. Zwerger. *Many-body physics with ultracold gases*. Reviews of Modern Physics **80**, 885–964 (2008).

[2] W. Pauli. *The Connection Between Spin and Statistics*. Physical Review **58**, 716–722 (1940).

[3] P. D. Lett, W. D. Phillips, S. L. Rolston, C. E. Tanner, R. N. Watts, and C. I. Westbrook. *Optical molasses*. Journal of the Optical Society of America B **6**, 2084–2107 (1989).

[4] W. Ketterle and N. Druten. *Evaporative cooling of trapped atoms*. Advances in Atomic, Molecular, and Optical Physics **37**, 181–236 (1996).

[5] M. Anderson, J. Ensher, M. Matthews, C. Wieman, and E. Cornell. *Observation of Bose-Einstein condensation in a dilute atomic vapor*. Science **269**, 198–198 (1995).

[6] K. Davis and W. Ketterle. *Bose-Einstein condensation in a gas of sodium atoms*. Physical Review Letters **75**, 3969–3973 (1995).

[7] Bose. *Plancks Gesetz und Lichtquantenhypothese*. Z Physik **26**, 178–181 (1924).

[8] A. Einstein. *Quantentheorie des einatomigen idealen Gases*. Sitzungsberichte der Preußischen Akademie der Wissenschaften **3**, 18 (1925).

[9] B. DeMarco and D. S. Jin. *Exploring a quantum degenerate gas of fermionic atoms*. Physical Review A **58**, R4267–R4270 (1998).

[10] A. G. Truscott, K. E. Strecker, W. I. McAlexander, G. B. Partridge, and R. G. Hulet. *Observation of Fermi pressure in a gas of trapped atoms*. Science **291**, 2570–2572 (2001).

[11] F. Schreck, L. Khaykovich, K. L. Corwin, G. Ferrari, T. Bourdel, J. Cubizolles, and C. Salomon. *Quasipure Bose-Einstein Condensate Immersed in a Fermi Sea*. Physical Review Letters **87**, 080403 (2001).

[12] J. McGreevy. *In pursuit of a nameless metal*. Physics **3**, 83 (2010).

[13] P. W. Anderson. *Absence of Diffusion in Certain Random Lattices*. Phys.Rev. **109**, 1492–1505 (1958).

[14] G. A. Baker. *The MBX Challenge Competition: A Neutron Matter Model*. In *Recent Progress in Many-Body Theories*, pages 15–21. (). URL `http://www.worldscientific.com/doi/abs/10.1142/9789812792754_0003`.

[15] W. Ketterle, D. S. Durfee, and D. M. Stamper-Kurn. *Making, probing and understanding Bose-Einstein condensates*. arXiv **cond-mat** (1999). URL `http://arxiv.org/abs/cond-mat/9904034v2`.

[16] R. Grimm, M. Weidemüller, and Y. B. Ovchinnikov. *Optical dipole traps for neutral atoms*. Advances in Atomic, Molecular, and Optical Physics **42**, 95–170 (2000).

[17] A. L. Gaunt and Z. Hadzibabic. *Robust Digital Holography For Ultracold Atom Trapping*. Scientific Reports **2** (2012).

[18] A. L. Gaunt, T. F. Schmidutz, I. Gotlibovych, R. P. Smith, and Z. Hadzibabic. *Bose-Einstein condensation of atoms in a uniform potential*. Physical Review Letters **110**, 200406 (2013).

[19] M. Cheneau. *Transition superfluide et potentiels géométriques dans le gaz de Bose bidimensionnel*. PhD thesis, Université Pierre et Marie Curie-Paris VI (2009). URL `http://hal.archives-ouvertes.fr/tel-00556002/`.

[20] D. Jaksch, C. Bruder, J. Cirac, C. Gardiner, and P. Zoller. *Cold Bosonic Atoms in Optical Lattices*. Physical Review Letters **81**, 3108–3111 (1998).

[21] W. S. Bakr, J. I. Gillen, A. Peng, S. Fölling, and M. Greiner. *A quantum gas microscope for detecting single atoms in a Hubbard-regime optical lattice*. Nature **462**, 74–77 (2009).

[22] J. F. Sherson, C. Weitenberg, M. Endres, M. Cheneau, I. Bloch, and S. Kuhr. *Single-atom-resolved fluorescence imaging of an atomic Mott insulator*. Nature **467**, 68–72 (2010).

[23] C. Weitenberg, M. Endres, J. F. Sherson, M. Cheneau, P. Schauß, T. Fukuhara, I. Bloch, and S. Kuhr. *Single-spin addressing in an atomic Mott insulator*. Nature **471**, 319–324 (2011).

[24] M. Greiner, O. Mandel, T. Esslinger, T. W. H. a. nsch, and I. Bloch. *Quantum phase transition from a superfluid to a Mott insulator in a gas of ultracold atoms*. Nature **415**, 39–44 (2002).

[25] M. Köhl, H. Moritz, T. Stöferle, K. Günter, and T. Esslinger. *Fermionic Atoms in a Three Dimensional Optical Lattice: Observing Fermi Surfaces, Dynamics, and Interactions*. Physical Review Letters **94**, 080403 (2005).

[26] J. Struck, C. Ölschläger, R. Le Targat, P. Soltan-Panahi, A. Eckardt, M. Lewenstein, P. Windpassinger, and K. Sengstock. *Quantum simulation of frustrated classical magnetism in triangular optical lattices*. Science **333**, 996–999 (2011).

[27] J. Simon, W. S. Bakr, R. Ma, M. E. Tai, P. M. Preiss, and M. Greiner. *Quantum simulation of antiferromagnetic spin chains in an optical lattice*. Nature **472**, 307–312 (2011).

[28] D. Greif, T. Uehlinger, G. Jotzu, L. Tarruell, and T. Esslinger. *Short-Range Quantum Magnetism of Ultracold Fermions in an Optical Lattice*. Science **340**, 1307–1310 (2013).

[29] V. L. Berezinskii. *Destruction of long-range order in one-dimensional and two-dimensional systems possessing a continuous symmetry group. ii. quantum systems*. Soviet Journal of Experimental and Theoretical Physics **34**, 610 (1972). URL `http://adsabs.harvard.edu/abs/1972JETP...34..610B`.

[30] J. M. Kosterlitz and D. J. Thouless. *Ordering, metastability and phase transitions in two-dimensional systems*. Journal of Physics C: Solid State Physics **6**, 1181 (1973).

[31] N. D. Mermin and H. Wagner. *Absence of Ferromagnetism or Antiferromagnetism in One- or Two-Dimensional Isotropic Heisenberg Models*. Phys.Rev.Lett. **17**, 1133–1136 (1966).

[32] Z. Hadzibabic, P. Krüger, M. Cheneau, B. Battelier, and J. Dalibard. *Berezinskii–Kosterlitz–Thouless crossover in a trapped atomic gas*. Nature **441**, 1118–1121 (2006).

[33] R. Desbuquois, L. Chomaz, T. Yefsah, J. Léonard, J. Beugnon, C. Weitenberg, and J. Dalibard. *Superfluid behaviour of a two-dimensional Bose gas*. Nature Physics **8**, 645–648 (2012).

[34] S. R. White. *Density matrix formulation for quantum renormalization groups*. Phys.Rev.Lett. **69**, 2863–2866 (1992).

[35] B. Paredes, A. Widera, V. Murg, O. Mandel, S. Fölling, I. Cirac, G. V. Shlyapnikov, T. W. Hänsch, and I. Bloch. *Tonks–Girardeau gas of ultracold atoms in an optical lattice*. Nature **429**, 277–281 (2004).

[36] T. Kinoshita, T. Wenger, and D. S. Weiss. *Observation of a one-dimensional Tonks-Girardeau gas*. Science **305**, 1125–1128 (2004).

[37] M. Gring, M. Kuhnert, T. Langen, T. Kitagawa, B. Rauer, M. Schreitl, I. Mazets, D. A. Smith, E. Demler, and J. Schmiedmayer. *Relaxation and prethermalization in an isolated quantum system*. Science **337**, 1318–1322 (2012).

[38] D. J. Thouless, M. Kohmoto, M. P. Nightingale, and M. Den Nijs. *Quantized Hall conductance in a two-dimensional periodic potential*. Phys.Rev.Lett. **49**, 405–408 (1982).

[39] M. Kohmoto. *Zero modes and the quantized Hall conductance of the two-dimensional lattice in a magnetic field*. Physical Review B **39**, 11943 (1989).

[40] D. R. Hofstadter. *Energy levels and wave functions of Bloch electrons in rational and irrational magnetic fields*. Physical Review B **14**, 2239 (1976).

[41] M. Matthews, B. Anderson, P. Haljan, D. Hall, C. Wieman, and E. Cornell. *Vortices in a Bose-Einstein condensate*. Physical Review Letters **83**, 2498–2501 (1999).

[42] K. W. Madison, F. Chevy, W. Wohlleben, and J. Dalibard. *Vortex formation in a stirred Bose-Einstein condensate*. Physical Review Letters **84**, 806 (2000).

[43] J. R. Abo-Shaeer, C. Raman, J. M. Vogels, and W. Ketterle. *Observation of Vortex Lattices in Bose-Einstein Condensates*. Science **292**, 476–479 (2001).

[44] E. Hodby, G. Hechenblaikner, S. Hopkins, O. Marago, and C. Foot. *Vortex nucleation in Bose-Einstein condensates in an oblate, purely magnetic potential*. Physical Review Letters **88**, 010405 (2001).

[45] M. W. Zwierlein, J. R. Abo-Shaeer, A. Schirotzek, C. H. Schunck, and W. Ketterle. *Vortices and superfluidity in a strongly interacting Fermi gas*. Nature **435**, 1047–1051 (2005).

[46] J. Dalibard, F. Gerbier, G. Juzeliūnas, and P. Öhberg. *Colloquium: Artificial gauge potentials for neutral atoms*. Reviews of Modern Physics **83**, 1523 (2011).

[47] H. Feshbach. *Unified Theory of Nuclear Reactions*. Reviews of Modern Physics **36**, 1076–1078 (1964).

[48] C. Chin, R. Grimm, P. Julienne, and E. Tiesinga. *Feshbach resonances in ultracold gases*. Reviews of Modern Physics **82**, 1225 (2010).

[49] E. Tiesinga, B. J. Verhaar, and H. T. C. Stoof. *Threshold and resonance phenomena in ultracold ground-state collisions*. Physical Review A **47**, 4114–4122 (1993).

[50] U. Fano. *Effects of configuration interaction on intensities and phase shifts*. Physical Review **124**, 1866 (1961).

[51] W. C. Stwalley. *Stability of Spin-Aligned Hydrogen at Low Temperatures and High Magnetic Fields: New Field-Dependent Scattering Resonances and Predissociations*. Physical Review Letters **37**, 1628–1631 (1976).

[52] M. W. Reynolds, I. Shinkoda, R. W. Cline, and W. N. Hardy. *Observation of inverse predissociation of spin-polarized atomic hydrogen at low temperatures*. Physical Review B **34**, 4912–4915 (1986).

[53] S. Inouye, M. R. Andrews, J. Stenger, H.-J. Miesner, D. M. Stamper-Kurn, and W. Ketterle. *Observation of Feshbach resonances in a Bose–Einstein condensate*. Nature **392**, 151–154 (1998).

[54] P. Courteille, R. S. Freeland, and D. J. Heinzen. *Observation of a Feshbach Resonance in Cold Atom Scattering*. Physical Review Letters **81**, 69–72 (1998).

[55] S. L. Cornish, N. R. Claussen, J. L. Roberts, E. A. Cornell, and C. E. Wieman. *Stable ^{85} Rb Bose-Einstein Condensates with Widely Tunable Interactions*. Physical Review Letters **85**, 1795 (2000).

[56] T. Weber, J. Herbig, M. Mark, H.-C. Nägerl, and R. Grimm. *Three-Body Recombination at Large Scattering Lengths in an Ultracold Atomic Gas*. Physical Review Letters **91**, 123201 (2003).

[57] T. Kraemer, J. Herbig, M. Mark, T. Weber, C. Chin, H. C. N gerl, and R. Grimm. *Optimized production of a cesium Bose-Einstein condensate*. Applied Physics B **79**, 1013–1019 (2004).

[58] G. Roati, M. Zaccanti, C. D'Errico, J. Catani, M. Modugno, A. Simoni, M. Inguscio, and G. Modugno. *^{39}K Bose-Einstein Condensate with Tunable Interactions*. Physical Review Letters **99**, 010403 (2007).

[59] F. Schreck. *Mixtures of ultracold gases: Fermi sea and Bose-Einstein condensate of lithium isotopes*. PhD thesis, Annales de Physique (2003). URL `http://adsabs.harvard.edu/abs/2003AnPh...28b...1S`.

[60] N. Gross and L. Khaykovich. *All-optical production of ^{7}Li Bose-Einstein condensation using Feshbach resonances*. Physical Review A **77**, 023604 (2008).

[61] S. Pollack, D. Dries, M. Junker, Y. Chen, T. Corcovilos, and R. Hulet. *Extreme Tunability of Interactions in a ^{7} Li Bose-Einstein Condensate*. Physical Review Letters **102**, 90402 (2009).

[62] E. A. Donley, N. R. Claussen, S. T. Thompson, and C. E. Wieman. *Atom–molecule coherence in a Bose–Einstein condensate*. Nature **417**, 529–533 (2002).

[63] C. Chin, A. Kerman, V. Vuletić, and S. Chu. *Sensitive Detection of Cold Cesium Molecules Formed on Feshbach Resonances*. Physical Review Letters **90**, 033201 (2003).

[64] J. Herbig, T. Kraemer, M. Mark, T. Weber, C. Chin, H.-C. Nägerl, and R. Grimm. *Preparation of a pure molecular quantum gas*. Science **301**, 1510–1513 (2003).

[65] S. Jochim, M. Bartenstein, A. Altmeyer, G. Hendl, S. Riedl, C. Chin, J. H. Denschlag, and R. Grimm. *Bose-Einstein condensation of molecules*. Science **302**, 2101–2103 (2003).

[66] M. Zwierlein, C. Stan, C. Schunck, S. Raupach, S. Gupta, Z. Hadzibabic, and W. Ketterle. *Observation of Bose-Einstein Condensation of Molecules*. Physical Review Letters **91**, 250401 (2003).

[67] T. Bourdel, L. Khaykovich, J. Cubizolles, J. Zhang, F. Chevy, M. Teichmann, L. Tarruell, S. Kokkelmans, and C. Salomon. *Experimental Study of the BEC-BCS Crossover Region in Lithium 6*. Physical Review Letters **93**, 050401 (2004).

[68] M. Greiner, C. A. Regal, and D. S. Jin. *Emergence of a molecular Bose–Einstein condensate from a Fermi gas*. Nature **426**, 537–540 (2003).

[69] K. Bergmann, H. Theuer, and B. Shore. *Coherent population transfer among quantum states of atoms and molecules*. Reviews of Modern Physics **70**, 1003–1025 (1998).

[70] S. Kokkelmans, H. Vissers, and B. Verhaar. *Formation of a Bose condensate of stable molecules via a Feshbach resonance*. Physical Review A **63**, 031601 (2001).

[71] K. Winkler, F. Lang, G. Thalhammer, P. Straten, R. Grimm, and J. Denschlag. *Coherent Optical Transfer of Feshbach Molecules to a Lower Vibrational State*. Physical Review Letters **98**, 043201 (2007).

[72] K.-K. Ni, S. Ospelkaus, M. De Miranda, A. Pe'er, B. Neyenhuis, J. J. Zirbel, S. Kotochigova, P. S. Julienne, D. S. Jin, and J. Ye. *A high phase-space-density gas of polar molecules*. Science **322**, 231–235 (2008).

[73] L. Cooper. *Bound Electron Pairs in a Degenerate Fermi Gas*. Physical Review **104**, 1189–1190 (1956).

[74] J. Bardeen, L. N. Cooper, and J. R. Schrieffer. *Theory of Superconductivity*. Physical Review **108**, 1175–1204 (1957).

[75] D. Eagles. *Possible Pairing without Superconductivity at Low Carrier Concentrations in Bulk and Thin-Film Superconducting Semiconductors*. Physical Review **186**, 456–463 (1969).

[76] A. J. Leggett. *Diatomic molecules and Cooper pairs*. In *Modern trends in the theory of condensed matter*, pages 13–27. Springer (1980). ISBN 978-3-540-09752-5. URL `http://link.springer.com/chapter/10.1007%2FBFb0120125`.

[77] P. Nozières and S. Schmitt-Rink. *Bose condensation in an attractive fermion gas: From weak to strong coupling superconductivity*. Journal of Low Temperature Physics **59**, 195–211 (1985).

[78] T. Loftus, C. Regal, C. Ticknor, J. Bohn, and D. Jin. *Resonant Control of Elastic Collisions in an Optically Trapped Fermi Gas of Atoms*. Physical Review Letters **88**, 173201 (2002).

[79] K. O'Hara, S. Hemmer, M. Gehm, S. Granade, and J. Thomas. *Observation of a strongly interacting degenerate Fermi gas of atoms*. Science **298**, 2179 (2002).

[80] J. Kinast, S. Hemmer, M. Gehm, A. Turlapov, and J. Thomas. *Evidence for Superfluidity in a Resonantly Interacting Fermi Gas*. Physical Review Letters **92**, 150402 (2004).

[81] M. Bartenstein, A. Altmeyer, S. Riedl, S. Jochim, C. Chin, J. H. Denschlag, and R. Grimm. *Collective excitations of a degenerate gas at the BEC-BCS crossover*. Physical Review Letters **92**, 203201 (2004).

[82] A. Altmeyer, S. Riedl, C. Kohstall, M. Wright, R. Geursen, M. Bartenstein, C. Chin, J. Denschlag, and R. Grimm. *Precision Measurements of Collective Oscillations in the BEC-BCS Crossover*. Physical Review Letters **98**, 040401 (2007).

[83] C. Chin. *Observation of the Pairing Gap in a Strongly Interacting Fermi Gas*. Science **305**, 1128–1130 (2004).

[84] S. Nascimbène, N. Navon, K. Jiang, F. Chevy, and C. Salomon. *Exploring the thermodynamics of a universal Fermi gas*. Nature **463**, 1057–1060 (2010).

[85] N. Navon, S. Nascimbène, F. Chevy, and C. Salomon. *The Equation of State of a Low-Temperature Fermi Gas with Tunable Interactions*. Science **328**, 729–732 (2010).

[86] M. J. Ku, A. T. Sommer, L. W. Cheuk, and M. W. Zwierlein. *Revealing the superfluid lambda transition in the universal thermodynamics of a unitary Fermi gas*. Science **335**, 563–567 (2012).

[87] S. Nascimbène, N. Navon, F. Chevy, and C. Salomon. *The equation of state of ultracold Bose and Fermi gases: a few examples*. New Journal of Physics **12**, 103026 (2010).

[88] K. Van Houcke, F. Werner, E. Kozik, N. Prokof'ev, B. Svistunov, M. J. H. Ku, A. T. Sommer, L. W. Cheuk, A. Schirotzek, and M. W. Zwierlein. *Feynman diagrams versus Fermi-gas Feynman emulator*. Nature Physics **8**, 366–370 (2012).

[89] F. Dalfovo, S. Giorgini, L. Pitaevskii, and S. Stringari. *Theory of Bose-Einstein condensation in trapped gases*. Reviews of Modern Physics **71**, 463–512 (1999).

[90] E. P. Gross. *Structure of a quantized vortex in boson systems*. Il Nuovo Cimento **20**, 454–477 (1961).

[91] L. P. Pitaevskii. *Vortex lines in an imperfect Bose gas*. Sov. Phys. JETP **13**, 451–454 (1961).

[92] T. Lee, K. Huang, and C. Yang. *Eigenvalues and eigenfunctions of a Bose system of hard spheres and its low-temperature properties*. Physical Review **106**, 1135–1145 (1957).

[93] S. B. Papp, J. M. Pino, R. J. Wild, S. Ronen, C. E. Wieman, D. S. Jin, and E. A. Cornell. *Bragg Spectroscopy of a Strongly Interacting ^{85}Rb Bose-Einstein Condensate*. Physical Review Letters **101**, 135301 (2008).

[94] Y.-i. Shin, A. Schirotzek, C. Schunck, and W. Ketterle. *Realization of a Strongly Interacting Bose-Fermi Mixture from a Two-Component Fermi Gas*. Physical Review Letters **101**, 070404 (2008).

[95] N. Navon, S. Piatecki, K. Günter, B. Rem, T. C. Nguyen, F. Chevy, W. Krauth, and C. Salomon. *Dynamics and thermodynamics of the low-temperature strongly interacting bose gas*. Physical Review Letters **107**, 135301 (2011).

[96] R. Wild, P. Makotyn, J. Pino, E. Cornell, and D. Jin. *Measurements of Tan's Contact in an Atomic Bose-Einstein Condensate*. Physical Review Letters **108**, 145305 (2012).

[97] K. Huang. *Statistical mechanics*. Wiley (1987). ISBN 9780471815181.

[98] L. D. Landau and E. M. Lifshitz. *Statistical Physics*, volume 5 of *Course of Theoretical Physics*. Pergamon Press, second revised and enlarged edition edition (1970).

[99] Y. Castin and F. Werner. *Le troisième coefficient du viriel du gaz de Bose unitaire*. Canadian Journal of Physics **91**, 382–389 (2013).

[100] T.-L. Ho. *Universal Thermodynamics of Degenerate Quantum Gases in the Unitarity Limit*. Physical Review Letters **92**, 090402 (2004).

[101] G. Baker. *Neutron matter model*. Physical Review C **60**, 054311 (1999).

[102] Y.-L. Lee and Y.-W. Lee. *Universality and stability for a dilute Bose gas with a Feshbach resonance*. Physical Review A **81**, 063613 (2010).

[103] J. Song and F. Zhou. *Ground State Properties of Cold Bosonic Atoms at Large Scattering Lengths*. Physical Review Letters **103**, 025302 (2009).

[104] S. Cowell, H. Heiselberg, I. Mazets, J. Morales, V. Pandharipande, and C. Pethick. *Cold Bose Gases with Large Scattering Lengths*. Physical Review Letters **88**, 210403 (2002).

[105] L. Radzihovsky, J. Park, and P. Weichman. *Superfluid Transitions in Bosonic Atom-Molecule Mixtures near a Feshbach Resonance*. Physical Review Letters **92**, 160402 (2004).

[106] M. Romans, R. Duine, S. Sachdev, and H. Stoof. *Quantum Phase Transition in an Atomic Bose Gas with a Feshbach Resonance*. Physical Review Letters **93**, 020405 (2004).

[107] L. Radzihovsky, P. B. Weichman, and J. I. Park. *Superfluidity and phase transitions in a resonant Bose gas*. arXiv.org (2007).

[108] Y.-W. Lee and Y.-L. Lee. *Quantum phase transition in an atomic Bose gas near a Feshbach resonance*. Physical Review B **70**, 224506 (2004).

[109] A. Koetsier, P. Massignan, R. Duine, and H. Stoof. *Strongly interacting Bose gas: Nozières and Schmitt-Rink theory and beyond*. Physical Review A **79**, 063609 (2009).

[110] R. Combescot, F. Alzetto, and X. Leyronas. *Particle distribution tail and related energy formula*. Physical Review A **79**, 053640 (2009).

[111] J. M. Diederix, T. C. F. van Heijst, and H. T. C. Stoof. *Ground state of a resonantly interacting Bose gas*. Physical Review A **84**, 033618 (2011).

[112] W. Li and T.-L. Ho. *Bose Gases near Unitarity*. Physical Review Letters **108**, 195301 (2012).

[113] P. Fedichev, M. Reynolds, and G. Shlyapnikov. *Three-Body Recombination of Ultracold Atoms to a Weakly Bound s Level*. Physical Review Letters **77**, 2921–2924 (1996).

[114] B. D. Esry, C. H. Greene, and J. P. Burke, Jr. *Recombination of three atoms in the ultracold limit*. Physical Review Letters **83**, 1751 (1999).

[115] E. Nielsen and J. H. Macek. *Low-Energy Recombination of Identical Bosons by Three-Body Collisions*. Physical Review Letters **83**, 1566–1569 (1999).

[116] P. F. Bedaque, E. Braaten, and H. W. Hammer. *Three-body recombination in Bose gases with large scattering length*. Physical Review Letters **85**, 908 (2000).

[117] E. Braaten and H. W. Hammer. *Three-Body Recombination into Deep Bound States in a Bose Gas with Large Scattering Length*. Physical Review Letters **87**, 160407 (2001).

[118] V. N. Efimov. *Weakly-Bound States of 3 Resonantly-Interacting Particles*. Sov. J. Nucl. Phys **12**, 589 (1971).

[119] V. Efimov. *Low-energy properties of three resonantly interacting particles*. Sov. J. Nucl. Phys **29**, 546 (1979).

[120] F. Ferlaino and R. Grimm. *Forty years of Efimov physics: How a bizarre prediction turned into a hot topic*. Physics **3**, 9 (2010).

[121] F. Ferlaino, A. Zenesini, M. Berninger, B. Huang, H. C. Nägerl, and R. Grimm. *Efimov resonances in ultracold quantum gases*. Few-Body Systems pages 1–21 (2011).

[122] T. Kraemer, M. Mark, P. Waldburger, J. G. Danzl, C. Chin, B. Engeser, A. D. Lange, K. Pilch, A. Jaakkola, H. C. Nägerl, and R. Grimm. *Evidence for Efimov quantum states in an ultracold gas of caesium atoms*. Nature **440**, 315–318 (2006).

[123] S. Knoop, F. Ferlaino, M. Mark, M. Berninger, H. Schöbel, H. C. Nägerl, and R. Grimm. *Observation of an Efimov-like trimer resonance in ultracold atom–dimer scattering*. Nature Physics **5**, 227–230 (2009).

[124] M. Zaccanti, B. Deissler, C. D'Errico, M. Fattori, M. Jona-Lasinio, S. Müller, G. Roati, M. Inguscio, and G. Modugno. *Observation of an Efimov spectrum in an atomic system*. Nature Physics **5**, 586–591 (2009).

[125] P. Dyke, S. E. Pollack, and R. G. Hulet. *Finite range corrections near a Feshbach resonance and their role in the Efimov effect*. Physical Review A **88**, 7 (2013).

[126] R. Grimm. *Talk at the BEC 2013 conference*. In *Sant Felliu Spain* (2013).

[127] N. Gross, Z. Shotan, S. Kokkelmans, and L. Khaykovich. *Observation of Universality in Ultracold ^{7}Li Three-Body Recombination*. Physical Review Letters **103**, 163202 (2009).

[128] N. Gross, Z. Shotan, S. Kokkelmans, and L. Khaykovich. *Nuclear-spin-independent short-range three-body physics in ultracold atoms*. Physical Review Letters **105**, 103203 (2010).

[129] M. Berninger, A. Zenesini, B. Huang, W. Harm, H. C. Nägerl, F. Ferlaino, R. Grimm, P. S. Julienne, and J. M. Hutson. *Universality of the Three-Body Parameter for Efimov States in Ultracold Cesium*. Physical Review Letters **107**, 120401 (2011).

[130] S. Roy, M. Landini, A. Trenkwalder, and G. Semeghini. *Test of the Universality of the Three-Body Efimov Parameter at Narrow Feshbach Resonances*. Physical Review (2013).

[131] D. S. Petrov. *Three-boson problem near a narrow Feshbach resonance*. Physical Review Letters **93**, 143201 (2004).

[132] P. Massignan and H. Stoof. *Efimov states near a Feshbach resonance*. Physical Review A **78**, 030701 (2008).

[133] Y. Wang, J. P. D'Incao, and B. D. Esry. *Ultracold three-body collisions near narrow Feshbach resonances*. Physical Review A **83**, 042710 (2011).

[134] M. Lee, T. Köhler, and P. Julienne. *Excited Thomas-Efimov levels in ultracold gases*. Physical Review A **76**, 012720 (2007).

[135] M. Jona-Lasinio and L. Pricoupenko. *Three resonant ultracold bosons: off-resonance effects*. Physical Review Letters **104**, 023201 (2010).

[136] P. Naidon, S. Endo, and M. Ueda. *Physical Origin of the Universal Three-body Parameter in Atomic Efimov Physics*. arXiv.org (2012). URL `http://arxiv.org/abs/1208.3912`.

[137] T. Lompe, T. B. Ottenstein, F. Serwane, A. N. Wenz, G. Zürn, and S. Jochim. *Radio-frequency association of Efimov trimers*. Science **330**, 940–944 (2010).

[138] G. Barontini, C. Weber, F. Rabatti, J. Catani, G. Thalhammer, M. Inguscio, and F. Minardi. *Observation of Heteronuclear Atomic Efimov Resonances*. Physical Review Letters **103**, 043201 (2009).

[139] R. S. Bloom, M.-G. Hu, T. D. Cumby, and D. S. Jin. *Tests of Universal Three-Body Physics in an Ultracold Bose-Fermi Mixture*. Physical Review Letters **111**, 105301 (2013).

[140] N. P. Mehta, S. T. Rittenhouse, J. P. D'Incao, J. von Stecher, and C. H. Greene. *A general theoretical description of N-body recombination*. Physical Review Letters **103**, 4 (2009).

[141] J. P. D'Incao, H. Suno, and B. D. Esry. *Limits on Universality in Ultracold Three-Boson Recombination*. Physical Review Letters **93**, 123201 (2004).

[142] J. P. D'Incao, C. H. Greene, and B. D. Esry. *The short-range three-body phase and other issues impacting the observation of Efimov physics in ultracold quantum gases*. Journal of Physics B: Atomic, Molecular and Optical Physics **42**, 044016 (2009).

[143] B. S. Rem, A. T. Grier, I. Ferrier-Barbut, U. Eismann, T. Langen, N. Navon, L. Khaykovich, F. Werner, D. S. Petrov, F. Chevy, and C. Salomon. *Lifetime of the Bose Gas with Resonant Interactions*. Physical Review Letters **110**, 163202 (2013).

[144] D. S. Petrov and F. Werner. *Lifetime of a Bose gas at and around unitarity*. unpublished pages 1–16 (2013).

[145] N. F. Mott and H. S. W. Massey. *The theory of atomic collisions*. International series of monographs on physics. Clarendon Press (1965).

[146] G. F. Gribakin and V. V. Flambaum. *Calculation of the scattering length in atomic collisions using the semiclassical approximation*. Physical Review A **48**, 546 (1993).

[147] B. Gao. *Solutions of the Schrödinger equation for an attractive* $1/r^6$ *potential*. Physical Review A **58**, 1728–1734 (1998).

[148] B. Gao. *Zero-energy bound or quasibound states and their implications for diatomic systems with an asymptotic van der Waals interaction*. Physical Review A **62**, 050702 (2000).

[149] K. Jones, E. Tiesinga, P. Lett, and P. Julienne. *Ultracold photoassociation spectroscopy: Long-range molecules and atomic scattering*. Reviews of Modern Physics **78**, 483–535 (2006).

[150] P. S. Julienne and F. H. Mies. *Collisions of ultracold. trapped atoms*. Journal of the Optical Society of America B **6**, 2257–2269 (1989).

[151] C. J. Joachain. *Quantum collision theory*. North-Holland (1975). ISBN 9780720402940.

[152] H. Bethe and R. Peierls. *Quantum theory of the diplon*. Proceedings of the Royal Society of London. Series A-Mathematical and Physical Sciences **148**, 146–156 (1935). URL `http://rspa.royalsocietypublishing.org/content/148/863/146.full.pdf`.

[153] A. J. Moerdijk, B. J. Verhaar, and A. Axelsson. *Resonances in ultracold collisions of* ^{6}*Li,* ^{7}*Li, and* ^{23}*Na*. Physical Review A **51**, 4852–4861 (1995).

[154] C. Cohen-Tannoudji, J. Dupont-Roc, and G. Grynberg. *Atom-Photon Interactions: Basic Processes and Applications*. A Wiley-Interscience publication. Wiley (1998). ISBN 9780471293361.

[155] J. Roberts, N. Claussen, S. Cornish, and C. Wieman. *Magnetic Field Dependence of Ultracold Inelastic Collisions near a Feshbach Resonance*. Physical Review Letters **85**, 728–731 (2000).

[156] A. Marte, T. Volz, J. Schuster, S. Durr, G. Rempe, E. van Kempen, and B. Verhaar. *Feshbach Resonances in Rubidium 87: Precision Measurement and Analysis*. Physical Review Letters **89**, 283202 (2002).

[157] G. Smirne, R. M. Godun, D. Cassettari, V. Boyer, C. J. Foot, T. Volz, N. Syassen, S. Durr, G. Rempe, M. D. Lee, K. Góral, and T. Köhler. *Collisional relaxation of Feshbach molecules and three-body recombination in* ^{87}*Rb Bose-Einstein condensates*. Physical Review A **75**, 020702 (2007).

[158] C. A. Regal, C. Ticknor, J. L. Bohn, and D. S. Jin. *Creation of ultracold molecules from a Fermi gas of atoms*. Nature **424**, 47–50 (2003).

[159] M. Bartenstein, A. Altmeyer, S. Riedl, R. Geursen, S. Jochim, C. Chin, J. Denschlag, R. Grimm, A. Simoni, E. Tiesinga, C. Williams, and P. Julienne. *Precise Determination of Li6 Cold Collision Parameters by Radio-Frequency Spectroscopy on Weakly Bound Molecules*. Physical Review Letters **94**, 103201 (2005).

[160] A. Lange, K. Pilch, A. Prantner, F. Ferlaino, B. Engeser, H. C. Nägerl, R. Grimm, and C. Chin. *Determination of atomic scattering lengths from measurements of molecular binding energies near Feshbach resonances*. Physical Review A **79**, 013622 (2009).

[161] G. Zurn, T. Lompe, A. N. Wenz, S. Jochim, P. S. Julienne, and J. M. Hutson. *Precise Characterization of ^{6}Li Feshbach Resonances Using Trap-Sideband-Resolved RF Spectroscopy of Weakly Bound Molecules*. Physical Review Letters **110**, 135301 (2013).

[162] V. Vuletić, A. J. Kerman, C. Chin, and S. Chu. *Observation of Low-Field Feshbach Resonances in Collisions of Cesium Atoms*. Physical Review Letters **82**, 1406–1409 (1999).

[163] J. L. Roberts, N. R. Claussen, J. P. Burke, C. H. Greene, E. A. Cornell, and C. E. Wieman. *Resonant Magnetic Field Control of Elastic Scattering in Cold ^{85}Rb*. Physical Review Letters **81**, 5109–5112 (1998).

[164] C. Chin, V. Vuletić, A. Kerman, and S. Chu. *High Resolution Feshbach Spectroscopy of Cesium*. Physical Review Letters **85**, 2717–2720 (2000).

[165] S. Jochim, M. Bartenstein, G. Hendl, J. Denschlag, R. Grimm, A. Mosk, and M. Weidemuller. *Magnetic Field Control of Elastic Scattering in a Cold Gas of Fermionic Lithium Atoms*. Physical Review Letters **89**, 273202 (2002).

[166] K. M. O'Hara, S. L. Hemmer, S. R. Granade, M. E. Gehm, and J. E. Thomas. *Measurement of the zero crossing in a Feshbach resonance of fermionic ^{6}Li*. Physical Review A **66**, 041401 (2002).

[167] M. Zaccanti, C. D'Errico, F. Ferlaino, G. Roati, M. Inguscio, and G. Modugno. *Control of the interaction in a Fermi-Bose mixture*. Physical Review A **74**, 041605 (2006).

[168] E. Braaten and H. W. Hammer. *Universality in few-body systems with large scattering length*. Physics Reports **428**, 259–390 (2006).

[169] F. Werner. *Trapped cold atoms with resonant interactions: unitary gas and three-body problem*. PhD thesis (2008).

[170] J. Macek, S. Ovchinnikov, and G. Gasaneo. *Solution for boson-diboson elastic scattering at zero energy in the shape-independent model*. Physical Review A **72**, 032709 (2005).

[171] Y. Castin and F. Werner. *Single-particle momentum distribution of an Efimov trimer*. Physical Review A **83**, 063614 (2011).

[172] R. J. Fletcher, A. L. Gaunt, N. Navon, R. P. Smith, and Z. Hadzibabic. *Stability of a Unitary Bose Gas*. Physical Review Letters **111**, 125303 (2013).

[173] U. Eismann. *Unpublished notes*. (2013).

[174] E. Braaten, H. W. Hammer, D. Kang, and L. Platter. *Three-body recombination of identical bosons with a large positive scattering length at nonzero temperature*. Physical Review A **78**, 043605 (2008).

[175] A. Härter, A. Krükow, M. Deiß, B. Drews, E. Tiemann, and J. H. Denschlag. *Population distribution of product states following three-body recombination in an ultracold atomic gas*. Nature Physics **9**, 512–517 (2013).

[176] S. Laurent. *Collisions à trois corps et pertes associées dans un gaz de Bose unitaire*. Report (2013).

[177] L. Khaykovich. *Unpublished notes*. (2013).

[178] O. Luiten, M. Reynolds, and J. Walraven. *Kinetic theory of the evaporative cooling of a trapped gas*. Physical Review A **53**, 381–389 (1996).

[179] M. Abramowitz and I. A. Stegun. *Handbook of Mathematical Functions with Formulas, Graphs, and Mathematical Tables. National Bureau of Standards Applied Mathematics Series 55. Tenth Printing.* ERIC (1972). URL `http://www.eric.ed.gov/ERICWebPortal/recordDetail?accno=ED250164`.

[180] L. Luo, B. Clancy, J. Joseph, J. Kinast, A. Turlapov, and J. E. Thomas. *Evaporative cooling of unitary Fermi gas mixtures in optical traps*. New Journal of Physics **8**, 213–213 (2006).

[181] C. Cohen-Tannoudji. *Année 1996-1997 : Atomes ultrafroids - Piègeage non dissipatif et refroidissement évaporatif*. pages 1–103 (1996). URL `http://www.phys.ens.fr/cours/college-de-france/1995-96/1995-96.pdf`.

[182] E. Mandonnet, A. Minguzzi, R. Dum, I. Carusotto, Y. Castin, and J. Dalibard. *Evaporative cooling of an atomic beam*. The European Physical Journal D-Atomic, Molecular, Optical and Plasma Physics **10**, 9–18 (2000).

[183] L. Tarruell. *Superfluidité dans un gaz de fermions ultrafroids*. PhD thesis, tel.archives-ouvertes.fr (2008). URL `http://tel.archives-ouvertes.fr/view_by_stamp.php?&halsid=ofn9lk05vf2c94po002bdjaef1&label=LKB-THESE&langue=en&action_todo=view&id=tel-00429181&version=1&view=extended_view`.

[184] S. Nascimbène. *Thermodynamique des gaz de fermions ultrafroids*. PhD thesis, École Normale Supérieure (2010). URL `http://hal.archives-ouvertes.fr/tel-00491711/`.

[185] N. Navon. *Thermodynamics of ultracold Bose and Fermi gases Thermodynamique des gaz de bosons et fermions ultrafroids*. PhD thesis, École Normale Supérieure (2011).

[186] W. R. Veazey, C. D. Hodgman, and Chemical Rubber Company. *Handbook of Chemistry and Physics*. Chemical Rubber Publishing Company (1914).

[187] J. S. Coursey, D. J. Schwab, J. J. Tsai, and R. A. Dragoset. *Atomic Weights and Isotopic Compositions (version 3.0)* (2013). URL `http://physics.nist.gov/Comp[2013,September10]`.

[188] U. Eismann, F. Gerbier, C. Canalias, A. Zukauskas, G. Trénec, J. Vigué, F. Chevy, and C. Salomon. *An all-solid-state laser source at 671 nm for cold-atom experiments with lithium*. Applied Physics B: Lasers and Optics **106**, 25–36 (2012).

[189] U. Eismann, B. Andrea, C. Salomon, and F. Chevy. *2.1-watts intracavity-frequency-doubled all-solid-state light source at 671 nm for laser cooling of lithium*. Optics Express **21**, 9091–9102 (2013).

[190] W. Phillips and H. Metcalf. *Laser Deceleration of an Atomic Beam*. Phys.Rev.Lett. **48**, 596–599 (1982).

[191] W. H. Wing. *On neutral particle trapping in quasistatic electromagnetic fields*. Progress in Quantum Electronics **8**, 181–199 (1984).

[192] A. Migdall, J. Prodan, W. Phillips, T. Bergeman, and H. Metcalf. *First Observation of Magnetically Trapped Neutral Atoms*. Physical Review Letters **54**, 2596–2599 (1985).

[193] D. E. Pritchard. *Cooling neutral atoms in a magnetic trap for precision spectroscopy*. Physical Review Letters **51**, 1336 (1983).

[194] G. Ferrari. *Piégeage simultané des isotopes fermionique et bosonique du lithium, étude théorique de la relaxation collisionelle dans un gaz de Fermi dégénéré*. PhD thesis, tel.archives-ouvertes.fr (2000). URL `http://tel.archives-ouvertes.fr/tel-00006145`.

[195] F. Schreck, G. Ferrari, K. Corwin, J. Cubizolles, L. Khaykovich, M.-O. Mewes, and C. Salomon. *Sympathetic cooling of bosonic and fermionic lithium gases towards quantum degeneracy*. Physical Review A **64**, 011402 (2001).

[196] A. E. Siegman. *Lasers*. University Science Books (1986). ISBN 9780935702118.

[197] J. M. Gerton, C. A. Sackett, B. J. Frew, and R. G. Hulet. *Dipolar relaxation collisions in magnetically trapped ^{7}Li*. Physical Review A **59**, 1514 (1999).

[198] L. Landau. *On the theory of transfer of energy at collisions II*. Phys. Z. Sowjetunion **2**, 46 (1932).

[199] C. Zener. *Non-adiabatic crossing of energy levels*. Proceedings of the Royal Society of London. Series A, Containing Papers of a Mathematical and Physical Character **137**, 696–702 (1932). URL `http://www.jstor.org/stable/10.2307/96038`.

[200] C.-L. Hung, X. Zhang, N. Gemelke, and C. Chin. *Accelerating evaporative cooling of atoms into Bose-Einstein condensation in optical traps*. Physical Review A **78**, 011604 (2008).

[201] N. Gross, Z. Shotan, O. Machtey, S. Kokkelmans, and L. Khaykovich. *Study of Efimov physics in two nuclear-spin sublevels of 7 Li*. Comptes Rendus Physique **12**, 4–12 (2011).

[202] S. E. Pollack, D. Dries, and R. G. Hulet. *Universality in Three- and Four-Body Bound States of Ultracold Atoms*. Science **326**, 1683–1685 (2009).

[203] H. C. Naegerl, T. Kraemer, M. Mark, P. Waldburger, J. G. Danzl, B. Engeser, A. D. Lange, K. Pilch, A. Jaakkola, C. Chin, and R. Grimm. *Experimental Evidence for Efimov Quantum States*. arXiv.org (2006). URL `http://arxiv.org/abs/cond-mat/0611629`.

[204] A. G. Sykes, J. P. Corson, J. P. D'Incao, A. P. Koller, C. H. Greene, A. M. Rey, K. R. A. Hazzard, and J. L. Bohn. *Quenching to unitarity: Quantum dynamics in a 3D Bose gas*. arXiv.org (2013). URL `http://arxiv.org/abs/1309.0828v1`.

[205] F. A. Van Abeelen and B. J. Verhaar. *Time-dependent Feshbach resonance scattering and anomalous decay of a Na Bose-Einstein condensate*. Physical Review Letters **83**, 1550 (1999).

[206] F. H. Mies, E. Tiesinga, and P. S. Julienne. *Manipulation of Feshbach resonances in ultracold atomic collisions using time-dependent magnetic fields*. Physical Review A **61**, 022721 (2000).

[207] E. Timmermans, P. Tommasini, M. Hussein, and A. Kerman. *Feshbach resonances in atomic Bose–Einstein condensates*. Physics Reports **315**, 199–230 (1999).

[208] A. T. Grier. *Unpublished notes*. (2012).

[209] M. Berninger, A. Zenesini, B. Huang, W. Harm, H.-C. Nägerl, F. Ferlaino, R. Grimm, P. S. Julienne, and J. M. Hutson. *Feshbach resonances, weakly bound molecular states, and coupled-channel potentials for cesium at high magnetic fields*. Physical Review A **87**, 032517 (2013).

[210] C. D'Errico, M. Zaccanti, M. Fattori, G. Roati, M. Inguscio, G. Modugno, and A. Simoni. *Feshbach resonances in ultracold ^{39}K*. New Journal of Physics **9**, 223 (2007).

[211] U. Eismann. *A novel all-solid-state laser source for lithium atoms and three-body recombination in the unitary Bose gas*. PhD thesis, hal.archives-ouvertes.fr (2012). URL `http://hal.archives-ouvertes.fr/docs/00/70/28/65/PDF/Thesis_Ulrich_Eismann.pdf`.

[212] J. J. R. M. van Heugten and H. T. C. Stoof. *Resummation of infrared divergencies in the theory of atomic Bose gases*. arXiv.org (2013). URL `http://arxiv.org/abs/1306.1104`.

[213] S. Piatecki and W. Krauth. *Efimov-driven phase transitions of the unitary Bose gas*. arXiv.org (2013). URL `http://arxiv.org/abs/1307.4671v1`.

[214] P. Makotyn, C. E. Klauss, D. L. Goldberger, E. A. Cornell, and D. S. Jin. *Universal dynamics of a degenerate unitary Bose gas*. arXiv.org (2013). URL `http://arxiv.org/abs/1308.3696`.

[215] S. Tan. *Large momentum part of fermions with large scattering length*. arXiv.org (2005). URL `http://arxiv.org/abs/cond-mat/0508320`.

[216] S. Tan. *Energetics of a strongly correlated Fermi gas*. Annals of Physics **323**, 2952–2970 (2008). URL `http://www.sciencedirect.com/science/article/pii/S0003491608000456`.

[217] K. Aikawa, A. Frisch, M. Mark, S. Baier, A. Rietzler, R. Grimm, and F. Ferlaino. *Bose-Einstein Condensation of Erbium*. Physical Review Letters **108**, 210401 (2012).

[218] J. Weiner, V. S. Bagnato, S. Zilio, and P. S. Julienne. *Experiments and theory in cold and ultracold collisions*. Reviews of Modern Physics **71**, 1 (1999).

[219] K. Maeda, G. Baym, and T. Hatsuda. *Simulating Dense QCD Matter with Ultracold Atomic Boson-Fermion Mixtures*. Physical Review Letters **103**, 085301 (2009).

[220] M. Delehaye. *Etude de quelques propriétés d'un gaz quantique de Lithium*. Report (2012).

[221] T.-L. Ho and V. Shenoy. *Binary Mixtures of Bose Condensates of Alkali Atoms*. Physical Review Letters **77**, 3276–3279 (1996).

[222] N. Claussen, S. Kokkelmans, S. Thompson, E. Donley, E. Hodby, and C. Wieman. *Very-high-precision bound-state spectroscopy near a ^{85}Rb Feshbach resonance*. Physical Review A **67**, 060701 (2003).

Abstract

Ultracold gases have become versatile systems to study quantum many-body effects. Their high degree of control and the tunability of the atomic interactions led to important advances in the understanding of strongly correlated matter. In the regime of strong interactions, unlike fermions, the study of bosons is hampered by three-particle recombination that leads to atom losses and keeps the system from reaching a real equilibrium state.

In this thesis, we have performed the first quantitative comparison between theory and experiment on the three-particle loss coefficient $L_3(a,T)$, for arbitrary scattering length a and temperature T. For unitary two-particle scattering ($|a| \to \infty$), we show that the three-particle loss coefficient follows the law $L_3(\infty,T) = \lambda_3/T^2$, that we have tested using a trapped non-degenerate ^{7}Li gas maintained at constant temperature. The measured value of $\lambda_3 = 2.5(3)_{\text{stat}}(6)_{\text{syst}} \times 10^{-20}(\mu\text{K})^2\text{cm}^6\text{s}^{-1}$ is, within the error bars in good agreement with the theory prediction $\lambda_3^{\text{th}} = 1.52 \times 10^{-20}(\mu\text{K})^2\text{cm}^6\text{s}^{-1}$.

We have extended our measurements to arbitrary values of the scattering length a. For $a<0$, the theory predicts a smooth connection between the previously derived zero-temperature model for $L_3(a,0)$ and the unitarity limited loss coefficient $L_3(\infty,T)$. We also show that a second Efimov resonance in ^{7}Li should be observable near $a \sim -500\ a_0$ for a temperature of 1 μK. Finally, we compare our theoretical prediction with measurements performed at Innsbruck with ^{133}Cs and at Cambridge with ^{39}K. The theory also shows remarkable quantitative agreement with these measurements.

Keywords: ultracold gases - strongly interacting Bose gas - Efimov Physics - three-particle problem - three-particle recombination - few-particle physics.

Résumé

Les gaz d'atomes ultra-froids sont devenus des systèmes polyvalente pour l'étude des effets à N corps. Le haut degré de contrôle qu'ils offrent ainsi que la possibilité de modifier les interactions inter-atomiques ont permis des avancées importantes dans la compréhension des états fortement corrélés de la matière. Dans le régime d'interactions fortes, l'étude des bosons, contrairement à celle des fermions, est entravée par la recombinaison à trois particules qui induisent des pertes d'atomes et empêche le système d'atteindre un réel état d'équilibre.

Dans cette thèse, nous présentons la première comparaison théorie-expérience quantitative du coefficient de perte à trois corps $L_3(a,T)$, pour des valeurs arbitraires de la longueur de diffusion a et de température T. Pour la diffusion à deux corps unitaire ($|a| \to \infty$), nous montrons que le coefficient de pertes à trois corps suit la loi $L_3(\infty,T) = \lambda_3/T^2$, ce que nous avons testé en étudiant un gaz piégée non-dégénéré de ^{7}Li maintenu à température constante. La valeur mesurée de $\lambda_3 = 2.5(3)_{\text{stat}}(6)_{\text{syst}} \times 10^{-20}(\mu\text{K})^2\text{cm}^6\text{s}^{-1}$ est, à la précision expérimentale, en bon accord avec la prédiction théorique $\lambda_3^{\text{th}} = 1.52 \times 10^{-20}(\mu\text{K})^2\text{cm}^6\text{s}^{-1}$.

Nous avons étendu ces mesures à des valeurs arbitraires de la longueur de diffusion. Pour $a<0$, la théorie se raccorde à un modèle à température effective nulle pré-existant et le régime unitaire. Nous montrons aussi qu'une seconde résonance d'Efimov devrait être observable autour de $a = -500\ a_0$ pour une température de 1 μK. Finalement, nous comparons la prédiction théorique est confirmée par les mesures effectuées à Innsbruck avec le ^{133}Cs et à Cambridge avec le ^{39}K.

Mots-clés : gaz quantiques, Gaz de Bose en interactions fortes, physique d'Efimov, problème à trois corps, recombinaison à trois corps, physique à peu de corps.